COMPUTATIONAL FLUID DYNAMICS STUDY OF AIRFLOW AND PARTICLE DEPOSITION IN DISEASED NASAL AIRWAY

VIZY NAZIRA BINTI RIAZUDDIN

SEPTEMBER 2017

DEPARTMENT OF AEROSPACE ENGINEERING,
FACULTY OF ENGINEERING
UNIVERSITI PUTRA MALAYSIA

DEPARTMENT OF BIOLOGICAL FUNCTIONS ENGINEERING
GRADUATE SCHOOL OF LIFE SCIENCES AND SYSTEM ENGINEERING
KYUSHU INSTITUTE OF TECHNOLOGY

COMPUTATIONAL FLUID DYNAMICS STUDY OF AIRFLOW AND PARTICLE DEPOSITION IN DISEASED NASAL AIRWAY

Name:	**Vizy Nazira binti Riazuddin**
Student Number:	**GS37711 (UPM) and 14899037 (KIT)**
Supervisor:	**Assoc. Prof. Ir. Dr. Kamarul Arifin bin Ahmad**
	Prof. Dr. Masaaki Tamagawa

DEPARTMENT OF AEROSPACE ENGINEERING,
FACULTY OF ENGINEERING
UNIVERSITI PUTRA MALAYSIA

DEPARTMENT OF BIOLOGICAL FUNCTIONS ENGINEERING
GRADUATE SCHOOL OF LIFE SCIENCES AND SYSTEM ENGINEERING
KYUSHU INSTITUTE OF TECHNOLOGY

ACKNOWLEDGEMENT

Alhamdulillah, all praise to Allah for blessing me with opportunity, strength and patience to conduct this study and complete this thesis.

First and foremost, I would like to take this opportunity to thank my supervisors, Assoc. Prof. Ir. Dr. Kamarul Arifin Ahmad and Prof. Dr. Masaaki Tamagawa for their continuous supervision, patient guidance and enthusiastic support throughout my study.

I would also like to express my appreciation to Assoc. Prof. Dr. Mohammad Zubair for his guidance in carrying out this work. My sincere appreciation also goes Dr. Nur Hashima Abdul Rashid who provided me the CT of upper airway image data so that I could start my research at the first place. I am also very grateful for her thoughtful advices and continuous guidance. I would also like to thank Dr. Norkhairunnisa Mazlan for her helpful advice. I am also grateful to Prof. Dr. Hiroshi Yamada and Prof. Dr. Hiroshi Ishiguro for their research advice. Special thanks also go to Mr. Mohamad Nasir Johari and Mr. Saffairus Salih for their help in setting up my experimental test rig.

I particularly acknowledge the research grant support provided through the Geran Putra Institut Pengajian Siswazah (IPS), project code GP-IPS/2015/9461700 by Universiti Putra Malaysia in carrying out this research work and also the support from Universiti Putra Malaysia through Special Graduate Research Assistant (SGRA) scholarship scheme during the last term of my study. I would also like to thank Japan Student Service Organization (JASSO) for the scholarship provided during my research stay in Japan. I sincerely thank the Malaysian government for the given scholarship through MYBRAIN scheme.

I would also like to thank my research colleague at Kyushu Institute of Technology and Universiti Putra Malaysia for their friendship and joyful memories. I would like to thank my parents, Riazuddin Ahmad Ali and Norizan Osman, and my father and

mother in law, Mohd Suan Tulis and Karsiah Bakri for their endless pray for my success. My sincere gratitude also goes to my dearest husband Mohd Shahadan Mohd Suan for his unconditional love, patience and encouragement through the ups and downs of my PhD journey. Last but not least to my dearest son, Muhammad Eusoff Muzaffar bin Mohd Shahadan, this thesis is dedicated to you.

TABLE OF CONTENTS

LIST OF FIGURES

LIST OF TABLES

LIST OF ABBREVIATIONS

2D	Two Dimensional
3D	Three Dimensional
AR	Acoustic Rhinometry
AAR	Active Anterior Rhinometry
BMI	Body Mass Index
CAD	Computer Aided Design
CFD	Computational Fluid Dynamics
CPAP	Continuous Positive Airway Pressure
CT	Computed Tomography
DE	Deposition Efficiency
DF	Deposition Fraction
DICOM	Digital Imaging and Communications in Medicine
DPM	Discrete Phase Modeling
DSE	Digitized Shape Editor
ENT	Ear Nose and Throat
EPA	Environmental Protection Agency
FESS	Functional Endoscopic Sinus Surgery
FSI	Fluid Structure Interaction
HU	Hounsfield Units
IGES	Initial Graphics Exchange Specification
LES	Large Eddy Simulation
LRN	Low Reynolds Number

MAS	Mandibular Advancement Splint
MMA	Middle Meatal Anstrostomy
MRI	Magnetic Resonance Image
NA	Not Available
NAR	Nasal Airway Resistance
OSA	Obstructive Sleep Apnea
PIV	Particle Image Velocimetry
RANS	Reynolds Averaged Navier Stokes
SST	Shear Stress Transport
UPPP	Uvulapalatopharyngoplasty
US	United States
USM	Universiti Sains Malaysia

LIST OF PUBLICATIONS

Journals

1. **V.N. Riazuddin**, M. Zubair, M. Ahmadi, M. Tamagawa, N.H.A. Rashid, N. Mazlan, K. A. Ahmad, 2016, Computational Fluid Dynamics study of airflow and microparticle deposition in a constricted pharyngeal section representing obstructive sleep apnea disease, Journal of Medical Imaging and Health Informatics, 6(6), pp. 1507-1512. (Published)
2. **V.N. Riazuddin**, K. A. Ahmad, M. Tamagawa, M. Zubair, N.H.A. Rashid, N. Mazlan, F. Mustapha, Numerical simulation of airflow and aerosol deposition in realistic human upper airway with chronic nasal obstruction and obstructive sleep apnea: pre- and post-surgery, PLoS ONE. (Submitted)
3. M. Ahmadi, M. Zubair, K.A. Ahmad, **V.N. Riazuddin**, Study on nasal deposition of micro particles and its relationship to airflow structure, 2016, International Journal of Fluids and Heat Transfer, 1(1), pp. 2-12. (Published)
4. E. Basri, A. Basri, **V.N. Riazuddin**, S.F. Shahwir, M.Zubair, K.A. Ahmad, Computational fluid dynamics study in biomedical applications: A review, 2016, International Journal of Fluids and Heat Transfer, 1(2), pp. 2-14. (Published)
5. M. Zubair, **V.N. Riazuddin**, K.A. Ahmad, Numerical study on the effect of gender on the airflow characteristics inside the nasal cavity, 2015, International Journal of Advanced Thermofluid Research, 1(1), pp. 2-16. (Published)
6. M. Zubair, **V.N. Riazuddin**, M.Z. Abdullah, I. Rushdan, I.L. Shuaib, K.A. Ahmad, Computational fluid dynamics study of pull and plug flow boundary condition on nasal airflow, 2013, Biomedical Engineering: Applications, Basis and Communications, 25(4), pp. 1-8. (Published)
7. M. Zubair, **V.N. Riazuddin**, K.A. Ahmad, S.M.A. Khader, A.A. Basri, Numerical study of a nasal cavity model having a constricted pharyngeal section representing obstructive sleep apnea, 2017, Journal of Computational Methods in Sciences and Engineering, 17, pp. 219-226. (Published)

8. M. Zubair, **V.N. Riazuddin**, M.Z. Abdullah, I. Rushdan, I.L. Shuaib, K.A. Ahmad, 2013, Computational fluid dynamics study of the effect of posture on airflow characteristics inside the nasal cavity, Asian Biomedicine, 7(6), pp. 835-840.

Conference Presentations

1. **V.N. Riazuddin**, K. A. Ahmad, M. Tamagawa, M. Zubair, M. Ahmadi, N.H.A. Rashid, N. Mazlan, F. Mustapha, Numerical investigation of inspiratory and expiratory airflow in a human upper airway with chronic nasal obstruction and obstructive sleep apnea, 4rd International Conference on Computational Methods in Engineering and Health Sciences (ICCMEH 2017), Manipal University, Kartanaka, India. (19-20 December 2017). (Abstract accepted)
2. **V.N. Riazuddin**, K. A. Ahmad, M. Zubair, M. Tamagawa, N.H.A. Rashid, N. Mazlan, Numerical simulation of airflow in diseased human nasal airway, Mechanical Engineering Research Day 2017 (MERD 2017), Universiti Teknikal Malaysia Melaka, Malaysia (30 March 2017).
3. **V.N. Riazuddin**, K. A. Ahmad, M. Zubair, M. Tamagawa, N.H.A. Rashid, N. Mazlan, Numerical investigation of airflow characteristics in a diseased nasal cavity with OSA: Pre- And Post-surgery, 3rd International Conference on Computational Methods in Engineering and Health Sciences (ICCMEH 2016), Kyushu Institute of Technology, Fukuoka, Japan (17-18 December 2016).
4. **V.N. Riazuddin,** K. A. Ahmad, M. Zubair, M. Tamagawa, N.H.A. Rashid, N. Mazlan, Numerical investigation on airflow characteristics in nasal cavity having turbinate hypertrophy, concha bullosa, and septum deviation: Pre- and Post-surgery, 4th International Symposium on Applied Engineering and Sciences (SAES 2016), Kyushu Institute of Technology, Fukuoka, Japan (17-18 December 2016).
5. **V.N. Riazuddin**, M. Zubair, M. Tamagawa, N.H.A. Rashid, K. A. Ahmad, Computational Fluid Dynamics study of airflow and micro-particles deposition in a constricted pharyngeal representing Obstructive Sleep Apnea, 2nd International Conference on Computational Methods in Engineering and Health Sciences (ICCMEH 2015), Universiti Putra Malaysia, Malaysia (19-20 December 2015).
6. **V.N. Riazuddin**, M. Zubair, M. Tamagawa, N.H.A. Rashid, K. A. Ahmad, Computational Fluid Dynamics study of airflow in upper airway with Obstructive

Sleep Apnea- A Review, Biomedical Fuzzy System Association 2015 (BMFSA 2015), Tokai University, Kumamoto, Japan (21-22 November 2015).

7. M. Ahmadi, M. Kojourimanesh, M. Zubair, **V.N. Riazuddin**, CFD analysis of mucus effect in the nasal cavity, 4rd International Conference on Computational Methods in Engineering and Health Sciences (ICCMEH 2017), Manipal University, Kartanaka, India. (19-20 December 2017).
8. M. Ahmadi, M. Zubair, **V.N, Riazuddin,** K.A. Ahmad, Study on nasal deposition of micro particles and its relationship to airflow structure, 2nd International Conference on Computational Methods in Engineering and Health Sciences, Universiti Putra Malaysia, Malaysia (19-20 December 2015).
9. E. Basri, M. Zubair, **V.N Riazuddin**, K.A. Ahmad, Computational fluid dynamics study in biomedical applications, 2nd International Conference on Computational Methods in Engineering and Health Sciences, Universiti Putra Malaysia, Malaysia (19-20 December 2015).
10. M. Tamagawa, R. Motooka, **V.N. Riazuddin**, K.A. Ahmad, CFD based prediction of Thrombus Formation Rate in Shear Blood Flows, Symposium on Applied Engineering and Sciences, Kyushu Institute of Technology, Japan (20-21 December 2014).

ABSTRACT

COMPUTATIONAL FLUID DYNAMICS STUDY OF AIRFLOW AND PARTICLE DEPOSITION IN DISEASED NASAL AIRWAY

Understanding the properties of airflow in the nasal cavity is very important in determining the nasal physiology and in diagnosis of various anomalies associated with the nose. The complex anatomy of the nasal cavity has proven to be a significant obstacle in the understanding of nasal obstructive disorders. Due to their non-invasiveness, Computational Fluid Dynamics (CFD) has now been utilized to assess the effects of surgical interventions on nasal morphological changes as well as local breathing airflow characteristics through the upper airway of individual patients. Furthermore, nasal inhalation is a major route of entry into body for airborne pollutions. Therefore, the function of the upper airway to filter out the inhaled toxic particles is considered important. The determination of the total particle filtering efficiency and the precise location of the induced lesion in the upper airway is the first step in understanding the critical factors involved in the pathogenesis of the upper airway injury. The present work involved development of three-dimensional diseased upper airway models from Computed Tomographic (CT) scan images derived from a nasal airway without any nasal diseased and an upper airway which was diagnosed with chronic nasal obstruction and obstructive sleep apnea. Numerical simulation of airflow and transport and deposition of inhaled pollutant through chronic diseased nasal airway, constricted pharyngeal representing Obstructive Sleep Apnea (OSA) and diseased upper airway with OSA for pre- and post-operative cases have been studied. Detailed flow pattern and characteristics for inspiratory airflow for various breathing rates (7.5-40 L/min) were evaluated. Simulation of the particle transport and

deposition of micro-sized particles with particle diameter ranging from 1-40 μm were also investigated. In the first part of this study, the surgical treatment performed in the nasal cavity which include septoplasty, inferior turbinate reduction and partial concha bullosa resection substantially increased nasal volume, which influenced flow partitioning and decreases the pressure drop and flow resistance of the nasal passage. The removal of the obstruction in the nasal airway significantly improve the breathing quality. However, the nasal airway experienced approximately about a 50 % decrease in total particle filtering efficiency after surgery. Therefore, careful consideration should be given to this matter before nasal operation especially for a patient with breathing allergic history. In the second part of this study, the morphology of the constricted pharyngeal representing OSA was found to significantly affect the airflow pattern and the deposition fraction of microparticles. The morphology of the upper airway, the size of the inhaled particle and breathing rate was found significantly affect the total particle deposition efficiency and local deposition fraction in the upper airway. The presented regional deposition fraction may be used in specifying the site of highest possibility for respiratory lesions according to the breathing rate and the size of the inhaled toxic particles. Results obtained from this study can be also used to estimate the location of airway obstruction in upper airway of patient with sleep apnea symptom. In the third part of this study, the surgical conducted procedure has cleared out the obstructions in the nasal airway hence improve the airflow distribution through the upper airway during inhalation process. This study shows that the nasal surgery alone can help improve the breathing quality in the upper airway with OSA. The reduction of the airflow resistance in the nasal cavity affect the pressure distribution in the lower part of the upper airway. Obstruction in the nasal passage and sudden airway expansion in the upper airway increased number of particles trap, recirculated and finally

deposited in the airway. Finally, the experimental data obtained from the experimental study utilizing the developed pharyngeal airway further validate the result obtained from the numerical study.

I certify that a Thesis Examination Committee has met on (date of viva voce) to conduct the final examination of Vizy Nazira binti Riazuddin on her thesis entitled "Computational Fluid Dynamics Study of Airflow and Particle Deposition in Diseased Nasal Airway" in accordance with the Universities and University Colleges Act 1971 and the Constitution of the Universiti Putra Malaysia [P.U.(A) 106] 15 March 1998. The Committee recommends that the student be awarded the Doctor of Philosophy.

Members of the Thesis Examination Committee were as follows:

Prof. Dr. Hiroshi Yamada, PhD
Professor
Department of Biological Function Engineering
Graduate School of Life Science and Systems Engineering
Kyushu Institute of Technology
Japan
(Chairman)

Prof. Ir. Dr. Mohd Khairol Anuar bin Mohd Aiman, PhD
Professor
Department of Mechanical and Manufacturing Engineering
Faculty of Engineering
Universiti Putra Malaysia
(Internal Examiner)

Prof. Dr. Koji Miyazaki, PhD
Professor
Department of Mechanical and Control Engineering
Faculty of Engineering
Kyushu Institute of Technology
Japan
(Internal Examiner)

Prof. Dr. Susumu Kudo, PhD
Professor
Department of Mechanical Engineering
Faculty of Engineering
Kyushu University
Japan
(External Examiner)

_____
NAME OF DEPUTY DEAN, PhD
Professor and Deputy Dean
School of Graduate Studies
Universiti Putra Malaysia
Date:

This thesis was submitted to the Senate of Universiti Putra Malaysia and has been accepted as fulfilment of the requirement for the degree of Doctor of Philosophy. The members of the Supervisory Committee were as follows:

Kamarul Arifin Ahmad, PhD
Associate Professor Ir.
Faculty of Engineering
Universiti Putra Malaysia
(Chairman)

Masaaki Tamagawa, PhD
Professor
Department of Biological Function & Engineering
Graduate School of Life Science and Systems Engineering
Kyushu Institute of Technology
Japan
(Member)

Hiroshi Yamada, PhD
Professor
Department of Biological Function & Engineering
Graduate School of Life Science and Systems Engineering
Kyushu Institute of Technology
Japan
(Member)

Hiroshi Ishiguro, PhD
Professor
Department of Biological Function & Engineering
Graduate School of Life Science and Systems Engineering
Kyushu Institute of Technology
Japan
(Member)

_____
BUJANG BIN KUM HUAT, PhD
Professor and Dean
School of Graduate Studies
Univeristi Putra Malaysia
Date:

CHAPTER 1

INTRODUCTION

1.1 Research Background

Upper airway which consisted of nasal cavity and pharynx is one of the most important components of human respiratory system. It provides the first line protection for lung by warming and humidifying the inspired air. Upper airway plays an important role to filter out the inhaled air from airborne contaminated particles, bacteria and pathogen. However, the success of upper airway physiological function is highly dependent on the fluid dynamics characteristic of airflow through the airway passage. Hence, better understanding of airflow characteristic and transport and deposition of inhaled particle through the upper airway is essential to understand the physiology of upper airway breathing pattern.

During inhalation, upper airway also plays an important role to filter out the inhaled toxic and contaminated particles from the polluted atmospheric air. Both the fine and coarse particles which enter the breathing airway during inhalation, not only can induce irritation, moreover, with extensive exposure and high concentration of inhaled airborne toxic and infectious particle, the airway is susceptible to chronic injury and could further aggravate upper airway disorder (Harkema *et al*., 2006). Harkema *et al*., (2006) and Grotberg (2001) also reported that the determination of the precise location of the induced lesion in the upper airway is the first step in understanding the critical factors involved in the pathogenesis of the upper airway

injury. As we already know that the toxic and contaminated particles could harm and affect the health of the human population. Hence it is important to investigate and improve understanding of the airflow distribution and particle transport and deposition in the human nasal airway. The location of the particle deposition in an airway is important information for correlating inhaled toxins or carcinogens to disease locations and for developing potential therapies.

Airflow through human upper airway has been studied numerically and experimentally by a number researchers (Garcia *et al*., 2007; Kim & Chung, 2004; Mylavarapu *et al*., 2009; Segal *et al*., 2008; Weinhold & Mlynski, 2004; Wen *et al*., 2008; Xiong et al., 2008). Furthermore, several researchers have undertaken studies pertaining to airflow through nasal cavity using measuring devices such as rhinomanometry and acoustic rhinometry (Hilberg *et al*., 1989; Jones & Lancer, 1987; Shelton & Eiser, 1992; Sipila & Suonpaa, 1997; Suzina *et al.*, 2003).

Rhinomanometry is used to measure the pressure required to produce airflow through the nasal airway and acoustic rhinometry is used to measure the cross-sectional area of the airway at various nasal planes. However, measuring the precise velocity of airflow and evaluating the local nasal resistance in every portion of the nasal cavity have proven to be difficult (Ishikawa *et al*., 2009). The anatomical complexity of the nasal cavity makes it difficult for the measurement of nasal resistance. The small sizes of the nasal cavity and its narrow flow passage can cause perturbations in the airflow with any inserted probe. Moreover, the reliability of the result obtained using this device depends on optimal cooperation from the subject, correct instructions from the investigator, and standardized techniques (Kjaergaard *et*

al., 2009). There are reports of failure rates of between 25 % and 50 % in the subjects examined by rhinomanometry (Austin & Foreman, 1994). Furthermore, direct measurement of the total particle deposition efficiency and local deposition fraction of inhaled contaminated particle in the human upper airway are highly impossible.

Due to the inherent limitations of the available measuring devices, Computational Fluid Dynamics (CFD) has been proposed as a viable alternative. CFD which refers to use of numerical methods to solve the partial differential equation governing the flow of a fluid, is becoming an increasingly popular research tool in fluid dynamics (Basri *et al*., 2016). The non-invasive CFD modelling allows investigation of a wide variety of flow situations and particle deposition through human upper airway. Several researchers have conducted studies on the airflow and particle transport and deposition through the human upper airway by using the CFD simulation technique (Abouali *et al*., 2012; Bahmanzadeh *et al*., 2015; Dastan *et al*., 2014; Ghalati *et al*., 2012; Riazuddin *et al*., 2011).

In the present study, initially the effect of nasal obstruction which include septum deviation, turbinate hypertrophy and concha bullosa were investigated. A comparative study was made between the pre- and post-operative model. The effect of nasal surgery on inhaled particle filtering function was also investigated. In order to improve the understanding of the pathophysiology of the Obstructive Sleep Apnea (OSA) disease, numerical simulation of inspiratory airflow through a constricted pharyngeal section representing OSA symptom was conducted. Studies were carried out for various flow rates of 7.5 L/min, 10 L/min, 20 L/min, 30 L/min and 40 L/min suggesting various breathing rates. Lagrangian particle tracking approach was used to

investigate the effect of the constricted pharyngeal section on the deposition rate and deposition patterns of microparticles. Microparticles in the size range of 1-40 μm were injected at the nostril inlet and the particle trajectories and regional deposition fractions of the particles were analyzed.

In order to investigate the effect of chronic nasal obstruction on the upper airway diagnosed with OSA disease, numerical simulation of airflow and aerosol deposition in a realistic human upper airway with chronic nasal airway and obstructive sleep apnea symptom for pre- and post-surgery were performed. Different inhalation rates of steady laminar airflows suggesting low breathing activity were simulated numerically through the upper airway models. The airflow characteristics and breathing resistance were analyzed. Lagrangian trajectory analysis approach was used to examine the transport and deposition of the inhaled microparticles through the upper airways before and after surgery. The focus of the final part of this study is to develop an experimental setup and perform experimental work on a pharyngeal airway model to compare and validate the results obtained from numerical study with that of experiment.

1.2 Problem Statement

Although treatment methods in upper airway surgery have constantly improved over time, due to the narrow and complicated structure of the human nasal airway and anatomical differences between each individual, the prediction of a successful individual therapy remains a challenging task. Hence, further studies are needed to improve the diagnosis method and the quality of the future upper airway surgical treatment. The highly detailed anatomy of the pre- and post-operative morphological

upper airway model and information derived from CFD analysis would be able to provide relevant information prior to a surgical intervention and medical treatment. The analyzed data of detailed aerodynamic behavior of the upper airways can be made available to the ENT surgeons so that it can be used to assist them in identifying possible sites of obstruction and direct toward the anatomic site of obstruction for surgical intervention. The location of the particle deposition in an airway can provide important information for correlating inhaled toxins or carcinogens to disease locations and for developing potential therapies. The main outcome will lead to the improvement of the diagnostics methodologies or even improved treatment strategies and outcome.

1.3 Research Objectives

The overall objective of the present study is focused on the investigation of the airflow characteristics and inhaled particle deposition in the diseased human upper airway. The main aims include:

i. To develop a three-dimensional computational model of human nasal airway for pre- and post-operative nasal computational models.
ii. To perform CFD analysis on both the pre- and post-operative diseased nasal airway.
iii. To analyze the impact of abnormal nasal passage on airflow characteristics and aerosol deposition.
iv. To investigate the effect of deformation of the pharyngeal section on the airflow and particle deposition in the human upper airway.

v. To develop experimental setup and perform experimental study to validate the results obtained from the numerical study.

1.4 Scope of Work

This research work was first carried out by procuring Computed Tomography (CT) scan images of the normal and diseased human upper airway. For the normal nasal airway, the CT scan data was provided by a radiologist from the Advanced Medical and Dental Institute, Universiti Sains Malaysia. For the diseased upper airway, the CT scan data was provided by a Head and Neck Surgeon from Hospital Serdang, Malaysia. A research proposal was prepared and submitted to the committee of the Clinical Research Centre and the Medical Research and Ethics Committee, Ministry of Health Malaysia to obtained research approval. The ethical approval letter issued by the committees are as presented in Appendix I and II in this thesis.

A normal nasal cavity of 39-year-old Malaysian female was selected for the normal nasal cavity model whereas a 38-year-old Malaysian male diagnosed with chronic nasal obstruction and prevalence of OSA were selected for this diseased upper airway study. The selected CT scan data were imported into an image processing software, Mimics in order to process the scan images and to generate a realistic three-dimensional computational aided design CAD model of the upper airways. This was then followed by construction of three-dimensional surface geometry by using a Computer Aid Design (CAD) software CATIA.

The 3D surface geometries were imported into GAMBIT, ANSYS ICEM CFD and ANSYS FLUENT Meshing for unstructured and hybrid mesh generation. Numerical simulation of airflow and particle transport and deposition were further carried out by using the available CFD commercial software, ANSYS FLUENT. Numerical inspiratory airflow was simulated for various breathing rates which includes 4, 7.5, 10, 20, 30 and 40 L/min. Particles were injected into the upper airway from the nostril inlet to investigate the transport and deposition in the upper airway. The size of the injected particle includes 1, 5, 10, 20 and 40 μm. Experimental test rig was developed, pharynx experimental model was fabricated, and experimental investigation was conducted to compare and validate the results obtained from the numerical study with that of the experimental results.

1.5 Organization of the Thesis

This thesis includes 9 chapters. The first chapter provides an introduction that review relevant research objectives, and related outlines of the purposes of this study. Chapter 2 presents an in-depth review of the background for the research. The chapter begins with an introduction to the anatomy and physiological function of the human upper airway and is followed by a review of previous studies related to the research. Chapter 3 presents the method used to construct and develop the three-dimensional realistic diseased human upper airway from the CT scan data. Chapter 4 presents the numerical method used to perform CFD simulation of airflow and particle transport and deposition in the upper airway computational model. Chapter 5 presents the numerical investigation on airflow characteristics and particle deposition in diseased nasal cavity having turbinate hypertrophy, concha bullosa, and septum deviation. A comparative study was made between pre- and post-operative model. Chapter 6

presents the computational fluid dynamics study of airflow and micro-particle deposition in a constricted pharyngeal section representing obstructive sleep apnea disease. Chapter 7 presents numerical simulation of airflow and aerosol deposition in realistic human upper airway with obstructive sleep apnea and chronic nasal obstruction for pre- and post-surgery. Chapter 8 presents the method used to develop the pharynx experimental model and the experiment test rig for both pre and post-operative cases. The main aim of this study was to analyze and validate the solutions obtained from numerical study. Finally, Chapter 9 presents the summary of the majors research findings derived from the research studied. Suggestions for future works are also presented in this chapter.

CHAPTER 2

LITERATURE REVIEW

2.1 Overview

The following chapter discusses the anatomy and physiology function of the human upper airway. The conventional method used to evaluate the diseased human upper airway has been highlighted. A brief summary of the computational fluid dynamics study of airflow and particle transport and deposition through the human upper airway carried out by other researchers has been presented.

2.2 Anatomy and Physiology of the Human Upper Airway

The anatomy of the human upper airway and its physiological function are presented in the following section.

2.2.1 Upper Airway Anatomy

Upper airway which consisted of the nasal cavity and pharynx is one of the most important components of the human respiratory system. The complex shape of the human upper airway provides the first line protection for lung by filtering, warming, and humidifying the inspired air. The nose is the only external part of the upper airway respiratory system. It is made of bone and cartilage and fibro fatty tissues. The two openings in the nose called nostrils, allow air to enter or leave the body during breathing.

The nasal cavity is divided into right and left cavities by a thin plate of bone and cartilage called the nasal septum. Septal cartilage not only forms a partition between the right and left nasal cavities but also provides support to the tip and dorsum of cartilaginous part of nose. The nasal cavity lies above the hard plate. The hard portion of the palate forms the floor of the nasal cavity, separating it from the oral cavity below. The nose can be divided axially into four regions the vestibule, the nasal valve, the turbinate and the nasopharynx regions. The vestibule is a pear-shaped cavity which located at the most anterior part of the nose. The nasal valve area is the narrowest portion of the nasal passage. The nasal valve structure regulates the breathing airflow in the nasal passage.

The nasal conchas or turbinates are important structures located laterally in the nasal cavity. There are three turbinates available on each side of the nose, namely, inferior, middle and superior. The inferior turbinate is the largest while the superior turbinate is the smallest in structure. The spiral or curved nature of the turbinates increases the surface area and contact with inspired air. As the turbinates compose most of the mucosal tissue of the nose, it can help warm, humidify and filter air inhaled through the nasal cavity. Pharynx is the medical name for the throat. Nasopharynx is located at the upper part of the throat behind the nose to the upper surface of the soft palate. The soft palate separates the nasopharynx from the oropharynx which located just below the soft palate. The epiglottis is a flexible flap located at the base on tongue. The vocal cord is located within the larynx section and the larynx in connected to trachea.

2.2.2 Upper Airway Physiology

The human nose has two primary functions. The first is olfaction, the sense of smell. The second function is air-conditioning. Inspired air is conditioned by a combination of heating, humidification and filtering to provide the first line protection for the lung (Elad *et al*., 2008). The nasal conchae help to slow down the passage air, causing it to swirl in the nasal cavity. The nose acts as the organ of olfaction and has a specially adapted mucosal lining along its roof for this purpose. In order to stimulate the olfactory system, the sense of smell, the odorant particles must interact with olfactory receptors located in the olfactory mucosa. Odorants must therefore be capable of being delivered to the olfactory region by inspired air and be able to dissolve sufficiently in the mucus covering the olfactory mucosa (Ishikawa *et al*., 2009).

The nasal cavity is lined by mucous membrane containing microscopic hair like structures called cilia. The cells of the membrane produce mucus, a thick gooey liquid. The mucus moistens the air and traps any bacteria or particles of air pollution. Microscopic finger-like projections on the surface of the mucosal cells lining the nasal cavity called cilia. The cilia wave back and forth in rhythmic movement. Cilia will slowly propel the mucus backwards into the pharynx where it is swallowed. In subjects with breathing allergy syndrome, the pharynx is often a reaction site to allergens, with common symptoms including burning and itching. The main function epiglottis is to protect the opening entrance to the larynx and trachea by closing it while swallowing so that the swallowed food is guided towards the esophagus and stomach. The vocal cord is located within the larynx section which is also recognized as the voice box. The vocal cord will usually vibrate and produce sound when the air flow pass through the

vocal cord especially during exhalation. The function of larynx is to connect the pharynx with trachea and protect trachea by only allowing air to pass through it.

2.3 Objective Measurement Methods

Objective measurement methods are the conventional tools utilized by medical practitioners to measure and assess the anatomy and physiology of the human upper airway. In this section, the main objective measurement methods are discussed namely rhinomanometry, acoustic rhinometry, endoscopy and polysomnography.

2.3.1 Rhinomanometry

Rhinomanometry is a tool which is used to measure nasal airway resistance by making a quantitative measurement of nasal flow and pressure. The European committee of standardization of Rhinomanometry has selected the formula $R = \Delta P/V$ at a fixed pressure of 150 Pa; to facilitate comparison of results, where R is resistance, ΔP is pressure drop, V is the velocity of flow. Rhinomanometry can be performed by anterior or posterior approaches. However this technique is time consuming and requires a great deal of patient cooperation, particularly difficult with children. It cannot be used in the presence of septal perforations and when one or both cavities are totally obstructed. It is affected by nasal cycle and errors as high as 25 % are reported for repetitions within 15 minutes (Hilberg *et al*., 1989). It cannot accurately assess a specific area of the nasal cavity. Rhinomanometry is time consuming, requires technical expertise, a high degree of subject cooperation and is impossible in subjects with severely congested nasal airways. There are reports of failure rates of between

25 % and 50 % in the subjects examined by rhinomanometry (Austin & Foreman, 1994). Suzina *et al*., (2003) concluded that active anterior rhinomanometry is a sensitive but not a specific tool for the detection of abnormalities in nasal air resistance and it failed to relate to the symptom of nasal obstruction.

2.3.2 Acoustic Rhinometry

Acoustic Rhinometry (AR) analyses ultrasound waves reflected from the nasal cavity to calculate the cross sectional area at any point in the nasal cavity as well as the nasal volume. Acoustic rhinometry was first described for clinical use in 1989. The list of clinical problems that can be analyzed objectively with acoustic rhinometry has expanded to include turbinoplasty, sleep disorders, more types of cosmetic/reconstructive procedures, sinus surgery, vasomotor rhinitis, maxillofacial expansion procedures, and aspirin and methacholine challenge (Corey, 2006).

Acoustic rhinometry is a tool that can aid in the assessment of nasal obstruction. The test is noninvasive, reliable, convenient, and easy to perform. Common clinical and practical uses of acoustic rhinometry for the rhinologic surgeon include assessment of "mixed" nasal blockage, documentation of nasal alar collapse, and preoperative planning for reduction rhinoplasty. Acoustic rhinometry can also be used to document the positive effect of surgery on nasal airway obstruction (Lal & Corey, 2004). However, AR may be unreliable due to artifacts & errors can occur in cross sectional area estimation (Tomkinson & Eccles, 1995; Tomkinson & Eccles, 1998). There is a poor correlation between

subjective sensation of nasal airflow and objective measurements (Eccles, 1998). Riechelmann et al., (1999) found unreliability of acoustic rhinometry in pediatric rhinology. Mean cross-sectional areas measured by AR were constantly less than those measured by CT of the nasal cavity up to 33 mm from the nostril, whereas areas measured by AR were greater than those measured by CT scans beyond that point (Min & Jang, 1995; Mamikoglu et al., 2000). AR is not a reliable method for the indication or evaluation of surgery for nasal obstruction (Reber et al., 1998).

2.3.3 Endoscopy

Endoscopy has been used to observe and measure upper airway morphology. The technique used to evaluate the morphology of the upper airway include the sleep endoscopy and awake endoscopy. Although endoscopy evaluation technique can be used to accurately measure the morphology of the human upper airway. However, the disadvantage of using this evaluation technique is due to the invasive nature and contribute to patient discomfort (Banabilh et al., 2010).

2.3.4 Polysomnography

Polysomnography has been used to diagnose the severity of obstructive sleep apnea disease ($5 < AHI < 50$). A standard polysomnography usually performed with continuous recording of electrocephalography, electrooculograpgy, electromyography, electrocardiography, chest wall and abdominal movement, oxygen saturation level, snoring sounds and body position. Apnea-hypopnea index (AHI) is an index used in sleep apnea studies. The AHI represents the sum of all apneas and hypopneas divided

by the amount of sleep hours. An apnea is defined as a complete cessation of airflow that lasts 10 s or longer. A hypopnea is defined as a reduction of airflow that last 10s or longer (Vos *et al*., 2007)**.** Even though, polysomnograpic data could not provide anatomical relevant information to surgeon in order to help in planning of upper airway treatments, polysomnographic study has been used to evaluate the treatment outcome.

2.4 Fluid Flow Studies in the Human Upper Airway

Recent developments in medical imaging, three-dimensional geometrical modeling, numerical mathematics, and high computational technologies have opened new possibilities for physically realistic numerical simulations of airflow based on anatomical precise computer models of the upper airway. To improve the understanding of the detailed flow phenomena inside the human upper airway without any intervention and clinical risk for the patient, CFD methods can be used to simulate the airflow and particle transport and deposition in the upper airway. Simulation results obtained through CFD analysis can provide a detailed picture of the local and global distribution of physical flow parameters like air velocities, airflow vortices, pressure drop or nasal resistance values, wall shear stress, and particle deposition.

2.4.1 Computational Model of the Human Upper Airway

The general process of developing three-dimensional upper airway computational model includes acquiring of MRI/CT scans images of the airway passage followed by carefully define threshold on the scanned images. Since the upper

airway especially the nasal cavity has complex geometries, proper selection of the important features is critical to create an appropriate upper airway passage. High quality MRI/CT scans data in Digital Imaging and Communications in Medicine (DICOM) format are usually used to reconstruct the 3D computational model of normal or diseased human upper airway. The increment between each slice of the scan images should be less than 1 mm to avoid stair-step artifact which usually appear on the curved surface of the model (Bailie *et al*., 2006). Kim *et al*., (2013) suggested that the CT images which are obtained after the decongestion of the nasal mucosa are not recommended since the volume of the mucosa would be decreased and nasal cavities become abnormally wider (Kim *et al*., 2013). In the case of surgical evaluation study, the head positions should be similar in the two CT data sets for each patient scanned before and after surgery. Table 2.1 summarized the specification of MRI and CT scan data used by researchers to develop the human upper airway model. Type of commercial software utilized by previous researchers to develop human upper airway computational model and software used to perform numerical analysis has been summarized by Kim *et al*., (2013).

Table 2.1: Summary of the specification MRI/CT scans data obtained to develop the nasal computational models

Researchers	Data source	Number, gender (M/F), age of subjects	Scan resolution (pixels)	Increment between slice (mm)	Power
Ghahramani *et al*., 2014	CT scans	1, F,24	NA	0.6	120 KV peak, 99 mA
Dastan *et al*., 2014	CT scans	2, M&F,24	512 x 512	0.6	Tube potential 120 KVP Tube current 160 mA
Cheng *et al.*, 2014	CT scans	10, NA, NA	NA	2.5	NA
Abouali *et al*., 2012	CT scans	1, M, NA	512 x 512	0.6	120 KV peak, 160 mA
Ghalati *et al*., 2012	CT scans	1, F, 24	NA	0.6	120 KV peak, 99 mA
Moghadas *et al*., 2011	CT scans	1, M, NA	512 x 512	2.0	NA
Xi *et al*., 2011	MRI	1, M, 5	NA	1.5	NA
Wang *et al*., 2009	CT scans	1, M, 25	NA	1-5	120 kV peak, 200 mA
Inthavong *et al*., 2008	CT scans	1, M, 25	NA	1-5	120 kV peak, 200 mA
Mihaescu *et al*., 2008	MRI	1, F, 18	0.85 x 0.85	0	NA
Shi *et al*., 2007	MRI	1, M, 53	NA	1.5	NA
Xu *et al*., 2006	MRI	3, NA, 3-5	NA	NA	NA

2.4.2 Fluid Flow Modelling

For many years, several researchers have been interested in studying airflow in the human upper airway (Elad et al. 1993; Keyhani et al. 1995; Subramaniam et al. 1998; Croce et al. 2006; Zamankhan et al. 2006; Wen et al. 2007; Segal et al. 2008; Wen et al. 2008). The following section explained the important parameters used by previous researchers to analyze the breathing airflow characteristics through the upper airway of the human respiratory system.

2.4.2.1 Velocity and Flow Distribution

Several studies have shown that, during inspiration air enters each nasal cavity through the oval shaped external nostrils into the vestibule. Then, the flow changes direction, 90 degrees towards the horizontal, before entering the nasal valve region. The flow increases in the nasal valve region where the cross-sectional area is smallest causing an acceleration of the air. Segal *et al*., (2008) in their study found that inspiratory flow velocity was highest in the nasal vestibule and nasal valve regions in all four test subjects. At the end of the nasal valve region the cross-sectional area of the nasal cavity increases suddenly. This expansion is the beginning of the turbinate region where the profile is complicated and asymmetrical. Croce *et al*., (2006) found that the velocity decreases considerably downstream from the nasal valve region due to the sudden expansion of the cross-sectional area posterior to the nasal valve especially in the vertical planes of the nose.

Several researchers found that the majority of the airflow passes through the inferior turbinate (Keyhani *et al*., 1995; Segal *et al*., 2008; Croce *et al*., 2006). Keyhani *et al*., (1995) performed numerical studies of laminar airflow through the right human nasal cavity which was constructed from CAT scans of a healthy adult nose. They observed that approximately 30 % of the inspired volumetric flow passed below the inferior turbinate and only 10 % passed through olfactory airway. Croce *et al*., (2006) performed numerical simulations of airflow in realistic nasal airway geometry for flow rates up to 253 ml/s. They showed that predominant flow was observed in the inferior part of the nasal cavities, under the middle turbinate, through the middle and inferior meatuses. At the nasopharyngeal region, the left and right cavities merge together causing the flow in this region to mix intensely (Wen *et al*., 2007).

Some researchers demonstrated that vortices were observed downstream from the nasal valve and toward the olfactory region (Wen *et al*., 2008; Croce *et al*., 2006). Croce *et al*., (2006) observed two main vortices downstream from the nasal valve and toward the olfactory region. The highest velocities were in the nasal valve region and the lowest velocities were in the upper part (olfactory region). For flow rate of 7.5 L/min Wen *et al*., (2008) found that the flow recirculation was prominent in the upper anterior part of the cavity, the olfactory region. The vortex is a result of the adverse pressure gradient caused by the abrupt increase in the cross-sectional area from the nasal valve to the main nasal passage.

Segal *et al*., (2008) conducted numerical analysis on human nasal cavities to investigate and compare the inhaled airflow patterns and distributions in the four different nasal anatomies. In all four subjects, they found that swirling flow was most

evident in the nasal vestibule and nasopharynx areas. However, the intensity of the swirling flow was found differ among them. Subramaniam *et al*., (1998) showed that prominent recirculating streams are found in the nasal vestibule and complex downward spiraling flow patterns in the nasopharynx. There were some differences in the size and location of the vortices between the models compared which may be attributed to geometrical differences such as increase in airway height that promote separation (Keyhani *et al*., 1997).

2.4.2.2 Airflow Resistance

Nasal resistance is an important factor in considering breathing airway resistance. In adults, nasal resistance can contribute up to half of the total breathing airway resistance. The influence of geometrical variations was found to produce dramatic increases in the resistance (Wen *et al*., 2008). Studies show that decrease in cross-sectional area of the nasal passage is associated with the increase in the pressure drop. Increase the passage cross-area through virtual surgery decreases the flow resistance of the passage (Wen *et al*., 2008; Abouali *et al*., 2012; Dastan *et al*., 2014). Wen *et al*., (2008) found that the nasal resistance value within the first 2-3 cm contributes up to 50 % of the total airway resistance.

2.4.2.3 Wall shear stress

A friction force is generated when moving air contacts the nasal walls, referred to as wall shear stress. This interaction enables heat and mass transfer between the air and the upper airway wall to condition the inhaled air (Bailie *et al*., 2006). As shear

stresses are linearly related to the local velocity, these values significantly increase as breathing effort increase. High shear stresses that are concentrated locally may cause irritation of the blood vessels within that area (Wen *et al*., 2008). Elad *et al*., (1993) showed that the maximum shear stresses at peak inspiration of 20 L/min located on the septal wall through the inferior turbinate in the range of 0.2 Pa. Wen *et al*., (2008) found that the wall shear stress decreases gradually corresponding to the airway expansion in the middle region where the velocity decreases. The wall shear stress values were found increased again when the left and right cavities merge at the posterior region of the nasal cavity. The increment is cause by the change in flow direction at the nasopharynx where the air travels downwards towards the lung.

2.5 Particle Deposition Studies in the Human Upper Airway

An adult human breathes in 10,000 to 20,000 liters of air per day. The air brings with it a large quantity of particulate matter: microorganisms, dust, smokes, allergens, and other toxic and non- toxic aerosols that may get deposited in the breathing airway during the inhalation process. Nasal inhalation is a major route of entry into body for the inhaled airborne pollutions. Therefore, the function of the nose to filter out toxic particles is considered important.

Inhalable particles range from a few nanometers to, typically, a few microns (Tsuda *et al.*, 2013). The size range of natural and manmade particles can be large. For-example, occupational dusts may be 0.001-1000 micrometer, pollen particles are 20-60 micrometer, consumer aerosol products are 2-6 micrometer, most cigarette smoke particles are 0.2-0.6 micrometer, and viruses and proteins may be in the range 0.001-0.05 micrometer (Guha, 2008). From the toxicology point of view, all particles

which are smaller than 10 μm in diameter can be biologically active and could cause allergic responses and even cancers is susceptible (Cheng, 2003). Where the aerosol lands in an airway is important information for correlating inhaled toxins or carcinogens to disease locations and for developing potential therapies (Grotberg, 2001). On the other hand, the airway can also provide an alternative route for drug delivery. Therefore, it is important to enhance knowledge on the airflow characteristics, particle transport and deposition in the human respiratory system. The knowledge obtained from the transport and deposition of inhaled particle can be used to further develop understanding of the therapeutic drug delivery through the upper airway.

2.5.1 Particle Modelling

Computational modeling approaches have the capability to conveniently estimate the regional deposition pattern of aerosol. The location of peak deposition in different parts of the respiratory tract can be identified. Studies of particle transport and deposition in the human nasal cavity have been performed by many researchers to understand the mechanisms and patterns of deposition (Wang *et al*., 2008; Dastan *et al*., 2014; Zamankhan *et al*., 2006; Abouali *et al*., 2012; Bahmanzadeh *et al*., 2015; Inthavong *et al*., 2008). Inthavong *et al*., (2008) constructed 3D nasal passage based on nasal geometry which obtained through a CT scan of a healthy human nose. The airflow analysis showed vortices present in nasal valve region enhanced fibre deposition by trapping and recirculating the fibre in the regions where the axial velocity is low.

Wang *et al*., (2008) investigated the influential factors of the transport and deposition efficiencies of glass fibers in three human nasal models. Glass fiber deposition was studied at five inhalation rates: 4, 8, 12, 15, and 18 L/min and four fiber length range: 10-19, 20-29, 30-39, and 40-49 μm. They found that deposition of fiber glass fibers with about 1 μm diameter in human nasal passage is mainly due to inertial impaction and these fibers oriented themselves normal to the flow direction before deposition occurs. Dastan *et al*., (2014) investigated the transport and deposition of fibrous particle in different human nasal passages. They developed an in-house code to solve the coupled transitional and rotational equation of motion of ellipsoids. For four different laminar breathing rates, different range of diameters and lengths of fiber were analyzed. They found that, the variation of nasal passages was found to significantly affect the deposition fraction. The deposition fraction is highly affected by the nasal geometry and of airflow rate in the nasal valve and main airway regions.

Another work was done by Zamankhan *et al*., (2006), who studied the airflow characteristics and transport and deposition of ultrafine particles ranging from 1 to 100 nm in a three dimensional model of human nasal passage by using an Eulerian-Lagrangian approach. They found that, for the smallest range of particles ranging from 1-30 nm, diffusion is the dominant deposition mechanism. Cheng, (2003) postulated that deposition in the nasal and oral airways is dominated by the inertial mechanism for particles larger than 0.5 μm and by the diffusion mechanism for particles smaller than 0.5 μm.

Other studies include Abouali *et al*., (2012), who investigated the effect of virtual Uncinectomy and Middle Meatal Antrostomy on the airflow distribution and

particle deposition in the nasal airway, maxillary and frontal sinuses. The virtual surgery was performed by performing the uncinate process and exposing the maxillary sinus antrum. Inhalation of micro and nanoparticles were considered in this study. For microparticle, the path and deposition of the particles in the nasal passages and maxillary sinuses was evaluated by using a Lagrangian trajectory analysis approach. For nanoparticles, the transport and deposition analysis were performed by using a diffusion model. The rate of particle deposition in the maxillary and frontal sinuses were analyzed and compared between pre and post-surgery conditions. They found that, for the pre-operative condition, almost no particles entered the sinuses. However, after surgery, the inhaled nano- and microparticles can easily enter the sinuses due to the increase of airflow penetration into the sinus cavity.

Bahmanzadeh *et al*., (2015) investigated the effect of endoscopic sphenoidotomy surgery on the flow patterns and deposition of micro-particles in the left side of the human nasal passage and sphenoid sinus. The Lagrangian approach was used to track the particle which was continuously entering the nasal airway during inhalation. They found that sphenoidotomy increased the airflow hence increased deposition of micro-particles in the sphenoid region. They also found that, for the post-operation case, particle size up to 25 μm were able to penetrate into the sphenoid region. During resting breathing condition, the highest deposition in the sphenoid was found for 10 μm particles at about 1.5 %. Table 2.2 summarized the parameter and modelling approached used by previous researchers to perform CFD study of airflow and particle transport and deposition through normal and diseased human nasal airway.

Table 2.2: Summary of grid size, flow rate and viscous models, particle size and particle tracking approach.

Researchers	Mesh	Flow rate; Viscous model	Particle size; Particle tracking approach
Karakosta *et al*., 2013	Tetrahedral 2,200,000	1,2,5,10 m/s; SST k-w	0.5-20 μm; Lagrangian
Ghahramani *et al*., 2014	Hybrid 4,660,000	30,45,60 L/min; LRN k-ε Turbulent	2.5, 5, 10 and 15 μm; Lagrangian
Moghadas *et al*., 2011	Tetrahedral 600,000	12 L/min; Laminar	1–50 μm Lagrangian
Zhang & Kleinstreuer, 2011	Hybrid 4,435,705	30 and 60 L/min	1–100 nm; Eulerian
Ghalati *et al*., 2012	Tetrahedral 2,600,000	5, 10 and 15 L/min; Laminar	5, 10 and 20 μm; Lagrangian 1, 3 and 5 nm; Eulerian
Dastan *et al*., 2014	Hybrid 3.5 million	10 L/min; Laminar	1,3,5,10, 15 μm (Ellipsoidal Fibers) ; Lagrangian
Abouali *et al*., 2012	Tetrahedral 3,500,000	4,7.5,10 L/min; Laminar	1,5,10,15,20 μm; Lagrangian 1, 3, 5, 10, 20 nm Eulerian

2.5.2 Factors Affecting Particle Deposition in Upper Airway

Particle transport and deposition in the nasal airway has been found to depend on the morphology of the respiratory tract, particle characteristics, and breathing rates and pattern. The subsections below present the factors affecting the deposition of inhaled particle through upper airway.

2.5.2.1 Morphology of Respiratory Tract

Particle deposition depends on the morphology of the respiratory tract. The impact of airway geometry on micron-particle deposition was demonstrated by Xi & Longest, (2007), who compared deposition results for a realistic and three simplified oral airway models. They reported that the modification made on the simplified airway model significantly affect the transport dynamic and the pattern of the aerosol deposition.

2.5.2.2 Particle Characteristics

The size of particle is one of the most important feature of an aerosol because it determines the stability of the particle (Karakosta *et al*., 2013). Heyder, (2004) reported that the distance a particle travels by diffusional transport increases with decreasing particle size. Xi & Longest, (2007) reported that, the location of deposited inhaled particles in the upper airway was highly dependent of the particle size. Dastan *et al*, (2014) found that fiber deposition rate increases as the fiber diameter and length increases. Ghalati *et al*., (2012) reported that the rate of particle deposition increases as particles diameter increase due to their higher inertia and deviation from streamlines.

2.5.2.3 Breathing Flow Rates

Deposition of particles depends not only on the particle characteristics but also on the subject's breathing pattern and rates (Heyder *et al*., 1986). Wen *et al*., (2008) reported that low flow in olfactory region is a defense mechanism that prevents particles whose trajectories are heavily dependent on flow patterns from being

deposited onto the sensitive olfactory nerve fibers, while vapors are allowed to diffuse for olfaction. Ghahramani *et al*., (2014) investigated deposition pattern of 5μm particle for three flow rates of breathing (30, 45, and 60 L/min). They found that the particle deposition increases as the breathing rates increased. This trend is expected since the impaction parameter that control the particle deposition, is directly proportional to volume flow rate.

2.6 Upper Airway Surgery

It is desirable to perform a virtual surgery in advance of the actual surgical treatment to assess the potential changes in the nasal airflow and the associated aerosol particles' deposition and filtration. Furthermore, virtual surgery would allow for testing various alternatives and for optimal surgical planning. Numerical study on airflow in the human upper airway has been the subject of several studies (Abouali *et al*., 2012; Moghadas *et al*., 2011; Zhao *et al*., 2004; Wexler *et al*., 2005; Garcia *et al*., 2007; Lindemann *et al*., 2005; Bahmanzadeh *et al*., 2015).

2.6.1 Diseased Nasal Airway

Using CFD modeling of one patient's nose pre and post-operative, Zhao *et al*., (2004) showed significant improvement in postsurgical ortho and retronasal airflow and odorant delivery rate to olfactory neuroepithelium, which correlated well with olfactory recovery. Ethmoid and sphenoid sinuses were included in their computational model, and it was shown that the airflow velocity within the sinus is very low, confirming the limited effect of the sinus on the overall nasal airflow field.

Another numerical analysis conducted on a 3D nasal model of a patient with sinonasal disease was done by Wexler *et al*., (2005). They investigated the aerodynamic consequences of conservative unilateral inferior turbinate reduction using CFD methods to accomplish detailed nasal airflow simulations. Steady-state, inspiratory laminar airflow simulations were conducted at 15 L/min. They found that inferior turbinate reduces the pressure along the nasal airway. Also, the airflow was minimally affected in the nasal valve region, increased in the lower portion of the middle and posterior nose, and decreased dorsally. Lindemann *et al*., (2005) investigated the intranasal airflow after radical sinus surgery. The numerical simulation was performed by assuming the nasal airflow as laminar at 14 L/min for quiet breathing rate. They performed an unusually aggressive virtual operation on the CT scan model of the nose, which included a bilateral model of the human nose with maxillectomy, ethmoidectomy, and resection of the lateral nasal wall and the turbinates. Result showed that aggressive sinus surgery with resection of the lateral nasal wall complex and the turbinates cause disturbance of the physiological airflow, an enlargement of the nasal cavity volume, as well as an increase in the ratio between nasal cavity volume and surface area.

Other studies include Garcia *et al*., (2007), who investigated airflow characteristics, water transport, and heat transfer in the nose of an Atrophic Rhinitis (AR). The patient underwent a nasal cavity narrowing procedure. Rib cartilage was implanted under the mucosa along the floor of the nose, and septum spur was removed. The reconstructed nose was simulated and the nasal airflow was assumed as laminar with 15 L/min corresponding to resting breathing rate. This study showed that the

atrophic nose geometry had a much lower surface area than the healthy nasal passages. The simulations indicated that the atrophic nose did not condition inspired air as effectively as the healthy geometries. Xiong *et al*., (2008) performed numerical study on the pre and post virtual functional endoscopic surgery (FESS). In the post-FESS model, they found an increase in airflow distribution in the maxillary, ethmoid and sphenoid sinuses, and a 13 % increase through the area connecting the middle meatus and the surgically opened ethmoid. Xiong *et al*. (2011) used CFD to compare nasal airflow after two different surgical interventions, which involved opening the paranasal sinuses, excising the ethmoid sinuses, and excising or preserving the uncinate process, in a cadaveric head model. They concluded that the preservation of the uncinate process may significantly reduce the alteration of nasal cavity airflow dynamics after functional endoscopic sinus surgery for chronic rhinosinusitis.

Abouali *et al*., (2012) investigated the effect of virtual Uncinectomy and Middle Meatal Antrostomy on the airflow distribution and particle deposition in the nasal airway, maxillary and frontal sinuses. The virtual surgery was performed by removing the uncinate process and exposing the maxillary sinus antrum. Inhalation of micro and nanoparticles were considered in this study. The rate of particle deposition in the maxillary and frontal sinuses were analyzed and compared between pre and post-surgery conditions. They found that, for the pre-operative condition, almost no particles entered the sinuses. However, after surgery, the inhaled nano- and microparticles can easily enter the sinuses due to the increase of airflow penetration into the sinus cavity. Bahmanzadeh *et al*., (2015) investigated the effect of endoscopic sphenoidotomy surgery on the flow patterns and deposition of micro-particles in the left side of the human nasal passage and sphenoid sinus. They found that

sphenoidotomy increased the airflow hence increased deposition of micro-particles in the sphenoid region. They also found that, for the post-operation case, particle size up to 25 μm were able to penetrate into the sphenoid region. During resting breathing condition, the highest deposition in the sphenoid was found for 10 μm particles at about 1.5 %. Table 2.3 shows the impact of the nasal surgical treatment on airflow and particle deposition.

Table 2.3: Summary of impact of surgical treatment on airflow and particle deposition.

Nasal Disease; Surgical Treatment	**Research Findings**	**References**
Chronic Rhinosinusitis; Functional Endoscopic Sinus Surgery (FESS): Uncinectomy Middle Meatal Anstrostomy (MMA)	• Increases the passage cross-area caused decreases of flow resistance through the nasal passage. • Airflow field inside the maxillary sinus changes dramatically, and part of the main airflow through the nasal passage enters the sinus. • Inhaled particles can easily enter the maxillary sinus due to penetration of the airflow into the maxillary sinus cavity. • In contrast to the preoperative condition in which almost no particles entered the sinuses. • The range of microparticle sizes for which the deposition in the maxillary sinus shows significant increase after Uncinectomy/MMA	Abouali *et al*., 2012
Septal deviation; Septoplasty	• Deviation decreased the cross-section areas in right nasal cavity and the total volume of the passage, which led to several breathing problems for the patient.	Moghadas *et al*., 2011

	• After the septoplasty, 16 % of the obstruction due to deviation was removed. • For a given pressure drop, the nasal airflow in the abnormal right nasal cavity before septoplasty is about 40-50 % less than that in the normal left passage. After septoplasty, the differences reduce to less than 6 %.	
Septal deviation and Inferior turbinate hypertrophy; Right balloon sinuplasty Left uncinectomy Septoplasty Bilateral inferior turbinate reduction	• The airflow patterns in the nasal cavity showed reasonably decreased resistance and slightly more even flow partitioning after the operation. • Maxillary sinus ventilation increased during inspiration in the left sinus after uncinectomy • Maxillary sinus ventilation increased during expiration in right sinus after balloon sinuplasty	Zhu *et al*., 2014

2.6.2 Obstructive sleep apnea (OSA)

Obstructive Sleep Apnea (OSA) is a potentially serious respiratory disorder and has become one of the most common public health problems. OSA is characterized by recurrent episodes of partial or complete pharyngeal airway collapse and obstruction during sleep which cause reduction in or complete cessation of airflow despite ongoing inspiratory efforts (Mihaescu *et al*., 2008). The short-term consequences of sleep apnea include sleep fragmentation, snoring, daytime sleepiness, and fatigue-related accidents. Without reasonable cure in the early stage of OSA, long-term adverse effects on cardiovascular functions may develop negative impacts on multiple organs and systems (Lipton & Gozal, 2003). A standard non-surgical treatment for OSA is continuous positive airway pressure (CPAP) therapy. CPAP

supplies constant air pressure through the throat to help the OSA patient breath more easily during sleep and to prevent airway collapse. However, the compliance of CPAP is a problem in some of the patients.

Other alternative treatment is upper airway surgical modification. The most common surgical procedures performed includes nasal reconstruction, uvulapalatopharyngoplasty (UPPP), advancement of genioplasty, mandibular osteotomy with genioglossus advancement, and hyoid myotomy suspension. In more severe cases, maxillomandibular advancement (MMA) with advancement genioplasty may be indicated. However, the success rate of upper airway surgery is not good (Ito *et al*., 2011; Lu *et al*., 2014). Even after appropriate surgical treatment, some patients may demonstrate continued obstruction with associated symptoms (Ephros *et al*., 2010).

Due to the non-invasiveness nature, CFD has now been utilized to visualize the fluid flow in the upper airway and to assess the effects of OSA treatment interventions that alter upper airway anatomical structure (Mihaescu *et al*., 2011; Xu *et al*., 2006). This is done by simulating airflow in reconstructed models of human upper airways from imaging data and analyzing different flow features such as flow velocity, static pressure, and wall-shear stress from the numerical results. It is also believed that the CFD simulation is possible to predict the surgical outcome of the upper airway.

Recently, Computational Fluid Dynamics (CFD) method has been utilized to analyze the flow dynamics in the human upper airway reconstructed from Magnetic Resonance Imaging (MRI) or Computed Tomography (CT) imaging data (De Backer

et al., 2007; Jeong *et al*., 2007; Mihaescu *et al*., 2008; Mihaescu *et al*., 2011; Mylavarapu *et al*., 2013; Mylavarapu *et al*., 2009; Xu *et al*., 2006; Vos *et al*., 2007; Zhao *et al*., 2013; Zhao *et al*., 2013; Riazuddin *et al*., 2011; Zubair *et al*., 2010; Zubair *et al*., 2013). Mihaescu *et al*., (2008) investigated the airflow distribution and characteristics in the pharyngeal airway model by using both RANS and LES approaches. The pharyngeal airway model was developed from nasopharynx to retroglossal pharynx region. They reported that, the geometry expansion in radial direction after the narrowing region produced flow separation, strong shear layers, and recirculation regions. Mylavarapu *et al*., (2009) conducted CFD simulation of 200 L/min expiratory flow to investigate the fluid flow in the upper airway regions where obstruction could occur. They reported that the highest positive pressures were observed in the retroglossal regions below the epiglottis, while the lowest negative pressures were recorded in the retropalatal region. The latter is a result of the airflow acceleration in the narrow retropalatal region. The largest pressure drop was observed at the tip of the soft palate where the smallest cross section area of the airway is located. They also found that, among the five different turbulence models used in the study, the standard k-ω model predictions were the closest to experimental results. This is attributed partly to the better treatment of adverse pressure gradient and viscous near-wall region with k-ω turbulence model as compared to k-ε and Spalart-Allmaras one equation.

Jeong *et al*., (2007) in their study, found that the pressure drop due to area restriction occurred primarily between the nasopharynx and oropharynx. Turbulent jet with higher shear and pressure force was observed in the narrowest segment of the pharyngeal airway. The constriction at the velopharynx produced pharyngeal jet as air

passes through the velopharynx. Similar to the work of Sung *et al*., (2006), the maximum velocity and minimum pressure of breathing airflow were observed at the velopharyngeal section. They concluded that the strength and intensity of the turbulent pharyngeal jet flow would be the main reason for the pharyngeal occlusion and OSA disease (nostril to pharynx). Vos *et al*., (2007) postulated that the combination of the three parameters which include smallest cross-sectional area, airflow resistance and body mass index (BMI) can be used to evaluate the severity of obstructive sleep apnea in patient.

The main anatomic risk factor for pediatric OSA is adenotonsillar hypertrophy. To improve understanding of the pathogenesis of OSA of children, Xu *et al*., (2006) investigated the effect of airway shape on pressure distribution and flow resistance in the upper airway of children ages 3-5 year-old. They found that, the minimum pressure occurred at the narrowest region which is located at the region of adeno-tonsillar overlap. High-velocity jet and higher turbulence energy was observed at the downstream of the narrowest cross section area. CFD has also been proposed as a tool to determine treatment response to Mandibular advancement splint (MAS) therapy using patient-specific airway geometries obtained from CT scans without and with MAS (De Backer *et al*., 2007). MAS is an alternative for the treatment of OSA. MAS treatment protrudes the lower jaw, enlarges the pharyngeal volume and stiffens surrounding tissue and its success was assessed by De Backer *et al*., (2007), Zhao *et al*., (2013a) and Zhao *et al*., (2013b) using CFD and FSI simulations.

De Backer *et al*., (2007) developed a patient specific upper airway model based on CT scans data obtained from nasopharynx to larynx. A patient specific boundary

condition obtained during split-night polysomnography was used for the airflow simulation. They found that decrease in upper airway resistance and an increase in upper airway volume correlate with both a clinical and an objective improvement. Although is likely to provide greater model accuracy, obtaining patient-specific boundary conditions through intensive overnight monitoring is likely to limit the clinical application of this type of prediction strategy (Zhao *et al*., 2013b).

Zhao *et al*., (2013a, 2013b) developed upper airways model between the hard palate and the vocal folds and performed CFD simulations of airflow at the maximum flow rate of 166 ml/s during inspiration. They reported that FSI model demonstrated full collapse of upper airway with maximum distance of 5.83 mm during pre-treatment. The upper airway collapse was found located at the oropharynx with low oropharyngeal pressure ranging from -51.18 Pa to -39.08 Pa, which was induced by velopharyngeal jet flow with maximum velocity equal to 10 m/s. However, for upper airway with MAS treatment, smaller deformation with maximum distance of 2.03 mm was found, matching the known clinical response. They concluded that, a clinical challenge remains in preselecting patients who will respond to MAS therapy.

Although morphology variation, narrow and collapsible of upper airway are believed to be the main cause of OSA, the etiology of this disorder and the exact mechanisms of upper airway collapse in OSA are still not completely understood. Hence, the accurate prediction of the abnormal airflow characteristics, airflow resistance and pressure distribution in the upper airway geometry associated with OSA is essential in understanding the relation between airway anatomy collapsibility and the pathophysiology of OSA.

CHAPTER 3

MODELLING THE HUMAN UPPER AIRWAY

3.1 Overview

This chapter presents the methods used in developing the three-dimensional computational models of the human upper airway from two-dimensional CT scan images. The method used to develop the unstructured and hybrid mesh for the human upper computational model is also presented. The overall process of the present numerical and experimental study was summarized in the flow chart shown in Figure 3.1.

3.2 Developing 3D Computational Model of the Human Upper Airway

The general process of developing the 3D human upper airway computational model basically consists of selection of CT scan data of the upper airway followed by converting the 2D CT scan images into 3D CAD data using a medical image processing software, MIMICs. After that, by using a reverse engineering method, the surface geometry was developed by using a CAD software, CATIA.

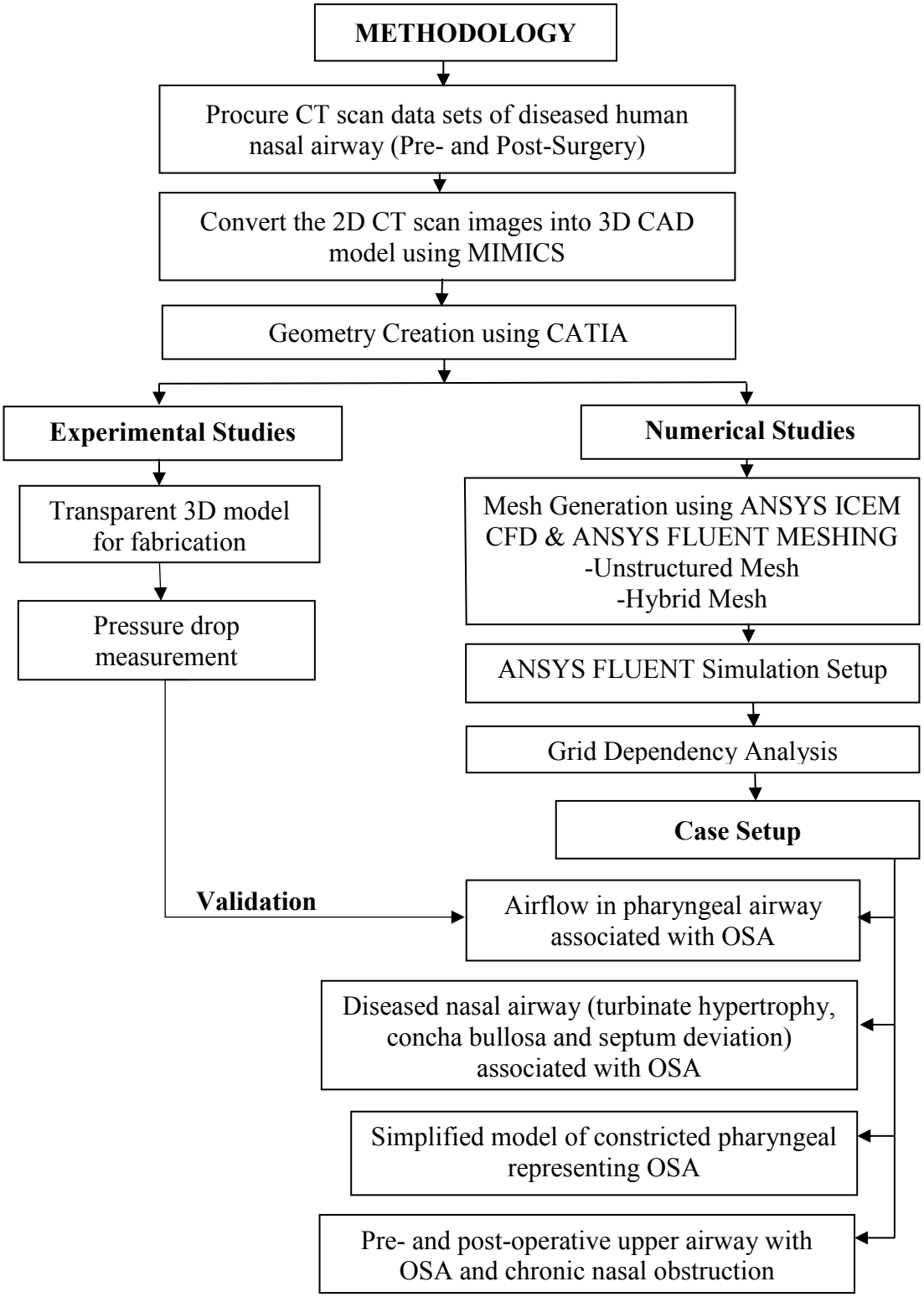

Figure 3.1: Flow chart for the present study.

3.2.1 Procuring CT Scans Data of Human Upper Airway

For the first case study, the constricted pharyngeal section representing Obstructive Sleep Apnea (OSA) disease, the three-dimensional nasal computational model was constructed based on the CT scans of a healthy 39-year old female. The CT scan images of the nasal airway was taken from pre-existing CT scan images. The CT scan of the nasal airway without nasal disease was obtained from the patient who was diagnosed with other type of disease which is not related to the breathing airway. Furthermore, the nasal anatomy was attested to be normal by the ear, nose and throat (ENT) surgeon.

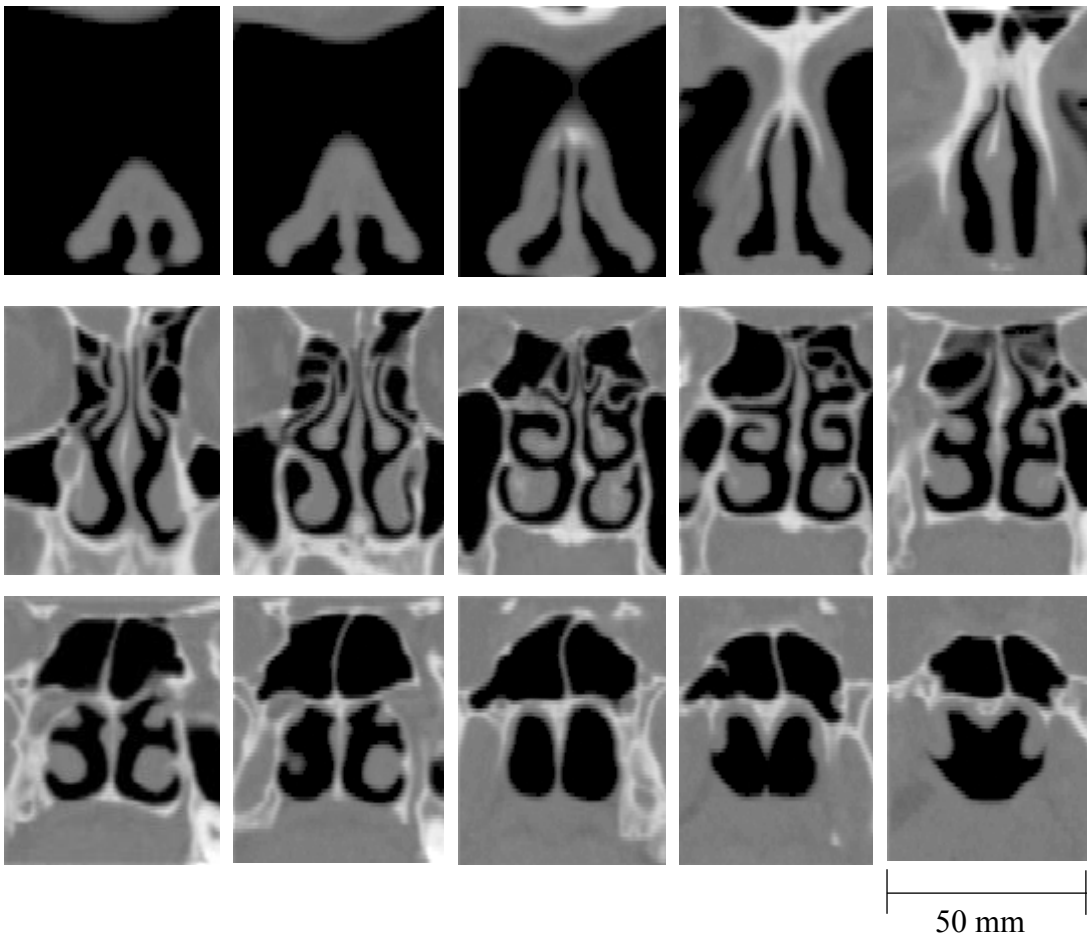

Figure 3.2: Coronal CT scan images along the axial distance of the human nasal cavity.

Figure 3.2 shows a series of CT scan images of the normal human nasal cavity obtained from coronal plane along the axial distance starting from nostril to nasopharynx. The increment between each slice of the scan images is 0.8 mm. It is important to make sure that the scan interval is less than 2 mm in order to accurately capture the complex geometry of the nasal cavity to avoid stair-step artifact which usually appear on the curved surface of the model.

For the second and third case studies, the anatomical models were developed from CT scan images of a 38-year-old male patient in Hospital Serdang. The subject was diagnosed with deviated nasal septum, hypertrophy of the inferior turbinates, left concha bullosa and also obstructive sleep apnea by the otorhinolaryngology and head and neck surgeon. He underwent nasal surgeries namely septoplasty, inferior turbinate reduction and concha bullosa resection. The pre- and post-treatment data of the upper airway were also taken from pre-existing CT scans data. The scan images were obtained from axial, coronal and sagittal plane and accounted for the upper airway respiratory system. CT scan images were acquired when the patient was awake and was in a supine position. A study proposal has been submitted to the Hospital Serdang and the study was approved by the Medical Research and Ethics Committee (MREC) of the Ministry of Health Malaysia. The certificate of approval is included in the Appendix I and II.

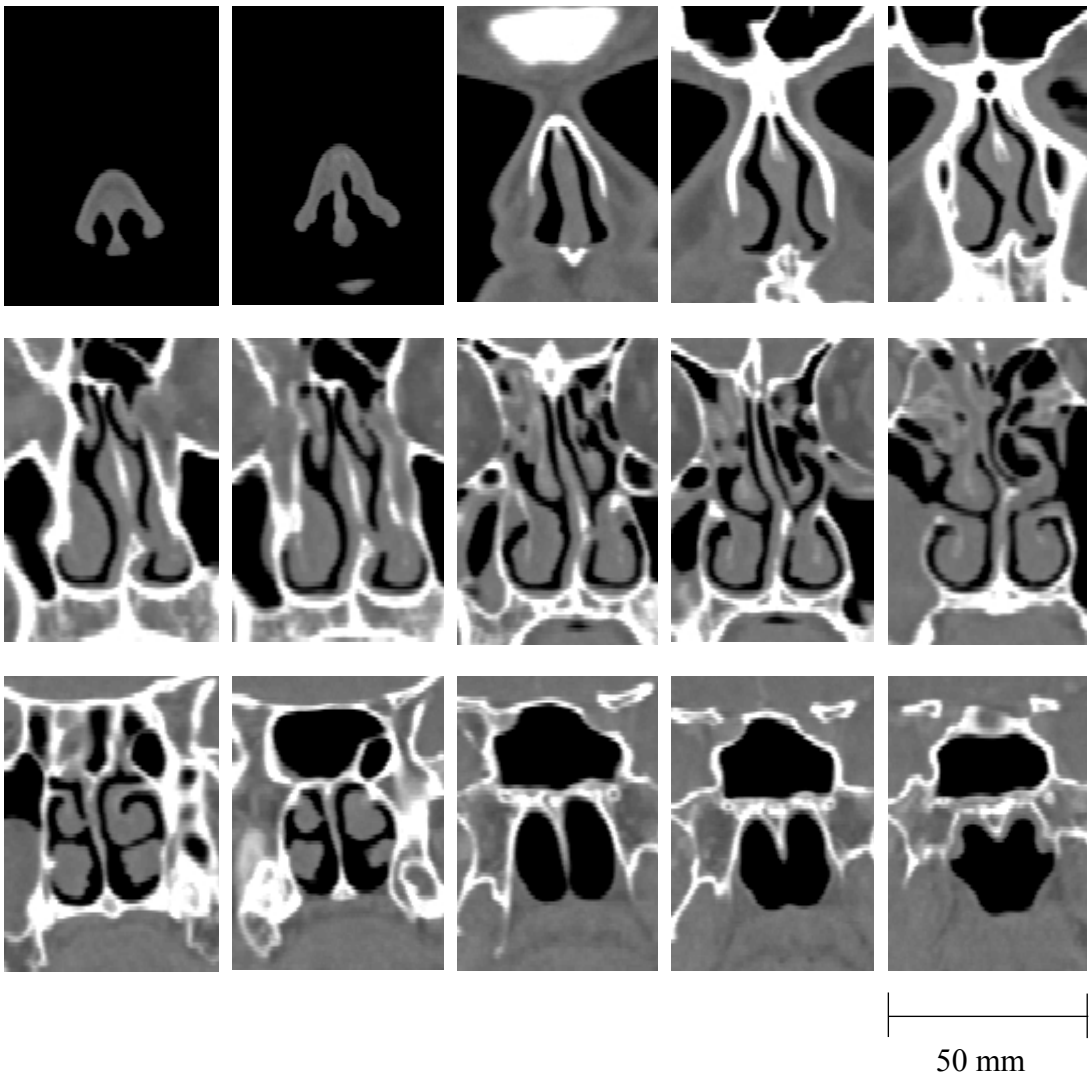

Figure 3.3: Coronal CT scan images along the axial distance of the diseased human nasal cavity before surgery.

Figures 3.3 shows the coronal view of CT scan images of the diseased human nasal cavity along the axial distance obtained before surgery. The slice increment for the pre-operative CT scans data is 0.5 mm. As can be seen in Figure 3.3, the patient has narrower nasal airway when compared to the normal nasal airway as depicted in Figure 3.2. The narrowed airway was caused by the septum deviation, enlarged inferior turbinate and concha bullosa which describes the presence of air pocket in the middle concha.

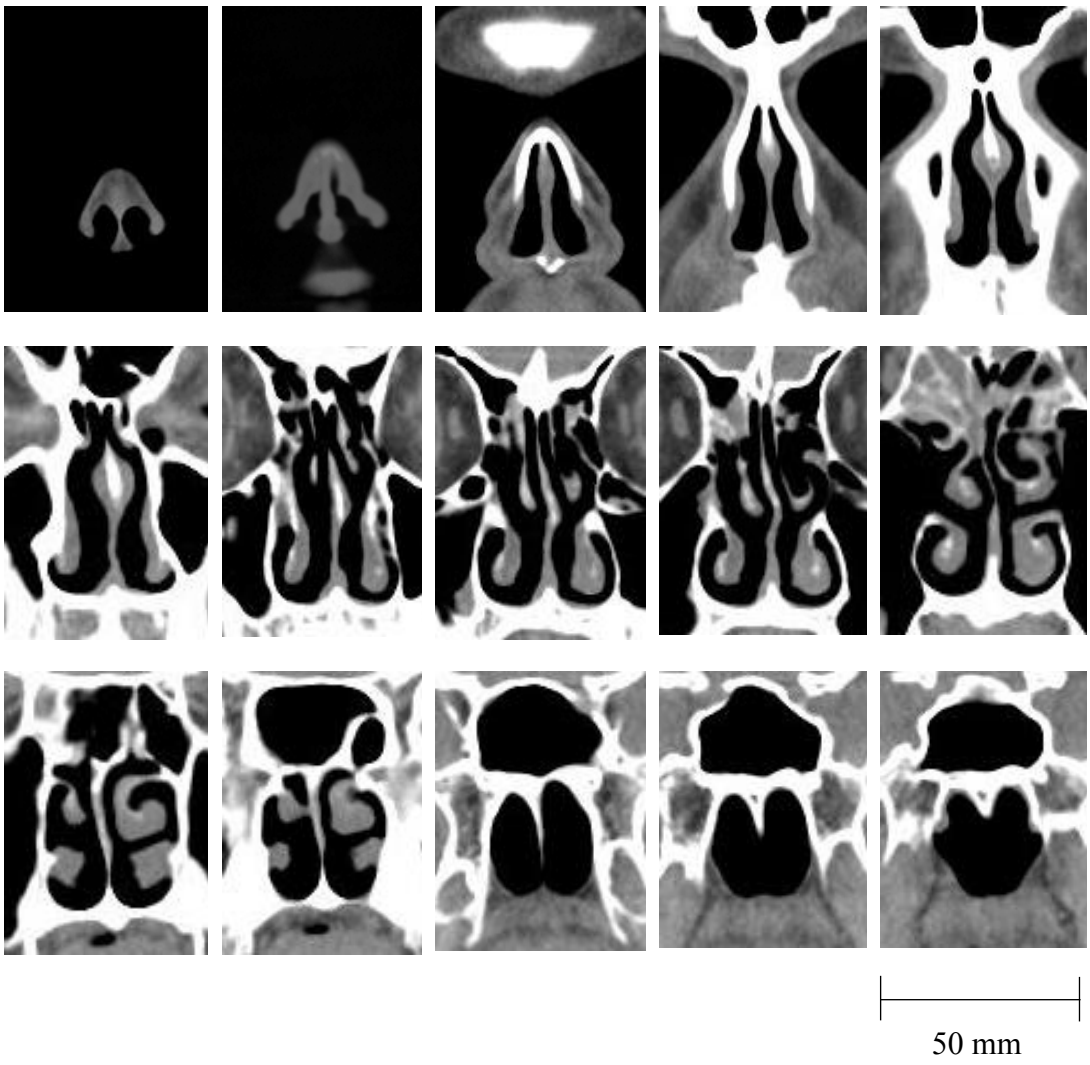

Figure 3.4: Coronal CT scan images along the axial distance of the diseased human nasal cavity after surgery.

Figures 3.4 shows the coronal view of CT scan images of the diseased human nasal cavity along the axial distance obtained before and after surgery respectively. The slice increment for the post-operative CT scans data is 0.6 mm. The post-operative CT scans data was obtained 7 months after the surgery was performed. As can be seen in Figure 3.4, after surgery, the overall nasal cavity airway has increased when compared to the pre-operative CT scan images.

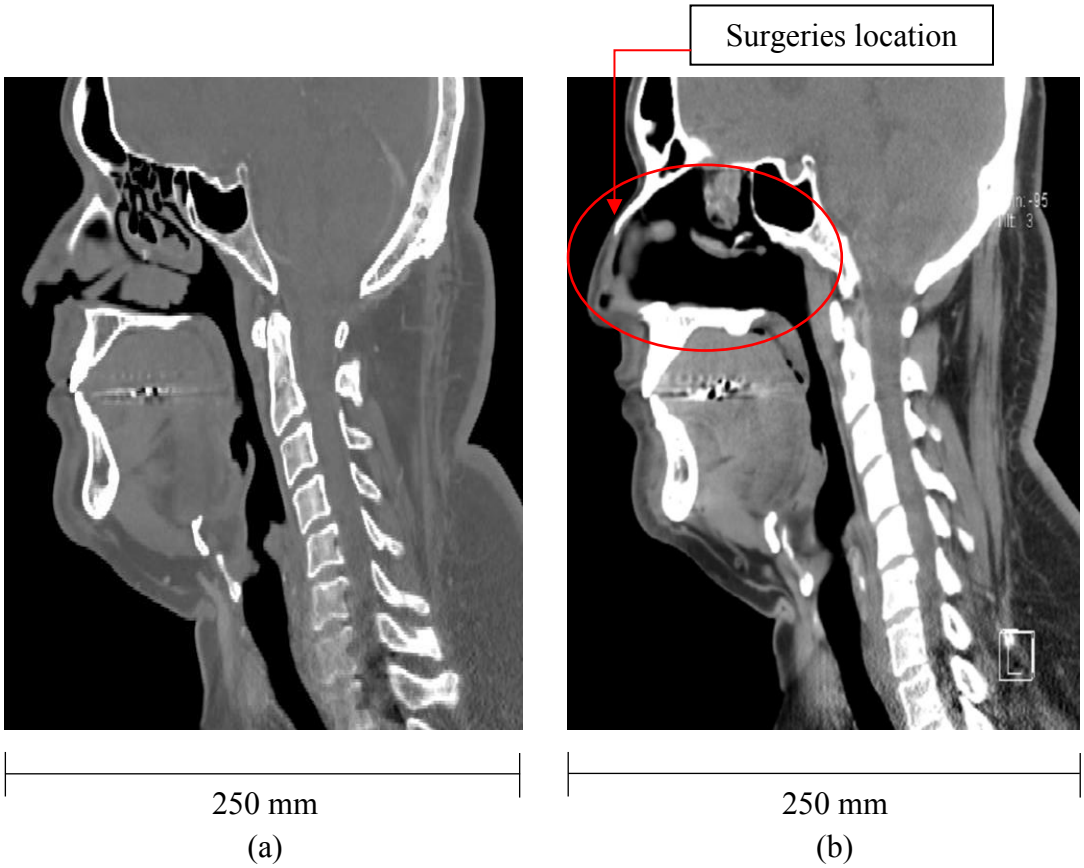

Figure 3.5: Sagittal plane of CT scan images of human upper airway obtained (a) before surgery and (b) after surgery.

Figures 3.5 (a) & (b) shows the sagittal view of the CT scan images obtained before and after surgery respectively. As can be seen in Figure 3.5 (a), before surgery, narrow air pathway was observed at the inferior, middle and superior meatus region in the diseased nasal cavity. However, after surgery, the air pathway in the turbinates region has increased when compared to that of CT scan image obtained prior to the surgery. The surgical treatment was only performed in the nasal cavity region. The surgeries performed includes septoplasty at the anterior part of the left nasal cavity, bilateral inferior turbinectomy and partial concha bullosa resection at the posterior part of the left nasal cavity. It can be observed that, in Figure 3.5 (b), the nasal airway and the overall upper airway volume increased after the patient underwent the surgical

treatment. Details explanation of the geometrical variation between pre- and post-operative case are include in Chapter 7.

3.2.2 Converting 2D CT Scans Image to 3D CAD Data

MIMICs is an image processing and editing software which provides tool for visualization and segmentation of CT images and also for 3D rendering of objects. Before the scan data can be processed, MIMICs reads a set of 2D CT scan images from the DICOM (*.dcm) file format and convert it into MIMICs (*.mcs) file format. MIMICs will compress and merge all the axial, coronal and sagittal scan images into a single volume file project based on the similar pixel size value.

The main step of airway geometry reconstruction from the CT scan data is the segmentation process in which the regions of interest are identified in the sliced image data. The CT scan images consist of gray values which represents material density. The segmentation was developed based on the gray values in the CT scan images. The gray values are expressed according to the Hounsfield scale. Hounsfield scale is a measure of the electron density of the tissue. Airway passages appear as black, the surrounding airway tissues as gray, and bony structures as white.

Figures 3.6 & 3.7 show segmentation process which was performed by defining a range of threshold value to create the segmentation mask. The range of the threshold value used for the first case study is between -444 to 2037 HU. For the second case study, the range of threshold value used is between 0 to 789 HU for both pre- and post-operative cases. The threshold value is used to differentiate between

bone and soft tissues and to determine the set of structure to be included in the 3D upper airway model. Medical reconstruction requires a good understanding of anatomy, which can only come with experience, and understanding the types of tissue that are preferentially imaged by radiographers. Hence the presence of an expert radiologist and ENT practitioner is essential in deciding the threshold and editing of the geometry.

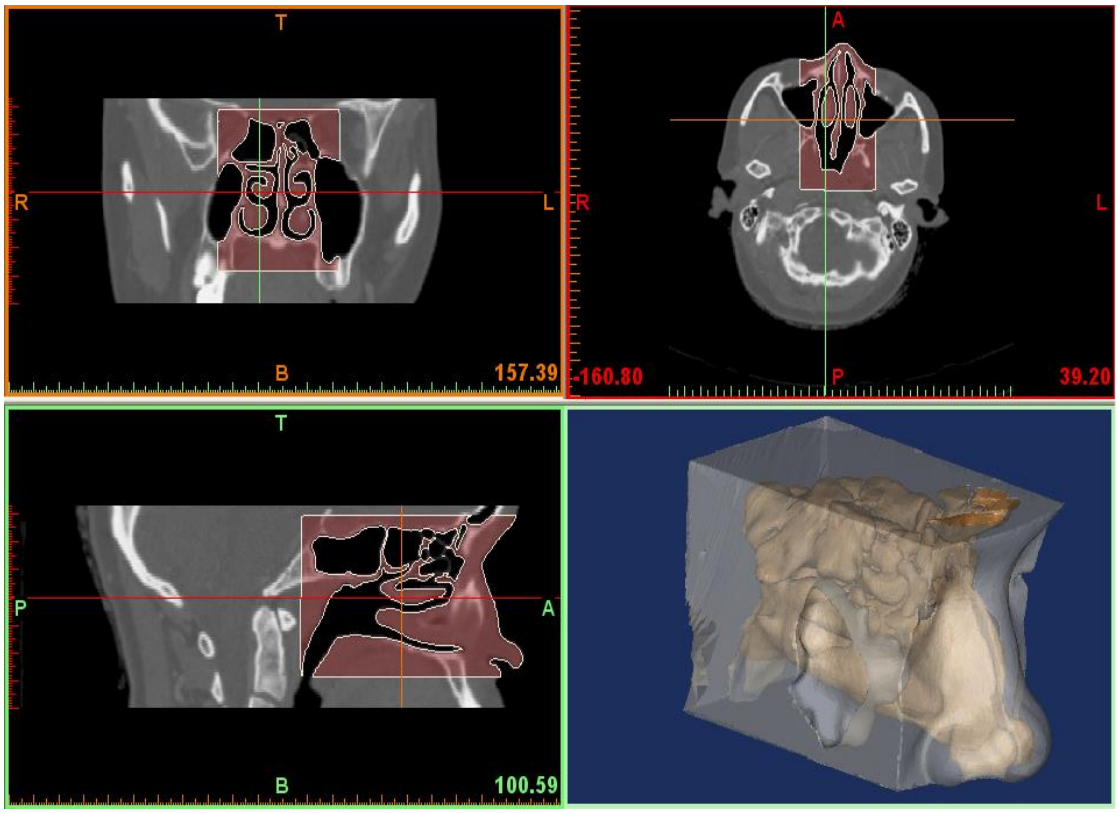

Figure 3.6: CT scan images obtained from axial, coronal and sagittal plane and 3D model of the female human nasal cavity.

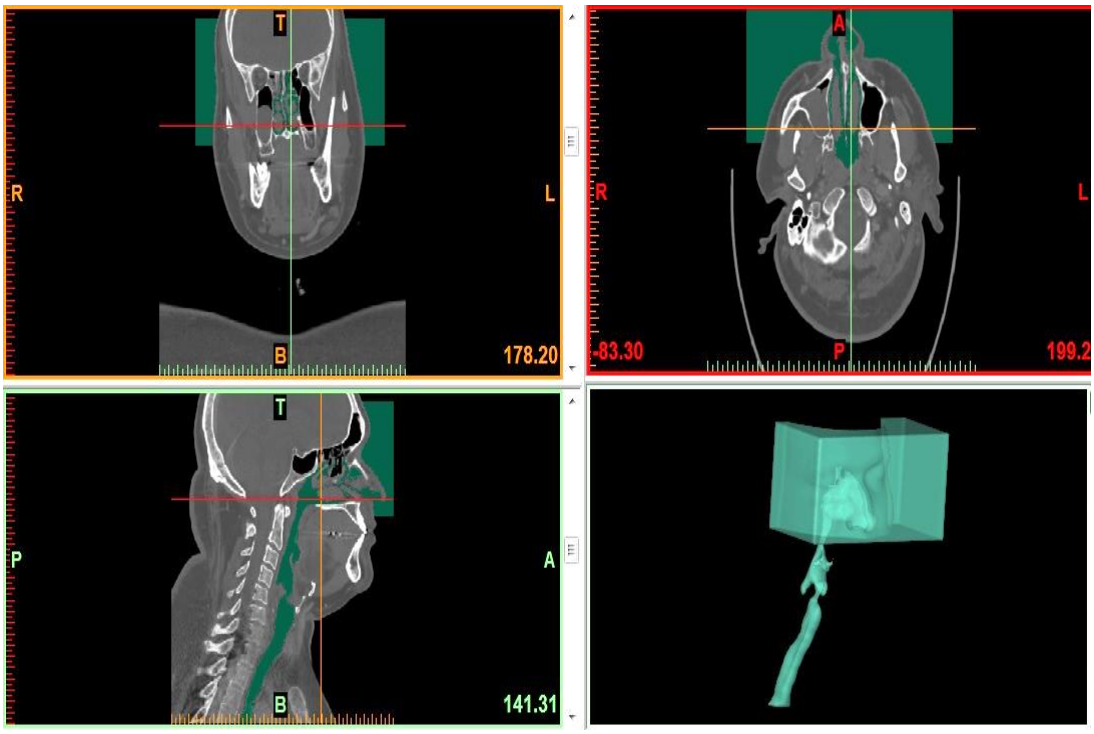

(a)

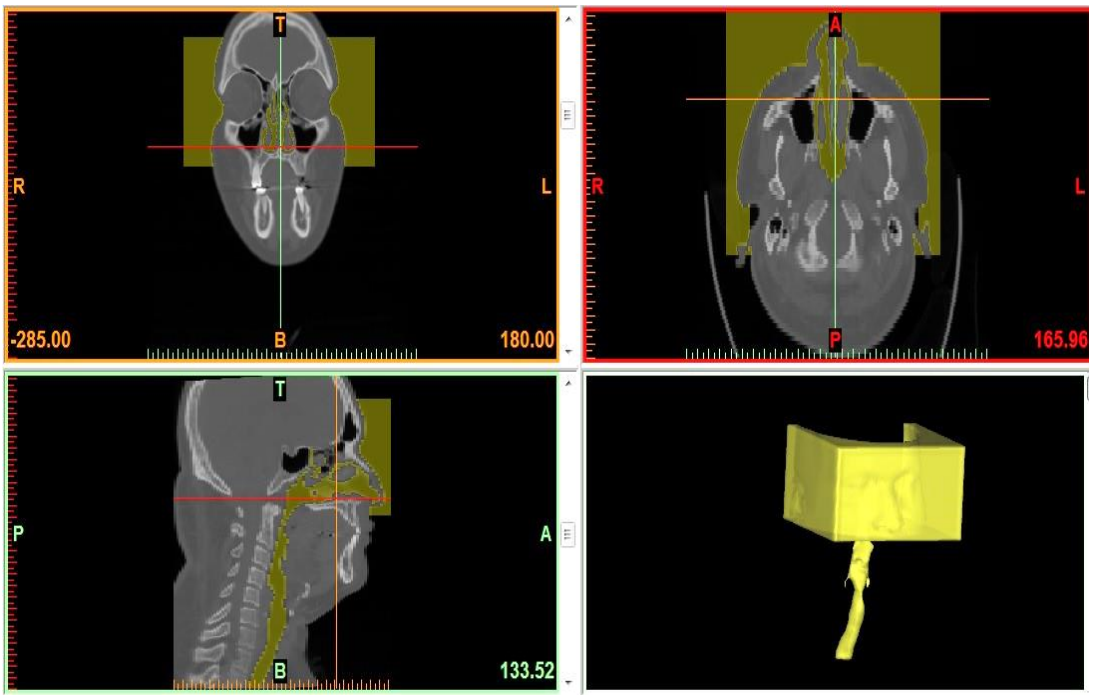

(b)

Figure 3.7: CT scan images obtained from axial, coronal and sagittal plane, (a) pre-operative OSA and (b) post-operative OSA.

An automatic region growing function was used to reconstruct the upper airway from the nostril to pharynx based on the segmented mask. The purpose of the region growing function was to reduce the noise, remove floating pixels and to split the unconnected structure. However, manual segmentation is also required to edit the mask which leak to surrounding region and remove unwanted parts which are still connected to the upper airway model. Manual editing function also makes it possible to draw and restore parts of the image on the segmented mask. By using the MIMICs editing tools, the scan images were segmented slice by slice on axial, coronal and sagittal plane by using the local threshold value.

MIMICs has the ability to generate and display the 3D anatomical model of the upper airway from the segmented mask. After all the necessary threshold editing, the 3D anatomical model of the upper airway was generated from the segmented mask. By using the 3D rendering tools, the 3D upper airway model generated was examined to ensure the suitability of the threshold and to confirm the presence of all the required structure for the physical anatomical model. MIMICs also provide the export function which can be used to export the 3D object generated from the segmented CT scan images into IGES file and can be directly used in any CAD software.

For the first case study, the polylines were created in MIMICs based on the segmented mask of the 3D object on each slice of the project by using ‘calculate polyline function’ as depicted in Figure 3.8. Later the 3D polylines data was exported as IGES (*.igs) file format, for the surface model generation using the CAD software,

CATIA. However, for the second case study, instead of using polylines function, the 3D upper airway can be directly export into 3D object as STL (*.stl) file format. Figure 3.9 shows the 3D model of the diseased human upper airway in .stl file format. Figure 3.9 (a) shows the 3D model generated for pre-operative and Figure 3.9 (b) shows for post-operative case. The direct export to STL file format function is only possible after the MIMICs software has been upgraded to a newer software version, Materialise MIMICs 19.0.

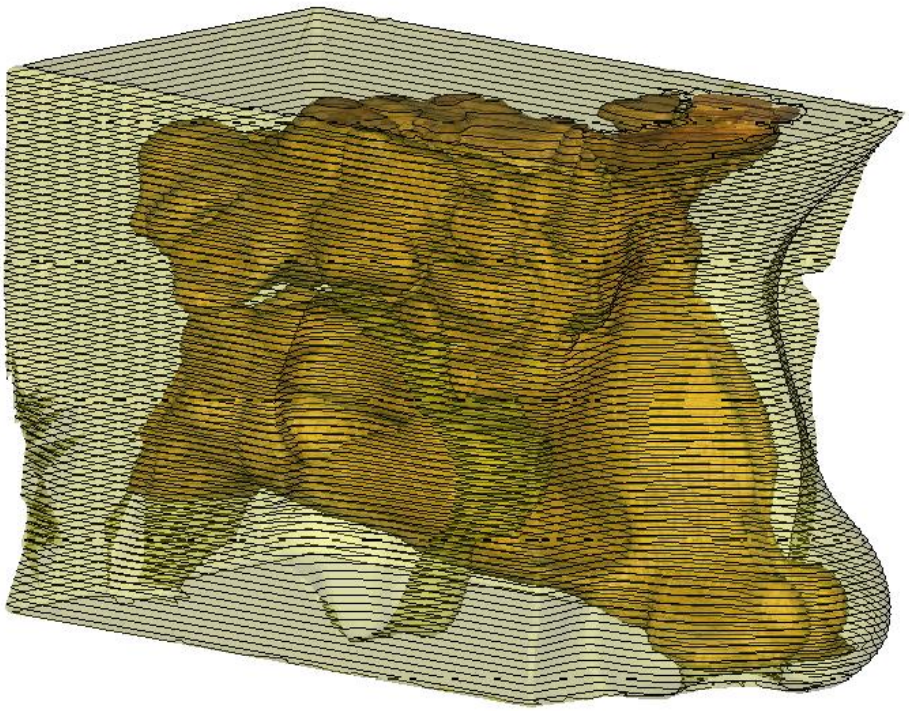

Figure 3.8: Polyline data of the 3D human nasal cavity.

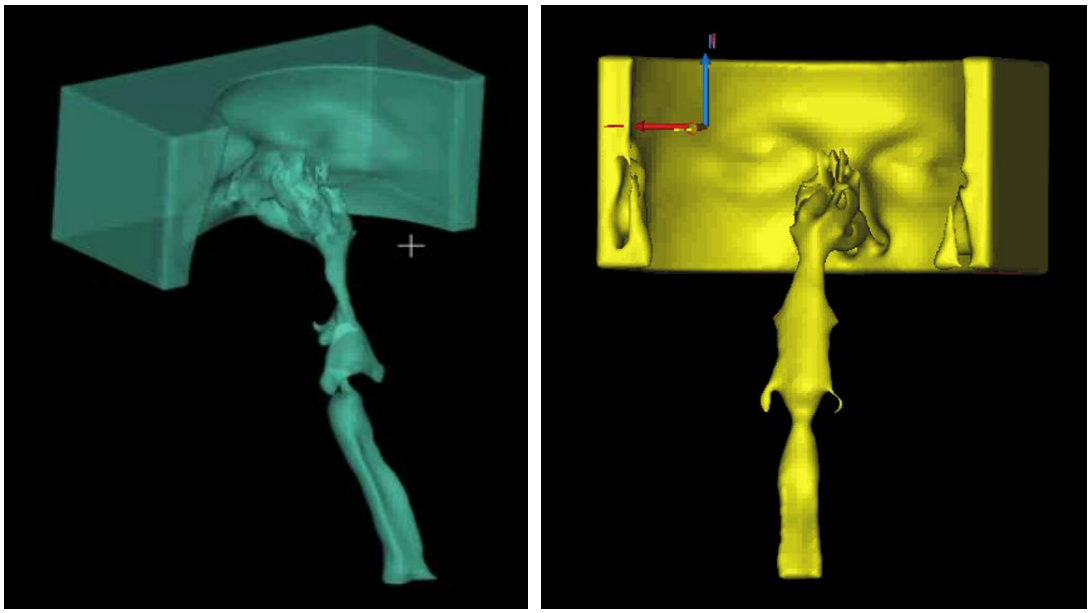

(a) (b)

Figure 3.9: The 3D model of the diseased human upper airway in .stl file format: (a) pre-operative and (b) post-operative.

3.2.3 Geometry Creation Using CATIA

The coordinate contour point extracted from the CT scan data of the human nasal cavity was imported into CAD software package, CATIA using Digitized Shape Editor (DSE) workbench for surface model generation. DSE is usually used at the initial stages of the reverse engineering process and it also provides tools for various operations on the imported digitized data. The IGES (*.igs) file can be imported and displayed in DSE workbench in the form of virtual mesh surface. The IGES (*.igs) file can be imported and displayed in DSE workbench in the form of cloud of points or polylines.

Due to anatomical complexity, the facets were created directly from the polylines instead of cloud of points. Figure 3.10 (a) shows the polylines data for the normal human nasal cavity whereas in Figure 3.10 (b), the facets were generated by using the mesh creation tools. The neighborhood parameter value was set to 7.5 mm to define the maximum length of the facet edge. The function of the neighborhood value is to close the unwanted holes of the mesh. Increasing the neighborhood parameter will lead to a non-manifold mesh. After the mesh surfaces have been created from the polylines, the next stage is to edit the 3D nasal mesh geometry by removing the unwanted mesh part.

In Figure 3.10 (c), the human face skin surface has been removed to simplify the geometry of the nasal computational model. As seen in Figure 3.10 (d), all the paranasal sinuses have also been removed in order to simplify the geometry and to reduce the computational cost. Editing was carefully carried out to preserve the original shape of the anatomical model of the human nasal cavity as depicted in Figure 3.10 (e). By using the cleaning mesh function, the defective mesh was removed to improve the quality of the mesh. The mesh cleaner helped analyze and delete all the defective mess which consisted of non-manifold edges, non-manifold vertices, isolated triangle, triangle with inconsistent orientations and the corrupted triangles. After all the necessary mesh cleaning, the 3D mesh geometry was smoothened using the mesh smoothing tool to improve mesh surface quality. Finally, the 3D computational model of the human nasal cavity was created based on the smooth mesh surface by using the automatic surface tool in Quick Surface Reconstruction workbench. Figure 3.10 (f) shows the final 3D model of the normal nasal cavity obtained from CATIA which can be used for computational modelling.

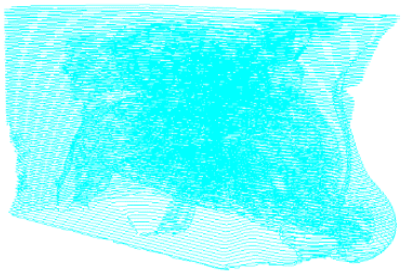

(a) Polyline data.

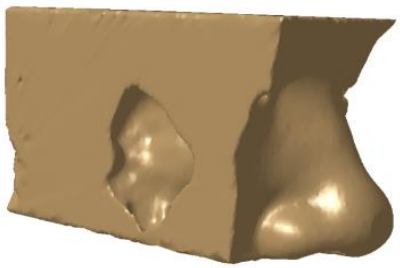

(b) Surface mesh generation.

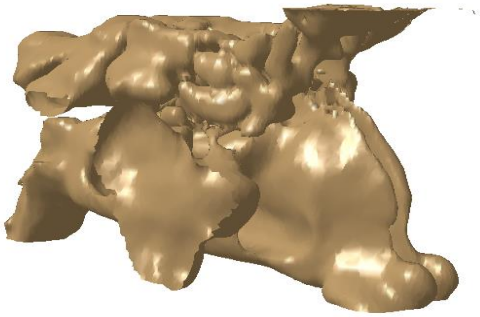

(c) Nasal cavity with paranasal sinuses.

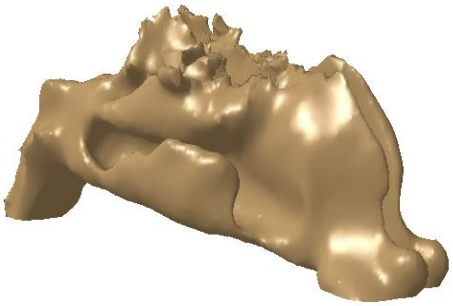

(d) Nasal cavity with paranasal sinuses removed.

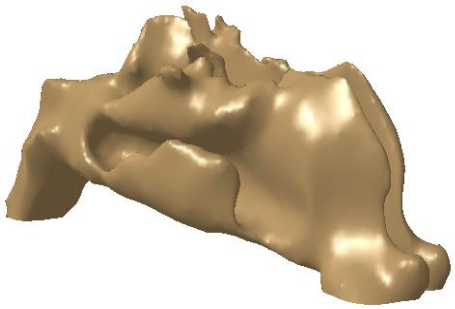

(e) Smoothing operation.

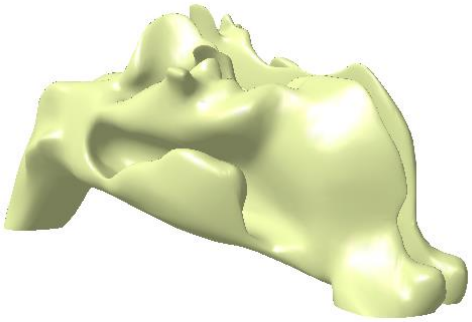

(f) The final 3D model of the nasal cavity

Figure 3.10: Steps involved in developing 3D model of the nasal cavity using CATIA.

Since it is highly difficult and very time consuming to obtain the CT scan data for subject suffering from Obstructive Sleep Apnea disease, therefore the first study case on OSA was carried out by modifying the control subject to represent the OSA disease. As can be seen in Figure 3.11 (a), the normal nasal geometry was extended from nasopharynx region to include the constricted pharyngeal section (Figure 3.11 (b)) to represent airway occlusion of the obstructive sleep apnea disease. The geometry was modified by using the Wireframe and Surface Design workbench in CATIA. The airway was modeled to have some area restrictions in the pharynx, which can be represented in terms of percentage stenosis. The details of the percentage stenosis developed for this model are further explained in Chapter 6.

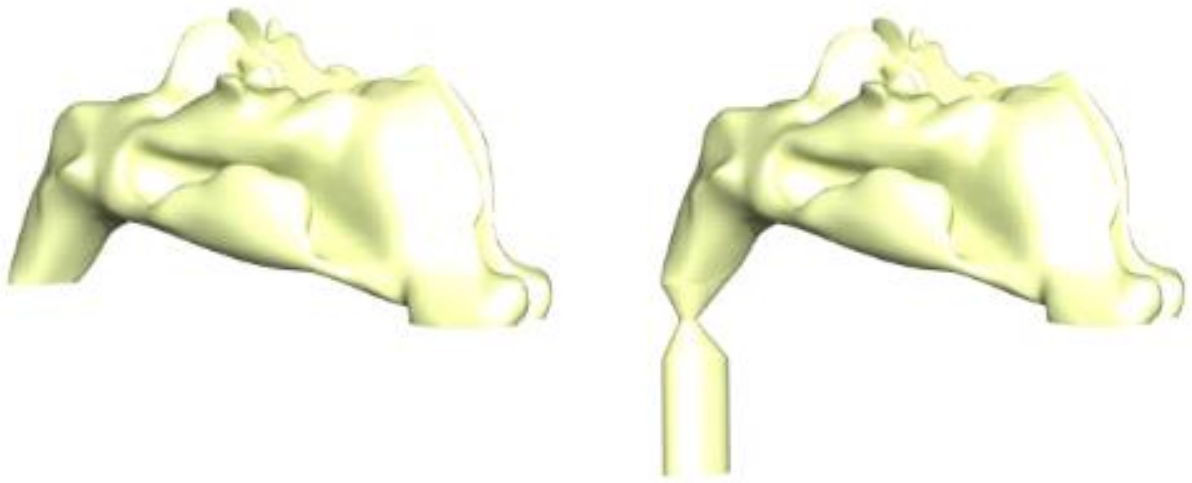

(a) (b)

Figure 3.11: Modification of control subject to represent OSA disease; (a) normal nasal cavity, (b) upper airway with constricted pharyngeal representing OSA.

In the third case study, full geometry of human upper airway starting from nostril inlet until pharynx region were developed both for pre- and post-surgery as depicted in Figures 3.12 & 3.13 respectively. Figures 3.12 (a) and 3.13 (a) show the initially the STL files were imported into CATIA using the Digitized Shape Editor (DSE) workbench for surface model generation. Then the mesh surfaces were generated in the same workbench. The patient's face has been removed in order to simplify the geometry and to reduce the computational cost.

As shown in Figures 3.12 (b) and 3.13 (b), mesh surface editing was carefully carried out to preserve the original shape of the nasal cavity inlet. Similarly, the mesh surface was cleaned up to remove all defective mesh. In Figures 3.12 (c) and 3.13 (c), the mesh was then smoothen to improve the mesh quality before the surface generation. Figures 3.12 (d) and 3.13 (d) show the final 3D model of the diseased upper airway with OSA for both pre- and post-operative cases respectively, which have been developed using CATIA.

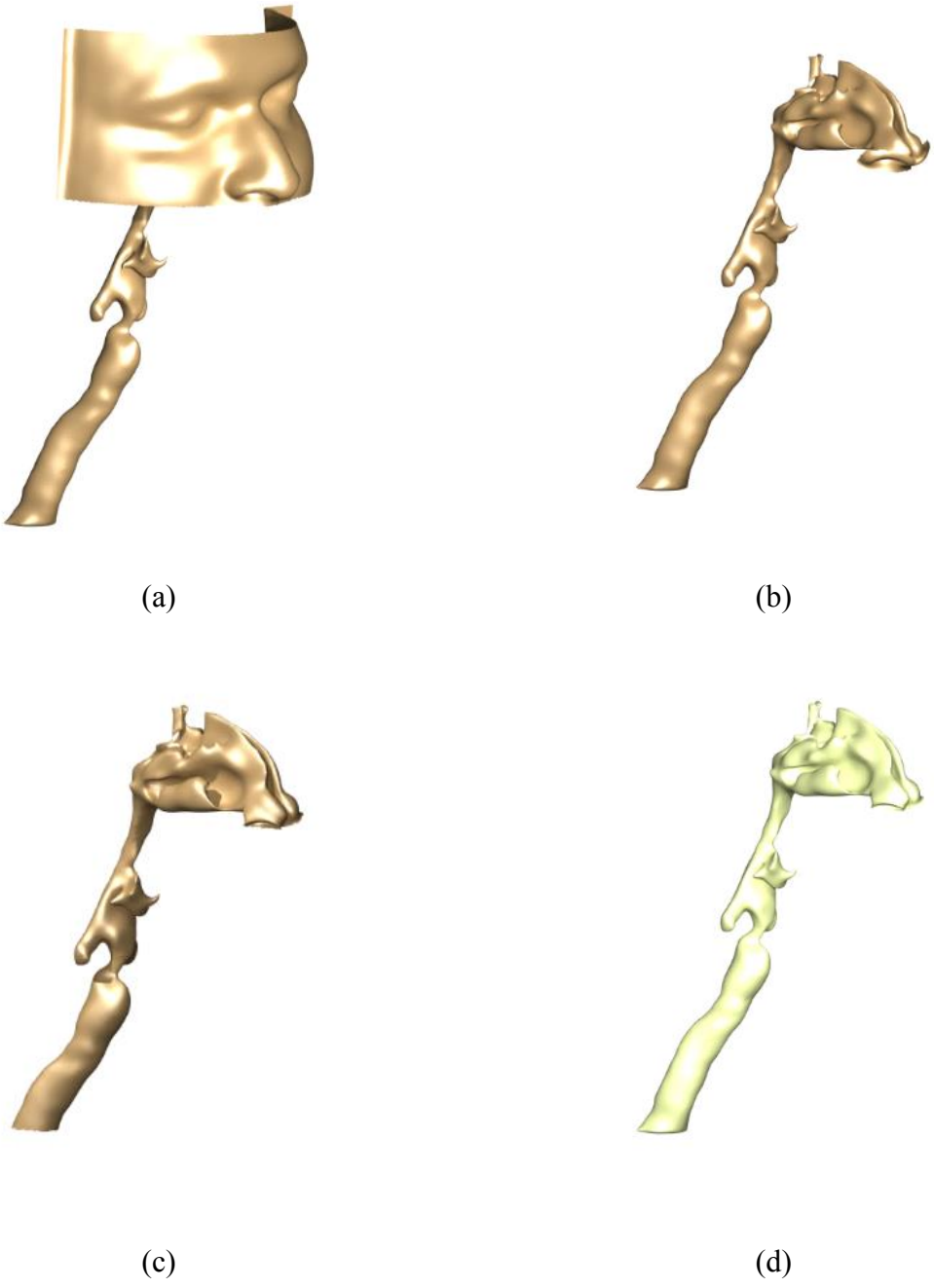

Figure 3.12: Steps involved in developing 3D model of the diseased human upper airway for the pre-operative case.

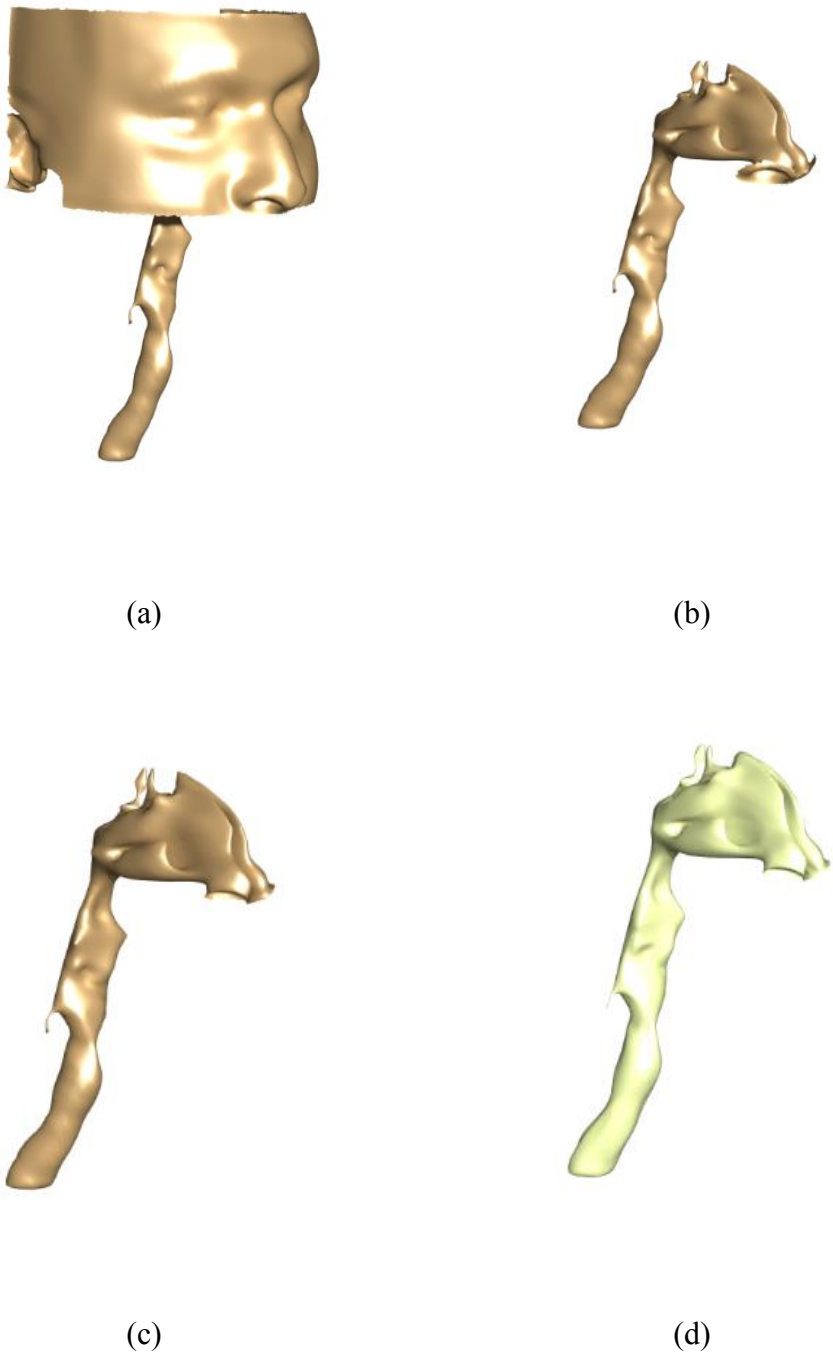

(a) (b)

(c) (d)

Figure 3.13: Steps involved in developing 3D model of the diseased human upper airway for post-operative case.

For the second case study, the effect of obstruction in the nasal cavity due to several nasal diseases and the effect of the nasal surgical treatment on breathing pattern and airflow characteristics and particle deposition were investigated. The 3D model of the diseased nasal airway was obtained from the upper airway geometry. The three-dimensional upper airway model of both pre and post-operative cases were modified by separating it into 2 parts namely, the nasal cavity region and the pharynx region. Figure 3.14 (a) shows the pre-operative nasal cavity model whereas Figure 3.15 (a) shows the post-operative nasal cavity model.

(a) (b)

Figure 3.14: The three-dimensional pre-operative upper airway model: (a) nasal cavity (b) pharynx.

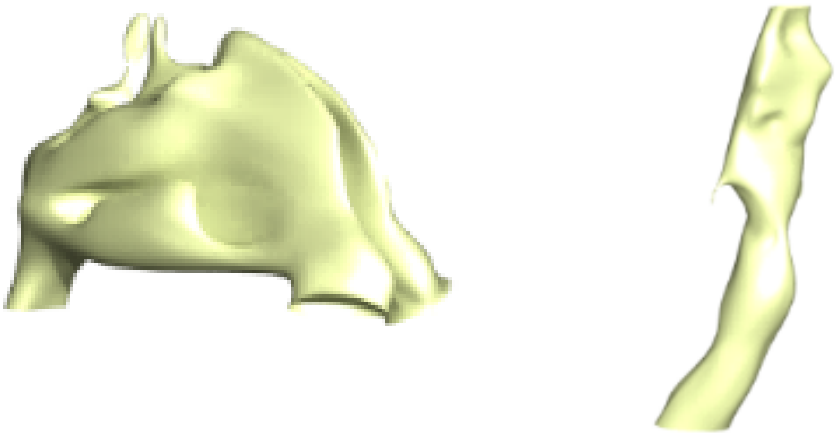

(a) (a)

Figure 3.15: The three-dimensional post-operative upper airway model: (a) nasal cavity (b) pharynx.

3.3 Hybrid Mesh Generation Using ANSYS Workbench

The 3D anatomical model of the human nasal cavity was imported into GAMBIT using STEP (*.stp) file format where the surface generated are detected as faces. The multiple faces are then stitched together to form a complete volume, which acts as the airflow domain. Before performing the face mesh generation, the nasal geometry was simplified by merging all the small faces into one face. This step is important in order to control the quality of the face and volume mesh of the domain to avoid creating a high aspect ratio and highly skewed mesh. A mesh with highly skewed cells can decrease accuracy and destabilize the solution. CFD simulation with structured grid usually gives faster solutions compared to unstructured grids. However, in the present case, as seen in Figure 3.16, due to the anatomical complex structure of the human upper airway, initially unstructured mesh consisting of tetrahedral elements was developed using GAMBIT.

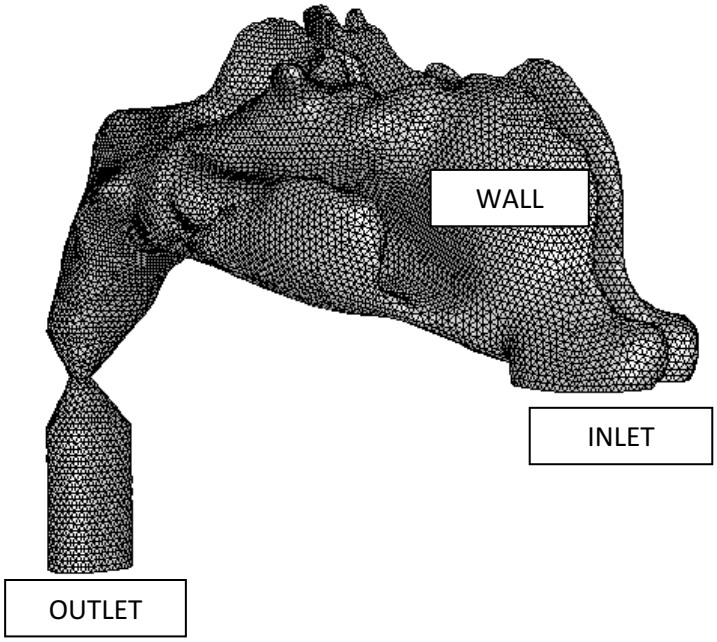

Figure 3.16: Volume mesh of the 3D computational model of human nasal cavity.

The complex geometry of nasal cavities requires a high-quality computational grid for resolving the airflow near the passage walls and to accurately model the particle-wall interactions. Hence, to improve numerical stability and accuracy, a hybrid mesh was generated with 1,580,000 elements, which consisted of a total 6 layers of prism cells near the wall boundary and tetrahedral elements were generated at the core of the domain as depicted in Figure 3.17. The hybrid mesh was developed by using ANSYS FLUENT MESHING. The first cell height (y value) was calculated based on the dimensionless wall distance y+=1. This confirms that the mesh quality of the airway models used for numerical simulations is sufficient for resolving the turbulent boundary layers in the airway models.

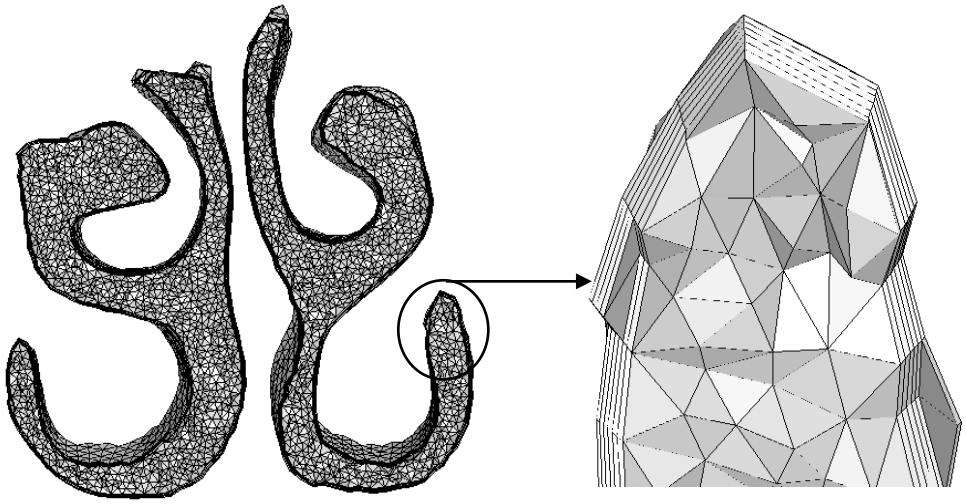

Figure 3.17: Hybrid mesh generated for the constricted pharyngeal representing OSA model.

For the second and third case studies, the initial unstructured mesh were developed using ANSYS ICEM WORKBENCH. The 3D anatomical model of the human upper airway was imported into ICEM WORKBENCH using IGES (*.igs) file format where the surface generated are detected as faces as depicted in Figures 3.18 (a) and 3.19 (a). Similarly, before performing the face mesh generation, the nasal geometry was simplified by merging all the small faces into one face. This step is important in order to control the quality of the face and volume mesh of the domain to avoid creating a high aspect ratio and skewed mesh. Figure 3.18 (b) shows the unstructured tetrahedral mesh generated for the pre-operative case and Figure 3.9 (b) shows for the post-operative case.

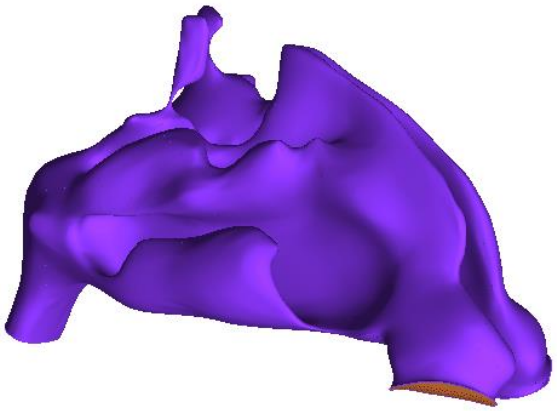

(a)

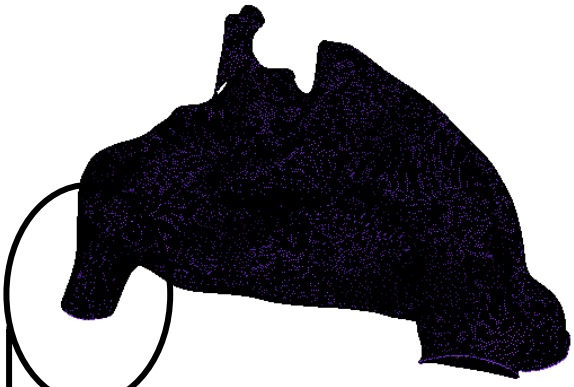

(b)

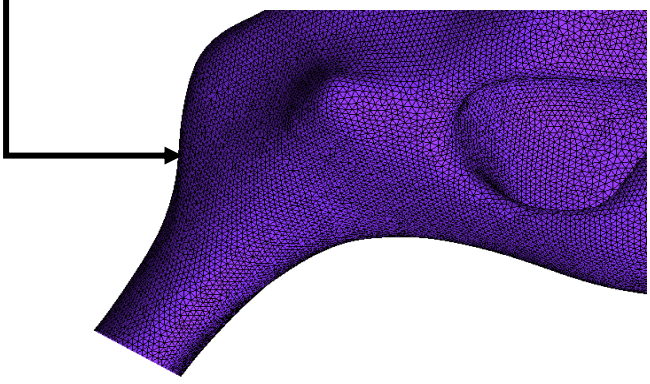

Figure 3.18: Unstructured tetrahedral mesh generation for the pre-operative nasal cavity model; (a) nasal model in IGES file format (b) volume mesh.

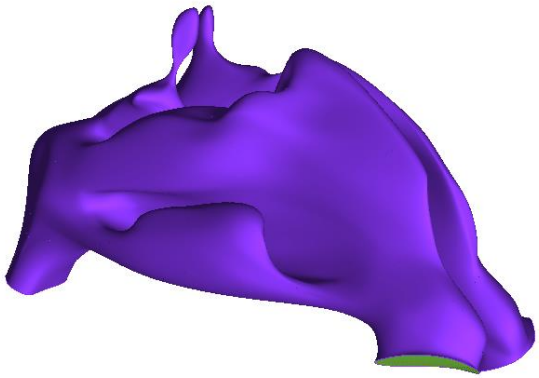

(a)

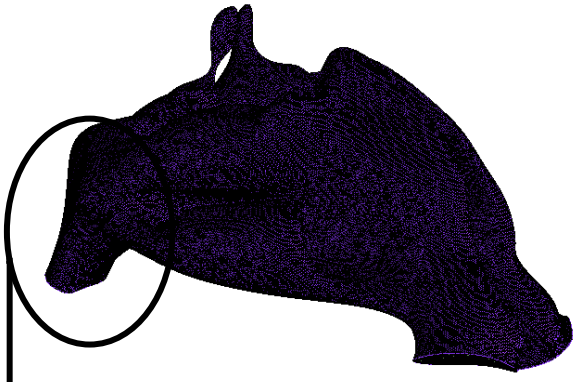

(b)

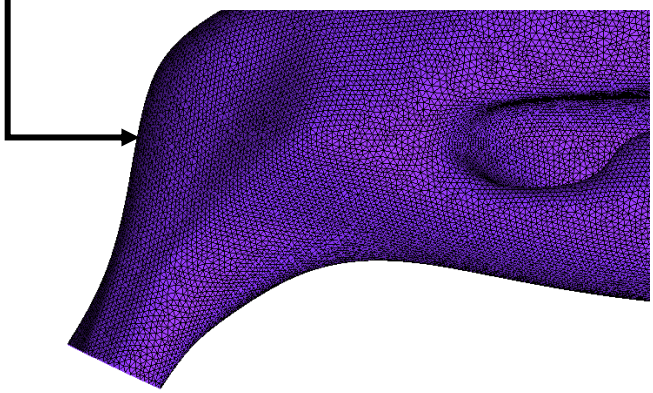

Figure 3.19: Unstructured tetrahedral mesh generation for the post-operative nasal cavity model; (a) nasal model in IGES file format (b) volume mesh.

Hybrid mesh were then generated by using ANSYS FLUENT MESHING with 4456725 elements for pre-operative and 3167403 elements for post-operative model. A total of 5 layers of prism mesh near the wall boundary, and tetrahedral elements in the remaining flow domain were obtained from a grid independent study. A detail explanation on grid dependency study are included in Chapter 5.

Figure 3.20 (a) and 3.21 (a) show the upper airway model in IGES file format for pre-operative and post-operative model respectively. Figures 3.20 (b) and 3.21 (b) show the unstructured tetrahedral mesh generated for the pre- and post-operative upper airway model with obstructive sleep apnea diseases. Hybrid mesh was then developed by using ANSYS FLUENT MESHING. A total of 4 layers of prism mesh near the wall boundary, and tetrahedral elements in the remaining flow domain were obtained from a grid independent study. A detail explanation on grid independent study are included in Chapter 7.

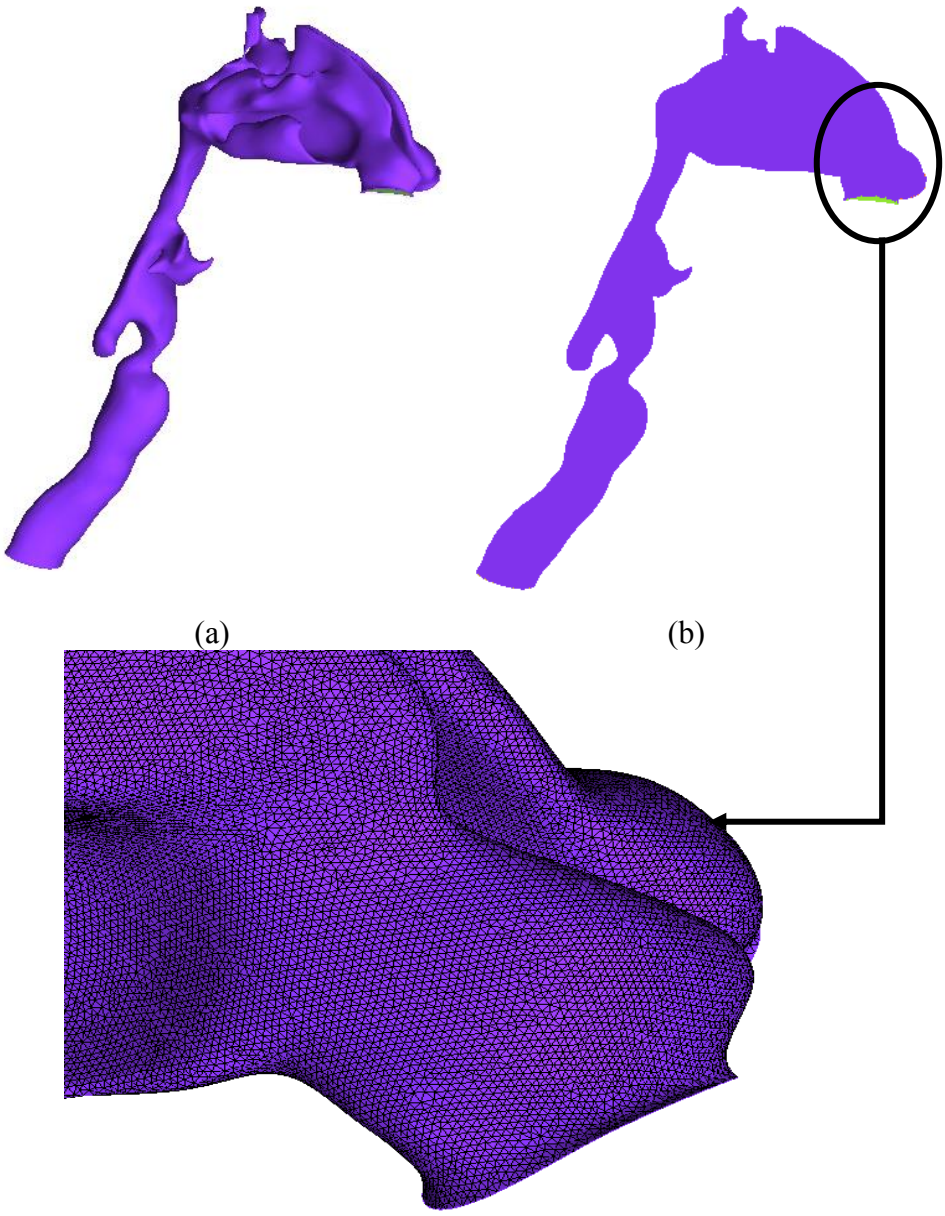

Figure 3.20: Tetrahedral mesh generation for pre-operative upper airway model.(a) upper airway model in IGES file format (b) volume mesh.

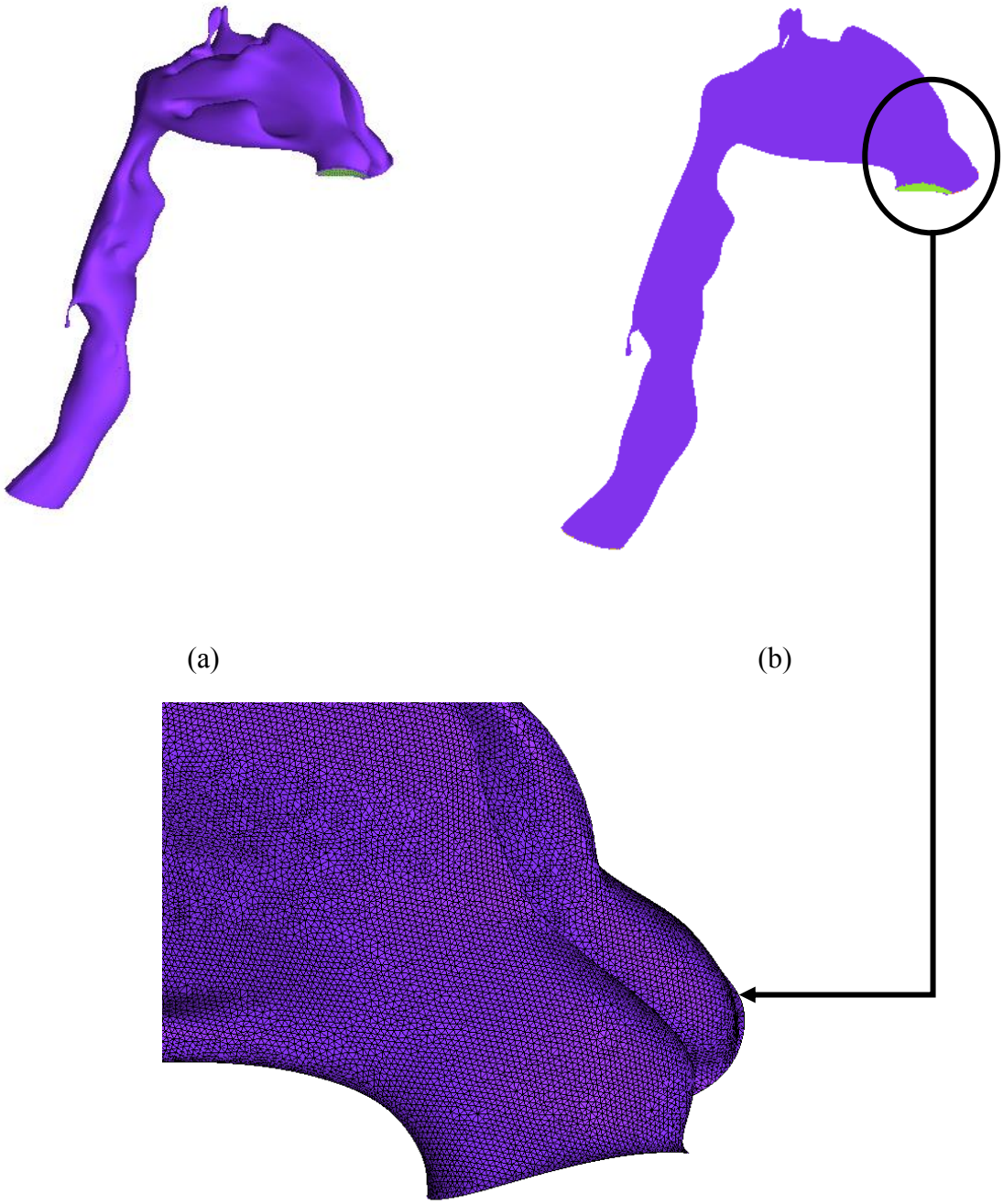

Figure 3.21: Tetrahedral mesh generation for post-operative upper airway model (a) upper airway model in IGES file format (b) volume mesh.

3.4 Calculation of First Grid Off the Wall, the y Values

The region close to the wall is usually characterized in term of dimensionless variables with respect to the local conditions at the wall. If we let y be the normal distance from the wall and U be the time averaged velocity parallel to the wall, then the dimensionless velocity U^+ and wall distance y^+ can be appropriately described as U/u_τ and $y\rho u_\tau/\mu$, respectively. This is called the law of the wall. By defining y^+equal to 1, the first grid point off the wall y value can be calculated by using the following equations (Versteeg & Malalasekera, 1995):

$$y^+ = \frac{\rho u_\tau y}{\mu} \tag{3.1}$$

and

$$y = \frac{y^+ \mu}{\rho u_\tau} \tag{3.2}$$

where μ is the dynamic viscosity, ρ is the air density, u_τ is the friction velocity at the nearest wall, and y is the distance to the nearest wall. Within this dimensionless parameters, the wall friction velocity u_τ is defined with respect to the wall shear stress τ_w

$$u_\tau = \sqrt{\frac{\tau_w}{\rho}} \tag{3.3}$$

where τ_w is the wall shear stress and ρ is the air density. The wall shear stress τ_w is defined as

$$\tau_w = \frac{C_f \rho U^2}{2} \tag{3.4}$$

where C_f is the skin friction coefficient, ρ is the air density, and U is the air velocity. The skin friction coefficient C_f is defined as

$$C_f = 0.079 Re^{-0.25} \tag{3.5}$$

where Re is the Reynolds number.

The Reynolds number Re is defined as

$$Re = \frac{\rho U d_H}{\mu} \tag{3.6}$$

where ρ is the air density, U is the air velocity, d_H is the hydraulic diameter and μ is the dynamic viscosity. The hydraulic diameter is defined as (Segal et al., 2008):

$$d_H = \frac{4A}{P} \tag{3.7}$$

where A is the cross section area at the pharynx section and P is the wetted perimeter at the pharynx section.

3.4.1 Pre-Operative Upper Airway Computational Model

By using the Equation 3.7, the hydraulic diameter d_H was calculated based on the perimeter measured at the pharynx section as depicted in Figure 3.22. The perimeter was measured by using the measure item tool which is available in the CAD software named CATIA. As shown in Figure 3.22, the red color lines which represent the curve edges were measured by using the edge selection mode. In the measure item toolbox, the calculation mode was set to exact, which means only exact measured value will be considered. The perimeter at the pharynx was then calculated by adding the measured length of each curve edges as shown in Figure 3.22. For the Pre-Operative OSA case, the perimeter obtained at pharynx section is $P_{pharynx}$ = 29.84 mm. The cross-section area obtained at the pharynx section is, $A_{pharynx} = 6.124 \times 10^{-5}$ m^2. Hence, the hydraulic diameter calculated for the pre-operative OSA case is $d_H = 8.21 \times 10^{-3}$ m.

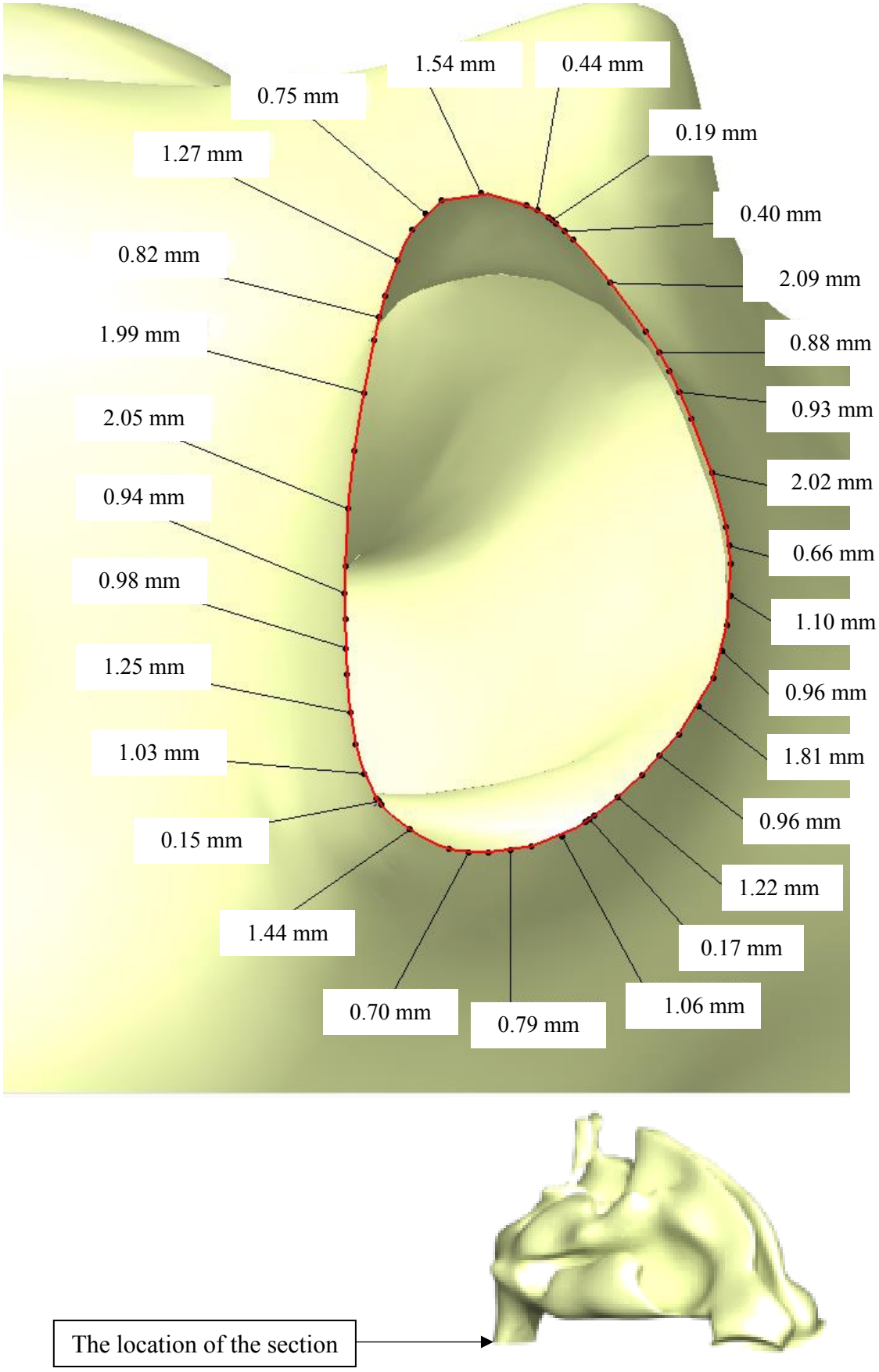

Figure 3.22: The measured perimeter at the pharynx section for pre-operative case.

The air velocity U were calculated based on the volume flow rate Q defined at the inlet boundary condition and the cross-section area obtained at the pharynx section. By using Equation 3.6, the Reynolds number Re were calculated for all flow rates ranging from 7.5 to 60 L/min. The air density is $\rho = 1.225\ \mathrm{kg/m^3}$, the dynamics viscosity is $\mu = 1.7894\times10^{-5}\ \mathrm{kg/ms}$ and the hydraulic diameter is $d_H = 8.21\times10^{-3}$ m. By using Equation 3.1 to 3.5, the skin friction coefficient C_f, the wall shear stress τ_w, the friction velocity at the nearest wall C_f and the first grid point off the wall y were calculated. Table 3.1 shows the summary of first grid point off the wall value for pre-operative cases.

Table 3.1: First grid point off the wall, y value for pre-operative OSA.

Volume Flow Rate, (L/min)	Velocity, (m/s)	Reynolds Number	Skin friction coefficient	Wall Shear Stress, (Pa)	Friction velocity at the nearest wall, (m/s)	First grid point off the wall, (mm)
4	1.089	605	-	-	-	-
7.5	2.041	1147	-	-	-	-
10	2.722	1529	-	-	-	-
20	5.443	3059	0.011	0.192	0.396	0.037
30	8.165	4589	0.010	0.392	0.566	0.026
40	10.886	6118	0.009	0.646	0.726	0.020

3.4.2 Post-Operative Upper Airway Computational Model

For the post-operative model, similarly, by using Equation 3.7, the hydraulic diameter d_H was calculated based on the pharynx perimeter obtained by using the measure item tool in CATIA. Figure 3.23 shows the measured perimeter at the pharynx section for the post-operative geometry. For the post-operative geometry, the perimeter obtained at the pharynx section is $P_{pharynx} = 34.30$ mm . The cross-section area obtained at the pharynx section is $A_{pharynx} = 7.685 \times 10^{-5}$ m^2. Hence, the hydraulic diameter calculated for post-operative OSA case is $d_H = 8.964 \times 10^{-3}$ m.

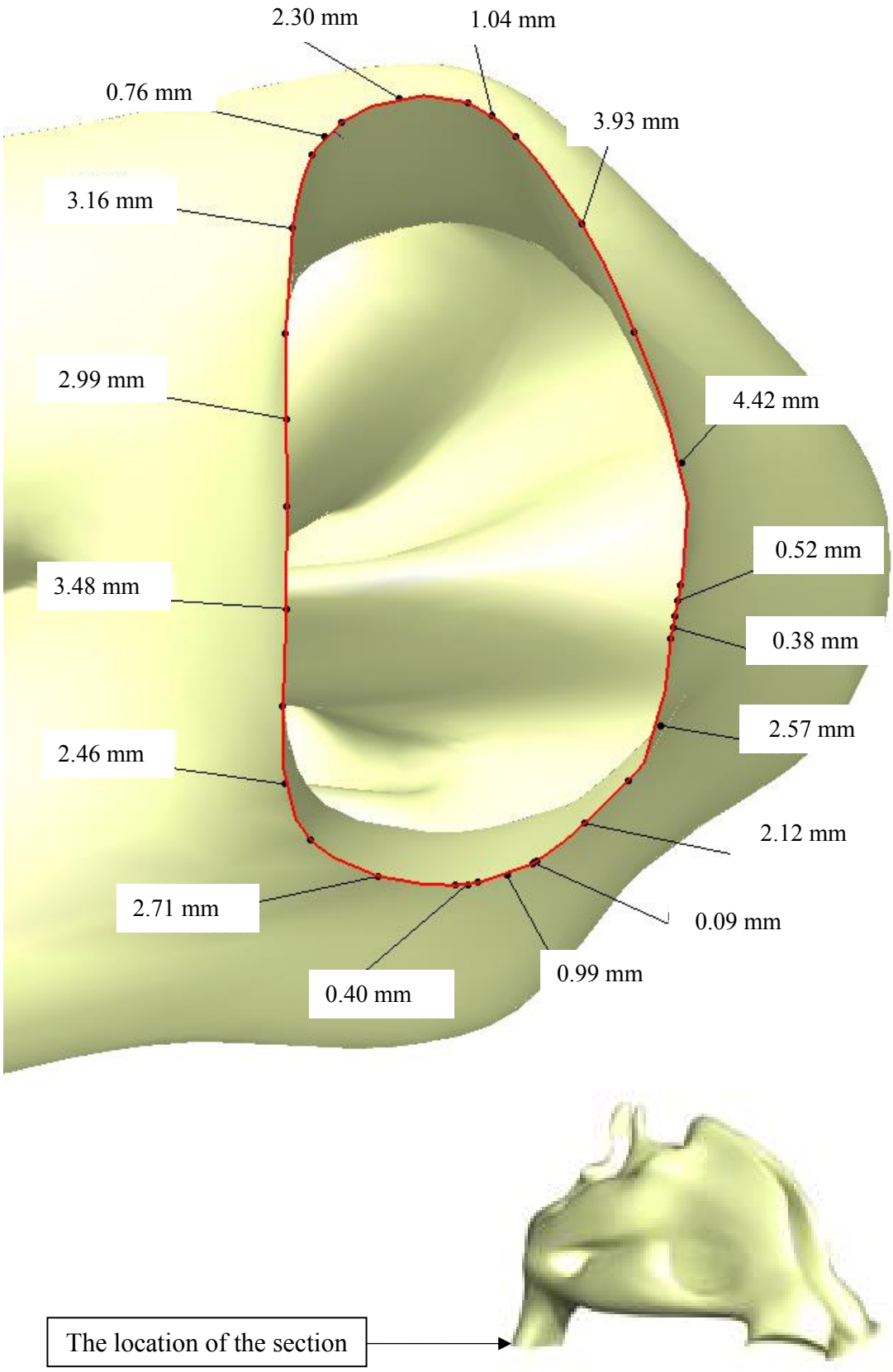

Figure 3.23: The measured perimeter at the pharynx section for post-operative case.

Table 3.2: First grid point off the wall, y value for post-operative OSA.

Volume Flow Rate, (L/min)	Velocity, (m/s)	Reynolds Number	Skin friction coefficient	Wall Shear Stress, (Pa)	Friction velocity at the nearest wall, (m/s)	First grid point off the wall, (mm)
4	0.867	532	-	-	-	-
7.5	1.627	998	-	-	-	-
10	2.169	1331	-	-	-	-
20	4.337	2661	0.011	0.127	0.322	0.045
30	6.506	3992	0.010	0.257	0.458	0.032
0	8.675	5323	0.009	0.424	0.588	0.025

The air velocity U were calculated based on the volume flow rate Q defined at the inlet boundary condition and the cross-section area obtained at the pharynx section. By using Equation 3.6, the Reynolds number Re were calculated for all flow rates ranging from 7.5 to 60 L/min. The air density is $\rho = 1.225\,\mathrm{kg/m^3}$, the dynamics viscosity is $\mu = 1.7894\times10^{-5}\mathrm{kg/ms}$ and the hydraulic diameter is $d_H = 8.964\times10^{-3}\mathrm{m}$. By using Equations 3.1 to 3.5, the skin friction coefficient C_f, the wall shear stress τ_w, the friction velocity at the nearest wall C_f and the first grid point off the wall y were calculated. Table 3.1 shows the summary of first grid point off the wall value for post-operative cases.

CHAPTER 4

NUMERICAL SIMULATION METHODOLOGY

4.1 Overview

This chapter presents the governing equation for the fluid phase and particle phase used to solve the numerical simulation of airflow and the transport and deposition of the inhaled particles in the diseased human upper airway model. The type of boundary condition defined on the computational domain and assumption made during simulation were also explained. The numerical methods used and the convergence criteria are also briefly discussed.

4.2 Governing Equations for Fluid Phase

CFD is fundamentally based on the governing equations of fluid dynamics. They represents mathematical statements of the conservation laws of physics, consisting of the continuity equation, three momentum equations and an energy equation which is also called the full Navier-Stokes equation.

4.2.1 General Equations for Fluid Phase

The CFD approach consists of solving the continuity and momentum equations in each cell of the discretized computational domain. For a general fluid property defined by ϕ, the governing equations of fluid flow for an incompressible fluid, such

as the airflow in the respiratory system, can be cast into the so-called transport equation form as (Versteeg & Malalasekera, 1995):

$$\frac{\partial \phi}{\partial t} + \frac{\partial (u\phi)}{\partial x} + \frac{\partial (v\phi)}{\partial y} + \frac{\partial (w\phi)}{\partial z} = \frac{\partial}{\partial x}\left[\Gamma \frac{\partial \phi}{\partial x}\right] + \frac{\partial}{\partial y}\left[\Gamma \frac{\partial \phi}{\partial y}\right] + \frac{\partial}{\partial z}\left[\Gamma \frac{\partial \phi}{\partial z}\right] + S_\phi \tag{4.1}$$

where t is time, u, v, w represents velocity components, Γ is the diffusion coefficient, and S_ϕ which is a general source term that may represent external variables. These source terms may include pressure and non-pressure gradient terms, gravity that influence the fluid motion and heat source sources or sinks within the flow domain, to name a few. Equation 4.1 represents the transport process of the fluid properties and hence is also known as the transport equations. In words, Equation 4.1 can be read as

Rate of increase of ϕ in a fluid element	+	*Net rate of flow of ϕ through a fluid element*	=	*Rate of increase of ϕ due to diffusion*	+	*Rate of increase of ϕ due to additional sources*
Local acceleration		Convection		Diffusion		Source terms

Equation 4.1 is commonly used as the starting point for computational procedures in the finite volume methods. By setting the property ϕ equal to 1, u, v, w and T and selecting appropriate value for the diffusion coefficient Γ, one can obtain the partial differential equations for the conservation of mass, momentum, and energy as shown in Table 4.1.

Table 4.1 The Navier-Stokes equations for the incompressible flow

Conservation of mass ($\phi = 1$)

$$\frac{\partial u}{\partial x} + \frac{\partial v}{\partial y} + \frac{\partial w}{\partial z} = 0 \tag{4.2}$$

Conservation of Momentum ($\phi = u, v, w$)

$$\frac{\partial u}{\partial t} + \frac{\partial (uu)}{\partial x} + \frac{\partial (vu)}{\partial y} + \frac{\partial (wu)}{\partial z} = -\frac{1}{\rho}\frac{\partial p}{\partial x} + \frac{\partial}{\partial x}\left[\nu \frac{\partial u}{\partial x}\right] + \frac{\partial}{\partial y}\left[\nu \frac{\partial u}{\partial y}\right] + \frac{\partial}{\partial z}\left[\nu \frac{\partial u}{\partial z}\right] + S_u \tag{4.3}$$

$$\frac{\partial v}{\partial t} + \frac{\partial (uv)}{\partial x} + \frac{\partial (vv)}{\partial y} + \frac{\partial (wv)}{\partial z} = -\frac{1}{\rho}\frac{\partial p}{\partial y} + \frac{\partial}{\partial x}\left[\nu \frac{\partial v}{\partial x}\right] + \frac{\partial}{\partial y}\left[\nu \frac{\partial v}{\partial y}\right] + \frac{\partial}{\partial z}\left[\nu \frac{\partial v}{\partial z}\right] + S_v \tag{4.4}$$

$$\frac{\partial w}{\partial t} + \frac{\partial (uw)}{\partial x} + \frac{\partial (vw)}{\partial y} + \frac{\partial (ww)}{\partial z} = -\frac{1}{\rho}\frac{\partial p}{\partial z} + \frac{\partial}{\partial x}\left[\nu \frac{\partial w}{\partial x}\right] + \frac{\partial}{\partial y}\left[\nu \frac{\partial w}{\partial y}\right] + \frac{\partial}{\partial z}\left[\nu \frac{\partial w}{\partial z}\right] + S_w \tag{4.5}$$

4.2.2 Reynolds-Averaged Navier-Stokes Equations

Turbulent flows are characterized by fluctuating velocity fields. These fluctuations mix transported quantities such as momentum, energy, and species concentration, and cause the transported quantities to fluctuate as well. Since these fluctuations can be of small scale and high frequency, they are too computationally expensive to simulate directly in practical engineering calculations. Instead, the instantaneous governing equations can be time-averaged, ensemble-averaged, or otherwise manipulated to remove the small scales, resulting in a modified equation

contain additional unknown variables, and turbulence models are needed to determine these variables in terms of known quantities. The additional terms in the governing equations need to be modeled in order to achieve "closure" which means that there are sufficient number of equations for all the unknowns.

The Reynolds-Average Navier-Stokes (RANS) equations represent transport for the mean flow quantities only, with all the scales of the turbulence being modeled. The approach of permitting a solution for the mean flow variables greatly reduces the computational effort. Osborne Reynolds first introduced the concept of Reynolds decomposition. In this concept, the solution variables in the instantaneous Navier-Stokes equations which defines ϕ are decomposed into the sum of a steady mean component $\bar{\phi}$ (ensemble averaged or time average) and a fluctuating component $\phi'(t)$ (ANSYS FLUENT Theory Guide, 2009):

$$\phi(t) = \bar{\phi} + \phi'(t) \tag{4.6}$$

Substituting expression of this form for the flow variables into the Navier-Stokes equations in Table 4.1 produces the Reynolds-Averaged Navier-Stokes (RANS) equations.

$$\frac{\partial \rho}{\partial t} + \frac{\partial}{\partial x_i}(\rho u_i) = 0 \tag{4.7}$$

$$\frac{\partial}{\partial t}(\rho u_i) + \frac{\partial}{\partial x_j}(\rho u_i u_j) = -\frac{\partial p}{\partial x_i} + \left[\mu\left(\frac{\partial u_i}{\partial x_j} + \frac{\partial u_j}{\partial x_i} - \frac{2}{3}\delta_{ij}\frac{\partial u_l}{\partial x_l}\right)\right] + \frac{\partial}{\partial x_j}\left(-\rho\overline{u_i' u_j'}\right) \tag{4.8}$$

where $\bar{u}_i$ and u_i' are the mean velocity and fluctuating velocity, respectively. Equation 4.7 and 4.8 represent the Reynolds-averaged Navier-Stokes (RANS) equations. They have the same general form as the instantaneous Navier-Stokes equations, with the velocities and other solution variables now representing ensemble-average (or time-average) values. Additional terms now appear that represent the effects of turbulence. Then Reynolds stresses $-\rho\overline{u_i' u_j'}$, must be modeled in order to close Equation 4.8.

The Reynolds-averaged approach to turbulence modeling requires that the Reynolds stresses in Equation 4.8 be appropriate modeled. A common method employs the Boussinesq hypothesis to relate the Reynolds stresses to the mean velocity gradients:

$$-\rho\overline{u_i' u_j'} = \mu_t\left(\frac{\partial u_i}{\partial x_j} + \frac{\partial u_j}{\partial x_i}\right) - \frac{2}{3}\left(\rho k + \mu_t\frac{\partial u_i}{\partial x_i}\right)\delta_{ij} \tag{4.9}$$

The advantage of this approach is the relatively low computational cost associated with the computation of the turbulent viscosity, μ_t. The disadvantage of the Boussinesq hypothesis as presented is that it assumes μ_t is an isotropic scalar quantity, which is not strictly true.

In the present study, simulation is based on the numerical solution of the Reynolds Average Navier-Stokes equation representing the general equation for 3D flow of incompressible and viscous fluids. The SST $k-\omega$ turbulence model, a two-equation turbulence model was employed. The shear stress transport (SST) $k-\omega$ model was developed by Menter, (1994) to effectively blend the robust and accurate formulation of the $k-\omega$ model in the near wall region with the free stream independence of the $k-\varepsilon$ model in the far field. To achieve this, the $k-\varepsilon$ model is converted into $k-\omega$ formulation. The SST $k-\omega$ model accounts for transport of turbulent shear stress and gives highly accurate predictions of the amount of flow separation under adverse pressure gradient. The SST model is blend between the $k-\omega$ turbulence model, which is applicable near the walls, and the $k-\varepsilon$ turbulence model which is applied at the core of the computational domain. Therefore, SST combines the advantages of both the $k-\varepsilon$ and $k-\omega$ methods. The combination is ideal for a flow in a complex geometry like the nasal cavity (Liu, Matida, Gu, & Johnson, 2007). The suitability of SST $k-\omega$ model also has been experimentally validated by (Mylavarapu et al., 2009b).

The shear-stress transport (SST) $k-\omega$ model was developed by Menter to effectively blend the robust and accurate formulation of the $k-\omega$ model in the near-wall region with the freestream independence of the $k-\varepsilon$ model in the far field. To achieve this, $k-\varepsilon$ model is converted into a $k-\omega$ formulation. The SST $k-\omega$ model is similar to the standard $k-\omega$ model, but includes the following refinements. First, the standard $k-\omega$ and the transformed $k-\varepsilon$ model are both multiplied by a blending function and both models are added together. The blending function is

designed to be one in the near-wall region, which activates the standard k − ω model, and zero away from the surface, which activates the transformed k − ε model. Second, the SST model incorporates a damped cross-diffusion derivative term in the ω equation. Third, the definition of the turbulent viscosity is modified to account for the transport of the turbulent shear stress. Fifth, the modeling constants are different. These features make the SST k − ω model more accurate and reliable for a wider class of flows, for example, adverse pressure gradient flows, than the standard k − ω model. The suitability of SST k − ω model has been experimentally validated by (Liu et al., 2007) and (Mylavarapu et al., 2009b).

The transport equations for the SST k − ω model can be defined as (ANSYS FLUENT Theory Guide, 2009)

$$\frac{\partial}{\partial t}(\rho k) + \frac{\partial}{\partial x_i}(\rho k u_i) = \frac{\partial}{\partial x_j}\left(\Gamma_k \frac{\partial k}{\partial x_j}\right) + G_k - Y_k + S_k \qquad (4.10)$$

$$\frac{\partial}{\partial t}(\rho \omega) + \frac{\partial}{\partial x_i}(\rho \omega u_i) = \frac{\partial}{\partial x_j}\left(\Gamma_\omega \frac{\partial \omega}{\partial x_j}\right) + G_\omega - Y_\omega + D_\omega + S_\omega \qquad (4.11)$$

In Equations 4.10 and 4.11, the term G_k is the production of turbulence kinetic energy due to mean velocity gradients, and is defined as

$$G_k = -\rho \overline{u_i' u_j'} \frac{\partial u_j}{\partial x_i} \qquad (4.12)$$

To evaluate G_k in a manner consistent with the Boussinesq hypothesis,

$$G_k = \mu_t S^2 \tag{4.13}$$

In Equation 4.13, S represents the modulus of the mean rate-of-strain tensor, which can be defined as

$$S \equiv \sqrt{2S_{ij}S_{ij}} \tag{4.14}$$

The term G_ω is the generation of the turbulence specific dissipation rate, ω and is given by

$$G_\omega = \frac{\alpha}{v_t} G_k \tag{4.15}$$

In Equation 4.15, the coefficient α is defined by

$$\alpha = \frac{\alpha_\infty}{\alpha^*}\left(\frac{\alpha_0 + Re_t/R_\omega}{1 + Re_t/R_\omega}\right) \tag{4.16}$$

$$R_\omega = 2.95.\alpha^* \tag{4.17}$$

$$\alpha^* = \alpha_\infty^*\left(\frac{\alpha_0^* + Re_t/R_k}{1 + Re_t/R_k}\right) \tag{4.18}$$

$$Re_t = \frac{\rho k}{\mu\omega} \tag{4.19}$$

where $R_k = 6$, $\alpha_0^* = \beta_i/3$ and $\beta_i = 0.072$. The terms Γ_k in Equations 4.10 represents the effective diffusivity k while the term Γ_ω in Equation 4.11 represents the effective diffusivity of and ω. The effective diffusivity for k and ω can be defined by:

$$\Gamma_k = \mu + \frac{\mu_t}{\sigma_k} \tag{4.20}$$

$$\Gamma_\omega = \mu + \frac{\mu_t}{\sigma_\omega} \tag{4.21}$$

In Equation 4.20, the term σ_k represents the turbulent Prandtl number for k while the term σ_ω is the turbulent Prandtl number for and ω. The turbulent viscosity, μ_t is computed as follows:

$$\mu_t = \frac{\rho k}{\omega} \frac{1}{max\left[\frac{1}{\alpha^*}, \frac{\Omega F_2}{\alpha_1 \omega}\right]} \tag{4.22}$$

In Equation 4.22, the term Ω is the strain rate magnitude and is given by

$$\Omega \equiv \sqrt{2\Omega_{ij}\Omega_{ij}} \tag{4.23}$$

$$\sigma_k = \frac{1}{\frac{F_1}{\sigma_{k,1}} + (1 - F_1)/\sigma_{k,2}} \tag{4.24}$$

$$\sigma_\omega = \frac{1}{\frac{F_1}{\sigma_{\omega,1}} + (1 - F_1)/\sigma_{\omega,2}} \tag{4.25}$$

In Equation 4.23, Ω_{ij} is the mean rate-of rotation tensor while the coefficient α^* is given in Equation 4.18. The blending functions, F_1 and F_2 are defined by

$$F_1 = tanh(\Phi_1^4) \tag{4.26}$$

$$\Phi_1 = min\left[max\left(\frac{\sqrt{k}}{0.09\omega y}, \frac{500\mu}{\rho y^2 \omega}\right), \frac{4\rho k}{\sigma_{\omega,2} D_\omega^+ y^2}\right] \tag{4.27}$$

$$D_{\omega}^{+} = max\left[2\rho\frac{1}{\sigma_{\omega,2}}\frac{1}{\omega}\frac{\partial k}{\partial x_j}\frac{\partial \omega}{\partial x_j}, 10^{-10}\right] \quad (4.28)$$

$$F_2 = tanh(\Phi_2^2) \quad (4.29)$$

$$\Phi_2 = max\left[2\frac{\sqrt{k}}{0.09\omega y}, \frac{500\mu}{\rho y^2 \omega}\right] \quad (4.30)$$

In Equation 4.27, y represents the distance to the next surface and D_{ω}^{+} represents the positive portion of the cross-diffusion term.

$$D_{\omega}^{+} = 2(1 - F_1)\rho\sigma_{w,2}\frac{1}{\omega}\frac{\partial k}{\partial x_j}\frac{\partial \omega}{\partial x_j} \quad (4.31)$$

The term $Y_k$represents the dissipation of the turbulence kinetic energy and is given by

$$Y_k = \rho\beta^* f_{\beta^*} k\omega \quad (4.32)$$

For SST $\mathrm{k}-\omega$ model, f_{β^*} =1. Thus,

$$Y_k = \rho\beta^* k\omega \quad (4.33)$$

In Equation 4.34, Y_{ω} is the dissipation of ω, and is given by

$$Y_{\omega} = \rho\beta f_{\beta}\omega^2 \quad (4.34)$$

For SST $\mathrm{k}-\omega$ model, $f_{\beta} = 1$. Thus

$$Y_{\omega} = \rho\beta\omega^2 \quad (4.35)$$

$$\beta = \beta_i \left[1 - \frac{\beta_i^*}{\beta_i} \zeta^* F(M_t)\right] \tag{4.36}$$

For SST $k-\omega$ model,β_i

$$\beta_i = F_1 \beta_{i,1} + (1 - F_1)\beta_{i,2} \tag{4.37}$$

In Equation 4.37, $\beta_{i,1} = 0.075$, $\beta_{i,2} = 0.0828$ and F_1 is calculated from the Equation 4.26. The SST $k-\omega$ model, is based on both the standard $k-\omega$ model and the standard $k-\varepsilon$ model. To blend these two models together, the standard $k-\varepsilon$ model has been transformed into equations based on k and ω, which leads to the introduction of a cross diffusion term D_ω. In Equation 4.11, D_ω is defined as

$$D_\omega = 2(1 - F_1)\rho \frac{1}{\omega \sigma_{\omega,2}} \frac{\partial k}{\partial x_j} \frac{\partial \omega}{\partial x_j} \tag{4.38}$$

The values of constants are as follows:

$$\sigma_{k,1} = 1.176$$

$$\sigma_{\omega,1} = 2.0$$

$$\sigma_{k,2} = 1.0$$

$$\sigma_{\omega,2} = 1.168$$

$$\alpha_1 = 0.31$$

$$\beta_{i,1} = 0.075$$

$$\beta_{i,2} = 0.0828$$

All additional model constants $(\alpha_{\infty}^{*}, \alpha_{\infty}, \alpha_{0}, \beta_{\infty}^{*}, R_{k}, R_{\omega}, \zeta^{*}, and\ M_{t0})$ have the similar values when compared with that of the standard k − ω model.

$$\alpha_{\infty}^{*} = 1$$

$$\alpha_{\infty} = 0.52$$

$$\alpha_{0} = \frac{1}{9}$$

$$\beta_{\infty}^{*} = 0.09$$

$$R_{k} = 6$$

$$R_{\omega} = 2.95$$

$$\zeta^{*} = 1.5$$

$$M_{t0} = 0.25$$

4.3 Governing Equation for Particle Phase

Generally, the fluid-particle flows can be investigated by utilizing the Eulerian-Lagrangian or Eulerian-Eulerian approaches. However, in the presents work, only the Eulerian-Lagrangian model was used. The Lagrangian particle tracking approach which is available in the CFD commercial software, ANSYS FLUENT, is used to track the particle dispersion along the trajectory. A one-way coupling assumption for particle transport was used as the concentration in the inhaled air is considered dilute. This means that the airflow transports the particle, but the effect of the particles on the flow is negligible and can be ignored. With this assumption, the airflow field is first evaluated and then used for particle trajectory analysis. The wall was set as the trap boundary. To achieve the uniform droplet concentration assumption, droplets were released at the same velocity as the free stream. It is assumed that the droplets will not

affect the fluid flow (one-way coupling) as the volume fraction of the droplets is relatively low which is less than 10% (Inthavong *et al*., 2009).

In the present work, the micro-particle deposition calculations were performed using a Lagrangian approach. This model tracks individual particles within the flow field. The primary advantage of this method is that a variety of forces, such as inertia, diffusivity and gravity terms, can be considered directly. Therefore, this model is appropriate for micro-particles; their inertia has a noticeable effect on their motion. Taking the above assumptions into consideration, the Lagrangian equations governing the particle motion can be written as:

$$\frac{dx_p}{dt} = u_p \tag{4.39}$$

$$\frac{du_p}{dt} = F \tag{4.40}$$

The left hand side of Equation 4.40 represents the acceleration term or the inertial force per unit mass, x_p in Equation 4.39 is the particle position, and u_p is the velocity of the particle. In Equation 4.40, F represents all the body forces and surface forces acting on the particle. An example of a body force acting on the mass of the particle is gravity, while the surface forces are due to drag.

$$F = F_{drag} + F_{gravity} + F_x \tag{4.41}$$

Additional source terms for the particle equation, such as the Brownian force and the Saffman lift force, are not included as the particles concerned are substantially greater

than submicron particles. The gravity force was also not considered. Hence the trajectories of the individual particles can be tracked by integrating the force balance equations on the particle as written below:

$$\frac{du_p}{dt} = F_D(u_g - u_p) \tag{4.42}$$

In Equation 4.42, u_p is the particle velocity vector and $u_g$is the air velocity vector.

The drag force per unit particle mass is expressed as

$$F_D = \frac{18u_g}{\rho_p d_p^2}\frac{c_D Re_D}{24} \tag{4.43}$$

In Equation 4.43, μ_g is the fluid dynamic viscosity and $d_p$is the particle diameter. As shown in Equation 4.44, Re_p is the particle's Reynolds number which can be defined by:

$$Re_p = \frac{\rho_p d_p |u_g - u_p|}{\mu_g} \tag{4.44}$$

FLUENT employs drag coefficient c_D by (Morsi & Alexander, 2006):

$$c_D = a_1 + \frac{a_2}{Re} + \frac{a_3}{Re_p^2} \tag{4.45}$$

In Equation 4.45, a_1, a_2 and a_3 are constants that apply to smooth spherical particle in a stipulated range of Re_p as given in the Table 4.2 (Jayaraju, 2009; Karakosta et al., 2013). Figure 4.1 shows the comparison of two formulations used by Schiller and Neumann, (1933) and Morsi & Alexander, (2006) for c_D with the experimental data of

Schlicthing, (1979). As can be seen In Figure 4.1, both models follow the same pattern of c_D obtained by Schlicthing (1979) until $Re_p = 1000$, after that, the model of Morsi & Alexander, (2006) shows good agreement with Schlicthing (1979) . However, the Re_p obtained in the current work are in the range of $10^1 - 10^3$, hence, both developed formulas can be used. By referring to the Table 2.4, based on the calculated particle Reynolds number, the constants values obtained are as follows: a_1= 1.222, a_2= 29.1667, and a_3= -3.8889.

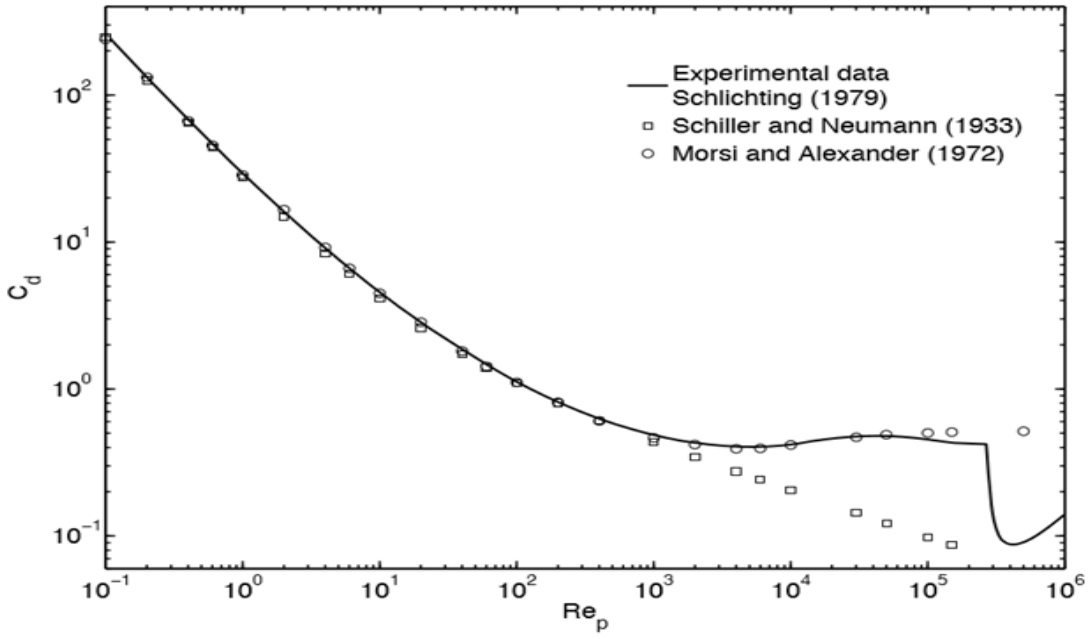

Figure 4.1: Drag coefficient for spheres as a function of Re_p.

Table 4.2: Constants for different intervals of the Reynolds number for the Morsi & Alexander, (2006) drag model.

Re_p	a_1	a_2	a_3
0< 0.1	0	24	0
0.1 < 1.0	3.69	22.73	0.0903
1 < 100.0	1.222	29.1667	-3.8889

10.0 < 100.0	0.6167	46.5	-116.67
100.0 < 1000.0	0.3644	98.33	-2778
1000.0 < 5000.0	0.357	148.62	-4.75
5000.0 < 10000.0	0.46	-490.546	57.87
10000.0 < 50000.0	0.5191	-1662.5	5.4167

4.4 Numerical Solver Procedure

The governing transport equations were discretized using the control volume-based technique. The domain is discretized into control volumes based on the created computational mesh. The governing equations were converted into an integral form to allow integration of the equation on each computational mesh. A set of algebraic equations of dependent variables such as velocities, pressure and temperature are then set up and solved. Discretization of the governing equations can be illustrated most easily by considering the steady-state conservation equation for transport of a scalar quantity Φ. This is demonstrated by the following equation written in integral form for an arbitrary control volume V as follows:

$$\oint \rho\phi\vec{v}.d\vec{A} = \oint \Gamma_\phi \nabla\phi.d\vec{A} + \int_V S_\phi dV \qquad (4.46)$$

where ρ is density, $\vec{v}$ is velocity vector, $\vec{A}$ is surface area vector, Γ_ϕ is diffusion coefficient for ϕ, $\nabla\phi$ is gradient of ϕ, and S_ϕ is source of ϕ per unit volume. Equation 4.46 is applied to each control volume in the computational domain. The two-

dimensional, triangular cell shown in Figure 4.2 is an example of such a control volume. Discretization of Equation 4.46 on a given cell yields

$$\sum_{f}^{N_{faces}} \rho_f \vec{v}_f \phi_f . \vec{A}_f = \sum_{f}^{N_{faces}} \Gamma_\phi (\nabla \phi)_n . \vec{A}_f + S_\phi V \tag{4.47}$$

where N_{faces} is the number of faces enclosing cell, ϕ_f is the value of ϕ convected through face f, $\rho_f \vec{v}_f \phi_f . \vec{A}_f$ is the mass flux through the face, $\vec{A}_f$ is the area of face f, $(\nabla \phi)_n$ is the magnitude of $\nabla \phi$ normal to face f and V is the cell volume.

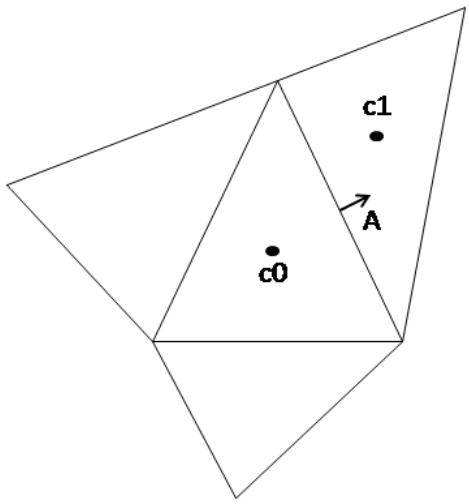

Figure 4.2: Control volume used to illustrate Discretization of a scalar transport equation.

FLUENT stores discrete values of the scalar ϕ at the cell centers ($c0$ and $c1$ in Figure 4.2). However, face values ϕ_f are required for the convection terms in Equation

4.47 and must be interpolated from the cell center values. This is accomplished by using an upwind scheme. The upwind differencing scheme takes into account the flow direction when determining the value at a cell face. The convected value of ϕ at a cell face is taken to be equal to the value at the upstream node. Upwinding means that the face value ϕ_f is derived from quantities in the cell upstream, or upwind, relative to the direction of the normal velocity v_n in Equation 4.47.

In the first order upwind scheme, the quantities at cell faces are determined by assuming that the cell-center values of any field variable represent a cell-average value and hold throughout the entire cell. The face quantities are identical to the cell quantities. Hence, the face value ϕ_f is set equal to the cell-center value of ϕ in the upstream cell. In the second-order upwind scheme, quantities at cell faces are computed using a multidimensional linear reconstruction approach. In this approach, higher-order accuracy is achieved at cell faces through a Taylor series expansion of the cell-centered solution about the cell centroid. Thus when second-order upwinding is selected, the face value ϕ_f is computed using the following expression:

$$\phi_f = \phi + \nabla\phi . \Delta\vec{s} \tag{4.48}$$

where ϕ and $\nabla\phi$ are the cell-centered value and its gradient in the upstream cell, and $\Delta\vec{s}$ is the displacement vector from the upstream cell centroid to the face centroid. This formulation requires the determination of the gradient $\nabla\phi$ in each cell. This gradient is computed using the divergence theorem, which in discrete form is written as

$$\nabla\phi = \frac{1}{V}\sum_{f}^{N_{faces}} \tilde{\phi}_f \vec{A} \tag{4.49}$$

here the face values $\tilde{\phi}_f$ are computed by averaging ϕ from the two cells adjacent to the face. Finally, the gradient $\nabla\phi$ is limited so that no new maxima or minima are introduced.

In this work, first order upwind and second order upwind scheme were used. Initially, the first order upwind scheme was used to stabilize the flow. Smaller under relaxation factor value was applied in order to gain flow stability. After the first order converged, the second order upwind scheme was then utilized to accomplish higher order accuracy of the flow solution. The quality of the second order upwind scheme has been proved for its reliability and accuracy in evaluating the scalar variables on unstructured meshes (FLUENT User manual).

The segregated pressure-based solver within FLUENT was chosen which solved the governing equations. The pressure-based approach is suitable for low-speed incompressible flows. In this pressure-based method, the velocity is obtained from the momentum equations, the pressure field is extracted by solving a pressure or pressure correction equation which is obtained by manipulating continuity equations. Figure 4.3 shows the flow chart of the iteration procedure based on the segregated pressure-based solution method. In the present study, the SIMPLE algorithm was used to obtain

the relationship between velocity and pressure corrections to enforce mass conservation and also to obtain the pressure.

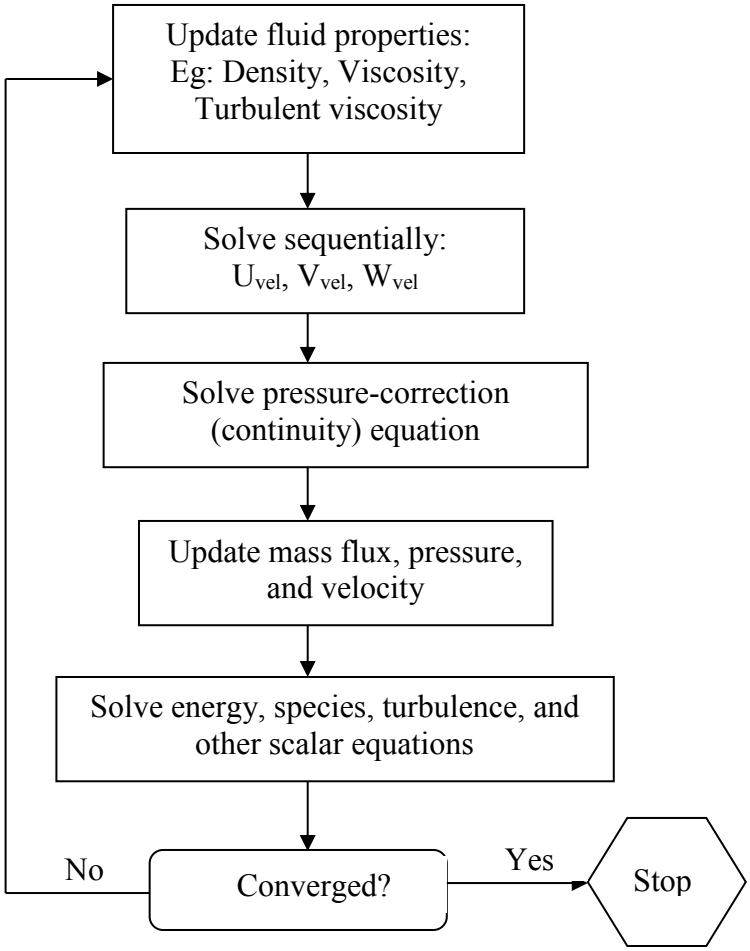

Figure 4.3: Pressure-based solution method.

The trajectories of the discrete particle injections can be computed without impacting the continuous phase. In turbulent flows, trajectories can be based on time-averaged continuous phase velocities or they can be impacted by instantaneous velocity fluctuations in the fluid. The particle trajectory can either be solved by using coupled or uncoupled method. The coupled tracking method allows particles to interact

with the fluid flow and affect the flow solution. In this research work, the uncoupled trajectory calculation method was used with stochastic tracking.

Figure 4.4 shows the flow chart of the particle trajectory calculations based on the uncoupled discrete phase calculation method. In this method, first the continuous flow field will be solved. Then the particle trajectories for the discrete phase injections will be calculated. This procedure is considered acceptable when the discrete phase is present at a low mass and momentum loading, in which case the continuous phase is not impacted by the presence of the discrete phase.

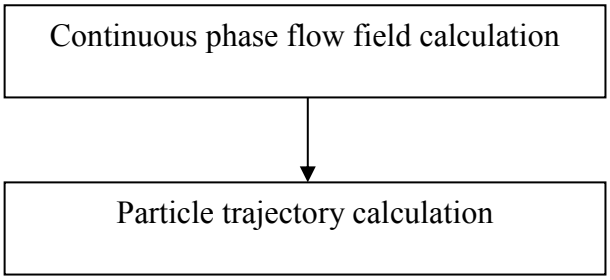

Figure 4.4: Uncoupled discrete phase calculation method.

The trajectory of each particle was computed over a large number of steps as it passes through the flow domain. Step length factor indicates the total number of steps each particle should make across a grid cell and maximum number of steps define the limit for the number of steps. If the maximum number of steps in too small, some particles will be terminated too early before they can reach the outlet or wall boundary. This particle will be reported as incomplete in FLUENT. Fluent also reported the

number of particles tracked, escaped, aborted, trapped and incomplete. The maximum number of steps can be used to stop the solver being trapped in a continuous loop when particles are trapped in a recirculation region in the computational domain. To model the effects of turbulent fluctuations on particle motion, a random walk method was employed. The tracking parameters used in this research work were 60,000 for the maximum number steps and 5 for the step length factor.

4.5 Boundary Condition Definition

The summary of boundary conditions defined in the case study are as depicted in Table 4.3. The nasal wall was assumed to be rigid and the simulation ignored the presence of mucus, a no-slip boundary condition was defined at the walls.

Table 4.3: Summary of the boundary conditions.

	Boundary Condition	Discrete Phase Model Conditions
Inlet	Mass flow inlet	Escape
Outlet	Outflow	Escape
Wall	No slip	Trap

The mass flow rate boundary condition was imposed at the nostril inlet and outflow boundary was defined at the pharynx outlet. Since the velocity and pressure at the pharynx are not known prior to the solution of the flow problem, we used outflow boundary condition to model the pharynx exit during inspiration. Outflow boundary condition assumes that flows is fully developed in the direction perpendicular to the outflow boundary surface. Outflow boundary condition also assumes a zero-normal gradient for all flow variables except pressure. For the DPM conditions, Escape boundary condition was imposed at the inlet and outlet. When the particle meets the inlet or outlet boundary, the escape boundary condition assumed the particle leaves the domain, hence stop the particle tracking. Figure 4.5 shows the illustrations for the escape boundary condition.

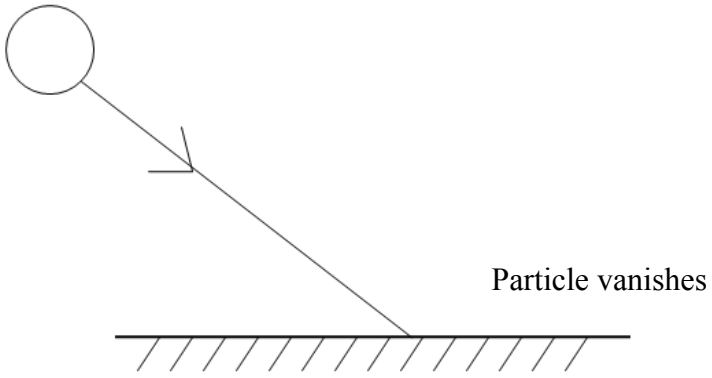

Figure 4.5: Escape boundary condition for the discrete phase.

The trap DPM boundary condition was defined at the wall surface. When the particle strike the flow boundary face, the trap boundary condition assumed the particle is removed, but its current mass and energy is imparted to the gas phase. The trajectory calculations are terminated and the fate of the particle is recorded as trapped. Figure

4.6 shows the illustration of the trap boundary condition for the discrete phase modeling. The particle rebounding from the surfaces was neglected, the particle was assumed to be trapped or deposited on the wall surface when the distance between the particle center and the wall surface was less than or equal to the particle radius.

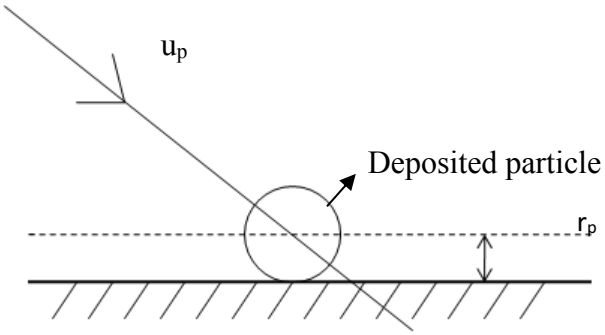

Figure 4.6: Illustration of the particle deposition with trap boundary condition.

Particle deposition was found by adding up the trapped particles. The regional deposition of microparticles in human airways can be quantified in terms of the deposition fraction (DF) or total deposition efficiency (TDE) in a specific region (e.g. nasal valve, nasal vestibule, main airway, and etc.) (Z. Zhang, Kleinstreuer, Donohue, & Kim, 2005). They can be defined as:

$$\mathrm{DF}_{particle} = \frac{Number\ of\ deposited\ particles\ in\ a\ specific\ region}{Number\ of\ particles\ entering\ the\ nostril} \times 100\% \quad (8.50)$$

$$\mathrm{TDE}_{particle} = \frac{Number\ of\ deposited\ particles\ in\ the\ airway}{Number\ of\ particles\ entering\ the\ nostril} \times 100\% \quad (2.51)$$

For the first study case, inspiratory steady state laminar and turbulent airflow simulations were modelled. The airflow was assumed to be laminar for flow rates of 7.5L/min and 10L/min and turbulent boundary condition were imposed on flow rate

of 20-40L/min. This was in general agreement with previous researchers who determined laminar nature of the flow, for flow less than 15L/min (Riazuddin et al., 2011; Segal, Kepler, & Kimbell, 2008; Wen, Inthavong, Tu, & Wang, 2008; Zubair et al., 2013; Zubair et al., 2010). Table 4.4 shows the summary of the particle injection properties defined in the case study. This injection properties defines the release conditions for the injected particles. By defining a surface injection type, one particle stream is released from each cell on the inlet surface. Uniform sized spherical particles ranging from 1 to 40 μm with a density of 600 kg/m^3 were simulated. The particles were considered to be inert and the interaction between particles were ignored. Initial particle velocities were assumed to be equal to the average fluid velocity at the nostril.

Table 4.4: Summary of the particle injection properties.

Particle diameter	1,5, 10, 20, 40 μm (monodisperse)
Particle type	Inert
Particle density	600 kg/m^3
Particle velocity	Velocity at nostril inlet
Injection type	Surface injection-particle released from each facet of the surface

As listed in Table 4.5, the following assumptions were invoked for the particle simulation. Micro-particles with aerodynamic diameters in the range of 1-40 μm were simulated to examine a wide range of nasal deposition efficiency. Local deposition fraction was also investigated by calculating the ratio of the number of trapped particles to the number of particles entering the nostril during inhalation.

Table 4.5: Assumptions for the particle modelling.

1. Particle is sphere
2. One way coupling
3. Particle-particle interactions are neglected.
4. The particle rotational and thermophoretic forces are assumed to be zero
5. The particles deposit as soon as they touch the wall.

4.5 Convergence Criteria

The residual is one of the most fundamental measures of an iterative solution`s convergence, as it directly quantifies the error in the solution of the system equations. In a CFD analysis, the residual measures the local imbalance of a conserved variable in each control volume. Therefore, every cell in the computational model will have its own residual value for each equation being solved. In an iterative numerical solution, the residual will never be exactly zero. However, the lower the residual value is, the more accurate the solution. Convergence was considered complete only when the residual values for all equations have reduced to an acceptable value typically at four orders of magnitude.

CHAPTER 5

NUMERICAL INVESTIGATION ON AIRFLOW CHARACTERISTICS AND PARTICLE DEPOSITION IN NASAL CAVITY HAVING TURBINATE HYPERTROPHY, CONCHA BULLOSA, AND SEPTUM DEVIATION: PRE- AND POST-OPERATIVE STUDY

5.1 Introduction

Nasal cavity is one of the most important component of the human respiratory system which provide first line defense against the contaminated particles, bacteria and pathogen to flow into the lower respiratory tract and then reach lung. During inhalation, nasal cavity plays an important role to filter out the inhaled toxic particles from the polluted atmospheric air. Both the fine and coarse particles which enter the nasal cavity during inhalation, not only can induce nasal irritation, moreover, with extensive exposure and high concentration of inhaled airborne toxic and infectious particle, the nose is susceptible to chronic injury and could further aggravate nasal disorder (Harkema *et al*., 2006). Study has shown that, extensive exposed to urban air pollution or the multicomponent mixtures such as fire combustion products, could affect and disturb the nasal physiological function. Harkema *et al*., (2006) also reported that the determination of the precise location of the induced lesion in the nose is the first step in understanding the critical factors involved in the pathogenesis of the injury. As we already know that the toxic and contaminated particles could harm and affect the health of the human population. Hence it is important to investigate and

improve understanding of the airflow distribution and particle transport and deposition in the human nasal airway.

Computational Fluid Dynamics study of airflow, particle transport and deposition through the diseased human nasal airway have been investigated by several number of researchers (Abouali et al., 2012; Dastan et al., 2014; Keyhani et al., 1997; Kimbell et al., 2013; Moghadas et al., 2011; Riazuddin et al., 2011; Wen et al, 2008; Zamankhan et al., 2006). (Keyhani *et al.*,1997) simulated the steady flow of 7.5 L/min and 12 L/min through the nasal cavity by using the finite element method in a commercial software named FIDAP. They developed only one side of the nasal cavity starting from the nostril to the end of the nasal turbinates from CAT scan of a healthy human nasal cavity. They reported that a large amount of the airflow passed through the middle and inferior part of the nasal passage. (Zamankhan et al., 2006) investigated steady state inspiratory airflow through nasal airway developed from MRI. By using the Eulerian-Lagrangian technique, the transport and deposition of the inhaled particles were also evaluated. They reported that effect of the gravitational force and difference of particle density does not affect the particle deposition efficiency in the nasal cavity. Keyhani et al., (1997) and Zamankhan et al., (2006) found that for a normal nasal cavity, most of the inhaled air passes through the middle and inferior part of the nasal passage. Only a small portion passes though the olfactory region.

(Garcia *et al*, 2007) investigated the effect of atrophic rhinitis and on the air conditioning performance in the human nasal airway. Through the CFD simulation of laminar inspiration, they evaluated the airflow, water transport and heat transfer in the

atrophic nasal cavity. They reported that the atrophic nasal cavity could not condition the inspired air as effectively as the normal nasal airway. (Moghadas et al., 2011) evaluated the effect of septoplasty on the flow pattern and particle deposition in the diseased nasal passage diagnosed with deviated septum. In this study, they simulated steady laminar inspiratory airflow and evaluated the transport and deposition of micro sized particle in the range of 1-50 μm by using Lagrangian particle tracking approaches. Moghadas et al., (2011) reported that, the total particle deposited in the deviated septum model in higher when compared to the post-surgery model. However, the volume of the airflow rate could passes though the nasal airway was found increased in the post-surgery model. (Dastan *et al.*, 2014) simulated the transport, the total and regional deposition of fibrous particle through the nasal airway for laminar inspiratory airflow. They developed a mathematical approach to investigate the coupled translational and rotational movement of the ellipsoidal fibers particle through the human nasal airway. They reported that the deposition fraction was affected by the variation of the nasal airway geometry inhalation rate. The number of deposited particle with higher impact factor increased in a location where there is sudden changes in flow direction in the nasal cavity.

(Abouali et al., 2012) utilized the numerical simulation technique to investigate the effect of the airflow through a diseased nasal airway diagnosed with chronic rhinosinusitis. In their research work, virtual uncinatetomy and middle meatal antrostomy were performed on the nasal cavity. Steady inspiratory airflow were simulated for flow rate of 4, 7.5 and 10 L/min. By using the Lagrangian approach, deposition and transport of microparticle of 1-25 μm were analyzed. They found that, the ventilation in the maxillary sinus improve significantly after surgery. However, the

number of particle deposited in the maxillary region increased after surgery due to the increased of airflow penetration into this region.

Numerical simulation of airflow and transport and deposition of inhaled pollutant through chronic diseased nasal airway with deviated septum, bilateral inferior turbinate hypertrophy and concha bullosa has never been study before. The main objective of this study is to investigate, the effect of the nasal surgery which include septoplasty, bilateral reduction and partial concha bullosa resection on airflow characteristics, breathing resistance and particle deposition efficiency. In this study, detailed flow pattern and characteristics for inspiratory airflow for various breathing rates (7.5-40 L/min) were evaluated. Simulation of the particle transport and deposition of micro sized particles with particle diameter ranging from 1-40 μm were also investigated.

5.2 Methodology

5.2.1 Three-Dimensional Nasal Computational Model

Three dimensional diseased nasal computational models was developed from CT scan images of 38 year-old Malaysian male patient with chronic obstruction in the nasal airway. The patient had undergone nasal surgical treatment which include septoplasty, bilateral inferior turbinate reduction and partial concha bullosa resection. The CT scan images of both pre- and post-operative conditions obtained from the Hospital Serdang, Selangor are as shown in Figures 5.1 and 5.2 respectively. Figure 5.1 shows the CT scan images of the obstructed nasal airway obtained before surgery.

Figures 5.1 (a) and (b) show the location of the inferior turbinate hypertrophy and deviated septum while Figure 5.1 (c) shows the location for the concha bullosa which refers to the existence of an air pocket inside the nasal turbinate. Figure 5.2 (a-c) shows the CT scan images of the treated nasal airway obtained after surgery. As can be observed in Figure 5.2, after the surgery was performed, the blockage in the nasal cavity has been removed and the airway passage increased.

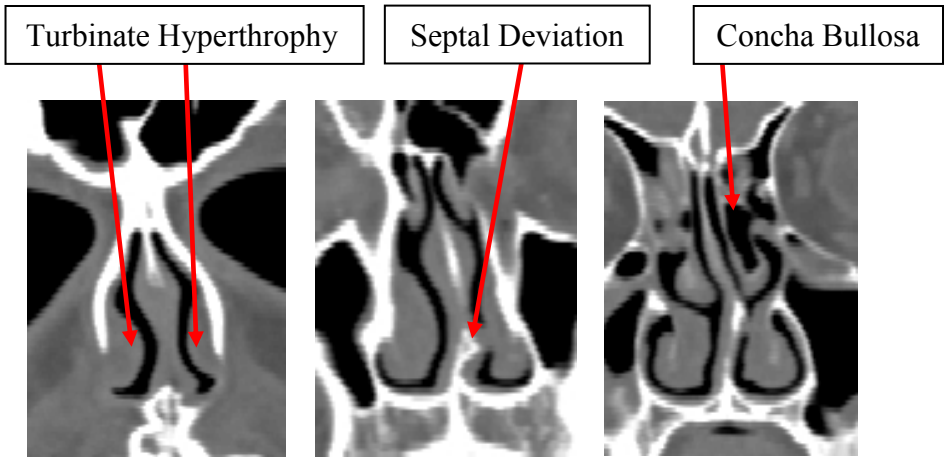

Figure 5.1: CT scan images for the obstructed nasal airway before surgery.

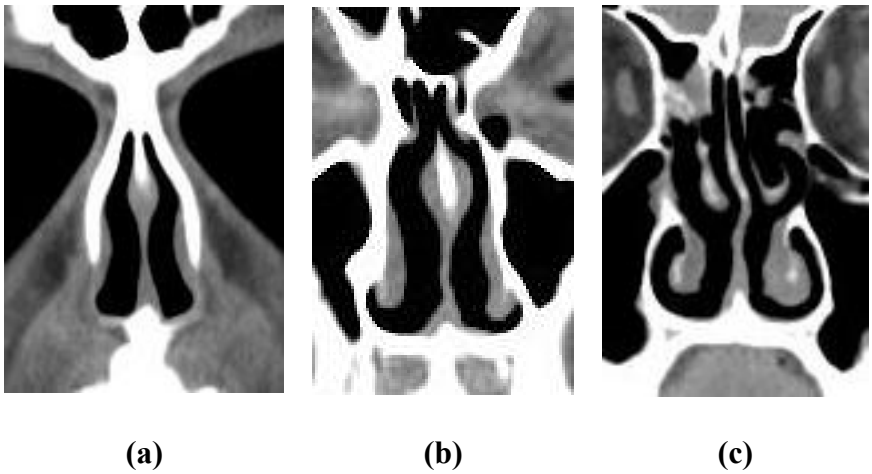

Figure 5.2: CT scan images for the treated nasal airway after surgery.

The airway passage is represented by the black colour in the each figures. The scans data were provided by the Hospital Serdang, Selangor. The scans were taken without nasal decongestion. The pre-operative CT scans data were processed 3 months before the surgery, and the post-operative scans data were processed 7 months after the surgery. A realistic three-dimensional computational model of the diseased nasal cavity was developed for both pre- and post-operative cases. Figure 5.3 shows the diseased nasal computational model for the pre-operative case, whereas, Figure 5.4 shows for the post-operative case. The inlet boundary condition is located at the nostril and the outlet boundary condition is located at the nasopharynx. The grey surface in Figure 5.3 and 5.4 represent the nasal wall boundary condition. As can be seen in Figure 5.3 the hollow in the nasal model represent the nasal blockage is caused by the deviated septum. The blockage was successfully removed after the surgery as shown in Figure 5.4.

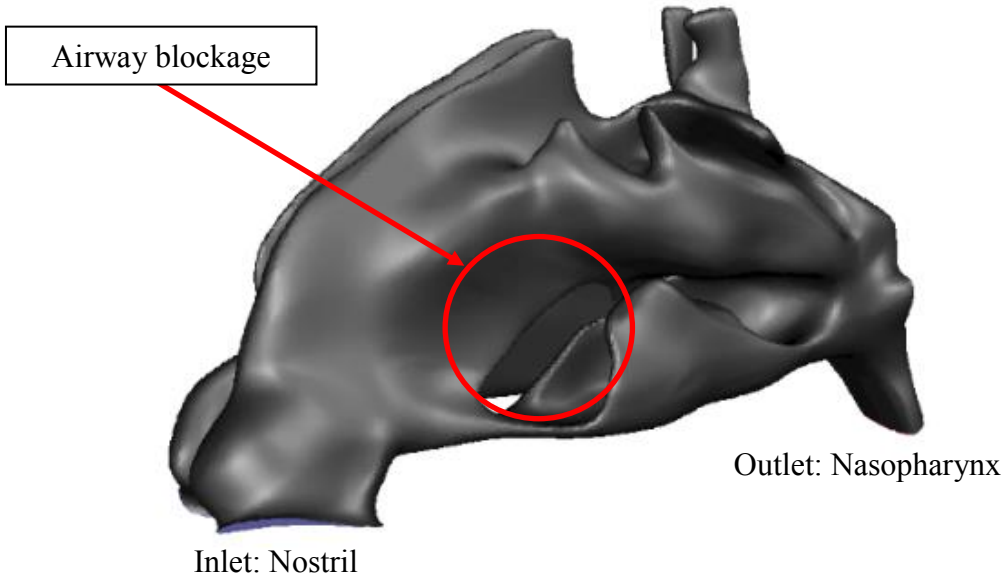

Figure 5.3: Diseased nasal computational model for pre-operative case.

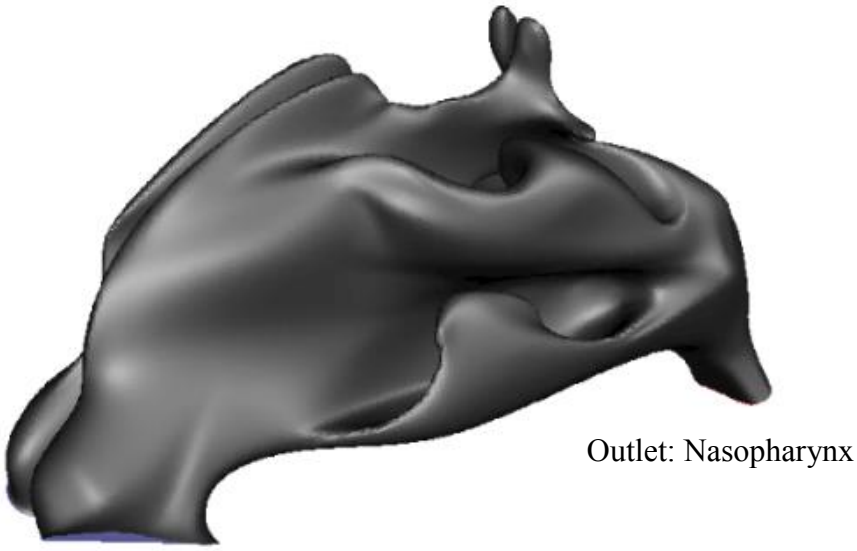

Figure 5.4: Diseased nasal computational model for post-operative case.

5.2.2 Numerical Methods

The numerical investigation was performed by using the commercial CFD solver ANSYS FLUENT. The simulation is based on the numerical solution of the RANS equation representing the general equation for the 3D flow of incompressible and viscous fluids. The CFD simulation adopted steady flow rates of 7.5 and 10 L/min for laminar cases, whereas flow rates of 20, 30 and 40 L/min were considered turbulent. This was in general agreement with previous researchers who determined the laminar nature of the flow, for flows less than 15 L/min. (Jian Wen et al., 2008).

A Lagrangian particle trajectory analysis was used to investigate the effect of the chronic nasal obstruction and surgical treatment on the transport and deposition of

the inhaled particles. In the present study, microparticles in the size range of 1–40 μm were introduced at the nostril inlet and the particle trajectories and deposition efficiency were analyzed. The details of the numerical methods implemented for the present study are as explained in Chapter 4. In this work, hybrid mesh were generated with 4456725 elements for pre-operative and 3167403 elements for post-operative model. A total of 5 layers of prism mesh near the wall boundary, and tetrahedral elements at the remaining flow domain were obtained from a grid independency study.

5.3 Results and Discussions

5.3.1 Grid Dependency Analysis

Two grid dependency studies have been performed for both pre- and post-operative diseased nasal models. Grid dependency studies were performed to reduce the influence of the number of mesh on the computational results. In the present work, initially unstructured tetrahedral mesh was generated by using the grid-generating software named ANSYS ICEM-CFD. The quality of the mesh plays a significant role in accuracy and stability of the numerical computation. Skewness is one of the primary quality measures for a mesh. Skewness is defined as the difference between the shape of the generated cell and the shape of equilateral cell. According to the definition of Tgrid skew in ANSYS ICEM CFD, a value of 0 indicates best mesh quality and value of 1 indicates worst mesh quality. In the present work, the maximum skewness for the boundary mesh and the volume mesh developed using ANSYS ICEM CFD was maintained to be less than 0.5.

The generated unstructured mesh in .msh files were then imported into FLUENT MESHING ANSYS to generate hybrid mesh which consisted of 5 layers of prism mesh near to the wall boundary and tetrahedral mesh was generated in the inner core of the computational domain. For pre-operative case, an initial thickness of $2.012 \times 10^{-5}\ m$ was maintained for the prism mesh to obtain a y+<1. The worst cell had the maximum value of skewness of about 0.83. For post-operative case, an initial thickness of $2.484 \times 10^{-5}\ m$ was maintained for the prism mesh and the maximum skewness obtained was 0.81.

There are two methods for measuring skewness quality. The first method is based on the equilateral volume which can be applied only to the tetrahedral mesh. The second method is based on the deviation from a normalized equilateral angle which can be applied to prism mesh.

For tetrahedral mesh:

$$Skewness = \frac{optimal\ cell\ size - cell\ size}{optimal\ cell\ size} \tag{5.1}$$

For prims mesh:

$$Skewness = max\left[\frac{\theta_{max} - 90}{90}, \frac{90 - \theta_{min}}{90}\right] \tag{5.2}$$

where θ_{max} is the largest angle in face or cell and θ_{min} is the smallest angle in face or cell. Equation 5.1 was used to evaluate skewness for the tetrahedral mesh whereas Equation 5.2 was used for prims mesh. Figure 5.5 shows the grid dependency plot for

the pre-operative case while Figure 5.6 show grid dependency plot for the post-operative case. The average static pressure and average wall shear stress were obtained at the nasal valve plane. The nasal valve plane is located at 23 mm from the anterior part of the nasal cavity. The facet average equation used in ANSYS FLUENT to calculate the facet average value for the selected flow property is as described in Equation 5.3 below:

$$\frac{\sum_{i=1}^{n} \phi_i}{n} \tag{5.3}$$

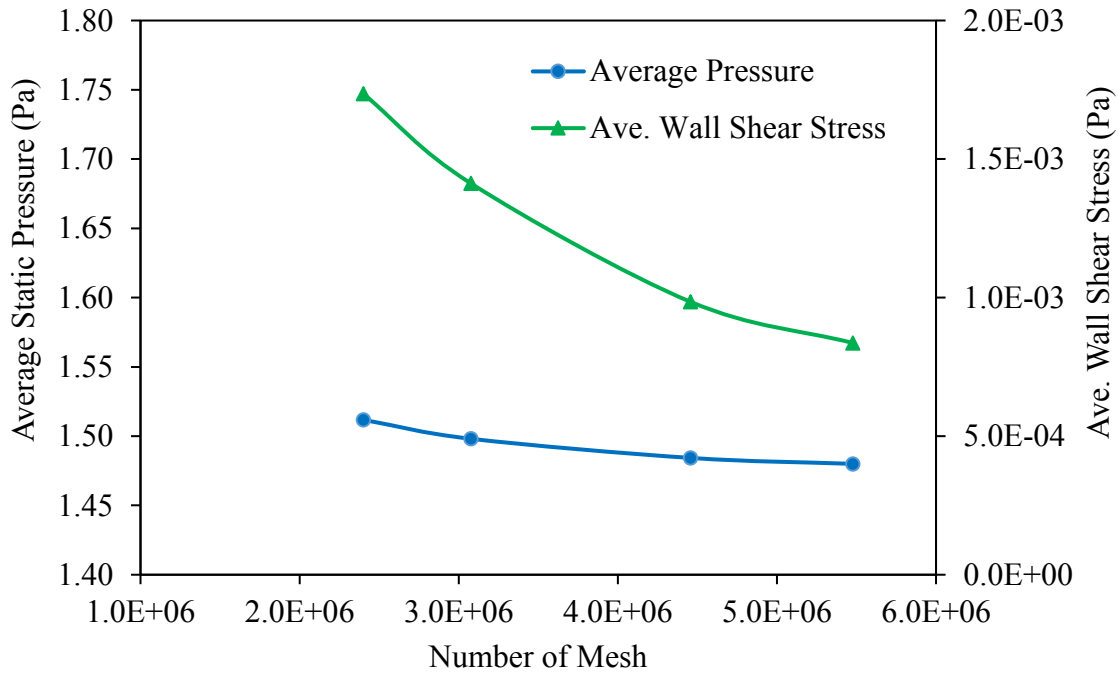

Figure 5.5: Grid dependency study for pre-operative nasal cavity model.

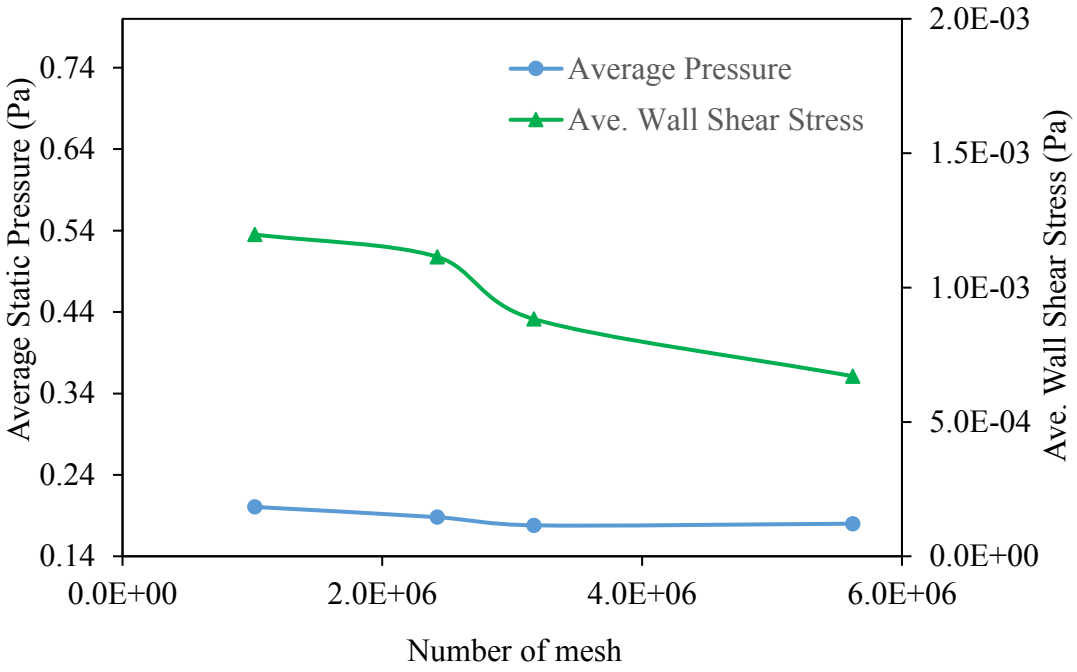

Figure 5.6: Grid dependency study for post-operative case nasal cavity model.

In the present study, the average pressure at the nasal valve plane was calculated by dividing the summation of the pressure on the facets by the total number of facets on the created plane. As can be seen in Figure 5.5, the initial mesh size for pre-operative case is 2400275. As the mesh was refined, grid cells become smaller and the number of mesh in the nasal computational domain increased. It can be observed from Figure 5.5 that, beyond 4456725 elements there is no major variation in the average pressure and average wall shear stresses obtained in the nasal valve region respectively. Similarly, in Figure 5.6, for post-operative case, grid refinement was performed and the total number of mesh has increased. As shown in Figure 5.6, the average pressure and average wall shear stress obtained do not change much as the mesh resolution increased from 3167403 to 5621171 elements. Therefore, the grid

consisting of 4456725 and 3167403 elements were selected for pre- and post-operative case respectively. The selected grid files were then imported into FLUENT ANSYS to perform numerical simulation inspiratory airflow and particle transport and deposition in the pre- and post-operative nasal cavity models.

5.3.2 Geometry Comparison

The fourteen planes created along the axial distance of the diseased human nasal cavity before surgery is as shown in Figure 5.7. The cross-sectional areas were created in ANSYS FLUENT and used to calculate the flow properties inside the nasal cavity. The anterior region of the nasal cavity is in the range of $x \leq 5$ and the posterior region is in the range of $x > 5$. The planes were created approximately perpendicular to the airflow through the nasal cavity.

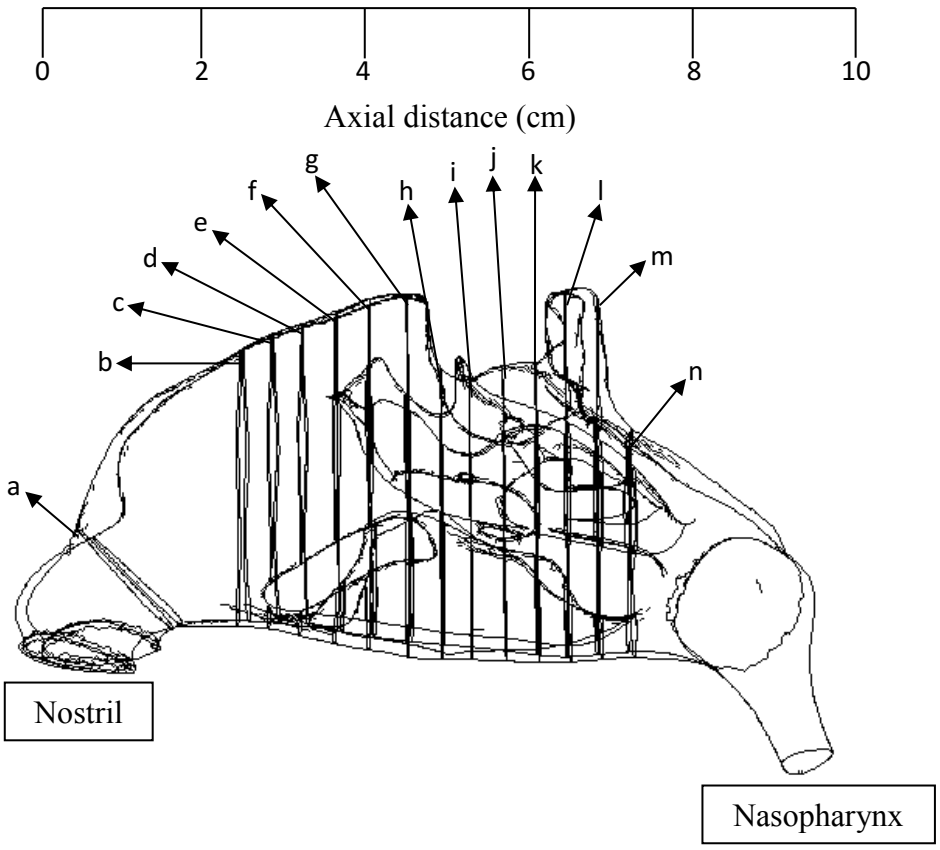

Figure 5.7: Fourteen cross section area along the axial distance of the nasal cavity for the pre-operative computational model.

Figure 5.8 shows the planes created for pre-operative nasal cavity corresponding to the area that has undergone surgery. The darkened grey area in the figure represents the air pathways. As can be observed in Figure 5.8 plane b, bilateral turbinate reduction was performed on both left and right side of the nasal cavity to restore the breathing air space. As can be seen in Figure 5.8 plane c-g, septoplasty was performed on the deviated nasal septum to remove the nasal blockage in the left nasal cavity. In Figure 5.8 plane h and plane i, partial concha bullosa resection was carried out on the middle turbinate to remove the air pocket at the posterior part of the left nasal cavity.

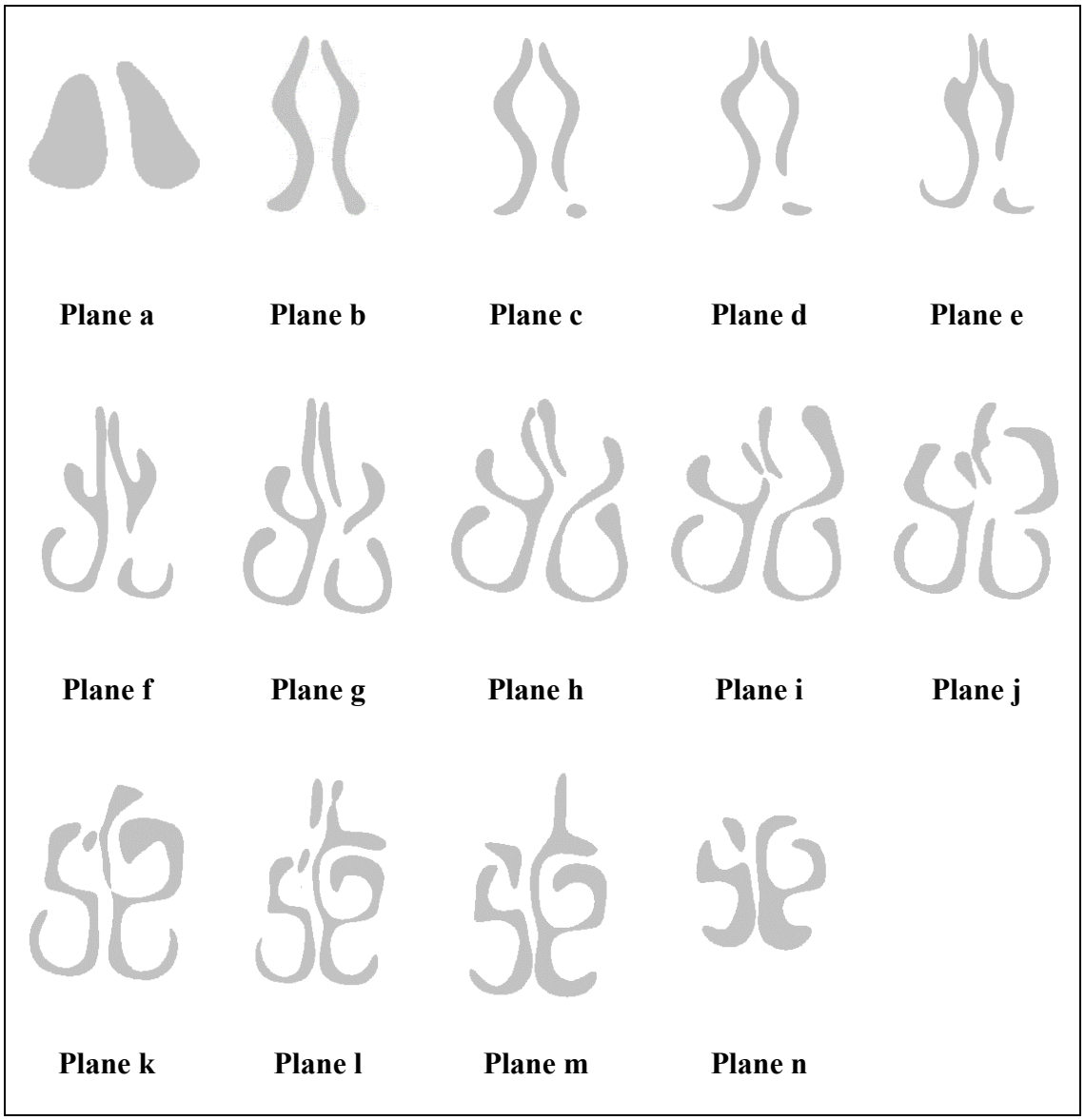

Figure 5.8: The fourteen planes created for pre-operative nasal cavity.

Figure 5.9 shows the total fourteen planes created through the axial distance of the post-operative case of the diseased nasal cavity. Similarly, the planes were created approximately perpendicular to the airflow and approximately at the similar location when compared to the pre-operative nasal cavity model.

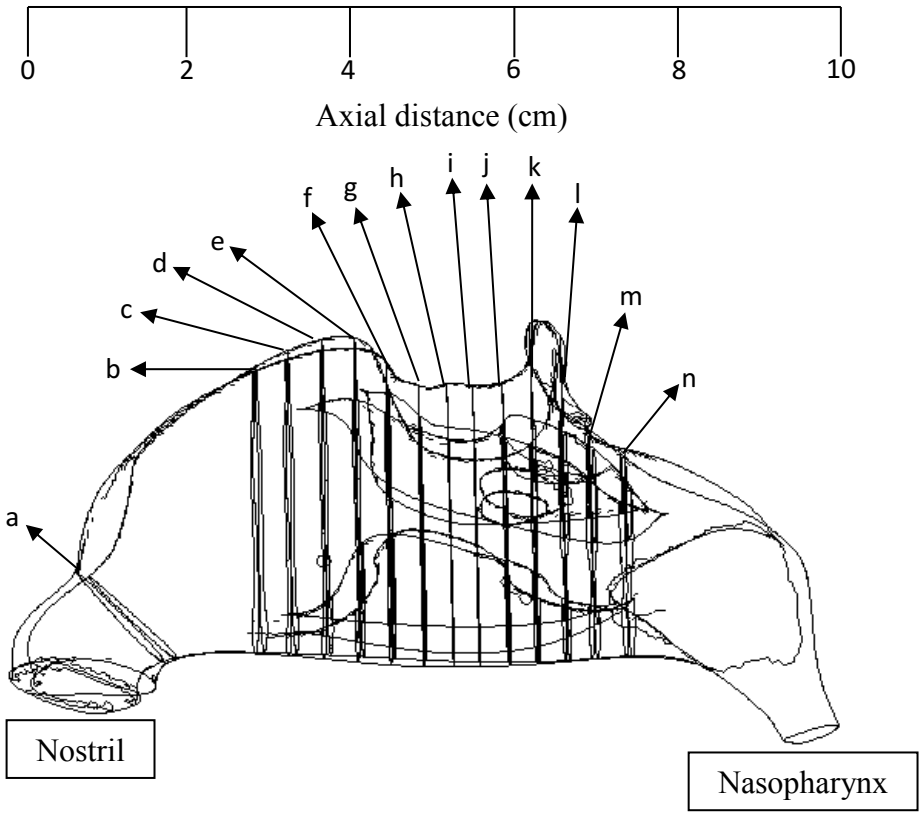

Figure 5.9: Fourteen cross section area along the axial distance of the nasal cavity for the post-operative model.

Figure 5.10 shows the planes created in the post-operative nasal cavity model. As can be seen in Figure 5.10 plane b, after the bilateral turbinate reduction surgery, the cross-section area in this region has increased and the air passage has expended. The effects of septoplasty on the nasal cavity can clearly be observed in Figure 5.10 plane c-g. The nasal obstruction caused by the deviated septum has successfully been removed and the normal nasal air pathway has be restored. In Figure 5.10 h and i, the removal of the concha bullosa at the left turbinate has also increased of the breathing pathway at the posterior part of the nasal cavity.

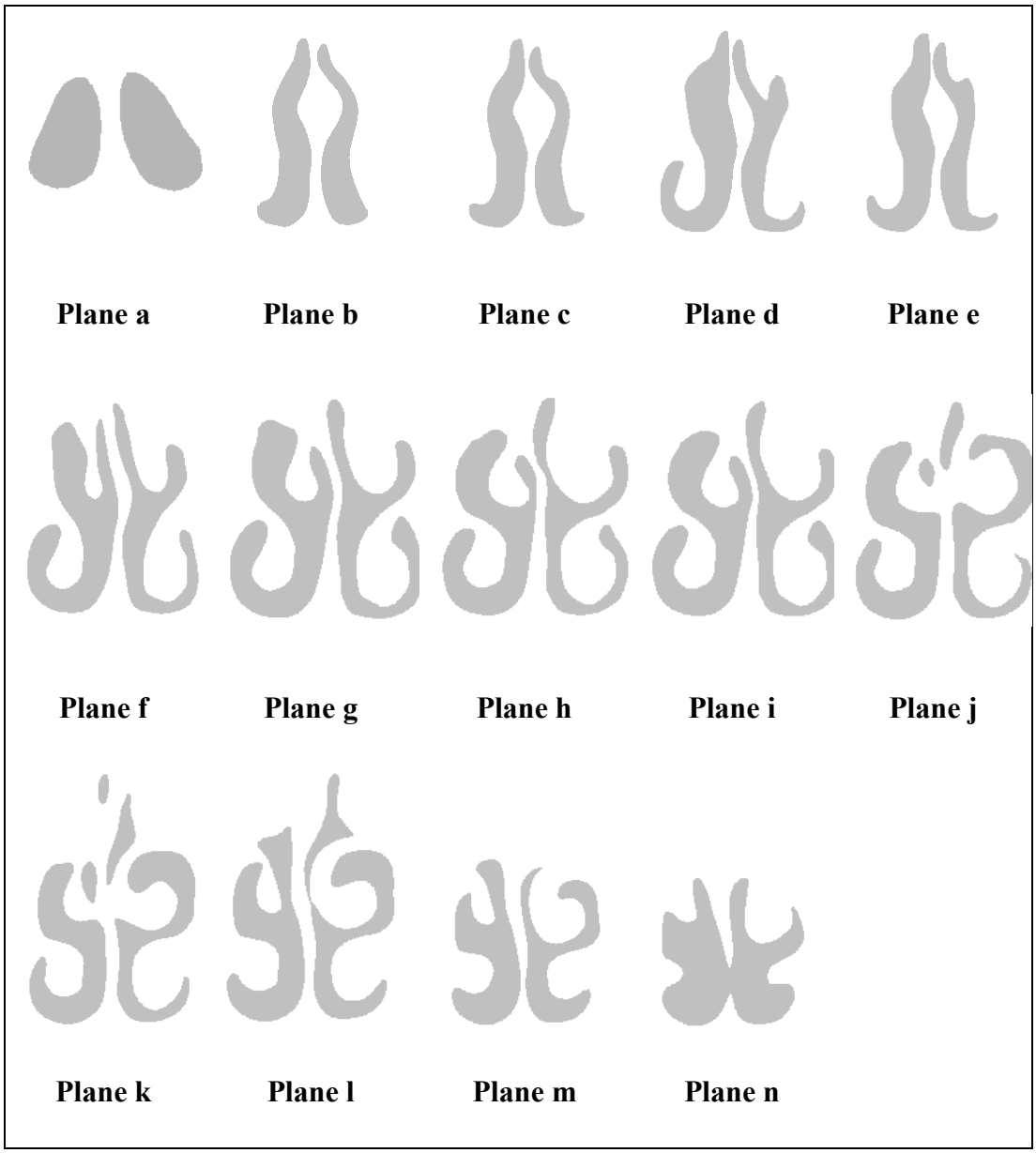

Figure 5.10: Fourteen planes created in the post-operative nasal cavity model**.**

Figure 5.11 compares the variations of the cross-sectional areas of the nasal passage with the distance from the anterior to the posterior part of the nasal cavity for pre- and post-operative models. In both study cases, the nasal valve region was found located at 0.7 cm from the tip of the nose.

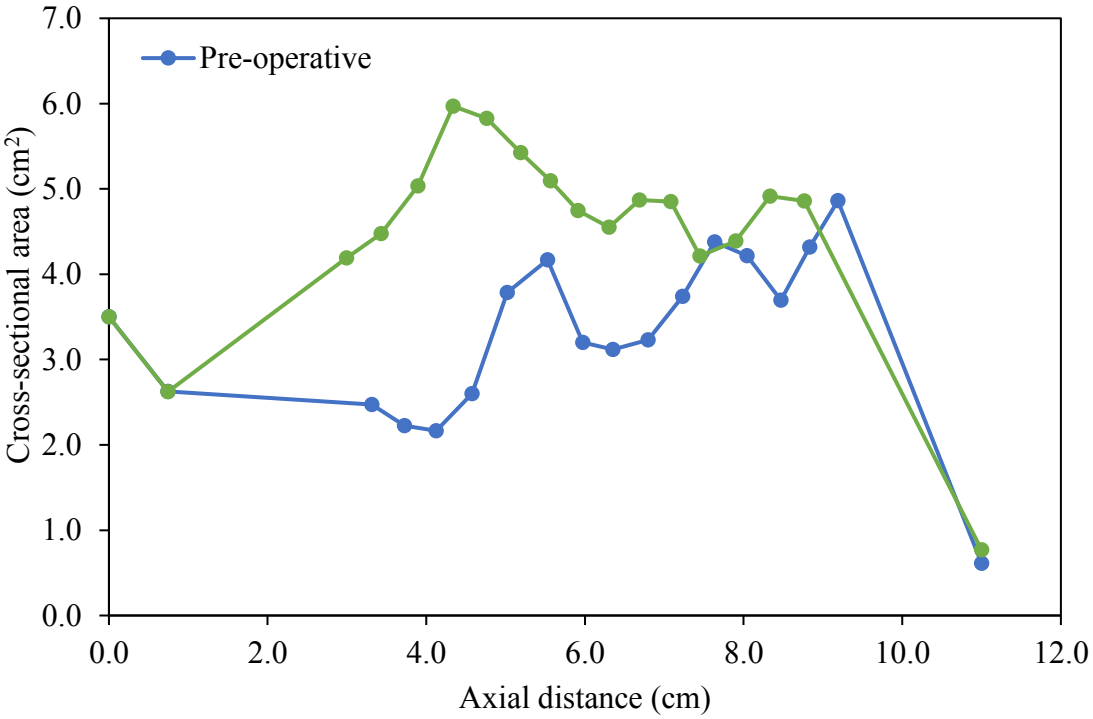

Figure 5.11: The comparison of cross-sectional area vs. axial distance from anterior to the posterior of the diseased nasal cavity.

The cross-section area for the nasal valve region for the pre-operative model is 2.6 cm^2. After surgery, the cross-section area obtained at the nasal valve does not change. However, it can be seen in the post-operative model that the overall nasal cross-section area after the nasal valve region has increased when compared with that of pre-operative model. The enlargement of the nasal passage was initiated from the nasal surgical operations. The increased of the cross section area after the nasal valve region was also observed by other researcher in the normal nasal cavity model (Jian Wen et al., 2008).The nasal valve plays an important role in distributing airflow through inferior, middle, superior turbinate and olfactory region of the nasal passage, hence, it is best to maintain the cross section area of the nasal valve during surgery.

5.3.3 Airflow Resistance

Pressure distribution through the nasal passage can be used to evaluate the impact of the morphology of the nasal airway on breathing airflow resistance. Airway flow resistance is extremely important for the evaluation of the effectiveness of the applied surgical operations and treatment. The nasal airflow resistance can be defined as the ratio of pressure drop to the volume flow rate, ($R= \Delta p/Q$), where Δp is pressure drop across the airway passage and Q is airflow rate.

Table 5.1: Pressure drop for flow rate of 7.5 L/min before and after surgery.

	Pressure difference (Pa)	Airflow resistance (Pa-min/L)
Pre-Operative	4.02	0.54
Post-Operative	1.99	0.27

The airflow field simulations were performed for breathing rates of 7.5 L/min for both pre- and post-operative nasal models. Table 5.1 compares the pressure drops obtained through the nasal passage for an inhalation rate of 7.5 L/min. It can be seen that the pressure different obtained between the nostril inlet and the outlet at the nasopharynx for pre-operation model was 4.02 Pa, whereas post-operative model demonstrated pressure drop of only 1.99 Pa. The nasal resistance obtained before surgery was about 0.54 Pa-min/L, whereas, the post-surgery model demonstrated only 0.27 Pa-min/L of airflow resistance. The post-operative model experienced about 50 % decrease in resistance. The nasal surgical procedures increase the nasal cavity cross-sectional area where the operation was performed consequently decreases the pressure

drop and flow resistance of the nasal passage. As the computed airway resistance has significantly improved after surgery. Hence, less effort is needed for breathing the same flow rate into the lung. The airflow resistance plotted against the inspiratory rates ranging from 7.5 to 40 L/min is as shown in Figure 5.12. As can be seen in Figure 5.12, as the breathing rates increased, the airflow resistance inside the nasal cavity also increased. Figure 5.13 shows the pressure drop obtained from the present study was compared and validated with previous published work by Wen et al., (2008) and Weinhold & Mlynski, (2004). The pressure drop between the nostril and nasopharynx was obtained at flow rates from 7.5 L/min to 40 L/min. As can be observed in Figure 5.13, the pressure drop in both pre and post-operative nasal cavity model was found follow the same pattern as that of the available published data by Wen et al., (2008) and Weinhold & Mlynski, (2004). The pressure drop obtained in the present nasal airway models increased as the flow rates increased.

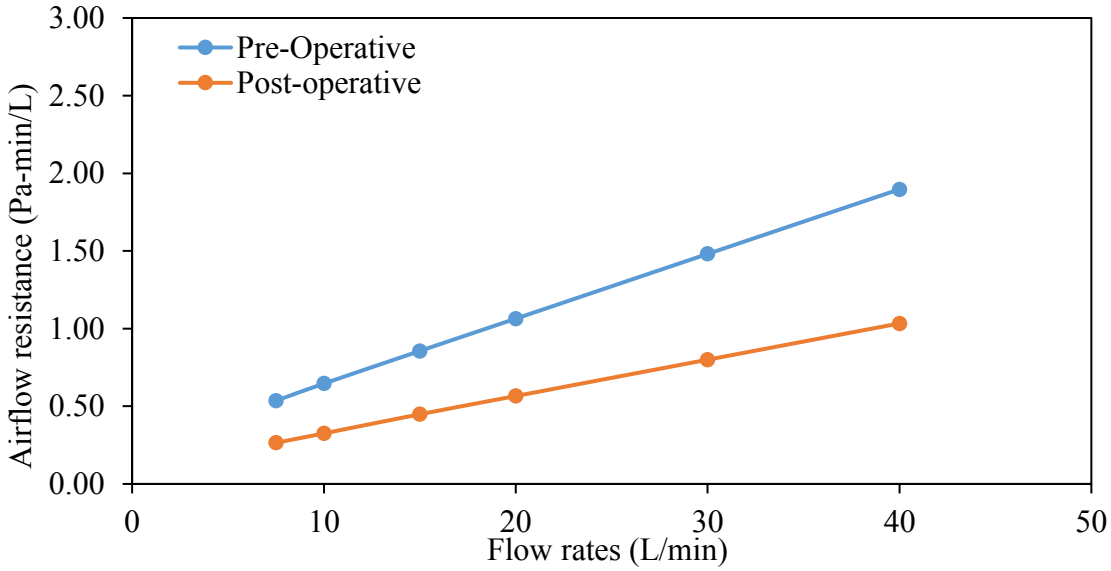

Figure 5.12: Airflow resistance for flow rates of 7.5 L/min – 40 L/min.

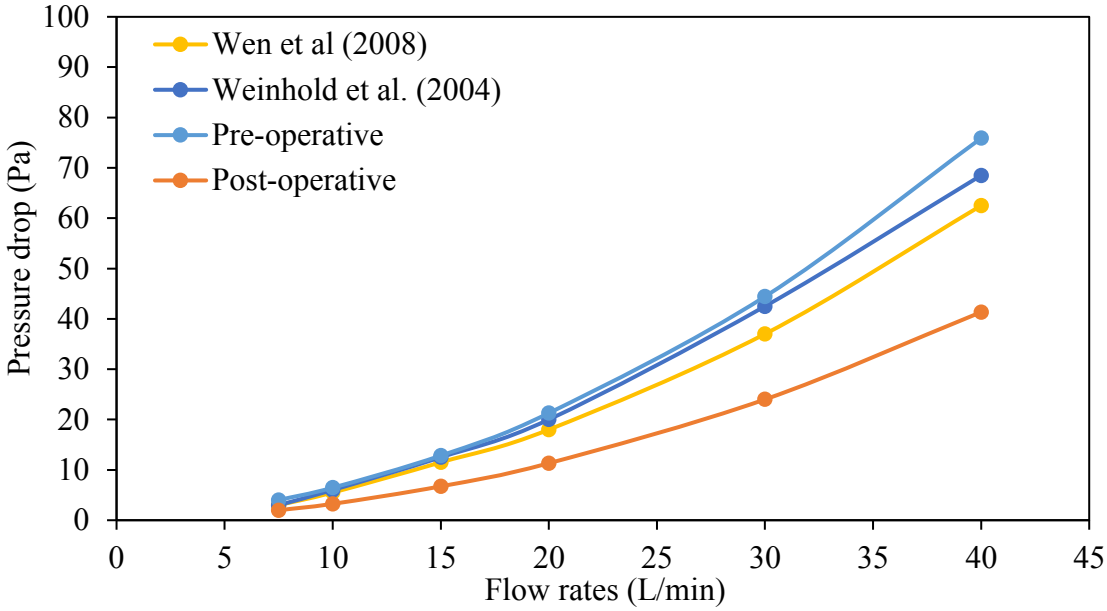

Figure 5.13: Pressure drop for inhalation flow rates of 7.5-40 L/min.

5.3.4 Velocity and Flow Distribution

The abnormal airflow distribution and pattern though the nasal passage may disturb the normal nasal sensation stimuli, cause excessive nasal dryness and lead to breathing difficulty during fully awake and sleep. Figure 5.14 shows the pathlines of the inhaled air for a flow rate of 7.5 L/min, colored according to the velocity magnitude with blue indicating the lowest and red indicating the highest velocity magnitude. The black colour represents the outer surface of the nasal airway, in wireframe view. Figure 5.14 also clearly demonstrates the difference in breathing flow patterns before and after nasal surgery. As can be seen in Figure 5.14, in the pre-operative model a larger amount of flow was observed passes through the middle and superior meatus when compared to the post-operative model. As shown in the in Figure 5.14 (a), the narrowed region in the inferior meatus divert the air to flow into the middle and

superior meatus. After septoplasty, turbinate reduction and concha bullosa resection, however, the flow field inside the nasal passage changes significantly.

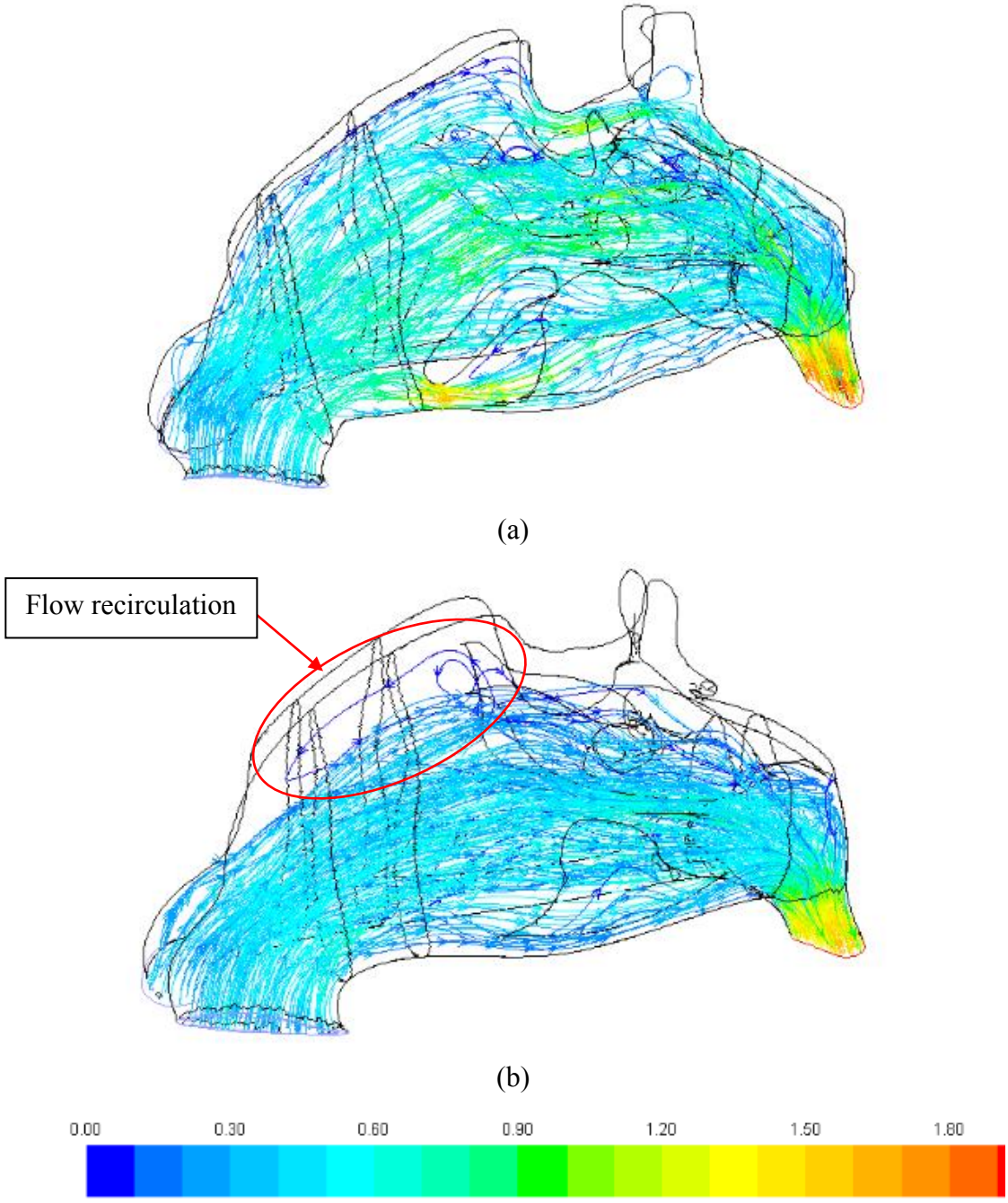

Figure 5.14: Pathlines for breathing rate of 7.5 L/min for (a) pre-operative and (a) post-operative surgery.

It can be seen in Figure 5.14 (b) that, after surgery, most of the flow pass through the middle and inferior meatus. This finding is consistent with previous

researchers who also found that in a normal nasal airway, most of the flow passes through the middle and inferior part of nasal airway during inhalation (Hahn *et al.*, 1993; Keyhani *et al.*, 1995). It can also be observed that, after surgery, only a small quantity of flow reach the superior region of the nasal passage. As the olfactory nerve located at the top anterior part of the nasal cavity, a lesser flow in this region means less stimulation of the sense of smell. However, the changes of airflow distribution in the post-operative model is physiologically consistent with that of a normal nose where at rest and low breathing rate, the sense of smell is less stimulated when compared to the high inhalation rate during sniffing. However, for a low breathing rate of 7.5 L/min, the low velocity magnitude of the recirculatory flow observed at the olfactory region in the post-operative model could improve the nasal sensation stimuli. As shown in Figures 5.14 (a) and (b), at the nasopharynx region, the left and right nasal cavities merge together, this caused the flow to mix intensely in this region.

5.3.5 Pressure Distribution

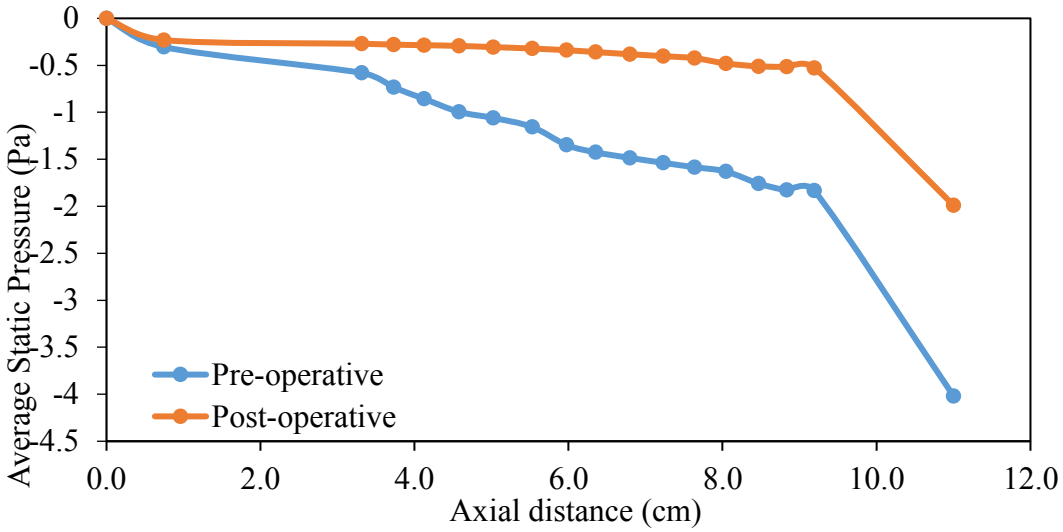

Figure 5.15: Comparison of pressure distribution through the nasal airway for pre-operative and post-operative study.

As can be seen in Figure 5.15, for both pre- and post-operative models, the pressure distribution decrease along the nasal passage. It is important to have a decreasing value of pressure in the nasal cavity because during inspiration the chest expands, therefore, the air enters the lung because the pressure within the lung is less than that of the atmosphere. It should be pointed out that, before operation, the average static pressure obtained at the nasal outlet was about -4.02 Pa. However, after the operation, the average static pressure decreased to -1.99 Pa. This implies that removing the nasal obstruction reduce the magnitude of negative inspiratory pressure, which is one of the major contributing factors to pharyngeal collapse in obstructive sleep apnea patients. This finding shows that nasal surgery can improve breathing quality for OSA patient without the patient has to goes through surgery at the pharynx part of the breathing airway.

5.4.6 Wall Shear Stress

Wall shear stress exerted on the nasal wall can contribute to nasal irritation and discomfort which could affect sleep quality. Figure 5.16 shows comparison of average wall shear stress obtained along the axial distance of the nasal cavity for inhalation rate of 7.5 L/min for pre- and post-operative cases. Figure 5.16 clearly demonstrate that after surgery the average wall shear stress along the nasal wall has decreased. Before surgery the highest average wall shear stress with $2.7 \times 10^{-3}\ Pa$ was found at region located at 3.7 cm from the tip of the nose which is represented by plane b in Figure 5.8. This is due to the increased of the velocity magnitude at the nasal blockage and narrow cross section area caused by the deviated septum in the left nasal cavity.

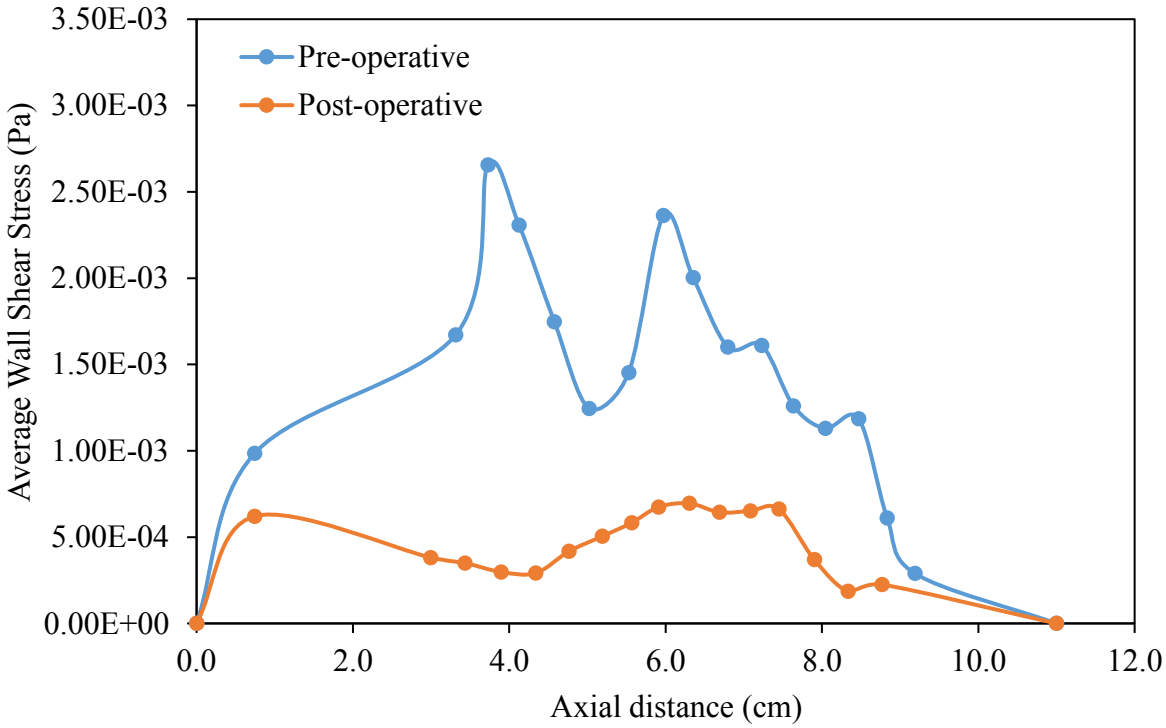

Figure 5.16: Comparison of average wall shear stress along the axial distance of the nasal cavity for flow rate of 7.5 L/min.

The second highest wall shear stress was observed located at approximately 6 cm from the nostril inlet. This location is represented by plane j in Figure 5.8. The abnormally increased of wall shear stress as high as $2.4 \times 10^{-3}\ Pa$ was observed in this region is caused by the increased of velocity magnitude in the narrow breathing passage caused by the concha bullosa in the nasal cavity. However, after surgery, the wall shear stress obtained at the same location in the nasal airway reduce for about 70%. Similar pattern of wall shear stress plots against the axial distance of the nasal cavity was observed as the inhalation flow rate increased from 7.5 to 20 L/min.

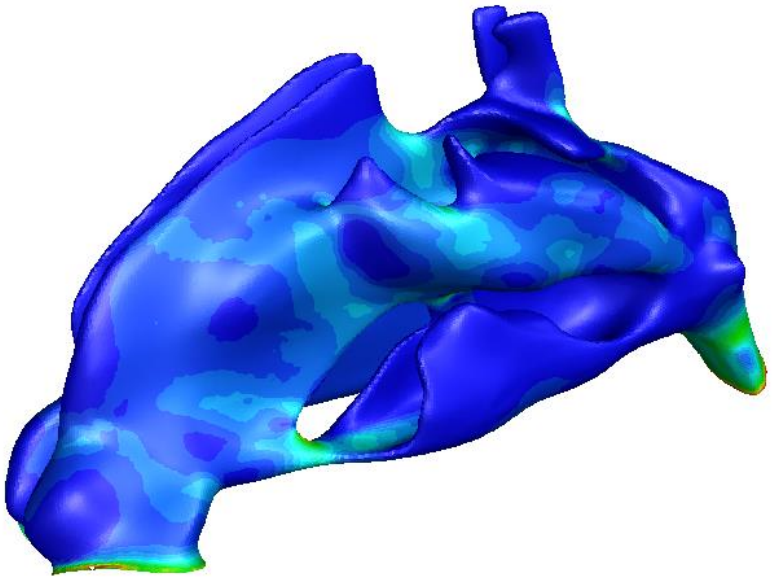

(a)

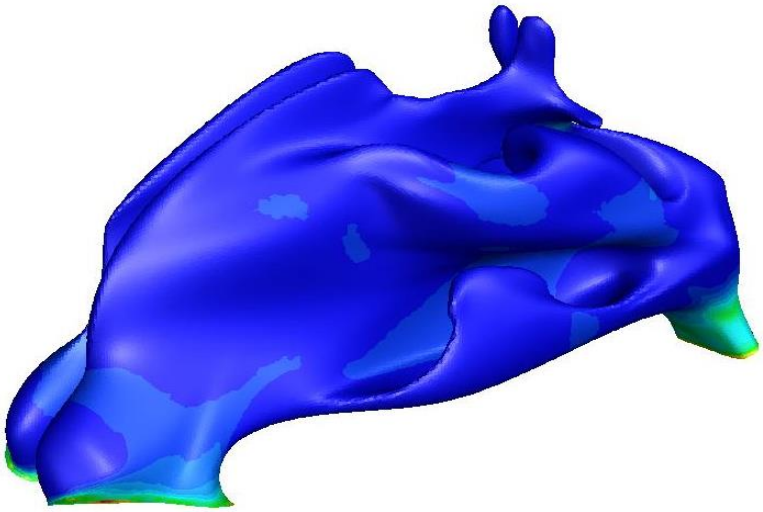

(b)

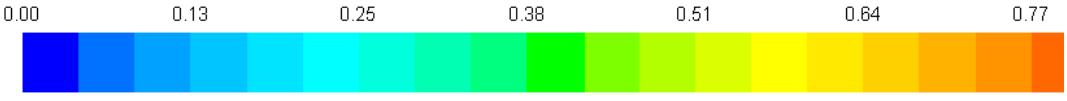

Figure 5.17: Average wall shear stress for inhalation rate of 20 L/min (a) pre-operative and (b) post-operative.

Figure 5.17 shows comparison of wall shear stress contour plot on the nasal wall for inhalation rate of 20 L/min for both pre- and post-operative cases. As can be observed in Figure 5.17 (b), after surgery, as the cross section area through the nasal airway increased, the wall shear stress obtained in the post-operative model has significantly reduced. A high magnitude of wall shear stress could contribute to nasal irritation and breathing discomfort to the patient during inspiration which could damage the cell lining and blood vessels located at the nasal wall. Hence, as the wall shear stress obtained after surgery has reduced, this shows that the nasal surgery has successfully improve the breathing comfort for the patient.

5.4.7 Particle Deposition

To compare the total deposition of microparticles for pre- and post-operation models, mono-dispersed 1, 5, 10, 20 and 40 μm particles were released at nostril inlet, and the particle trajectories were analysed. Figure 5.18 shows a comparison of the total particle deposition efficiency obtained for a range of particle diameter (1, 5, 10, 20 and 40 μm) and inhalation rate of 7.5 L/min before and after surgery. It can be seen in Figure 5.28 that for both pre and post-operative models, as the particle size increased, the total particle deposition efficiency increased. This implies that as the size of the inhaled particles increased, the number of particles being filtered within the nasal cavity will increase.

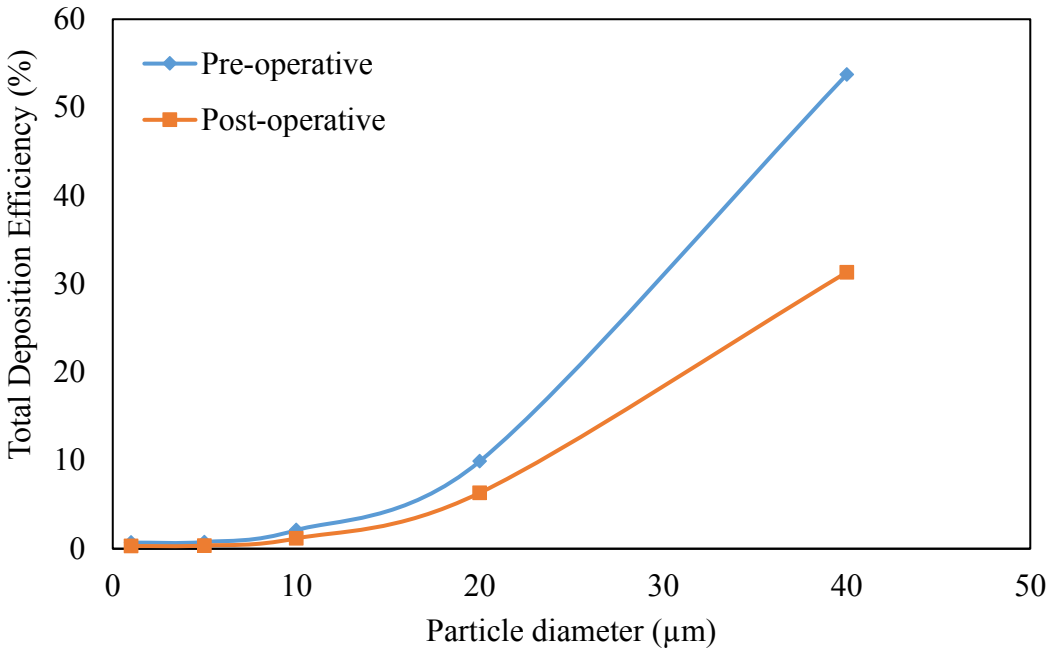

Figure 5.18: Comparison of total deposition efficiency, before and after surgery.

The effect of the nasal surgery on the total particle deposition efficiency can be clearly observed in Figure 5.18. Before surgery, the total deposition efficiency obtained for the particle diameter of 1 µm was 0.7 %. However, after the surgery the total deposition efficiency obtained was reduced to a value of 0.3 %. Similarly, the total deposition efficiency obtained for particle diameter of 40 µm before surgery was about 53.73 %, whereas after surgery the total deposition reduced to a value of 31.32 %. For low breathing rate of 7.5 L/min, the post-operative model experienced approximately about a 50 % decrease in total particle filtering efficiency. Hence, after surgery, more particles can pass through the nasal passage and flow into the lower respiratory tract. Hence, with lower particle filtering efficiency and high exposure to this inhalable toxic particle can increase the risk of developing particle-related respiratory diseases.

5.5 Conclusions

The septoplasty, inferior turbinate reduction and partial concha bullosa resection substantially increased nasal volume, which influenced flow partitioning and decreases the pressure drop and flow resistance of the nasal passage. Hence, the computed airway resistance has significantly improved after surgery and less effort is needed for breathing the same flow rate into the lung. After surgery, the average static pressure obtained at the nasopharynx outlet decreased to -1.99 Pa. This implies that removing the nasal obstruction reduce the magnitude of negative inspiratory pressure, which is one of the major contributing factors to pharyngeal collapse in obstructive sleep apnea patients. The abnormal shape and obstruction in the diseased nasal airway increased the number of particle deposition in the nasal cavity. However, the post-operative model experienced approximately about a 50 % decrease in total particle filtering efficiency. Hence, based on this finding, it can be conclude that after surgery, by removing the nasal obstruction, more particles can pass through the nasal passage and flow into the lower respiratory tract which can cause adverse health effect. Therefore, careful consideration should be given to this matter before nasal operation especially for a patient with breathing allergic history.

CHAPTER 6

COMPUTATIONAL FLUID DYNAMICS STUDY OF AIRFLOW AND MICROPARTICLE DEPOSITION IN A CONSTRICTED PHARYNGEAL SECTION REPRESENTING OBSTRUCTIVE SLEEP APNEA DISEASE

6.1 Introduction

Obstructive Sleep Apnea (OSA) is a potentially serious respiratory disorder and has become one of the most common public health problems. OSA is characterized by recurrent episodes of partial or complete pharyngeal airway collapse and obstruction during sleep (Mihaescu, *et al.*, 2008). The collapse of the pharyngeal airway during inspiration, having particular anatomical conditions such as an abnormally large tongue, too much tissue at the back of the throat (the uvula) and the soft palate that hangs down can lead to OSA, whose the symptoms are snoring, difficulty in breathing and sleep disorders. The collapse of the pharyngeal airway causes a reduction in or complete cessation of airflow despite ongoing inspiratory efforts (Ephros, *et al*.,2010; Fogel *et al*., 2004).

A schematic depiction of OSA, referring to the collapse of the pharyngeal section, is as shown in Figure 6.1 (Suratt *et al.*, 1983). Although the narrow and collapsible upper airway are believed to be the main causes of OSA, the etiology of this disorder and the exact mechanisms of upper airway collapse in OSA are not completely understood. Hence, the accurate prediction of the abnormal airflow characteristics, pressure distribution and airflow resistance in the upper airway

geometry associated with OSA is essential in understanding the relation between airway anatomy collapsibility and the pathophysiology of OSA.

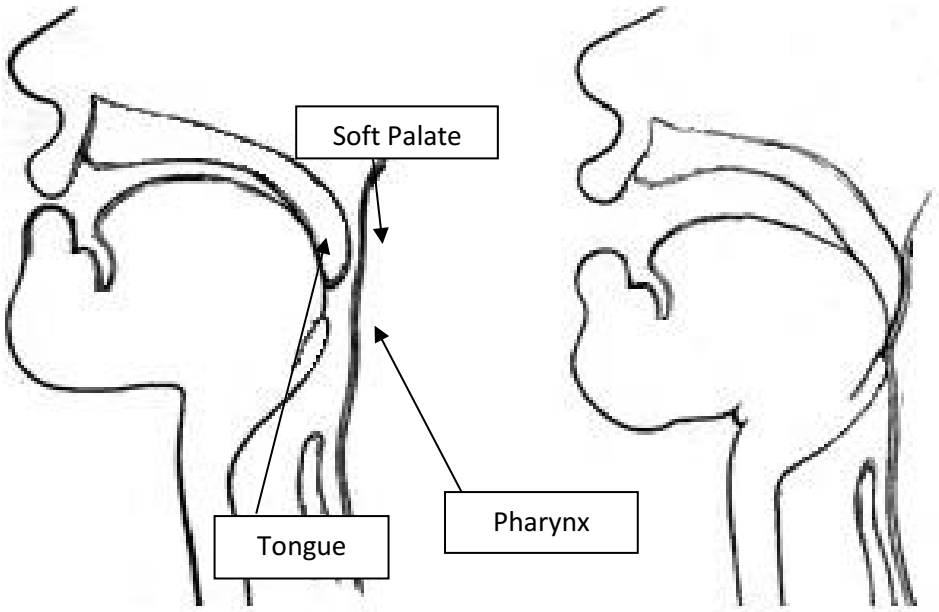

Figure 6.1: Left panel shows position of tongue, soft palate, and posterior pharynx during unobstructed breathing in sleeping patients. Right panel shows the position of these structures in OSA patients.

Recently, a Computational Fluid Dynamics (CFD) approach has been utilized to analyze flow patterns and characteristics through pharyngeal airway models reconstructed from magnetic resonance (MR) or the computed tomography (CT) imaging data of patients with OSA *(Jeong et al*., 2007; Mihaescu et al., 2008; Mihaescu *et al.* 2011; Vos et al., 2007; Xu et al., 2006; Zhao, *et al*., 2013a, 2013b). Mihaescu *et al.* (2008) investigated the airflow distribution and characteristics in the pharyngeal airway model by using both Reynolds-Averaged Navier-Stokes (RANS) approaches. The pharyngeal airway model was developed from the nasopharynx to the retroglossal pharynx region. As in their report, Mihaescu *et al.* (2008) stated that the

geometry expansion in the radial direction after the narrowing region has produced flow separation, strong shear layers, and recirculation regions. They also found that, compared to k-ε, the k-w results are the closest to the LES results due to its treatment of the viscous near-wall region and in its accounting for the effects of adverse pressure gradients. To increase understanding of the pathogenesis of OSA, Xu *et al.* (2006) investigated the effect of airway shape on pressure distribution and flow resistance in the upper airway of children age 3-5 years old. They found that the minimum pressure occurred at the narrowest region which is located at the region of adeno-tonsillar overlap. High-velocity jet and higher turbulence energy was observed at the downstream of the narrowest cross-sectional area.

In another study, Jeong *et al.* (2007) , found that the pressure drop due to area restriction occurred primarily between the nasopharynx and the oropharynx. Turbulent jet with higher shear and pressure force was observed in the narrowest segment of the pharyngeal airway. The constriction at the velopharynx produced pharyngeal jet flow as air passed through the velopharynx. Similar to the work of Sung *et al.* (2006), the maximum velocity and minimum pressure of the breathing airflow were observed at the velopharyngeal section. They concluded that the strength and intensity of the turbulent pharyngeal jet flow would be the main reason for pharyngeal occlusion and OSA diseases. Vos *et al*. (2007) postulated that the combination of the three parameters, which include the smallest cross-sectional area, airflow resistance and body mass index (BMI) can be used to evaluate the severity of obstructive sleep apnea in patients.

Most of the previous studies were limited to the oropharynx section and did not include the entire upper airway anatomy. Indeed, it is not easy to obtain the CT data for a subject suffering from OSA. Therefore, the present study on OSA was carried out by modifying the control subject to represent the OSA case study. This was accomplished by including a constricted pharyngeal section as shown in Figure 6.2. This OSA model was used for carrying out CFD simulation in order to understand the effect of pharyngeal constriction on the actual flow phenomenon.

One issue which has not been studied before is the effect of OSA on the increased potential for inhaled pollutants and particles to enter and deposit in the pharyngeal section and lung. Enhanced deposition of inhaled particles in the pharyngeal section is important for the assessment of exposure to aerosol pollutants, as well as for therapeutic drug delivery. The study of coal ash deposition in the human respiratory tract is of great importance because of the potential for serious health effects. The Environmental Protection Agency (EPA) in the United States has found that living near to a coal ash disposal site can increase the risk of cancer or some other serious diseases. In Malaysia, fly ash is one of the largest industrial waste material which commonly deposited in landfills. The total production of fly ash in Malaysia is approximately about 2 million tons annually (Shaheen *et al*., 2014). Coal ash is hazardous waste. It is one of the naturally-occurring products from the coal combustion process and is a material that is nearly the same as volcanic ash. Most coal ash comes from coal-fired electric power plants. The toxic remains of coal burning in power plants are full of chemicals that cause cancer and developmental disorders. Individuals with pre-existing lung disease, including asthma, can be at increased risk of their symptoms being exacerbated after being exposed to the inhalable ash particles.

Coal ash includes fly ash (fine powdery particles that are carried up in the smoke and captured by pollution control devices) as well as coarser materials that fall to the bottom of the furnace. Fly ash particles are generally spherical in shape and range in size from 0.5 μm to 60 μm (Sarkar *et al*., 2005). One study has shown that exposure to fly ash may cause irritation to the mucous membrane of the respiratory tract and even pulmonary fibrosis in humans. The ash particles that are inhaled into the lungs could trigger inflammation and immunological reactions (Cho & Cho, 1994). The adverse effects of particulates depend on the region of the airway in which the particles or ash are deposited. Thus, the knowledge of the deposition of ash in the respiratory tract is of considerable importance. The information about local deposition might be used in health risk assessment, because a high local dose may cause tissue injuries or initiate a disease process.

In this study, CFD simulation of laminar and turbulent inspiratory airflow through a constricted pharyngeal section is conducted to explore and improve the understanding of the pathophysiology of the OSA disease. A Lagrangian particle tracking approach is used to investigate the effect of the constricted pharyngeal section on the deposition rate and deposition patterns of microparticles in the upper airway model which represents OSA disease. Microparticles in the size range of 1-40 μm are introduced at the nostril inlet and the particle trajectories and regional deposition fractions of the particles were analyzed.

6.2 3D Model Generation and Meshing

A three-dimensional nasal computational model was developed based on the computed tomography (CT) scans of a healthy 39-year old female. The scans data was procured at the Universiti Sains Malaysia (USM), Medical Campus Hospital. The CT scan images were obtained from the axial, coronal and sagittal planes. The increment between each slice of the scan images is 0.8 mm. The scan images were segmented by defining threshold values ranging from -444 to 2037 HU. Segmentation was performed slice by slice on the scan images to ensure the accuracy of the selected region of interest (Riazuddin *et al.*, 2011). By using the image processing software MIMICs, the 2D scan images were converted into a 3D nasal cavity model

Figure 6.2 shows the reconstruction of the upper airway with a constricted pharyngeal section which was made in CATIA (Dassault Systems, SA). As can be seen in Figure 6.2 (b), the upper airway geometry modification was made by extending the outlet part of the normal nasal cavity model in Figure 6.2 (a). After that, a converging and diverging geometry was included at the normal nasal cavity outlet to mimic the pharyngeal occlusion in the upper airway. The geometry modification was made based on the discussion with an ENT surgeon from the Hospital Universiti Sains Malaysia.

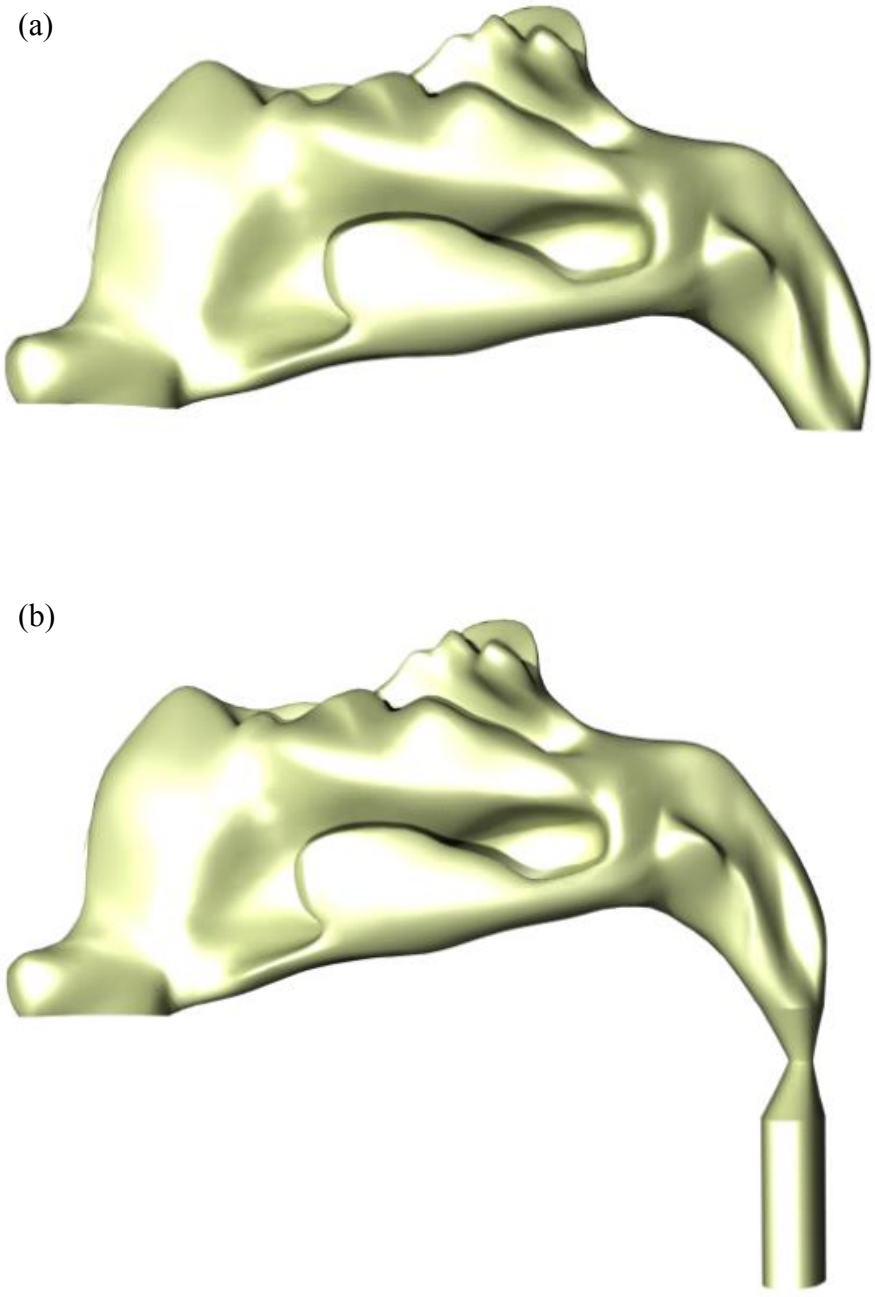

Figure 6.2: Computational domain: (a) normal nasal cavity, (b) upper airway with constricted pharyngeal representing Obstructive Sleep Apnea.

The most predominant feature of the pharyngeal airway is that stenosis converges and diverges at the pharynx. Hence, the airway was modeled to have some area restrictions at the pharynx region, which can be represented in terms of percentage stenosis in accordance with Xu et al., (2006) as written in Equation 6.1:

$$\% \text{ stenosis} = (1AOL/ACH) \text{ x}100\%. \quad (6.9)$$

In Equation 6.1, A_{CH} is the cross-sectional area perpendicular to the airway centerline at the choanae and A_{OL} is the minimum cross-sectional area in the constricted `pharyngeal region. Thus the model developed in this study has a percentage stenosis of around 89 % to represent the pharyngeal airway occlusion in OSA. Schwab *et al.* (1993) reported CT data showing that the retropalatal area was approximately 90 mm^2 for a snorer/mild apneic subject and 50 mm^2 for an apneic subject. In the present study, the minimum constricted area at the pharyngeal section was about 5.53 mm^2 (A_{OL}), which is smaller when compared to the observations of Schwab *et al.* (1993) and Sung *et al*. (2006).

6.3 Numerical Methods

The numerical simulation was performed using the commercial CFD solver ANSYS FLUENT. The simulation is based on the numerical solution of the RANS equation representing the general equation for the 3D flow of imcompressible and viscous fluids. In the present study, simulations for the modeled nasal configuration were performed under the steady condition for breathing rates of 7.5, 10, 20, 30, and

40 L/min. The details numerical methods implemented for this study are as described in Chapter 3. In the present work, initially, the upper airway computational domain was meshed with an unstructured tetrahedron using GAMBIT. After that, a hybrid mesh was generated by using a mesh generation software named TGRID with 1,580,000 elements, which consisted of a total of 6 layers of prism mesh near the wall boundary, and tetrahedral elements at the remaining flow domain. The generated hybrid mesh are as illustrated in Figure 3.16 and 3.17 in Chapter 3, section 3.3.

6.4 Results and discussion

6.4.1 Velocity distribution

Understanding the properties of airflow in the nasal cavity is very important in determining the nasal physiology and in diagnosis of various diseases associated with the nose. The inspiratory flow rates for adults can range between 5 L/min and 12 L/min for light breathing and 12-40 L/min for non-normal conditions such as during exertion and physical exercise (Wen *et al*.,2008). In this study, the airflow field simulations were performed for breathing rates of 7.5, 10, 20, 30 and 40 L/min. The flow was considered as laminar for breathing flow rate up to 10 L/min and turbulent for flow rate of 20 to 40 L/min. Figure 6.3 shows comparison of velocity streamlines between inhalation rate of 7.5 and 20 L/min. As can be seen in Figure 6.3 (b), as the inhalation rate increase, the amount of recirculatory flow was observed also increased at the anterior top part of the nasal cavity. Increased of flow recirculation in this region increased interaction between airflow and nasal wall.

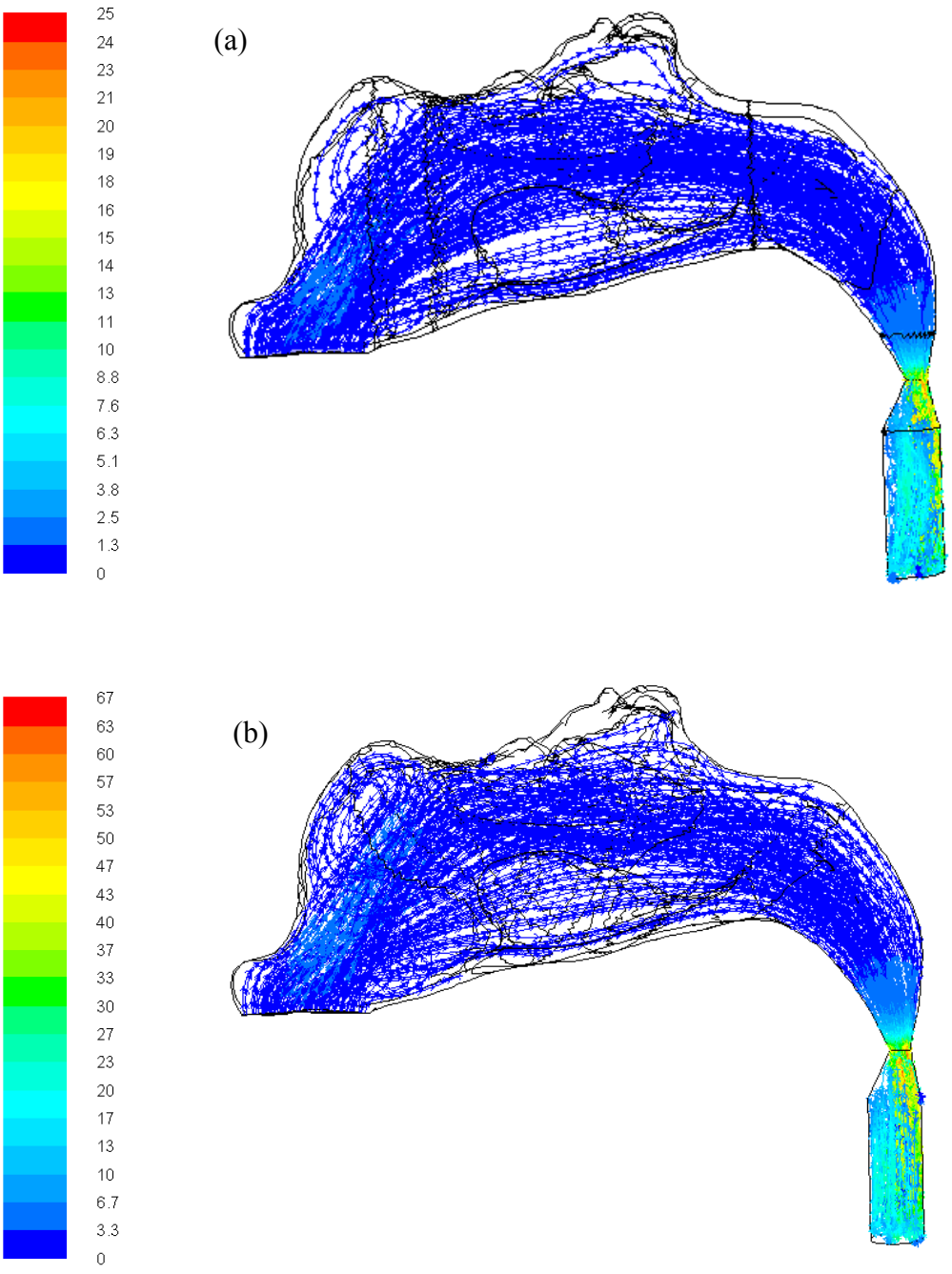

Figure 6.3: Velocity streamlines for inhalation rates of 7.5 and 20 L/min.

As can be observed in Figure 6.3 (a) and (b), for both breathing rate, most of the air flow pass through the middle airway region. The increase of inhalation rate does not change the location of the most air passed through the nasal airway. Even for a low laminar breathing rate of 7.5 L/min, intense flow recirculation can be observed occurred at the lower part of the pharyngeal section. The recirculatory flow was observed caused by the sudden expansion of the pharyngeal airway.

Figure 6.4 shows the coronal view of the velocity vector obtained for inhalation rate of 20 L/min. As shown in Figure 6.4 (a)-(e) several vortex flow formation were found in the inferior, middle and superior meatuses. The vortex flow formation were observed caused by the present of the inferior, middle and superior turbinates which obstruct the inhaled air through the nasal airway. As can be seen in Figure 6.4 (d), at the end of turbinates region, high swirling flow was observed. The airflow was observed intensely mixed at the nasopharynx region were the airflow from the left and right nasal cavity meet.

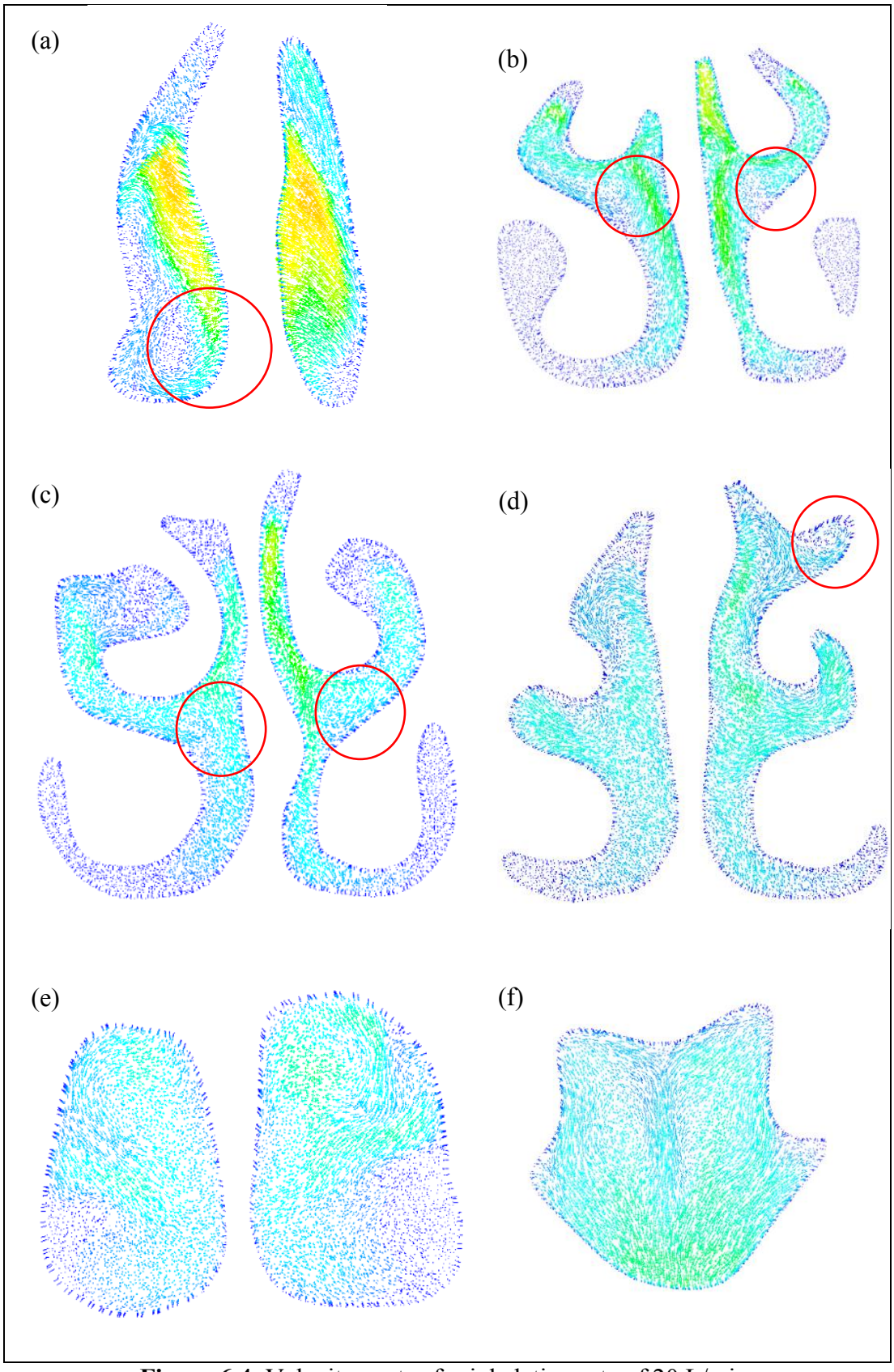

Figure 6.4: Velocity vector for inhalation rate of 20 L/min.

Figure 6.5 shows the velocity contour of inspiratory flow rate of 20 L/min. As can be seen in this figure one of the main factors that affect to the airflow patterns is the morphology of the upper airway. It can be seen that, at the constricted pharyngeal airway, firstly acceleration of the flow was observed then the flow decelerates due to increase cross-sectional area of the airway. The maximum velocity magnitude is found located at the smallest cross section in the pharyngeal section, with a value of 56.76 m/s.

Figure 6.5: Velocity contour of 20 L/min flow rate.

As shown in Figure 6.6, due to the area restriction, a turbulent jet is observed at the constricted area of pharyngeal section. Two flow recirculation region at the downstream of the smallest cross-sectional area were prominently formed at the posterior region of airway wall. The flow recirculation causes flow instability at the region further downstream of the pharyngeal airway.

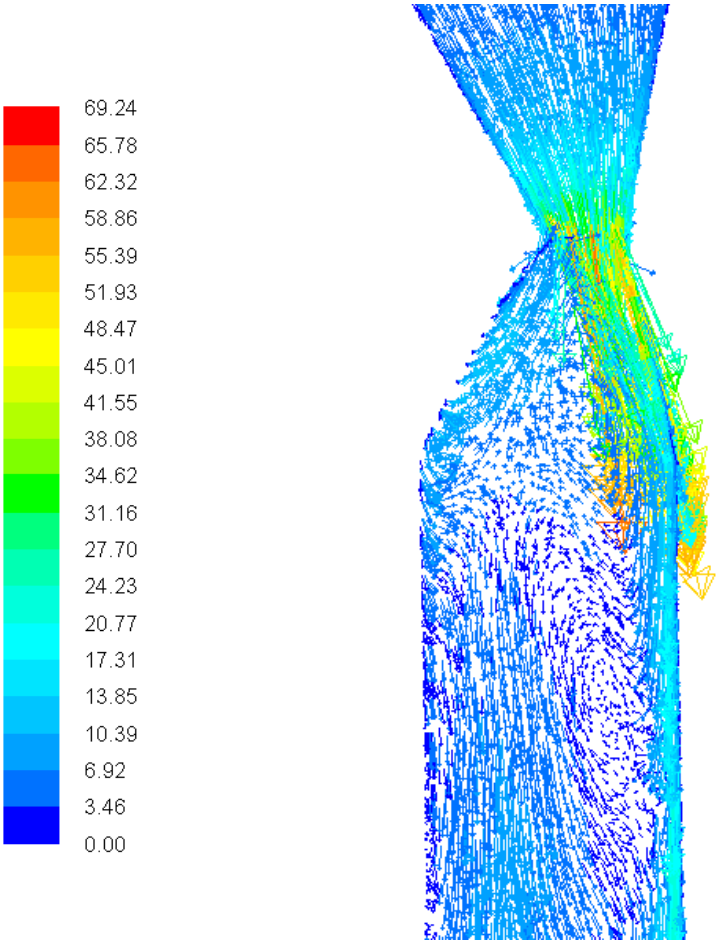

Figure 6.6: Recirculation regions downstream of the constricted pharyngeal section.

6.4.2 Pressure distribution

The pressure distribution through the upper airway of OSA for breathing airflow of 20 L/min is depicted in Figure 6.7. It can be observed that the pressure drop from the choanae to the OSA region was larger than the pressure drops through the nasal passages highlighting the effect of OSA on adverse flow behavior in that region. The resistance along the nasal passage was about 0.053 kPa/L/s, whereas the pressure drop from the choanae to the constricted OSA was 3.132 kPa/L/s. The effects of the negative pressure gradient due to the abrupt cross-sectional area expansion are

observed from the back flow and vortex downstream of the constricted region. The force induced by negative pressure is strong enough to cause pharyngeal wall displacement, further narrowing the constricted region which could lead to complete pharyngeal airway obstruction. A larger negative value of the pressure effort indicates that the patient needs to breathe harder to inhale the specified air volume to reach the lung.

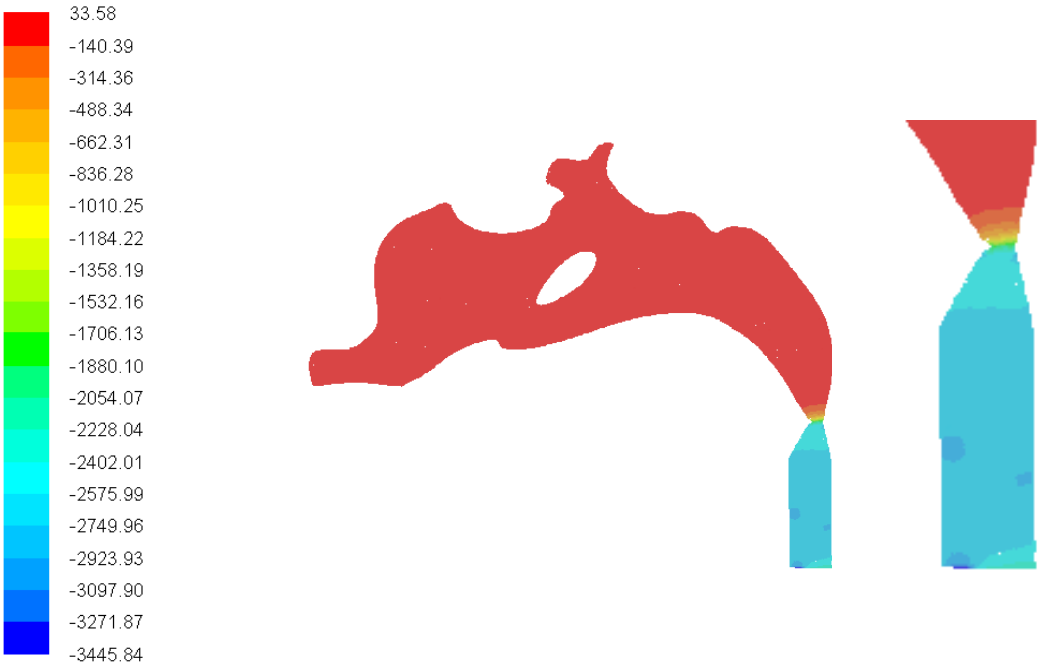

Figure 6.7: Pressure distribution for 20 L/min.

The average static pressure obtained through the upper airway for inhalation rate ranging from 4 to 40 L/min are as depicted in Figure 6.8. For a normal nasal cavity, for inhalation rate of 20 L/min, the pressure drop obtained is the nasal cavity was approximately 14.7 Pa. However, for the same flow rate, the pressure drop was found significantly increase to 2724.4 Pa as the flow passes through the constricted region in

the pharyngeal airway. The increased of pressure drop values in this region is due to the sudden geometrical changes which cause pressure lost after the constricted region in the pharyngeal section. As can be observed in Figure 6.8, as the inhalation rate increase, the pressure drop through the upper airway was found increased.

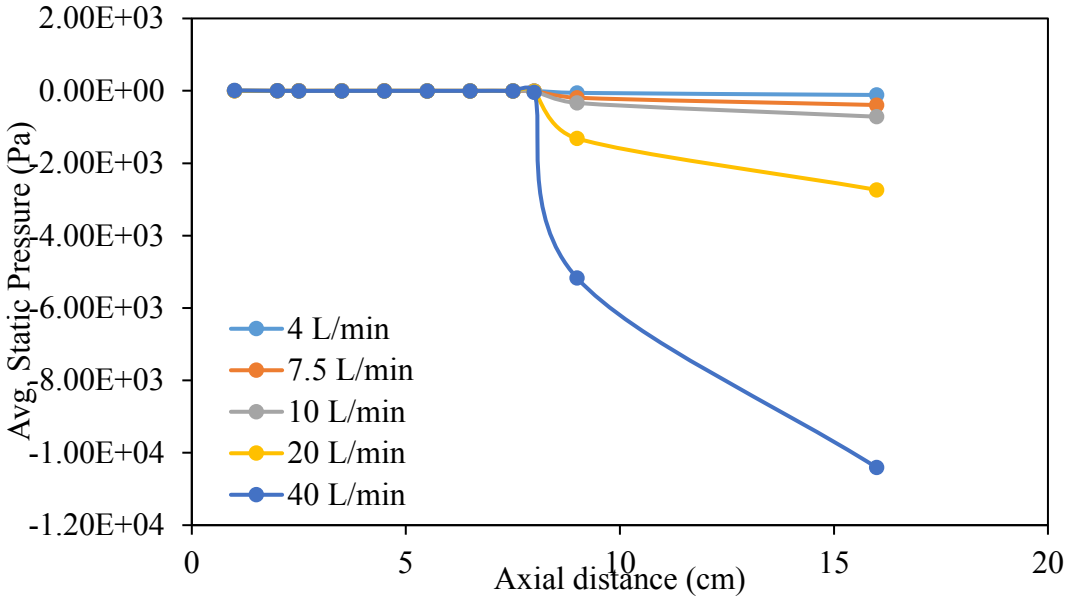

Figure 6.8: Average static pressure for inhalation rates of 4 to 40 L/min.

6.4.3 Microparticles deposition

When the distance between the particle centre and the surface is less than or equal to the particle radius the inhaled particle is assumed to be deposited on the wall. The local deposition fraction in a specific upper airway region can be defined by the ratio of particles depositing within a region to the particles entering the nostrils. To investigate the effect of particle size on the regional deposition through the upper airway with constricted pharyngeal, particle in the size range of 1-40 μm are released

at the nostril inlet and the particles trajectories are analyzed. Figure 6.9 shows the total particles deposition efficiency for inhalation rates of 4 to 40 L/min. The diameter of the injected particles are 1, 5, 10, 20 and 40 µm.

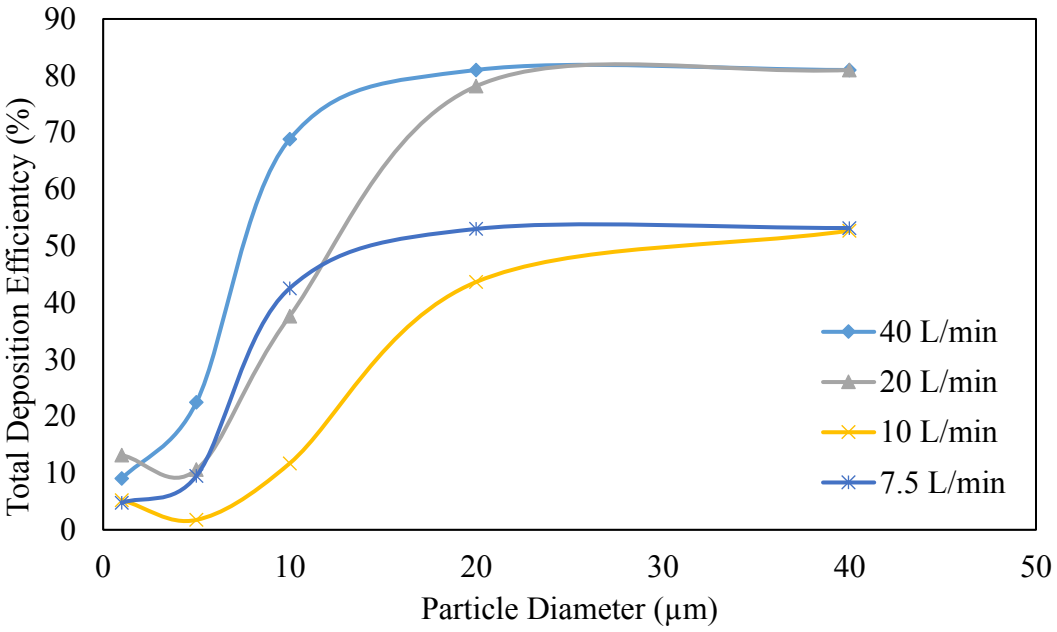

Figure 6.9: Total deposition efficiency for inhalation rates of 4-40 L/min.

As can be seen in Figure 6.9, as the inhalation rate increase, the total number of inhaled particles found deposited in the upper airway increased. As shown in Figure 6.3 (b), the increased of inhalation rate produced more recirculatory flow and increased vortex flow formation in the nasal airway. Hence increased the total number of particles trap and deposited in the upper airway.

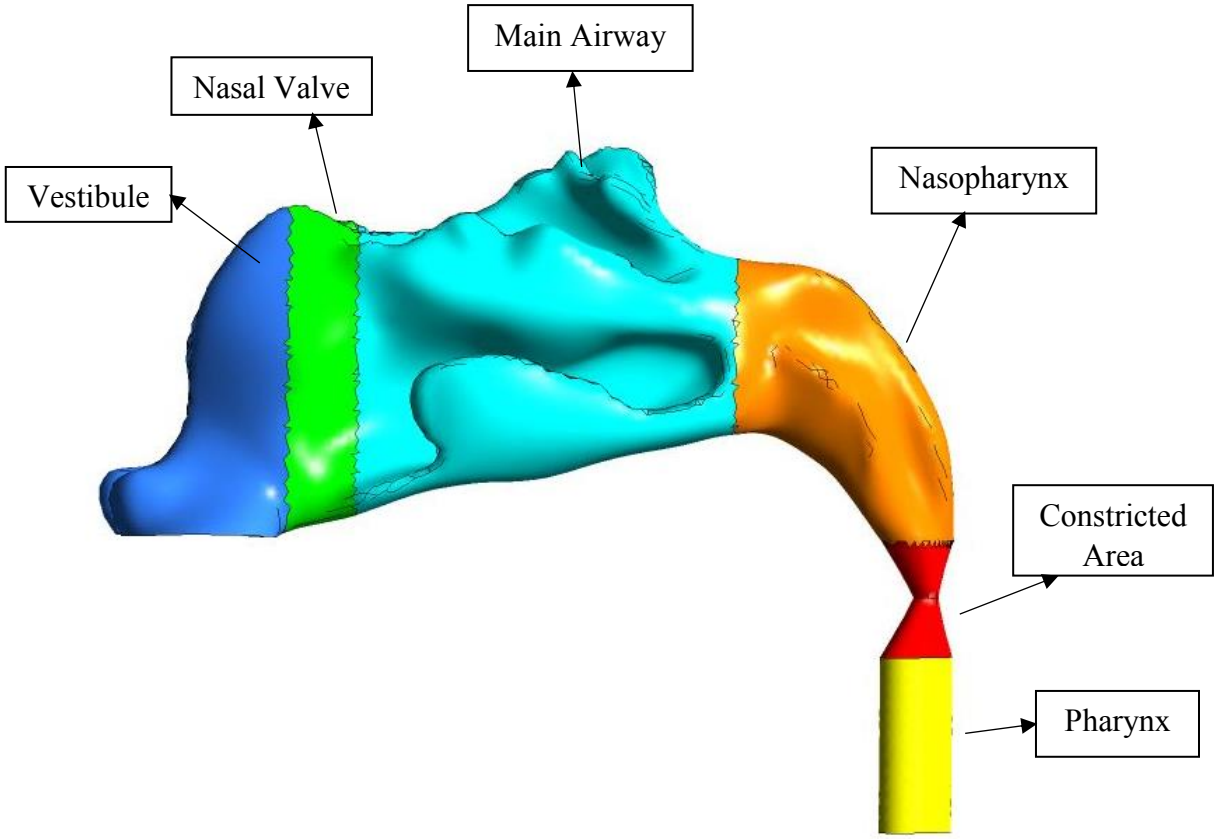

Figure 6.10: The six different regions created in the constricted pharyngeal airway model.

Figure 6.10 shows the six different regions defined through the upper airway computational model. The main purpose of dividing the upper airway into 6 major regions is to facilitate the calculation of the total number of particles deposited on the wall located in each region. Figure 6.11 shows the calculated percentage of particle deposition fraction obtained in each region for inhalation rate of 7.5 L/min. Deposition fraction of microparticles in upper airway for inhalation flow rates of 7.5 and 20 L/min are shown in Figure 6.11 and Figure 6.12 accordingly.

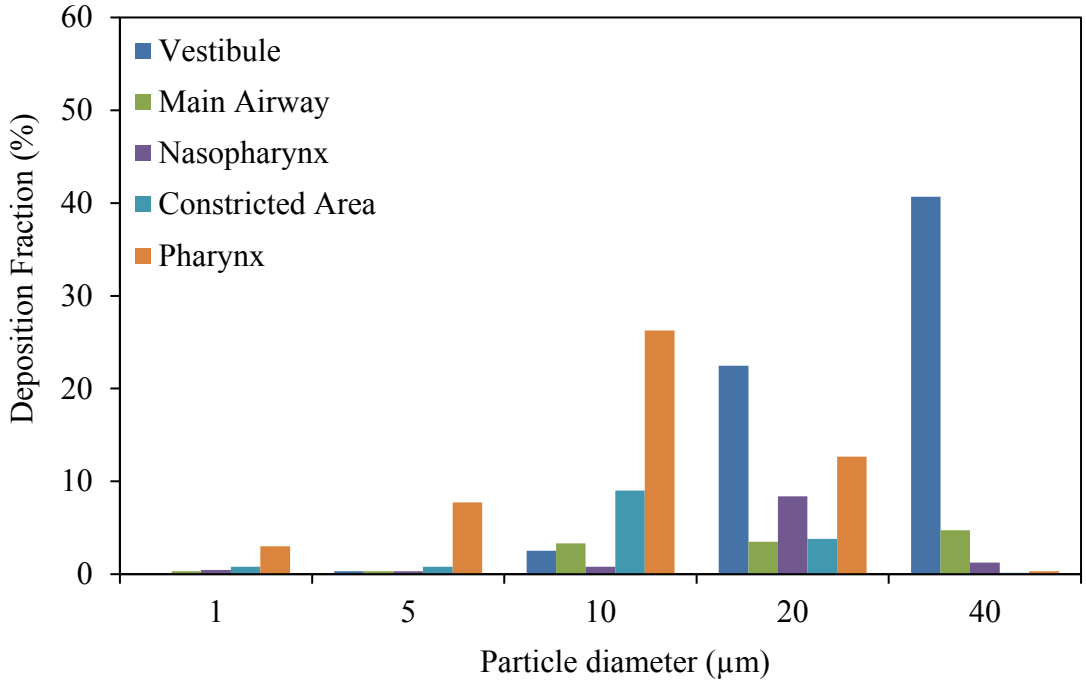

Figure 6.11: Deposition fraction of microparticles in upper airway for inhalation rates of 7.5 L/min.

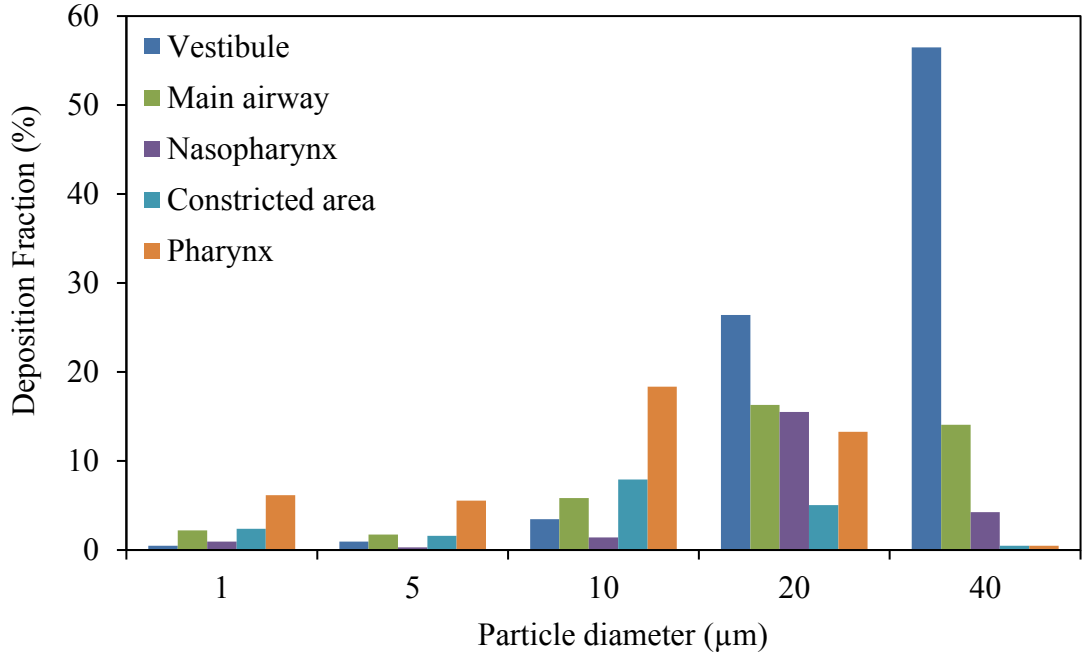

Figure 6.12: Deposition fraction of microparticles in upper airway for inhalation rates of 20 L/min.

As can be seen in Figure 6.11 and 6.12 for both 7.5 and 20 L/min inspiratory rates, the highest deposition fraction for the size of particle with the diameter of 20 and 40 μm particle are located at the vestibule region. For 20 μm, the deposition fraction obtained in the vestibule region for flow rate of 7.5 and 20 L/min are around 22 % and 26 % respectively. For 40 μm, the deposition fraction obtained in the vestibule region for flow rate of 7.5 and 20 L/min are 41 % and 57 % accordingly. However, it can be seen in Figure 6.11 and 6.12 that for the same flow rates, the highest deposition fraction for particle size of 1-10 μm are observed at the pharynx region. Hence, it can be concluded that, as the diameter of the particle increase, the location of the highest particle deposited region will shift to the anterior part of the nasal airway. For 20 μm and 40 μm particle, most particles were captured deposited at the vestibule region compared to the pharynx region. This is due to the higher particle inertia and deviation from the flow streamlines at the vestibule region. As shown in Figure 6.10 and 6.11, for particle with diameter of 1-10 μm, due to lower inertia, most particles can penetrate to the pharyngeal section. The results obtained from this study shows that, as the diameter of the particles increased, the number of particle deposited in the upper airway increased.

As shown in Figure 6.13, the deposition fraction of microparticles in the vestibule region was plotted against the inhaled particle diameter for flow rate ranging from 7.5 to 40 L/min. As can be seen in Figure 6.13, for all particles size, as the flow rates increase, the number of particles deposited in the vestibule region also increased. During inspiration, air enter the nasal cavity through the nostril inlet. After that, the flow was observed changed about 90 degree from its original direction to enter the

nasal valve region. Due to the higher inertial impaction, the particles with a higher diameter sized will maintain its original pathway and deposit in the vestibule region. It can also be observed that, most of the particle in a size range of 1-10 µm with lower inertia could pass through the nasal vestibule region and flow into the lower part of the upper airway.

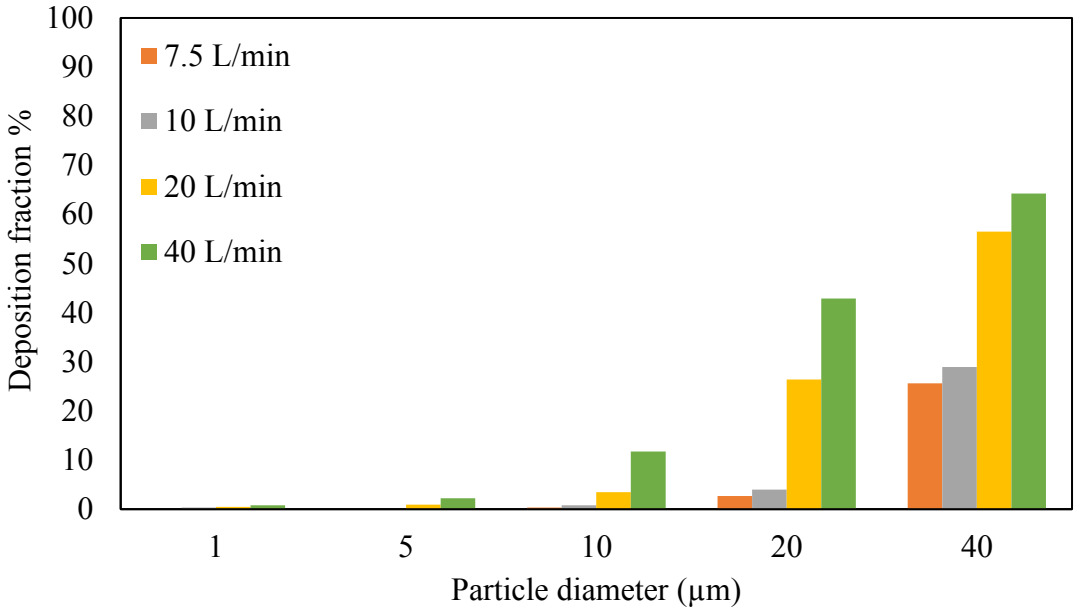

Figure 6.13: Comparison of deposition fraction of microparticles deposited in the upper airway for inhalation rate of 7.5 to 40 L/min: (a) Vestibule region.

6.5 Conclusions

The morphology of the upper airway was found to significantly affect the airflow pattern and the deposition fraction of microparticles. Results obtained can be used to estimate the location of airway obstruction in upper airway of patient with sleep apnea symptom. The local deposition fractions proved that the upper airway plays a significant role in filtering large micro-particles. The size of the inhaled particle significantly affects the total particle deposition efficiency in the upper airway.

Breathing rate was also found significantly influence the particle filtering efficiency in the upper airway. The inhalation of toxic particles through the upper airway has been found to cause adverse responses. The presented regional deposition fraction may be used in specifying the site of highest possibility for respiratory lesions according the breathing rate and the size of the inhaled toxic particles.

CHAPTER 7

NUMERICAL SIMULATION OF AIRFLOW AND AEROSOL DEPOSITION IN REALISTIC HUMAN UPPER AIRWAY WITH CHRONIC NASAL OBSTRUCTION AND OBSTRUCTIVE SLEEP APNEA: PRE- AND POST-SURGERY

7.1 Introduction

Obstructive sleep apnea (OSA) is one of the potentially chronic upper airway disease and has affected a significant portion of population. OSA disorder is known caused by the narrowed and small structure of the upper airway and loss of dilator muscle function when the patient is asleep. The apnea has been defined as a cessation of airflow due to airway collapse within the upper airway during sleep (Guilleminault *et al.*,1976).These partial or full cessation of breathing, influence the quality of sleep, reduce brain oxygen saturation and have linked to hypertension, neuropsychological dysfunction and heart failures (Chouly *et al.,* 2008; Sittitavornwong *et al., 2009)*. However, success rate of the surgical treatment in treating OSA is limited because the etiology of the OSA disorder is still not fully understood.

Due to the non-invasive approach, the computational fluid dynamics (CFD) simulations have been used to investigate the biological flow characteristics in the normal and diseased human upper airway. CFD can also be used to investigate the effect of surgical intervention on upper airway anatomical structure and breathing mechanics. Zhao *et al*., (2013) investigated the effect of mandibular advancement

splint device which enlarge the pharyngeal airway on the OSA treatment. They developed upper airway geometry from the nasopharynx to the hypopharynx region. In order to understand the pathogenesis of OSA in children, Xu *et al.*, (2006) investigated the effect of airway shape on pressure distribution and flow resistance in the upper airway of children ages 3-5 year-old. They reported that the highest pressure drop was found in the nasopharynx region at the location of adenoid and tonsils overlap. (Wang et al., 2012) compare the aerodynamics airflow patterns in upper airways and soft palate movements between preoperative and postoperative models. Reduced nasal resistance and decrease soft palate volume due to odema contribute to the decrease of airflow resistance through pharyngeal section. On the other hand, determination of the precise location of the induced lesion in the upper airway is the first step in understanding the critical factors involved in the pathogenesis of the injury (Harkema *et al*., 2006).

The existence of obstruction in the nasal cavity has impact on the overall breathing performance in the upper airway and may further aggravate the OSA symptom. However, there is not much study investigated the difference of upper airway characteristics at pre- and post-treatment particularly to analyze the effect of chronic nasal obstruction on OSA. In this study we discussed the results obtained from the numerical simulation of airflow through the realistic human upper airway with OSA disease and chronic nasal obstruction for pre- and post-operative cases. The objective of this study was to evaluate the effect of geometrical changes in the nasal airway section on pressure drop and breathing resistance though the upper airway particularly in the pharyngeal section before and after surgery. The comparison between pre- and post-operative cases in terms of the velocity magnitude, static

pressure distribution, wall shear stress and particle deposition efficiency were systematically studied.

7.2 Three-Dimensional Upper Airway Computational Model

A 38-year-old Malaysian male patient was diagnosed with chronic nasal airway obstruction and obstructive sleep apnea disease in Hospital Serdang, Selangor, Malaysia. His symptoms include, septum deviation which cause nasal obstruction in the left nasal cavity. Inferior turbinate hypertrophy was observed in both left and right side of the nasal cavity and concha bullosa which resulting in narrowing of the nasal airway at the posterior region on the left nasal cavity. The patient had undergone a surgical treatment performed in the nasal cavity. The CT scan data were taken without nasal decongestion. The CT scans were obtained while the patient was fully awake. The pre-operative scans were taken before the surgery, and the post-operative scans were taken 7 months after the surgery. Realistic three-dimensional human upper airways were developed for both pre- and post-operative cases.

Figure 7.1 shows comparison of the CT scan images of the diseased human upper airway obtained before and after surgery. As can be observed in Figure 7.1 (a), before surgery, the patient has a major obstruction in the nasal cavity and a structurally narrowed pharynx.

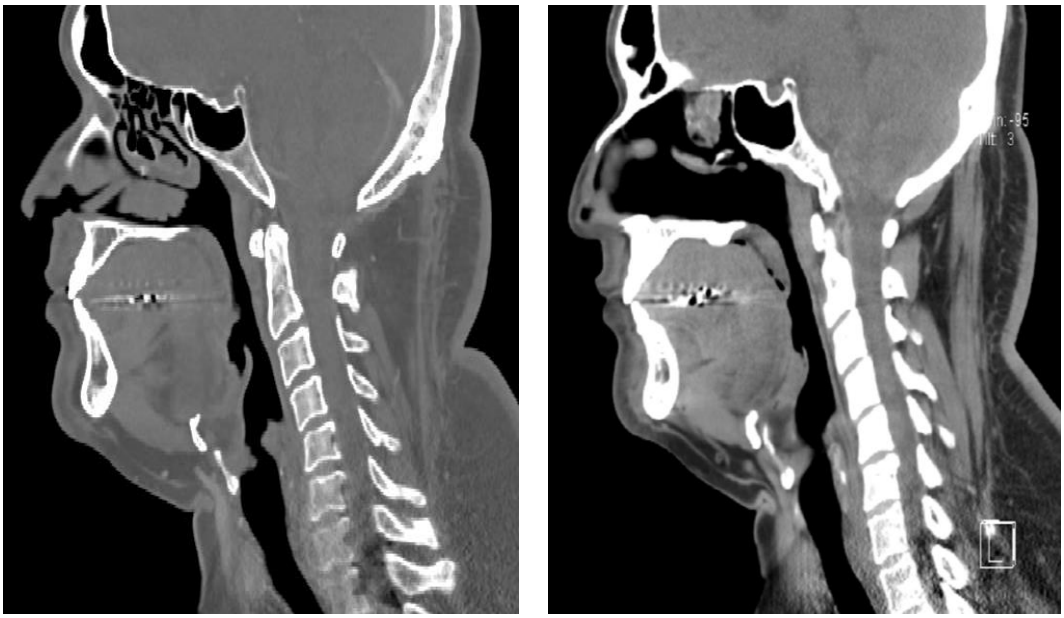

(a) (b)

Figure 7.1: Comparison of the CT scan images of human upper airway; (a) before surgery and (b) after surgery.

The most restricted region was found at the hypopharynx near to the vocal cord. However, as can be seen in Figure 7.1 (b), after surgery, the nasal blockage has been removed and simultaneously the airflow passage at the pharyngeal section has increased. The 3D realistic human upper airways were then reconstructed from the 2D CT scan images by using the image processing software, Mimics and CAD software named CATIA. Mesh were developed using ANSYS ICEM CFD and the hybrid mesh were generated using ANSYS FLUENT Meshing.

In ICEM CFD, the maximum skewness obtained for the generated unstructured mesh was maintained to be less than 0.5. After that, the mesh files were imported into ANSYS FLUENT MESHING to develop the hybrid mesh which consisted of 4 layers of prism mesh near to the nasal wall and unstructured tetrahedral mesh at the inner

region of the upper airway. For both pre- and post-operative upper airway model, the maximum skewness obtained for the generated hybrid mesh was maintained to be less than 0.85. Figure 7.2 shows the hybrid mesh generated for the pre-operative upper airway model.

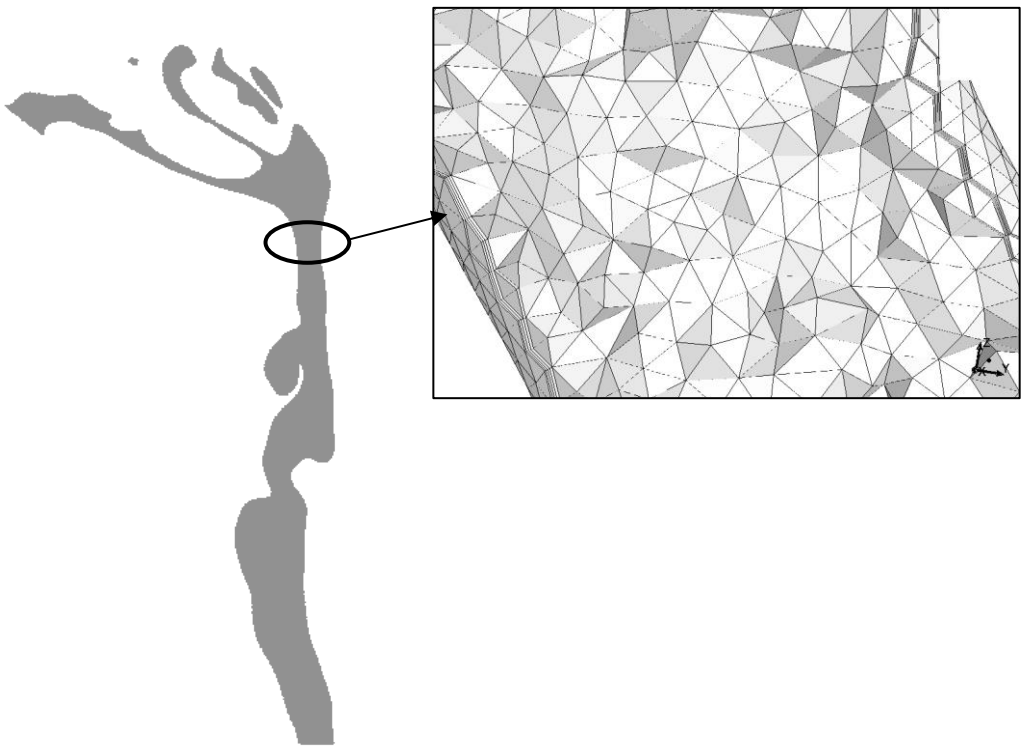

Figure 7.2: Hybrid mesh generated for the pre-operative upper airway model.

As shown in Figure 7.2, 4 layers of prism mesh were developed near to the wall whereas the unstructured tetrahedral mesh was developed at the remaining part of the computational domain. Figure 7.3 shows the hybrid mesh generated for the post-operative upper airway model. As highlighted in Figure 7.3, similarly, 4 layers of prism mesh were developed at the wall and unstructured tetrahedral mesh was generated at the inner part of the computational domain.

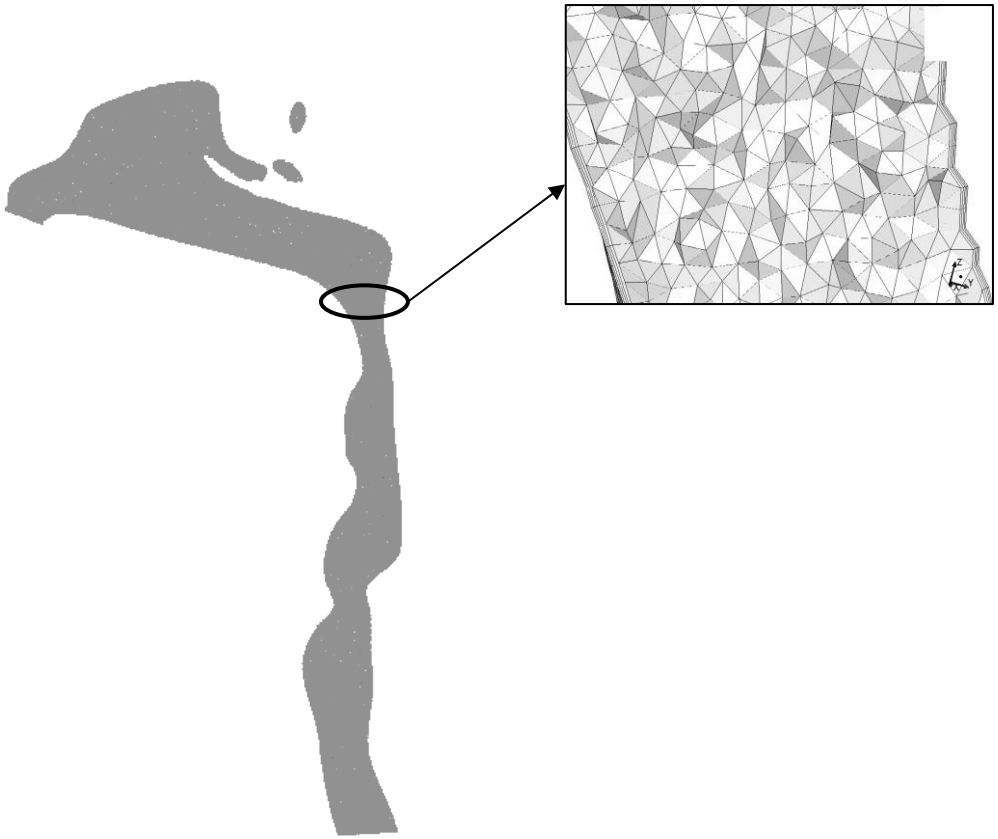

Figure 7.3: Hybrid mesh generated for the post-operative upper airway model.

7.3 Numerical Methods

The numerical simulations of the inspiratory airflow through the upper airway mdoel for both pre-and post-operative cases were performed using the commercial CFD solver named ANSYS FLUENT. In the present study, numerical simulation for the inspiratory airflow for the modeled upper airway configuration were performed under the steady condition for breathing rates of 4, 7.5and 10 L/min. For the pre-operative case, the Reynolds number obtained for the selected inhalation rates are 605, 1147 and 1529. On the other hand, for the post-operative case, the calculated Reynolds

number are 532, 998 and 1331. Hence, in both pre- and post-operative cases, the flow were considered as laminar inspiratory airflow. In this study, mass flow inlet was boundary condition was defined at the nostril inlet while outflow boundary condition was defined at the outlet. A no slip boundary condition was assumed and defined at the nasal wall, ignoring the presence of the mucus layer in the airway passage. The numerical methods implemented for this study has been presented in detailes in Chapter 4.

Figure 7.4 shows the three-dimensional realistic human upper airway model with obstructive sleep apnea disease developed for the pre-operative case study. The blue colour surfaces in Figure 7.4 represents the inlet boundary condition for the upper airway model. The grey surface represents the wall boundary condition. The outlet boundary condition was define at the bottom part of the upper airway model.

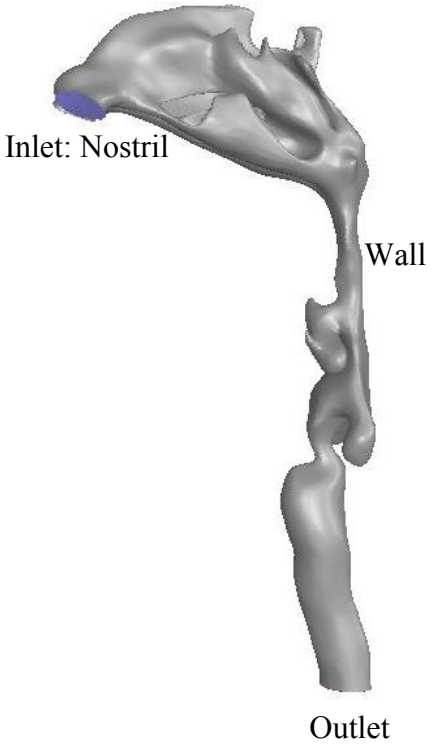

Figure 7.4: 3D realistic human upper airway computational model with obstructive sleep apnea diseases for pre-operative case.

Figure 7.5 shows the three-dimensional realistic human upper airway model with obstructive sleep apnea developed for the post-operative case study. As shown in Figure 7.5, similarly, the red surfaces were defined as the inlet boundary condition for the post-operative upper airway model. The grey surface represents the wall boundary condition. The outlet boundary condition was defined at the bottom part of the upper airway model.

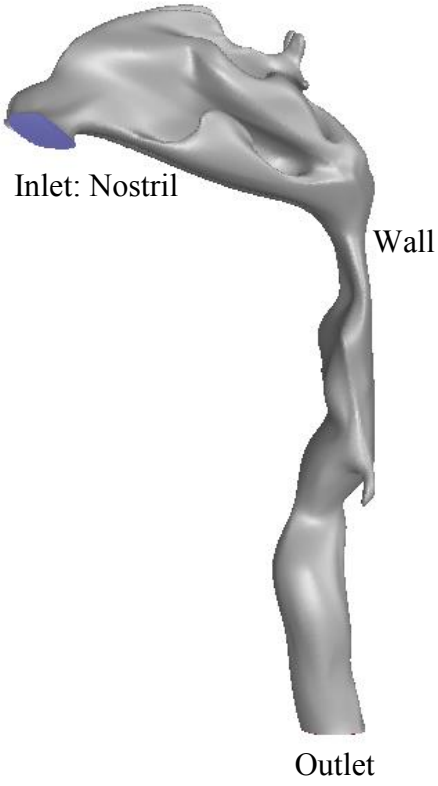

Figure 7.5: 3D realistic human upper airway computational model with obstructive sleep apnea disease for post-operative case.

7.4 Grid Dependency Analysis

Grid dependency studies have been performed for the pre- and post-operative diseased human upper airway models. As shown in Figure 7.6 and 7.7, the mesh size represents the total number of mesh generated for the upper airway computational domain. The average static pressure was obtained at the constricted region. The plane created at the constricted region is as shown in Figure 7.8 plane j.

Figure 7.6 shows the grid dependency study for the developed upper airway with OSA before surgery. The first model with number of mesh of 3426150 was initially used to solve the inspiratory airflow in the upper airway at a flow rate of 7.5

L/min. The model was then improved by refining the cells by reducing the size of the mesh with each refinement producing a higher total number of mesh in the upper airway model. As can be seen in Figure 7.6, the grid dependency analysis shows that the results obtained for average static pressure converge as the mesh approached 7354273 cells. Hence, in this study, the upper airway model with 7354273 cells was used for the pre-operative case study.

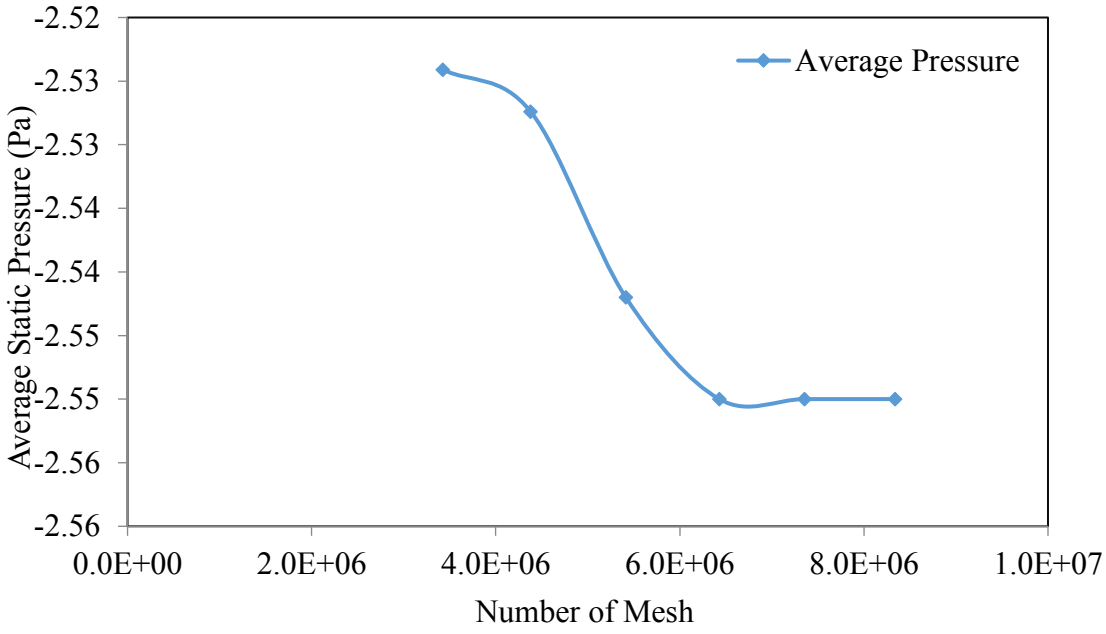

Figure 7.6: Grid dependency analysis for pre-operative human upper airway with OSA**.**

Figure 7.7 shows the grid dependency study for the post-operative upper airway with OSA disease. For this model, an initial mesh size of 3389924 cells was used to simulate the inspiratory airflow in the post-operative upper airway for flow rates of 7.5 L/min. After that, similarly the mesh was refined by reducing the mesh size, resulting in an increased of the total number of mesh in the post-operative upper airway model. As can be observed in Figure 7.7, the average static pressure obtained

at the constricted region converge as the mesh resolution approached 7465763 cells. Hence, the post-operative upper airway model with 7465763 cells was used in this study in order to compromise between the computational cost and results accuracy.

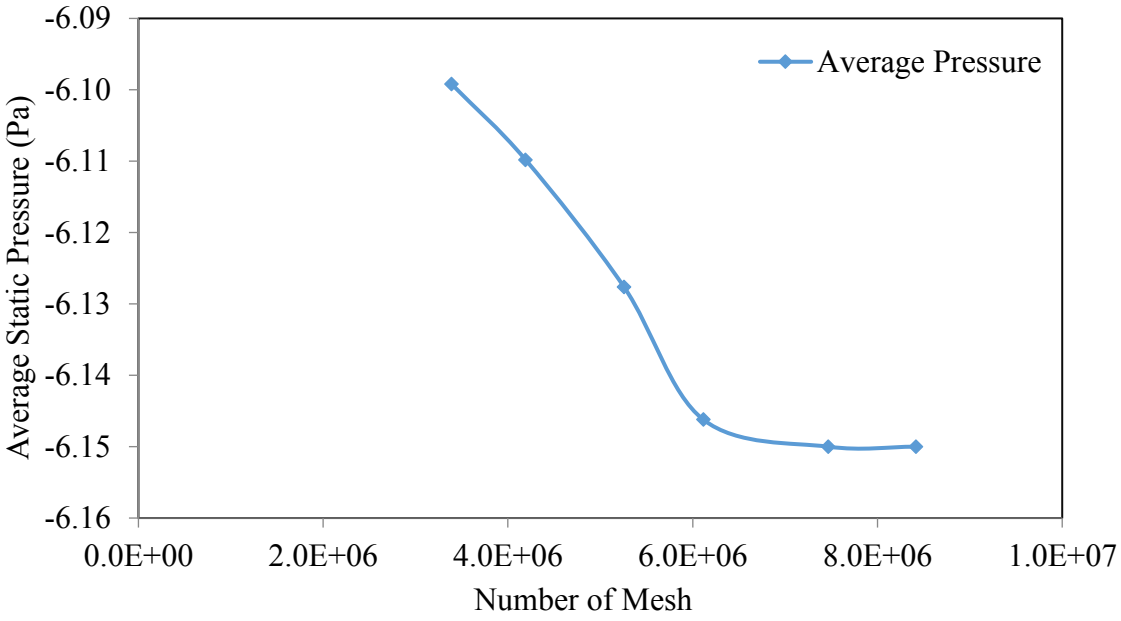

Figure 7.7: Grid dependency analysis for post-operative human upper airway with Obstructive Sleep Apnea.

7.5 Geometry Comparison

The pre- and post-operative upper airway models were compared to observe the geometrical changes in the upper airway model after the surgical treatment. Figure 7.8 shows the eighteen cross-section area created along the upper airway for the pre-operative computational model.

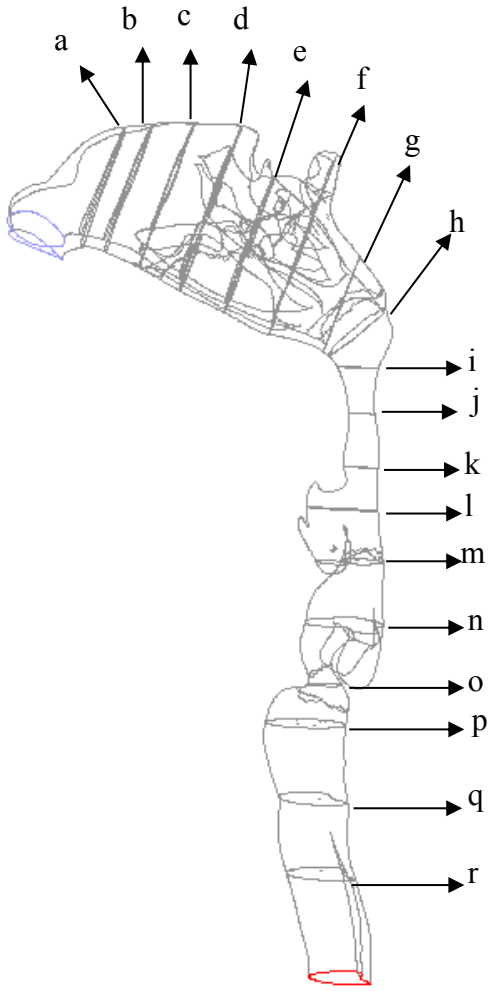

Figure 7.8: Cross section area along the upper airway for the pre-operative computational model.

As can be seen in Figure 7.8, plane a to plane h were created in the nasal cavity region, whereas, plane i to plane r were created in the pharynx region. As shown in Figure 7.8, plane k marks the end of nasopharynx section. Plane l and m are located at the back of the tongue, the oropharynx section. Plane n and o are located at the hypopharynx section. Plane m is located near to the epiglottis, whereas, plane o is located near to the glottis. Plane p and are located at the larynx section. Finally, plane r is located at the trachea region. As can be observed in Figure 7.8, two constricted

regions were found in the pharyngeal airway passage. The first constricted region was found located at the back of the tongue (Plane k), in the oropharynx region. The second constricted region was found located in the hypopharynx region as depicted by plane o in Figure 7.8. Figure 7.9 shows the ten planes created from the nasopharynx region to the larynx. As shown in Figure 7.9, for the pre-operative model, the smallest cross section area in the pharynx section was observed at plane j and plane o which located at the oropharynx region and hypopharynx region respectively. As can be observed in Figure 7.9, the geometry of the cross-section area along the pharynx region change dramatically from nasopharynx to trachea region.

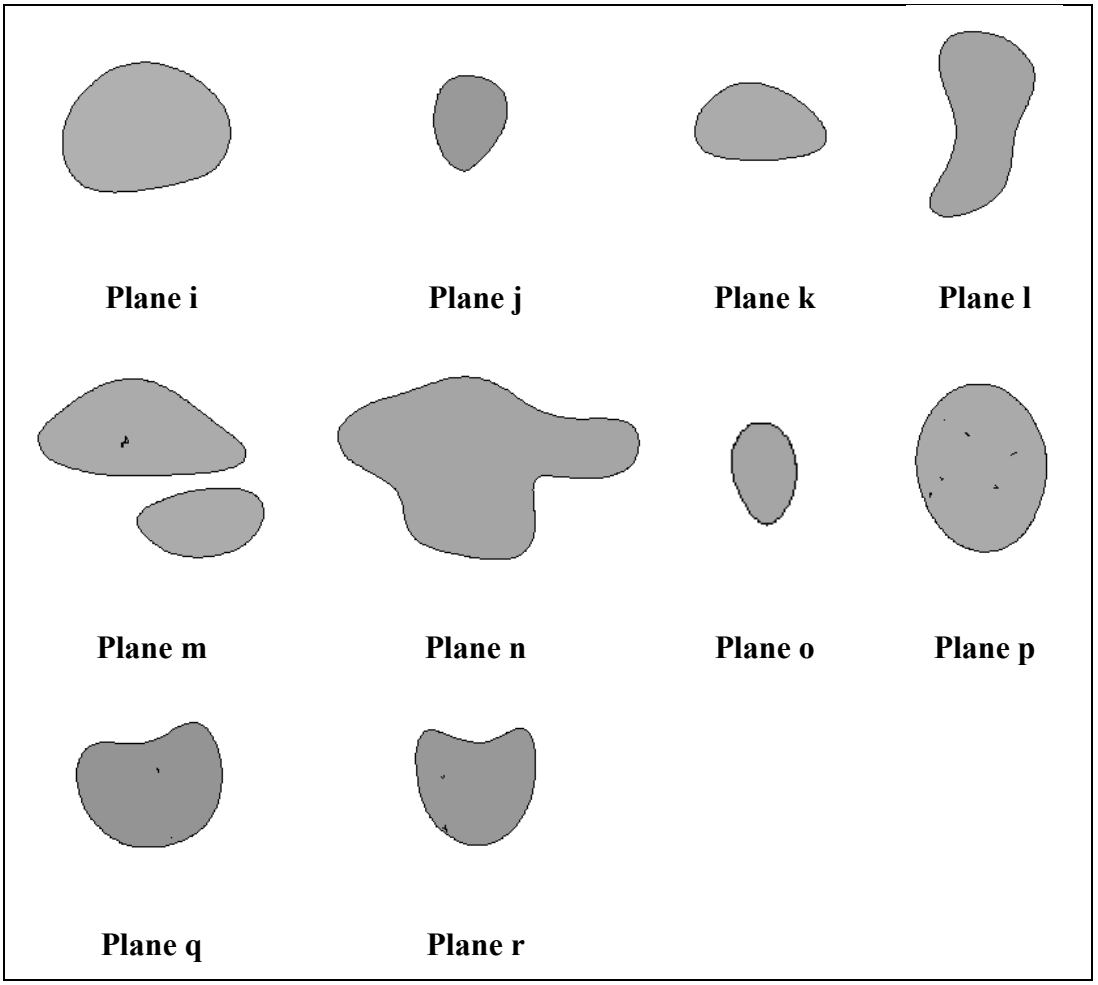

Figure 7.9: The planes created from nasopharynx to larynx region for pre-operative model.

Figure 7.10 shows the cross-section area along the upper airway for the post-operative computational model. Similarly, plane a to plane h were created in the nasal passage region, where, plane i to plane q were created in the pharynx region. As can be seen in Figure 7.8, plane k marks the end of the nasopharynx region. Plane l and m were created at the oropharynx region while plane n and o were created in the hypopharynx region. Plane m was created near to the epiglottis, whereas, plane o was created near to the glottis. Finally, Plane p and q are created in the larynx and trachea region respectively.

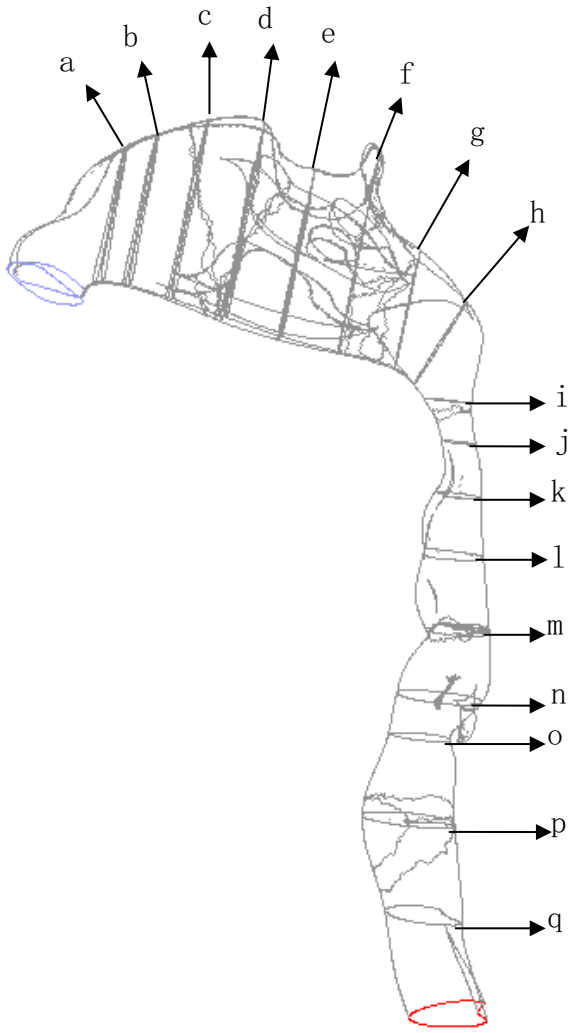

Figure 7.10: Cross section area along the upper airway for the post-operative computational model.

Figure 7.11 shows the planes created from nasopharynx to the larynx region for the post-operative computational model. As can be seen in Figure 7.11, for post-operative case, the smallest cross section area was also observed located at the oropharynx region and hypopharynx region. The smallest cross section area in the oropharynx region is represents by plane j and the smallest cross section area in the hypopharynx region is represents by plane o.

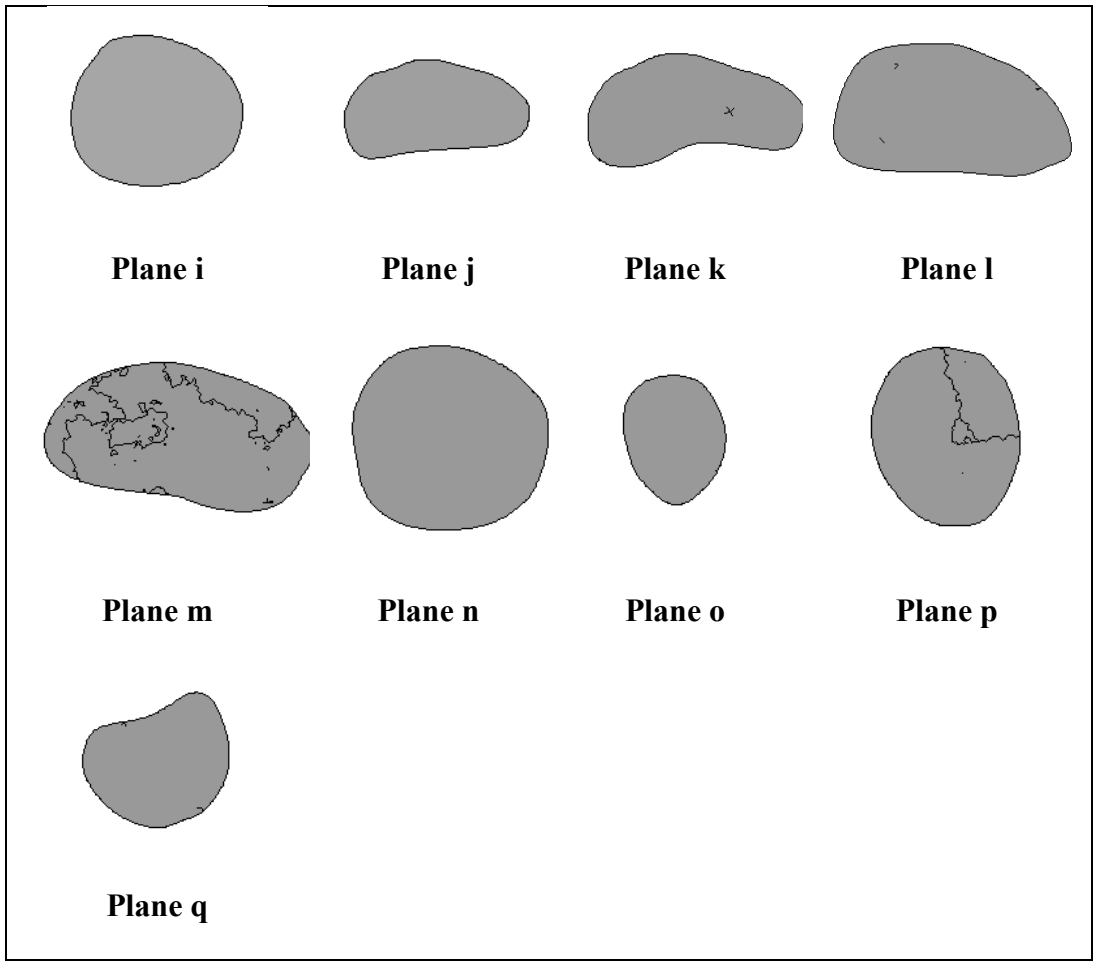

Figure 7.11: The planes created from nasopharynx to larynx region for post-operative case.

Figure 7.12 shows comparison of the cross-sectional area obtained along the axial distance through the nasal cavity region for pre- and post-operative upper airway models. Initially, both pre- and post-operative model starts with the same cross section area at the nostril. After that, a bilateral inferior turbinate reduction surgery was performed at the anterior part of the nasal cavity. Then a septoplasty surgery was performed in the left nasal cavity to remove the nasal blockage and to restore the nasal septum position. Therefore, as can be seen in Figure 7.12, the cross-section area for the post-operative case increased after the nostril inlet. The nasal blockage which was located approximately at the 4 cm from the tip of the nose was removed. Finally, a concha bullosa resection was performed at approximately 6 to 10 cm from the tip of the nose resulting in an increased of cross section area in the posterior part of the post-operative nasal passage.

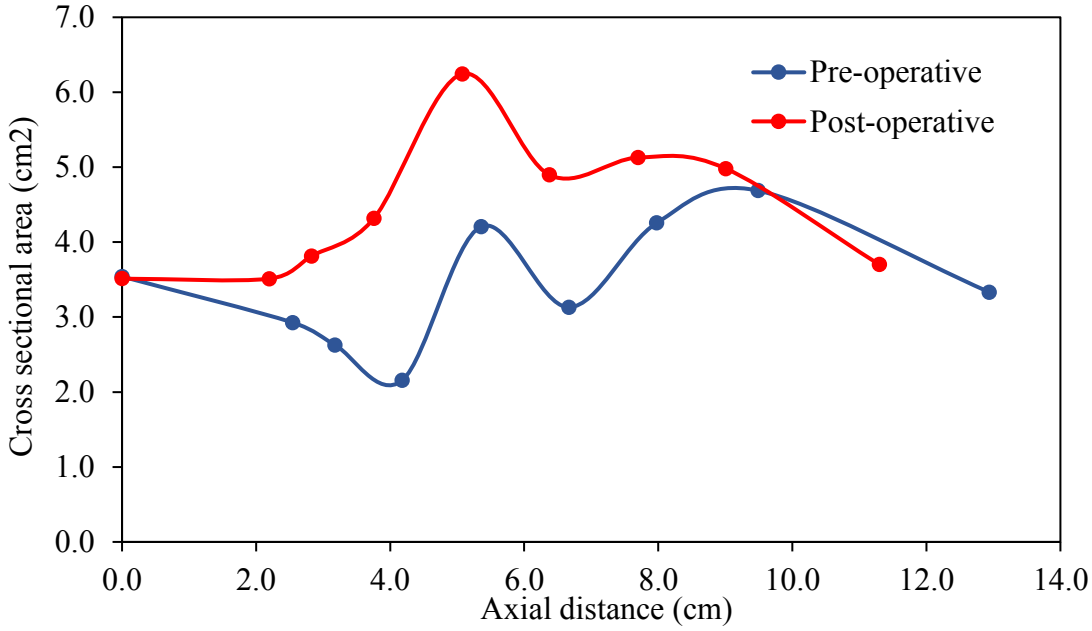

Figure 7.12: Cross-sectional area along the axial distance through the nasal airway.

Figure 7.13 shows the cross-sectional area plots along the sagittal distance through the pharynx section of the pre and post-operative upper airway model. As can be seen in Figure 7.13, both pre- and post-operative cases have almost the same magnitude of the cross-section area at the nasopharynx plane. However, after the nasopharynx plane, the cross-sectional area for the post-operative upper airway model started increased. It is worth to mention that, no surgical treatment was performed in the pharynx part of the upper airway model. The geometrical changes in the pharynx region was generally affected by the nasal surgical treatment.

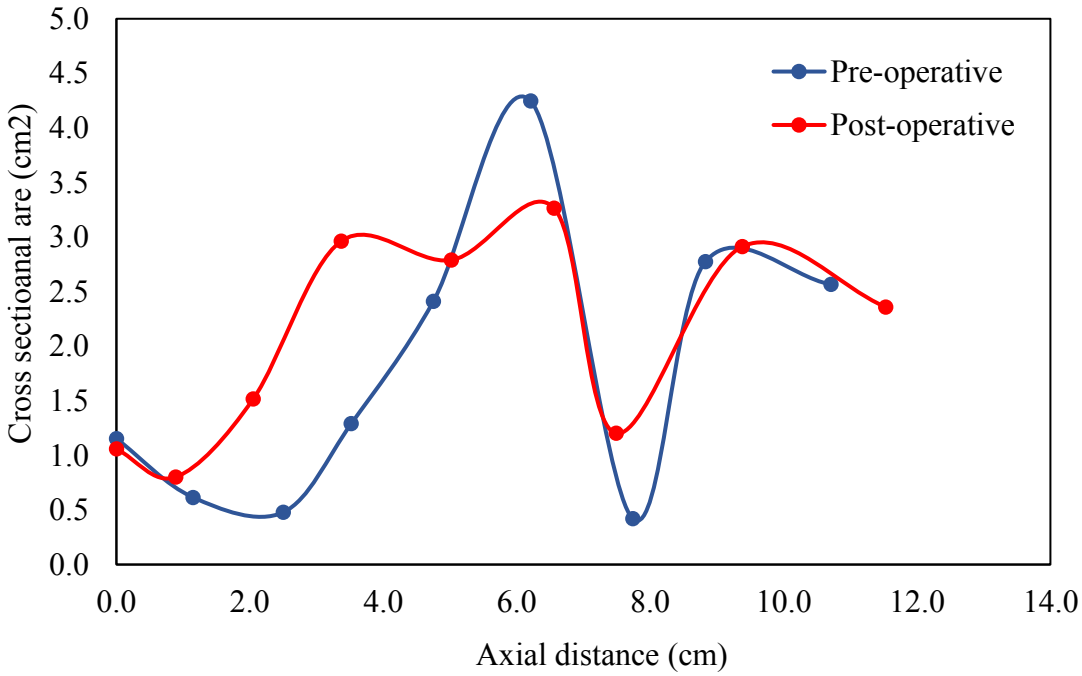

Figure 7.13: Cross-sectional area along the sagittal distance through the pharyngeal section.

As depicted in Figure 7.13, before surgery, the smallest cross section area obtained in the oropharynx region was found located at the 2.5 cm from the nasopharynx plane (plane i in Figure 7.8). However, after surgery, the smallest cross

section area was found located at 0.9 cm from the nasopharynx plane. As can be observed in Figure 7.13, after surgery, the cross-section area at the oropharynx region was found increased. However, the cross-section area at the hypopharynx area was found decreased. The cross-section area at the glottis region increased in the post-operative model. There were no significant changes in cross section area in the larynx region after surgery. As shown in Figure 7.13, before surgery, the smallest cross section area was found in the glottis region, which is located at 8 cm from the plane i. However, after surgery, the smallest cross section area was found in the oropharynx region, which is located at 0.9 cm from the plane i. The cross-section area at the glottis has increased from 0.4 cm^2 to 1.2 cm^2.

7.6 Pressure and Flow Resistance

Figure 7.14 shows comparison of pressure contour obtained along the upper airway model for pre- and post-operative cases. As can be observed in Figure 7.14, for both cases, the highest pressure magnitude was found located at the nostril. The pressure was observed decreased throughout the upper airway model. As the air flow through the upper airway model, negative pressure was observed. The negative pressure represents the air suction into the lung during physiological breathing.

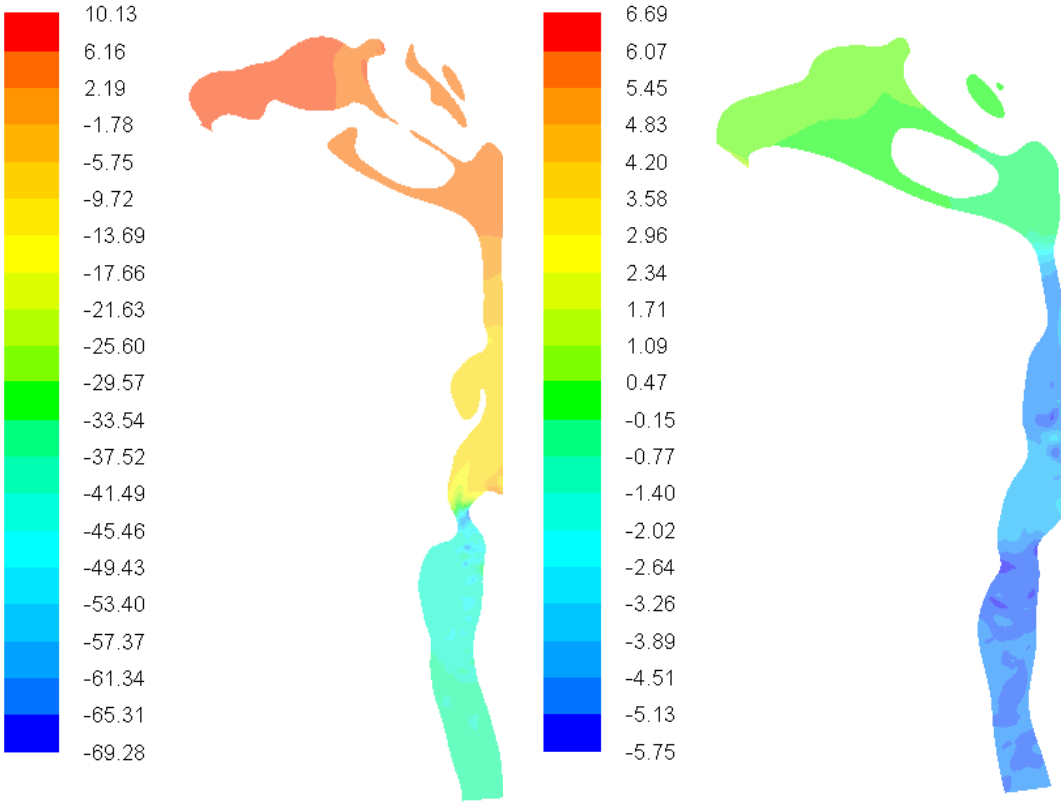

Figure 7.14: Comparison of pressure contour obtained for inhalation rate of 10 L/min: (a) pre- and (b) post-surgery.

As can be observed in Figure 7.14, the maximum negative pressure obtained after surgery was significantly reduced as compared to that of before surgery. Before surgery, the maximum negative pressure obtained in the pharynx section is 69.28 Pa, whereas, after surgery, the maximum negative pressure reduces for about 92 % with 5.75 Pa. As the negative pressure in the pharyngeal airway during inspiration is one of the contributing factor of collapse of the pharyngeal airway. The reduction of the negative pressure in the post-operative model could contribute to the reduction of the possibility of the airway occlusion in the pharyngeal airway. Figure 7.15 shows the pressure comparison between pre- and post-operative model for flow rate of 10 L/min.

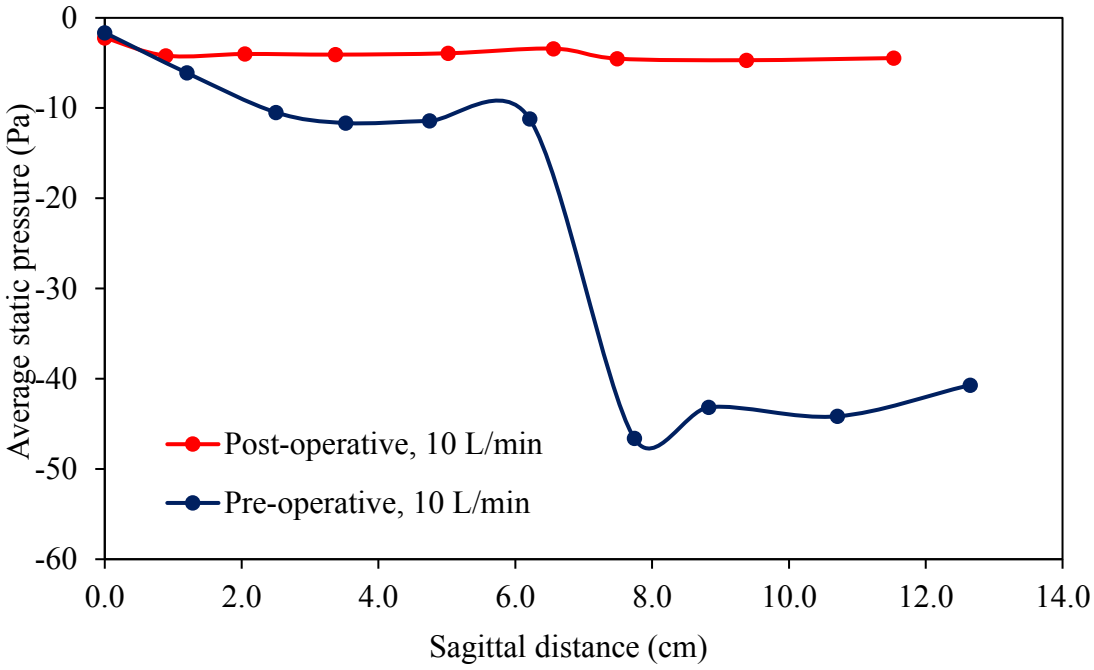

Figure 7.15: Pressure comparison between pre- and post-operative model for flow rate of 10 L/min.

As be seen in Figure 7.15, before surgery, the average static pressure was observed decreased drastically as the flow passes through the hypopharynx region. However, after surgery, there was only small changes in pressure distribution in the hypopharynx region. Before surgery, the average static pressure obtained at plane l is -11.19 Pa and plane m is -46.60 Pa. However, after surgery, the average static pressure obtained in plane l is -3.41 Pa and plane m is -4.52 Pa. As can be observed in Figure 7.15, before surgery, the highest pressure drop, 19.43 Pa, was found in the hypopharynx region during inspiration, whereas after surgery, highest pressure drop, with only 1.2 Pa, was found in oropharynx region. Figure 7.16 shows the average static pressure obtained along the pharynx section of pre-operative upper airway for various flow rates ranging from 4 to 10 L/min.

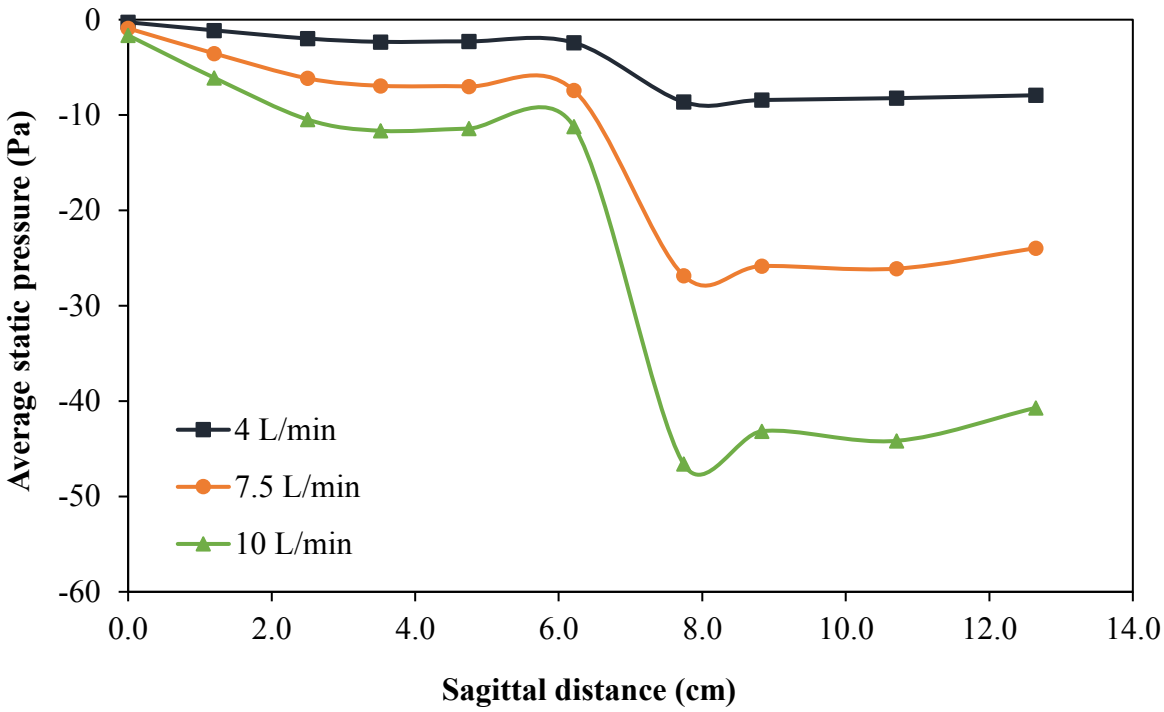

Figure 7.16: Pressure along the pre-operative upper airway model for various flow rates.

As shown in Figure 7.16, the average static pressure along the pharynx section was found increased as the inhalation rate increased. As can be observed in Figure 7.16, before surgery, as the flow rate increased. The average pressure obtained in the hypopharynx region increased significantly when compared to pressure obtained in the oropharynx region. For inhalation rate of 7.5 L/min, the average static pressure calculated at plane m is -26.83 Pa, whereas, for 10 L/min, the calculated average static pressure is -46.60 Pa. Figure 7.17 shows the average static pressure obtained along the pharynx section of the post-operative model for flow rate of 4, 7.5 and 10 L/min.

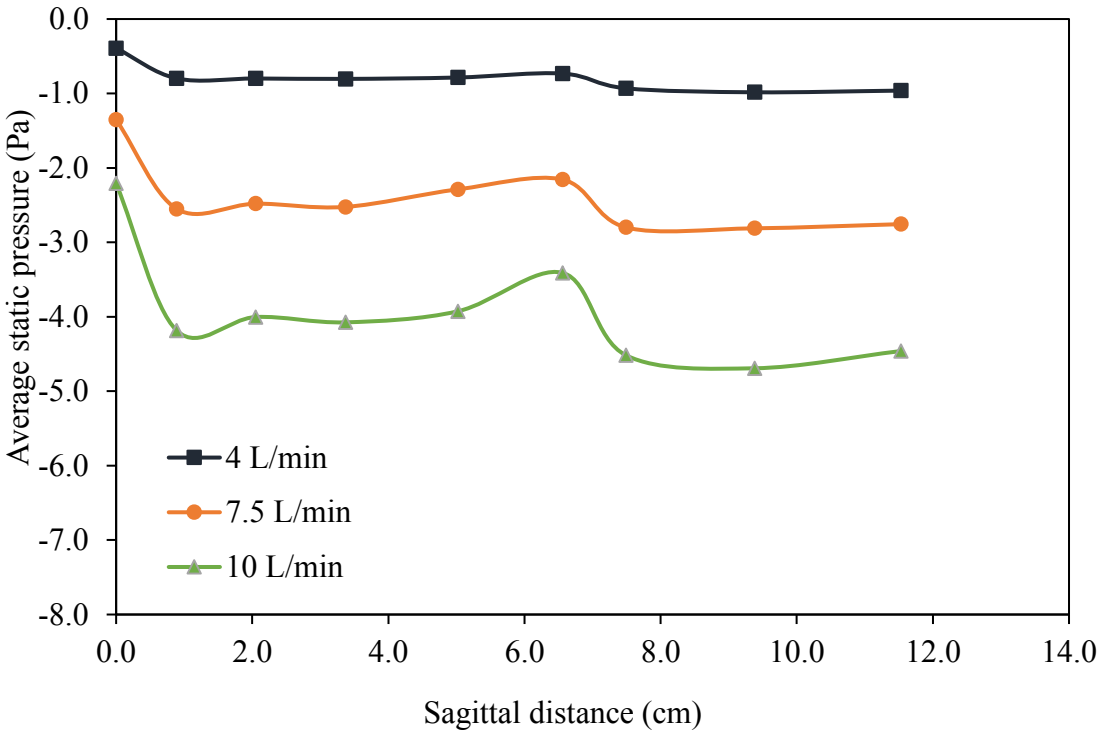

Figure 7.17: Pressure along the post-operative upper airway model for various flow rates.

For the post-operative model, as the flow rate increased, the average static pressure along the pharynx section was also increased. However, there was not much different in pressure increment in the hypopharynx as compared to oropharynx. For inhalation rate of 7.5 L/min, the average static pressure obtained at plane m is -2.80 Pa whereas for 10 L/min, the average static pressure obtained is -4.52 Pa. The pressure drop and airflow resistance were usually used to analyze the effect of airway morphological changes on breathing resistance. Table 7.1 shows the pressure drop and airflow resistance obtained through the upper airway for inhalation rate of 7.5 L/min.

Table 7.1: Pressure drop for flow rate of 7.5 L/min before and after surgery.

	Pressure drop (Pa)	**Airflow resistance (Pa-min/L)**
Pre-Operative (Nasal)	3.19	0.43
Post-Operative (Nasal)	1.84	0.25
Pre-Operative (Pharynx)	38.38	5.12
Post-Operative (Pharynx)	1.44	0.19
Pre-operative (Full upper airway)	43.34	5.78
Post-operative (Full upper airway)	3.27	0.44

As shown in Table 7.1, before surgery the airflow resistance obtained in the nasal cavity is 0.43 Pa-min/L. However, after surgery, the airflow resistance in the nasal cavity decreased about 42 % to 0.25 Pa-min/L. The reduction of the airflow resistance in the nasal cavity affect the pressure distribution in the lower part of the upper airway. As can be observed in Table 7.1, after surgery, the airflow resistance obtained in the pharynx section decreased significantly from 5.12 Pa-min/L to 0.19 Pa-min/L, about 96 % from the preoperative case.

As can be seen in Table 7.1, before surgery, the pressure different obtained between the nostril inlet and pharynx outlet is 43.34 Pa, whereas after surgery, the pressure different decreased to only 3.27 Pa. The total airflow resistance through the upper airway was found reduced about 92 % from 5.78 Pa-min/L to 0.44 Pa-min/L after surgery. This indicate that the nasal surgery has successfully improved the overall breathing quality in upper airway with OSA. During the follow-up visits after the surgery, the patient reports that his main symptom i.e nasal obstruction, has been

greatly reduced. Secondly, the improvement of the breathing quality can be observed by reduction of the breathing resistance for about 92 % after surgery. Obstruction in the nasal passage increased in the airflow resistance in the nasal cavity and affect the total airflow resistance in the upper airway during inspiration. However, the removal of the nasal obstruction has increase the airway passage and smoothen the airflow through the airway resulted in reduction of pressure drop and airflow resistance through the upper airway during inspiration. Figure 7.18 shows the comparison of airflow resistance plots between pre and post-operative cases against inhalation rates of 4, 7.5 and 10 L/min. As can be observed in Figure 7.19, for both cases, the airflow resistance increased as the inhalation rates increase. However, for pre-operative case, the increment for the airflow resistance through the diseased upper airway is steeper as compared to the post-operative case.

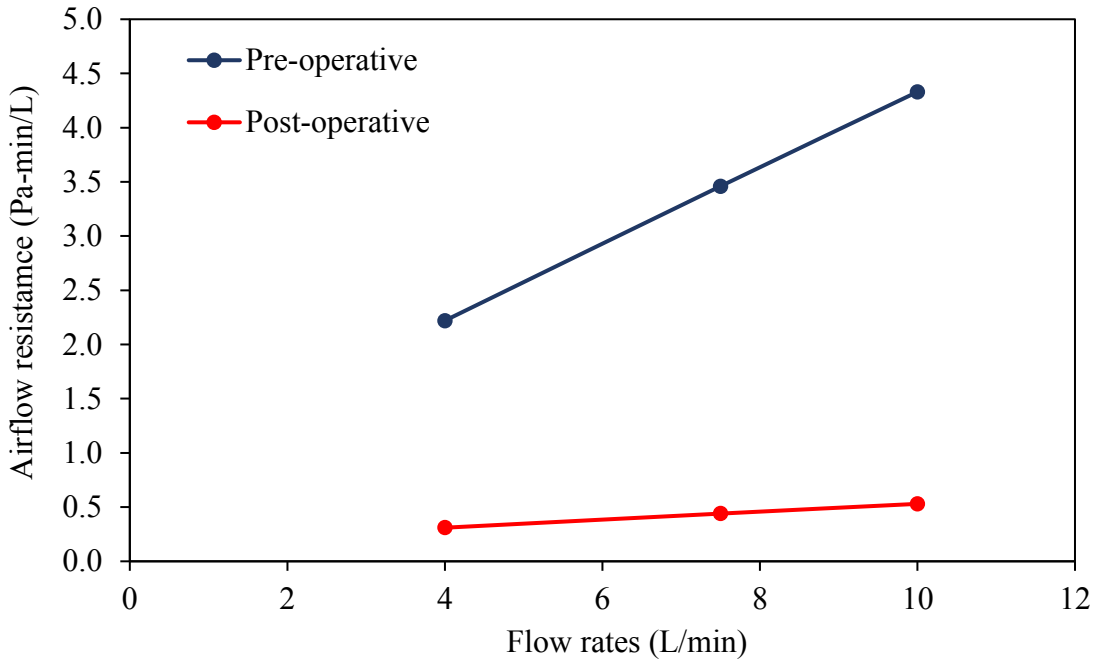

Figure 7.18: Comparison of airflow resistance plot for inhalation rates ranging from 4 to 10 L/min.

7.7 Velocity and Flow Distribution

Figure 7.19 shows the velocity vector obtained through the upper airway for the pre-operative models. As shown in Figure 7.19, the velocity jet was found located at the oropharynx region. The velocity magnitude increased when the flow passes through a smaller cross section area from nasopharynx to oropharynx, at the back of the soft palate. As can be seen in Figure 7.19 (a), low recirculating flow was observed as the flow hit the epiglottis wall. At the end of the velocity jet, as the flow entered larger airway volume in the hypopharynx region, flow separation can be observed at the anterior part of the hyhopharynx region. As can be observed in Figure 7.19 (c), second velocity jet was observed as the flow passes through the glottis region. After that, the flow was directed to the posterior part of the larynx section. The sudden airway expansion caused flow instability in this region. Few vortices were observed located at the anterior part of the larynx section.

Figure 7.20 shows the velocity vector obtained for the post-operative model. As can be seen in Figure 7.20, after surgery, the maximum velocity magnitude obtained in the upper airway decreased from 9.52 m/s to 2.81 m/s. Similar to the pre-operative, two velocity jets were observed at the back of the soft palate and at the glottis region. However, the magnitude of the velocity is lower as compared to the pre-operative case. As can be observed in Figure 7.20 (c), at the larynx region, flow separation and recirculation were observed at both at the anterior and posterior part of the larynx section. The higher magnitude of velocity vectors were not observed at the

posterior part of the larynx section. Instead, the flow was observed directed to the center part of the larynx section.

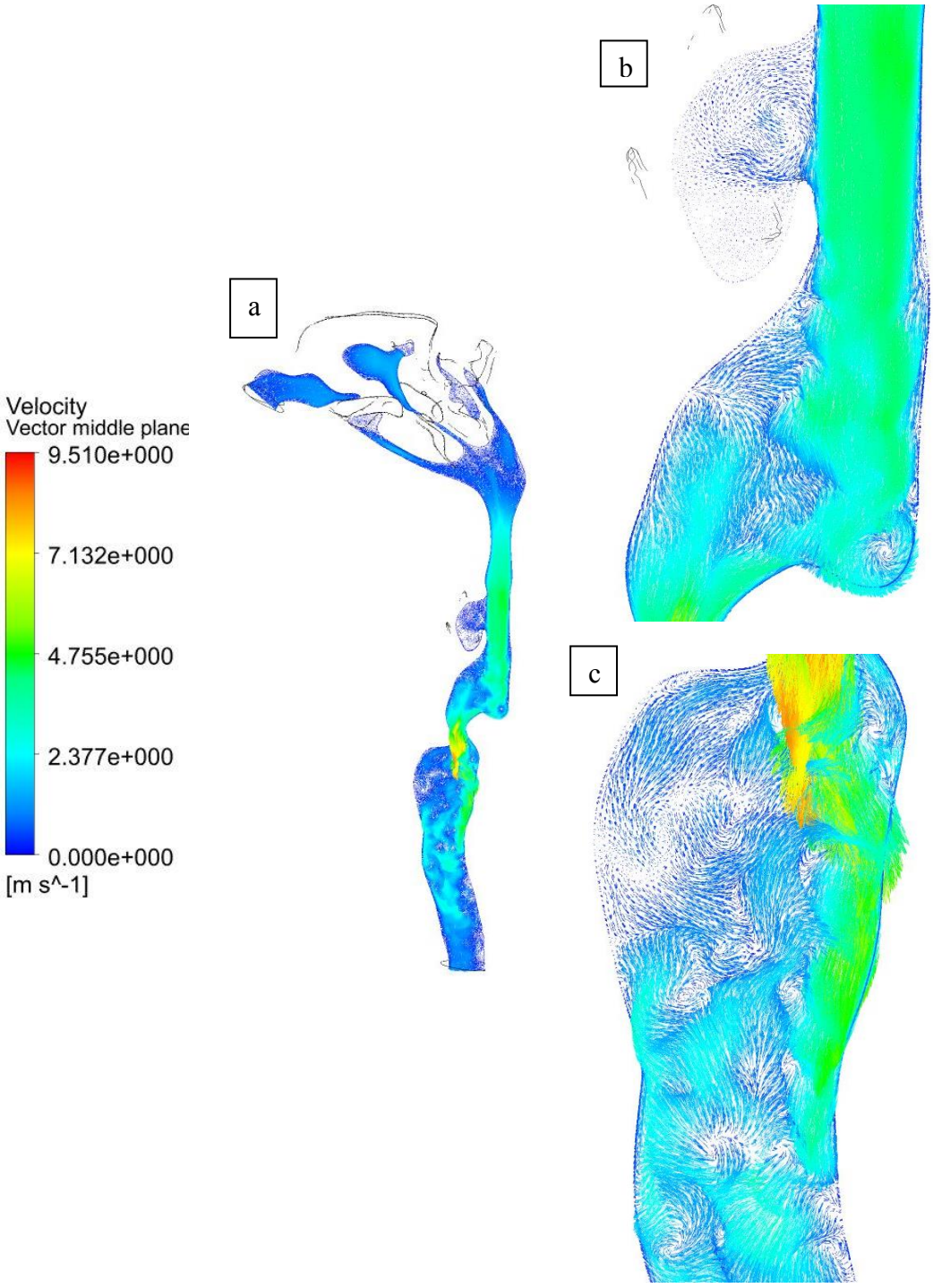

Figure 7.19: Velocity vector for inhalation rate of 10L/min, pre-operative case.

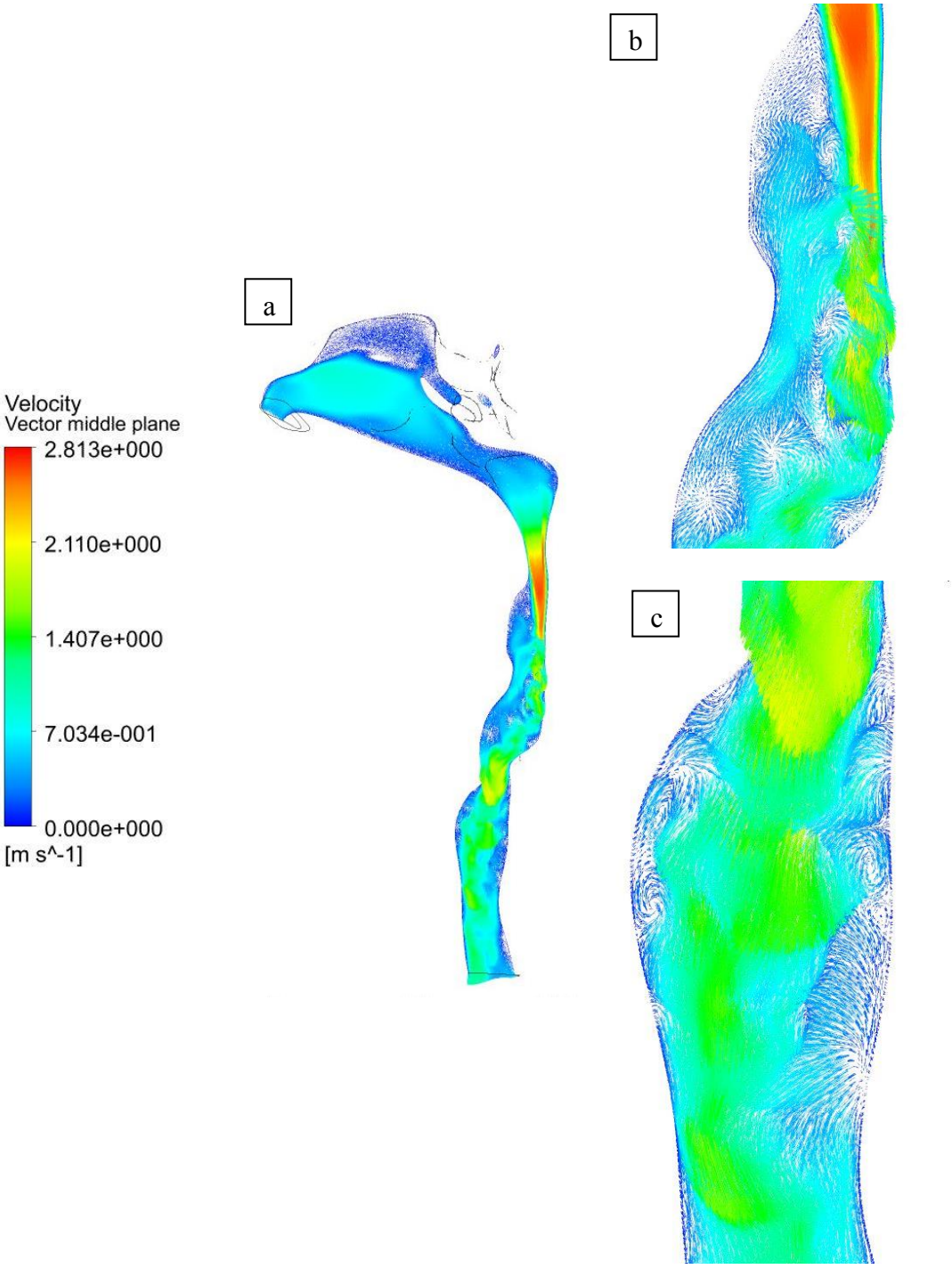

Figure 7.20: Velocity vector for inhalation rate of 10 L/min, post-operative case.

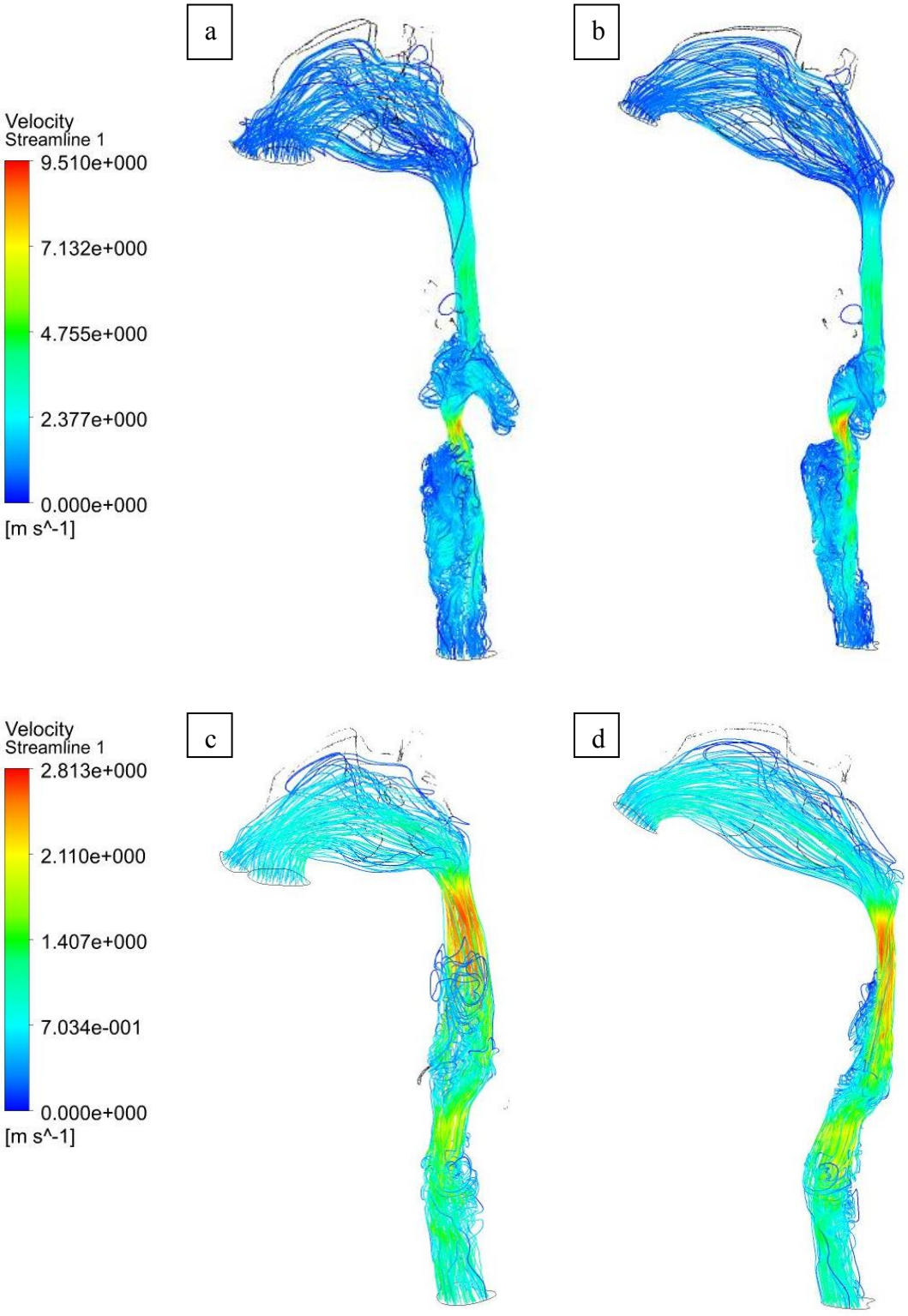

Figure 7.21: Velocity streamlines for inhalation rate of 10 L/min for pre- and post-operative cases.

Figure 7.21 shows the 3D velocity streamline for inhalation rate of 10 L/min for the pre-and post-operative cases. As can be observed in Figure 7.21 the velocity of the inspiratory airflow increased as the flow pass through the oropharynx region.

Figure 7.23 shows the average velocity obtained along the pre-operative upper airway model for various flow rates ranging from 4 to 10 L/min. As can be seen in Figure 7.23, as the inhalation rate increased, the average velocity through the upper airway increased. Figure 7.24 shows the average velocity obtained through the post-operative upper airway for flow rates of 4, 7.5 and 10 L/min. Similarly, as shown in Figure 7.24, the velocity obtained along the upper airway increased as the inspiratory rate increased. In both cases, the average velocity of the inspiratory airflow was observed increased as the flow passes though the smallest cross section area in oropharynx and hypopharynx region. As the inhalation rate increased, the location of the highest velocity obtained in the pharynx section does not changed.

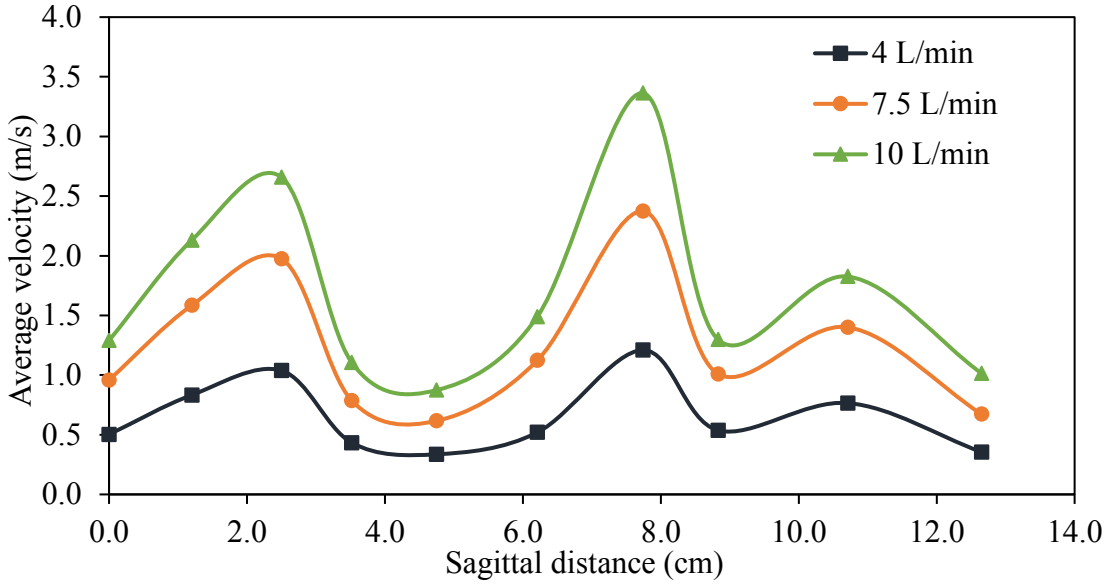

Figure 7.23: Average velocity along pre-operative upper airway for flow rates of 4-10 L/min.

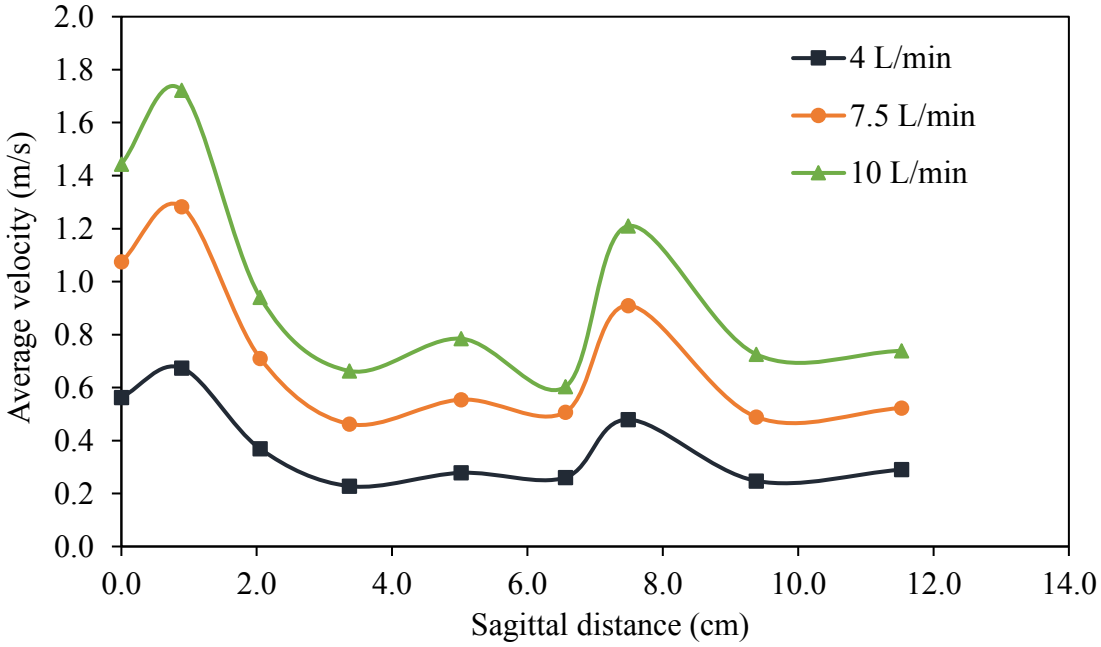

Figure 7.24: Average velocity along post-operative upper airway for flow rates of 4-10 L/min.

7.8 Wall Shear Stress

Figure 7.24 shows the wall shear stress contour obtained on the pre-operative upper airway wall for inhalation rate of 10 L/min.

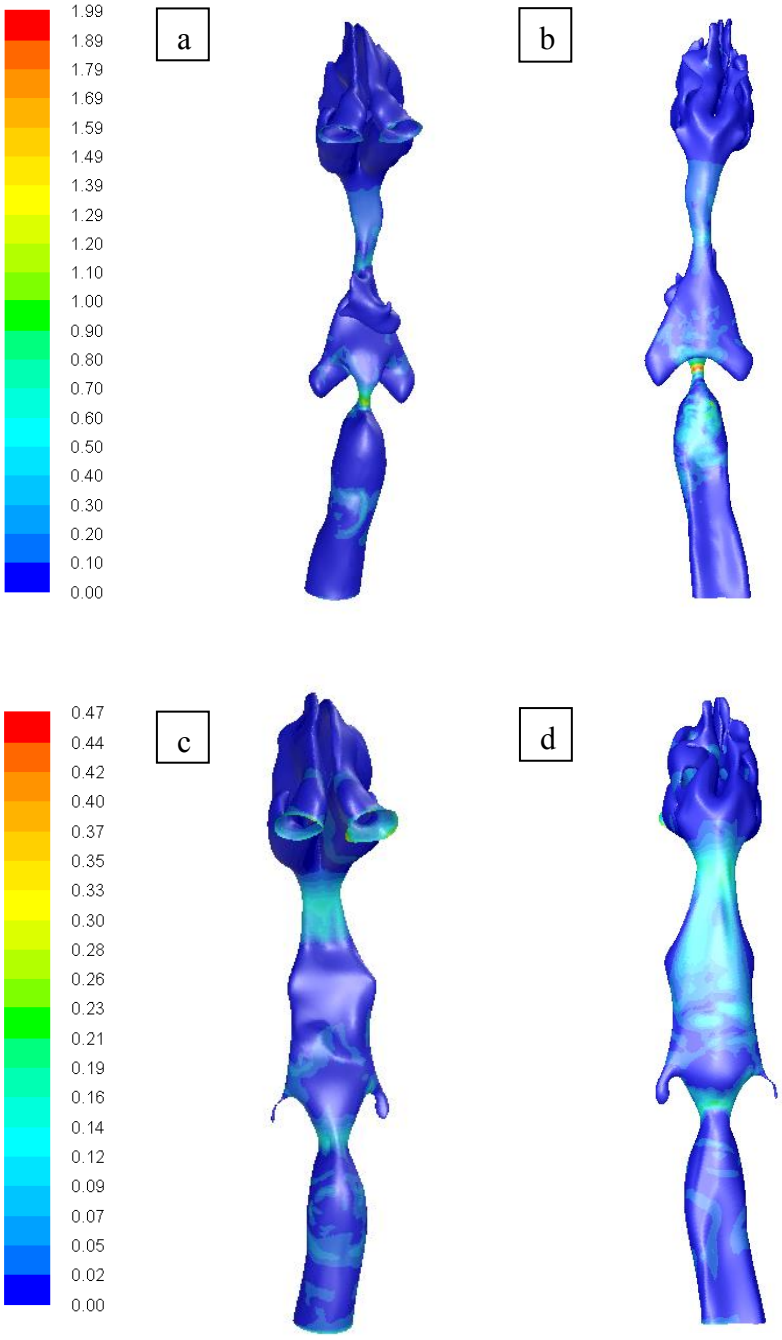

Figure 7.24: Wall shear stress contour on pre-operative upper airway wall for inhalation rate of 10 L/min.

As can be seen in Figure 7.24, for the pre-operative case, the highest wall shear stress was observed at the smallest cross section area at the hypopharynx region near to the glottis. Figure 7.24 shows the wall shear stress contour obtained on the post-operative upper airway model wall for inhalation rate of 10 L/min.

As can be seen in Figure 7.24, the wall shear stress increases as the flow passes through the oropharynx and the glottis section in the hypopharynx region. The highest wall shear stress with 0.47 Pa was found located approximately at the glottis. Figure 7.24 shows comparison between anterior and posterior part of the pharyngeal wall of the upper airway shows that, the posterior wall experience higher wall shear stress during inspiration. Because as the flow passes through the oropharynx, the high velocity airflow was observed directed to the posterior part of the pharyngeal section. Figure 7.25 shows comparison of average wall shear stress obtained for inhalation rate of 10 L/min for pre- and post-operative cases. As can be seen in Figure 6.25, the highest wall shear stress for the pre-operative case was observed located at about 2 cm from the plane (nasopharynx plane) whereas, for the post-operative case, the highest wall shear stress was observed at the nasopharynx plane.

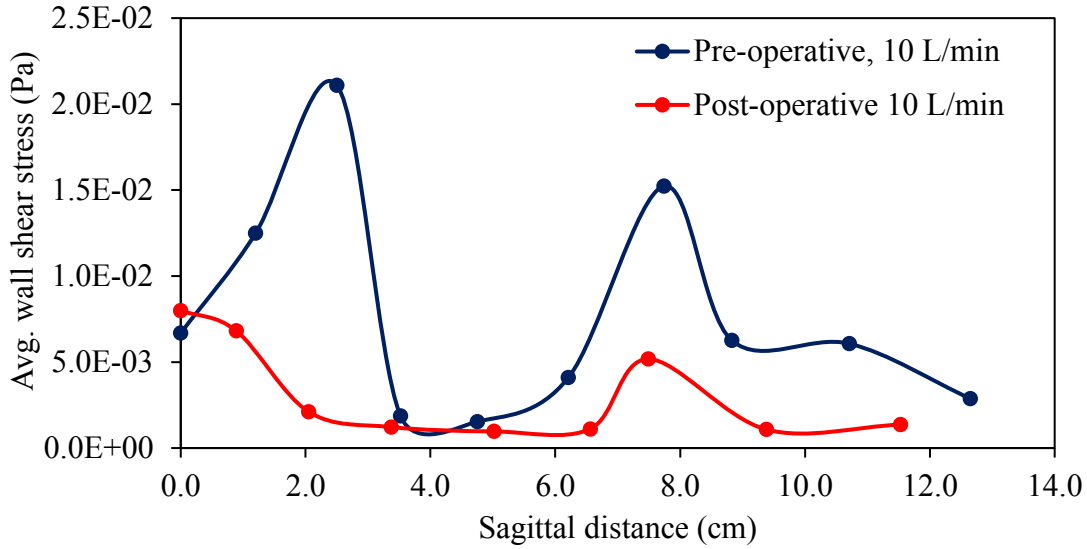

Figure 7.25: Comparison of average wall shear stress obtained for inhalation rate 10 L/min: pre- and post-operative model.

7.9 Particle Deposition

Figure 7.26 shows the developed three-dimensional pre-operative diseased upper airway which was further divided into 8 different regions which include the vestibule, nasal valve, main airway, nasopharynx, oropharynx, hypopharynx, larynx and trachea region. Similarly, Figure 7.27 shows the eight different regions created in the three-dimensional post-operative model. The purpose of dividing the upper airway into several different regions is to investigate the effect of the morphology of the upper airway on the particle deposition fraction during inhalation. Based on the morphology of the upper airway of this patient, it can be observed that the most important area of concern is located in the main airway region where the structural nasal obstruction is found. The obstruction in the main airway contribute to the increase of the total breathing resistance. Furthermore, the obstruction in the main airway region also contribute to the increase of the possibility of the pharyngeal collapse due to the increase of negative pressure in the lower part of the upper airway.

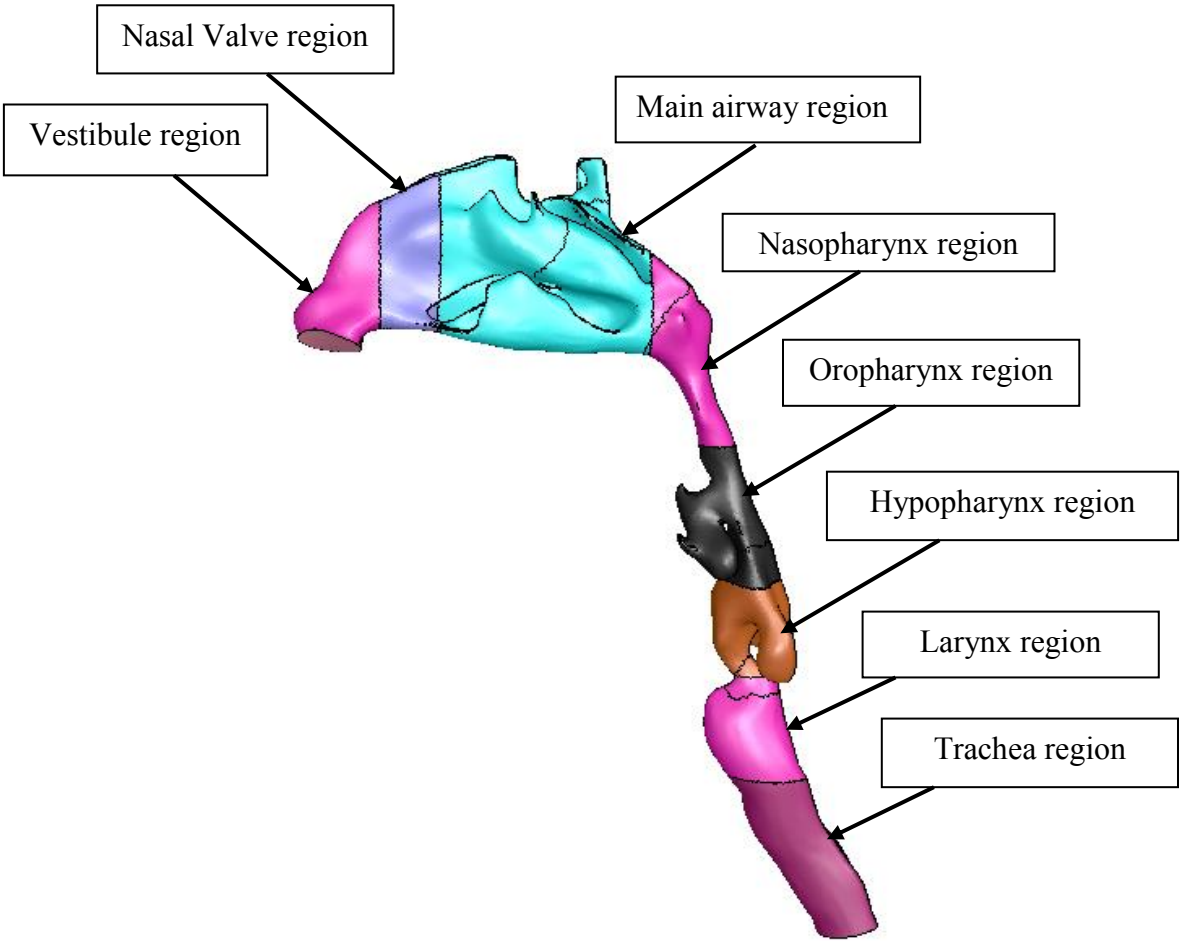

Figure 7.26: The developed 3D pre-operative upper airway model divided by region

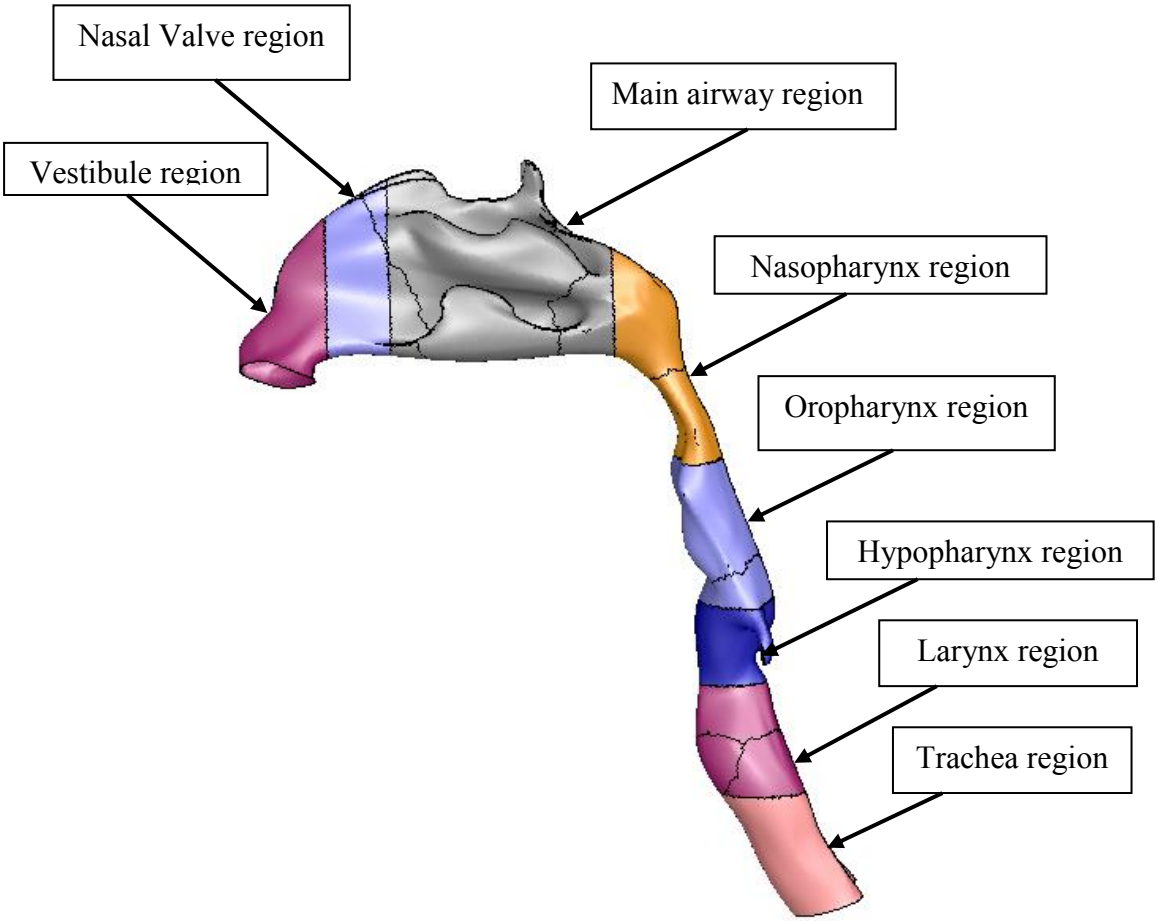

Figure 7.27: The developed 3D post-operative upper airway model divided by region

Figure 7.28 shows upper airway total deposition efficiency plots against the diameter of the inhaled particles. Figure 7.28 also shows the comparison of the total deposition efficiency calculated for inhalation rate of 4, 7.5 and 10 L/min for pre- and post –operative models.

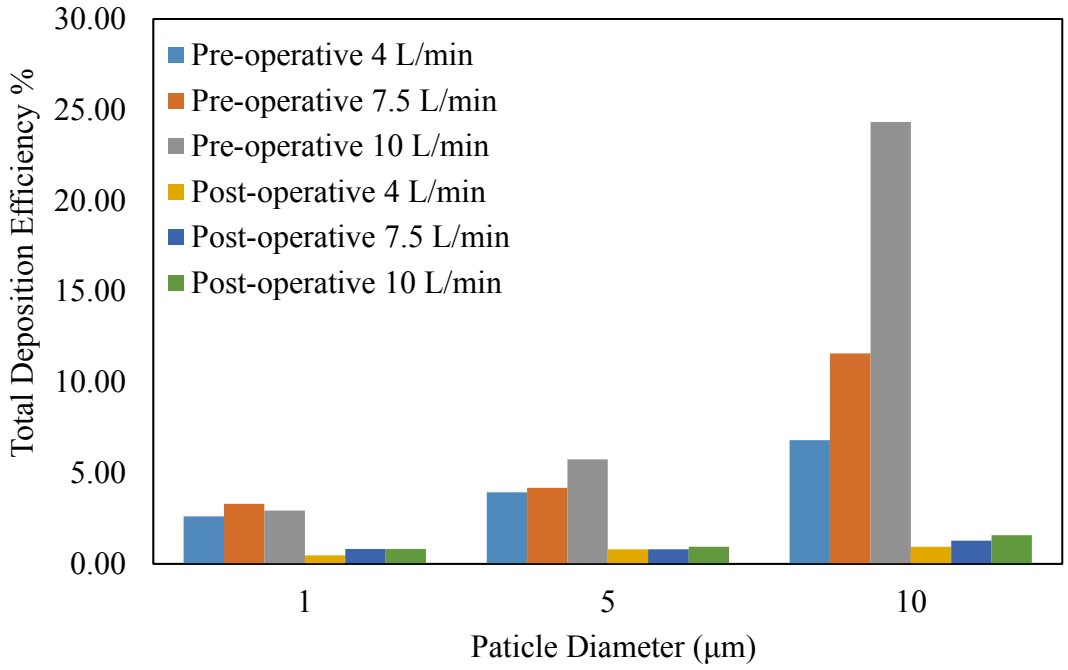

Figure 7.28: Comparison of total deposition efficiency for inhalation rate of 4-10 L/min for pre- and post-operative model.

As depicted in Figure 7.28, for both the pre-and post-operative cases, as the inhalation rate increased, the total deposition efficiency was observed increased. Likewise, for a constant inhalation rate, as the size of the inhaled particle increased, the total deposition efficiency was also observed increased. Hence, we can conclude that, the total deposition efficiency is dependent of the inhalation rate and the size of the inhaled particles. However, as compared to the pre-operative case, for the post-operative case the increased of inhalation rate and particle diameter has a lesser impact on the total particle deposition efficiency. For example, for particle diameter of 5 µm, the total deposition efficiency obtained for inhalation rate of 7.5 L/min was 0.80 %. However, as the inhalation rate increased to 10 L/min, the total deposition efficiency obtained increased for about only 17.5 %. For the post-operative case, as the obstructions in the nasal airway were removed, a lesser number of particles were found

deposited in the upper airway. For inhalation rate of 10 L/min, and particle size of 10 µm, the total deposition efficiency obtained before surgery was about 24.3 % whereas after surgery, the total deposition efficiency reduces to 1.58 %. The total decrease of the total deposition efficiency after surgery is about 93.5 %. This shows that after surgery, as the obstructions in the nasal cavity were removed, more particles can pass through the upper airway. Figure 7.29 shows the deposition fraction for inhalation rate of 10 L/min with inhaled particle diameter ranging from 1-10 µm for the pre-operative model, whereas Figure 7.30 shows for the post-operative model.

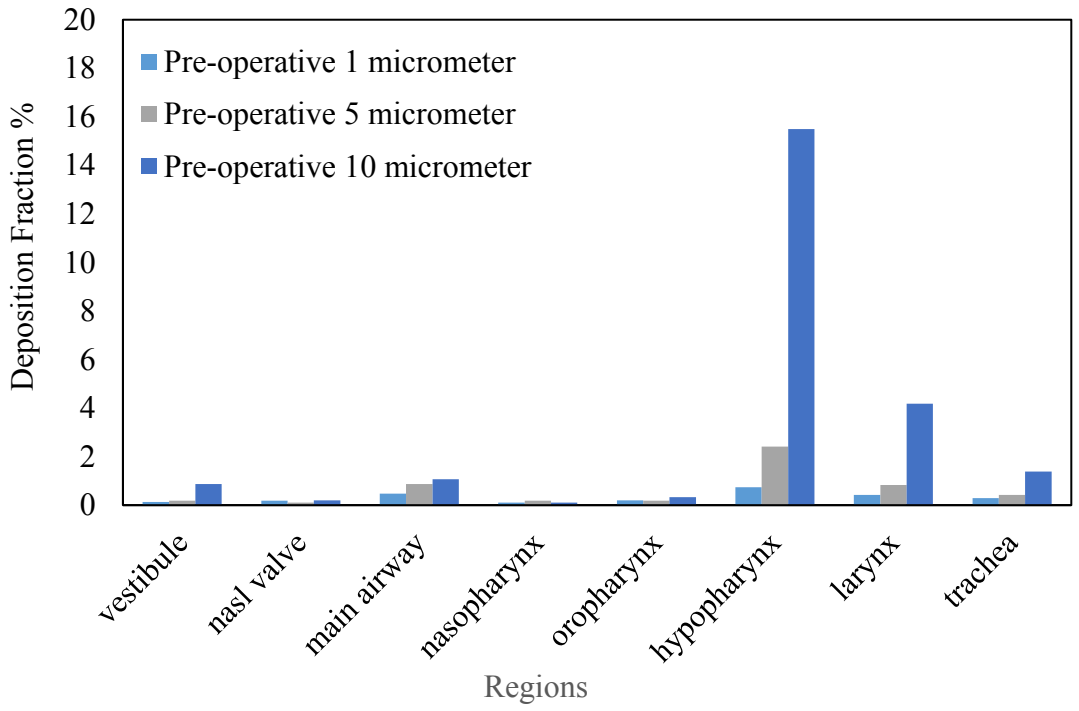

Figure 7.29: Particle deposition fraction for inhalation rate of 10 L/min for pre-operation model.

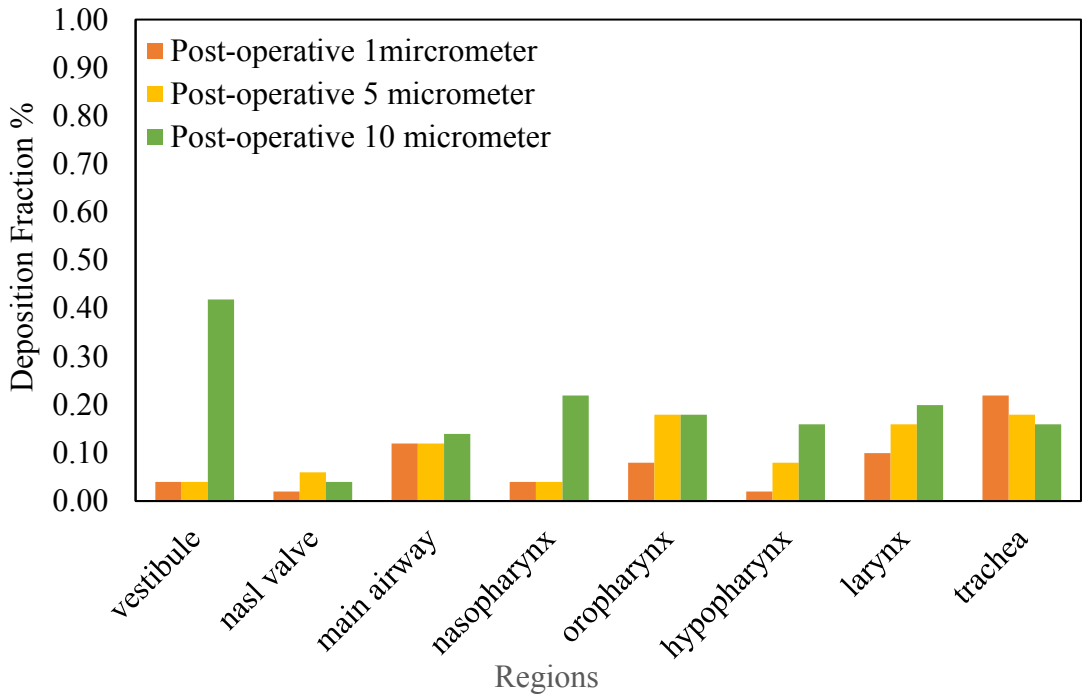

Figure 7.30: Particle deposition fraction for inhalation rate of 10 L/min for the post-operative model.

As can be seen in Figure 7.29, for the pre-operative model, for all particle sizes, the local particle deposition hot spot with approximately 15.5 % of filtering efficiency was found at the hypopharynx region. The recirculating flow observed in the hypopharynx region could contribute to the increased of the particle filtering efficiency as the flow can trap more particles in this region. On the other hand, in the post-operative model, the local particle deposition hot spot changed as the for different particle size. For particle size of 10 µm, due to a higher inertia, the local deposition hot spot with 0.42 % deposition efficiency was found in the vestibule region. For particle size of 5 µm, the deposition hot spot area was found in oropharynx. However, as the particle size decrease 1 µm, local hot spot area was found in trachea region with 0.22 % of deposition efficiency. Even though the total particle deposition efficiency

was found reduced after surgery, Figure 7.30 shows that, after surgery, the vestibule plays a significant role in filtering out larger size particles.

7.9 Conclusions

The surgical procedure has cleared out the obstructions in the nasal airway hence improve the airflow distribution through the upper airway during inhalation process. This study shows that the nasal surgery alone can help improve the breathing quality in the upper airway with OSA. The reduction of the airflow resistance in the nasal cavity affect the pressure distribution in the lower part of the upper airway. The combination of the decrease of the airflow resistance and decrease of the magnitude of the negative pressure found in the pharynx region contribute to the improvement of the breathing quality for the OSA patient and reduce the risk of pharyngeal collapse during inspiration. The total particle deposition efficiency was found affected by the inhalation rate and the inhaled particle diameter. The total deposition efficiency increased as the inhalation rate and particle size increased. The total particle deposition efficiency and particle deposition fraction in regions were found affected by the morphology of the upper airway. Obstruction in the nasal airway increased number of deposited particle in the airway. Sudden airway expansion in the hypopharynx region which caused flow recirculation also increased number of particles trap, recirculated by finally deposited in the airway. For the post-operative case, as the morphology of the upper airway changed after surgery, the local particle deposition hot spot was found located in different region as compared to the pre-operative case.

CHAPTER 8

EXPERIMENTAL INVESTIGATION

8.1 Introduction

This chapter presents the process of developing the experiment test rig and the pharynx experimental model for both pre and post-operative cases. The main aim of this study was to analyze and validate the solutions obtained from numerical simulation with that of experimental results.

8.2 Development of 3D Model

The pharynx experimental model was developed by modifying the upper airway computational model developed for the numerical simulation study. The reconstruction of the three-dimensional realistic anatomical model of the human upper airway from CT scan images is already presented in Chapter 3. For the pharynx experimental model, initially, the upper airway model was modified in CATIA by excluding the nasal cavity part from the upper airway model. The exclusion of the nasal cavity part was done considering the complicated and narrowed diseased nasal airway geometry which is not possible to fabricate furthermore it will make flow measurement and visualization through the full upper airway model difficult. Figure 8.1 (a) and 8.2 (a) show the pharynx part of the diseased upper airway for the pre-operative and post-operative cases respectively. After that, two connectors were constructed at the inlet and the outlet of the pharynx model.

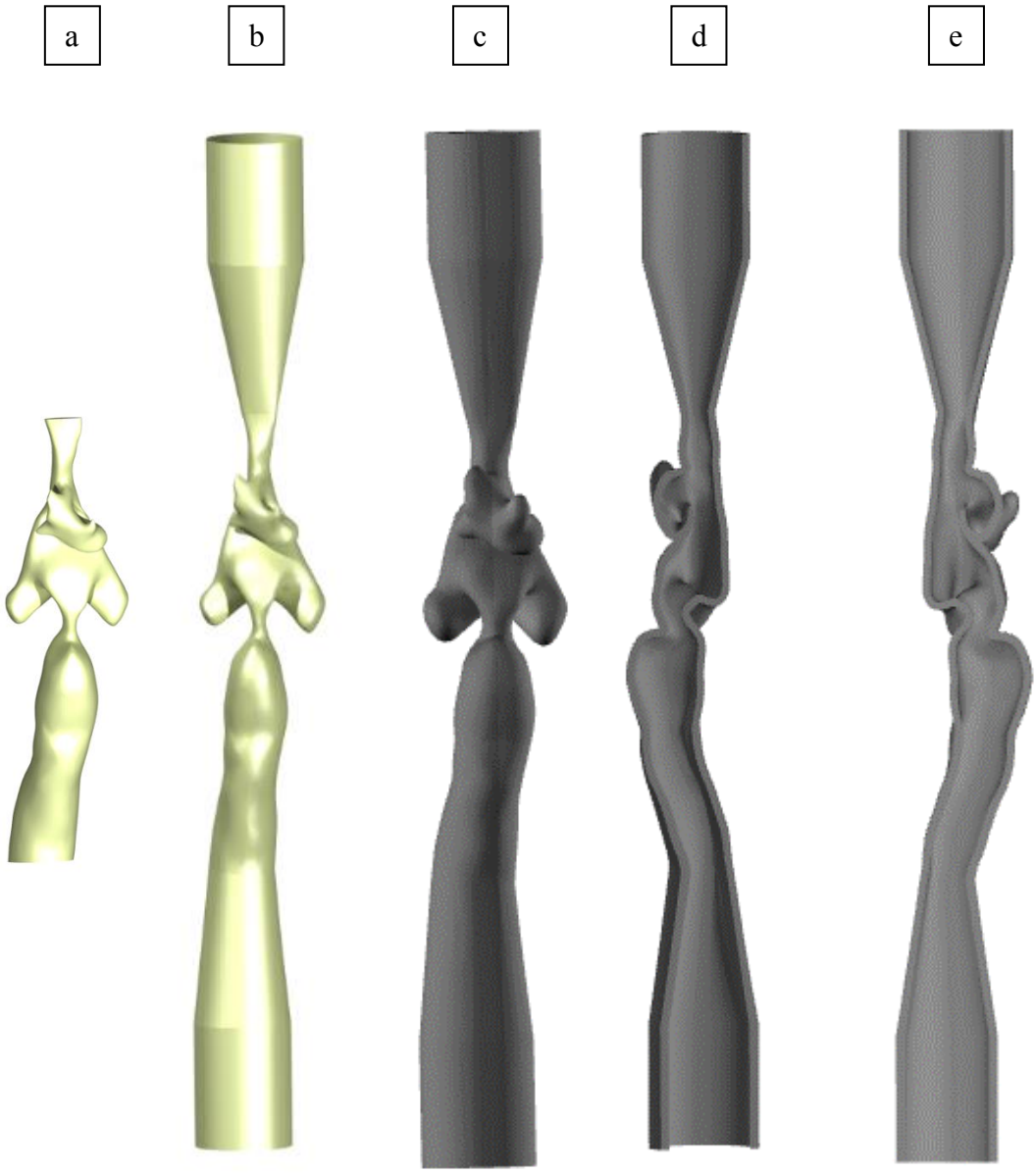

Figure 8.1: Pharynx experimental model for the pre-operative case: (a) pharynx, (b) pharynx with connector, (c) extruded 2.5 mm thickness, (d) right part, (e) left part.

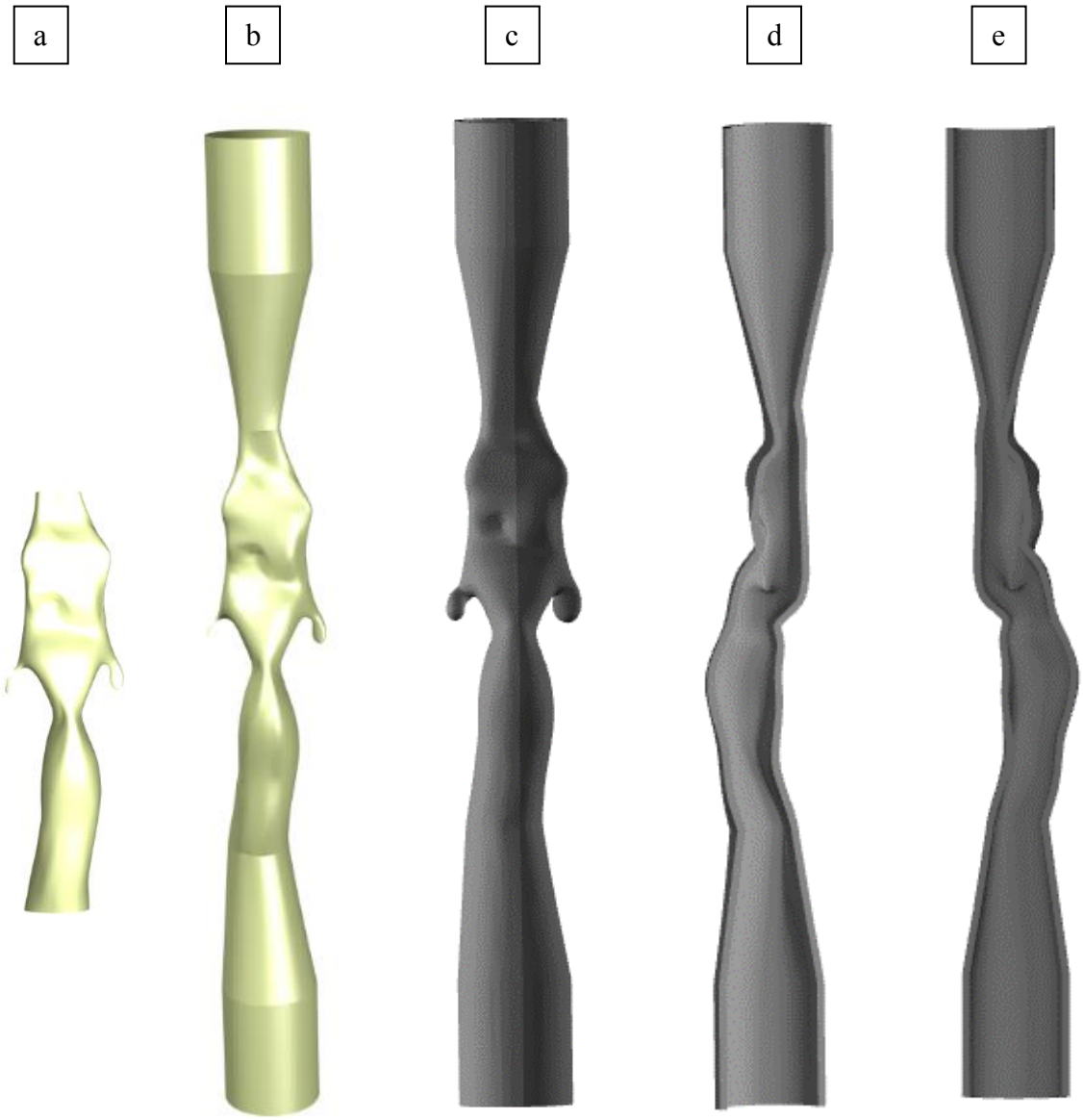

Figure 8.2: Pharynx experimental model for the post-operative case: (a) pharynx, (b) pharynx with connector, (c) extruded 2.5 mm thickness, (d) right part, (e) left part.

As shown in Figure 8.1 (b) and 8.2 (b) **t**he modification of the upper airway models was made using a CAD software named CATIA. The pharynx model was modified to include connector at the inlet and the outlet part of the geometry. This modification was considered necessary to facilitate pipe connection without affecting the pharynx geometry. After that the .stl files generated in CATIA were then imported

into another 3D modelling software named Materialise 3-matic. In this software, the upper airway wall was extruded to give a minimum thickness of 2.5 mm for the model fabrication purpose. As shown in Figure 8.1 (c) and 8.2 (c), the outer surface of the pharynx models was extruded with 2.5 mm thickness specification. After that, the pharynx models were separated into two parts as depicted in Figure 8.1 (d) and (e) for the pre-operative case and Figure 8.2 (d) and (e) for the post-operative case. Finally the extruded wall surface was smoothen in the 3-matic software to improve the surface quality and roughness before fabrication process.

8.3 Model Fabrication

Several number of researchers have used several techniques to fabricate the human nasal cavity model (Chun et al., 2006; Doorly *et al*., 2008; Hahn *et al*., 1993; Hopkins *et al*., 2000; Zubair *et al*., 2015). Hahn *et al*., (1993) developed an enlarged 20X scale of the human nasal cavity model. Hopkins *et al*., (2000) and Doorly *et al*., (2008) used 2X scale of human nasal cavity model produced by using the three dimensional printer named Zprinter 310 from the Z Corporation. Mylavarapu *et al*., (2009) constructed 2X scale of the human airway model. They used Stereolithography process and selected a SLA resin named Somos Watershed 11,110 material to fabricate the airway. In the present work, the pharynx experimental model was fabricated by using the Stereolithography process. Stereolithography is a laser-based technology that uses a UV-sensitive liquid resin. A UV laser beam scans the surface of the resin and selectively hardens the material corresponding to a cross section of the product, building the 3D part from the bottom to the top. The required supports for overhangs and cavities are automatically generated, and later manually removed. Finally, the

surface of the model is then finished and cleaned. Figure 8.5 shows the steps involved in fabricating the pharynx models by using the Stereolithography technology.

(a) The 3D model

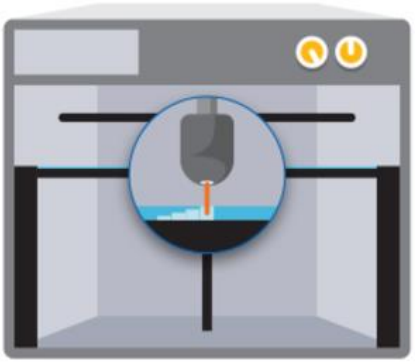

(b) A laser hardens UV curable liquid

(c) The platform cotaining liquid

(d) The liquid is vanished away and the support is removed

(e) The part is finished

Figure 8.3: Stereolithography method.

Before we can start to fabricate the pharynx models, we need to select a good and high-quality material which can produce a high quality transparency product. In this study, as shown in Figure 8.4, a Stereolithography resin named TuskXC2700T was used to fabricate the developed pharynx experimental models. Tusk XC2700T was selected to fabricate the 3D pharynx model because it can produce strong, tough, water-resistant parts with good transparency quality.

Figure 8.4: Material selection, TuskXC2700T.

Table 8.1 shows the mechanical properties of the selected material to fabricate the pharynx experimental model. Table 8.2 shows the surface finishing degrees can be applied on the printed parts. After the printing process, the auto-generated support will be manually removed from the printed part. Then, a surface finishing process was performed. The surface finishing process include support removal, curing, sandblasting, smoothing, primer and coating.

Table 8.1: TuskXC2700T material properties datasheet.

	Units	ASTM#	Range
Density	g/cm^3		1.18 – 1.2
Tensile Strength	MPa	D638M	47.1 – 53.6
Tensile Modulus	MPa	D638M	2650 – 2880
Elongation at break	%	D638M	11 – 20
Flexural Strength	MPa	D790M	63.1 – 74.16
Flexural Modulus	MPa	D790M	2040 – 2370
Notched Izod Impact	J/m	D256A	20 – 30
Hardness	Shore D	D2240	81
Heat Deflection Temp	^0C	D648-98c	At 0.46 MPa: 45.9 – 54.5 At 1.81 MPa: 49.0 – 49.7

Table 8.2: Finishing degrees for Stereolithography parts.

Finishing	Support removal	Curing	Sandblasting	Smoothing	Primer	Coating
Basic	✓	✓				
Cosmetic transparent	✓	✓	✓	✓	✓	✓

Figure 8.5 shows the example of the surface finishing degrees done on the SLA parts. As can be seen in Figure 8.5 (a) with a basic surface finishing degree, the building layers can still be observed on the surface even after the curing process. Figure

8.5 (b) shows the SLA part with cosmetic transparent on both inside and outside surfaces. For the cosmetic transparent finishing degree, sandblasting, surface smoothing, primer and transparent coating will be applied onto the inner and outer surface of the printed SLA part.

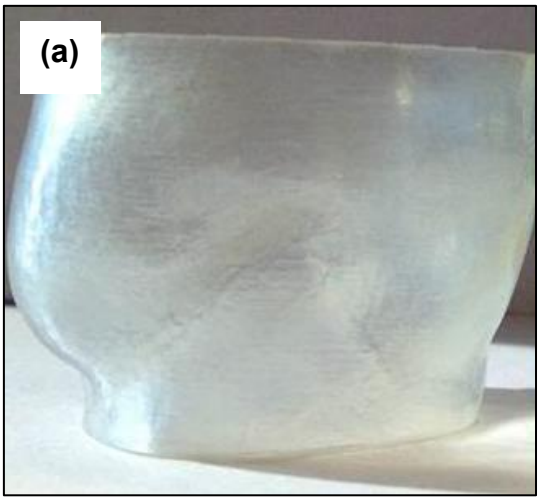

- SLA basic finishing

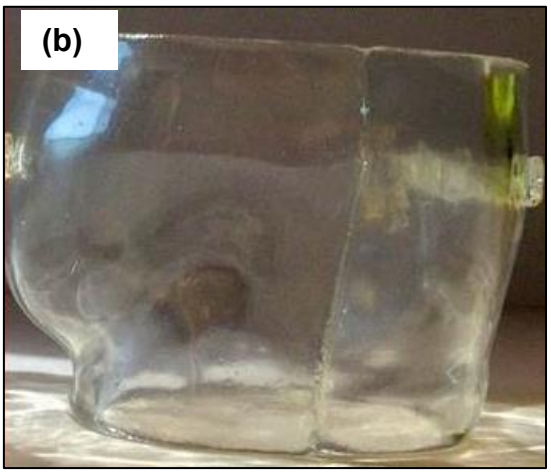

- SLA
- Cosmetic transparent outside
- Cosmetic transparent inside

Figure 8.5: Examples of the printed part with (a) basic and (b) cosmetic transparent surface finishing.

Figure 8.6 shows the transparent pharynx experimental model fabricated by using the Stereolithography machine with cosmetic transparent finishing degree. The

surface quality of the fabricated pharynx experimental models were improved by utilizing the cosmetic transparent surface finishing degree on the inner and outer surface of the printed model. Initially the support material generated during the printing process was removed. After that the model was cured by exposing the model surface under UV light to harden the surface. Next, the model surface was sandblasted and sandpapered to smoothen the model surface. During the smoothing process, the building layer observed on the printed surface was removed. After that, in order to improve the surface adhesion, primer was applied on the inner and outer surface of the pharynx experimental model prior to cosmetic transparent painting. Then, a transparent paint was applied on the inner and outer surface of the printer part to improve the transparency quality of the pharynx experimental model. As can be observed in Figure 8.6 (a) and (b), after the surface finishing process, both models show a very good transparency quality. The fabricated pharynx experimental model has uniform wall thickness of 2.5 mm.

Figure 8.6: The transparent pharynx model produced from the Stereolithography machine: (a) pre-operative model and (b) post-operative model.

8.4 Experimental Setup

Figure 8.7 shows the experimental test setup developed in the Propulsion Laboratory, Universiti Putra Malaysia. As can be seen in Figure 8.7, the air pressure can be controlled by using the control valve and air flow was driven by the air compressor. The flow will pass through the experimental model and exit to the atmosphere. The air compressor has capacity to pump to a maximum pressure of about 138 kPa.

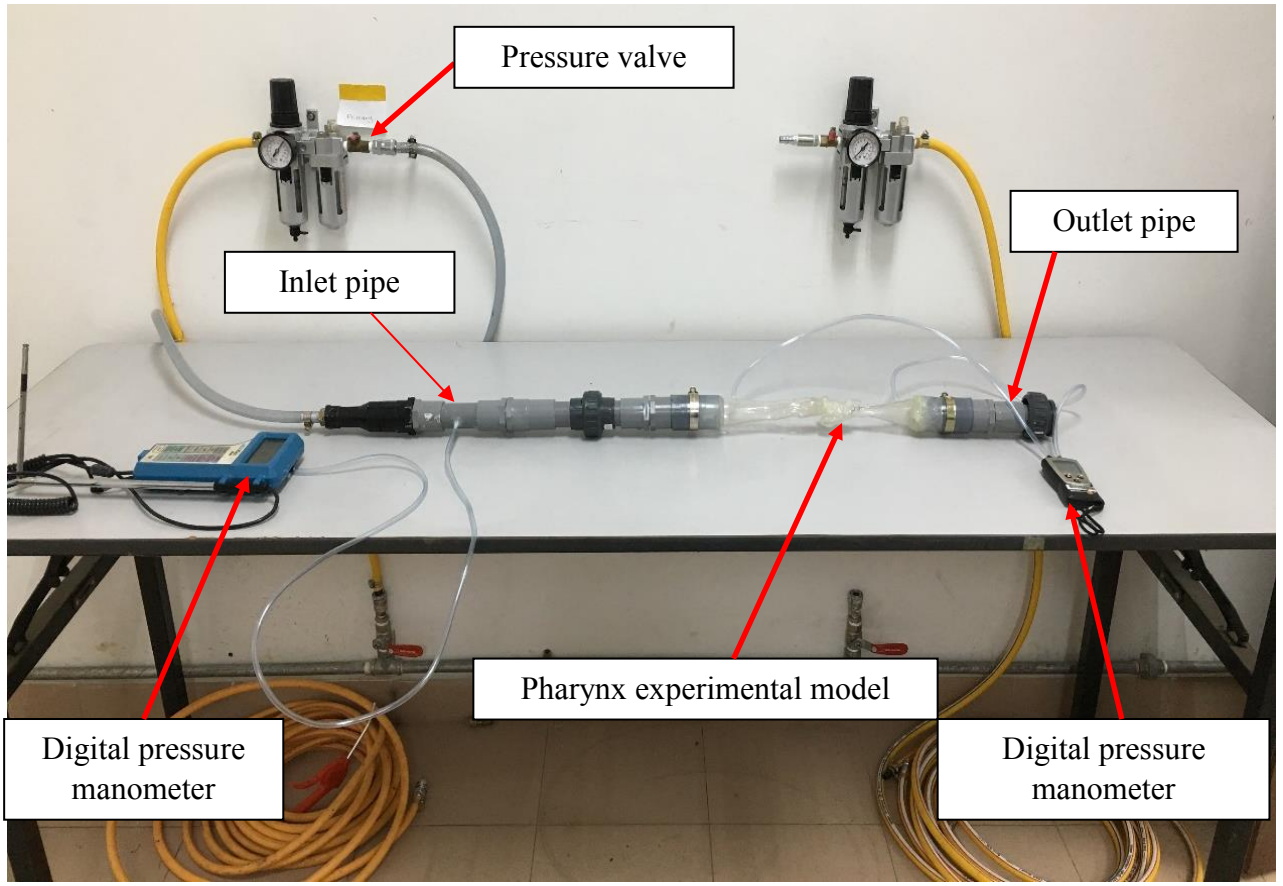

Figure 8.7: Flow measurement apparatus.

Two pressure taps were included on each of the pharynx experimental models for the purpose of pressure measurement. Another one pressure tap was located at the pipe located at the beginning to the test model to measure the pressure inlet. The location of the pressure taps used for measuring pressure drop across the pharynx experimental model is as shown in Figure 8.8.

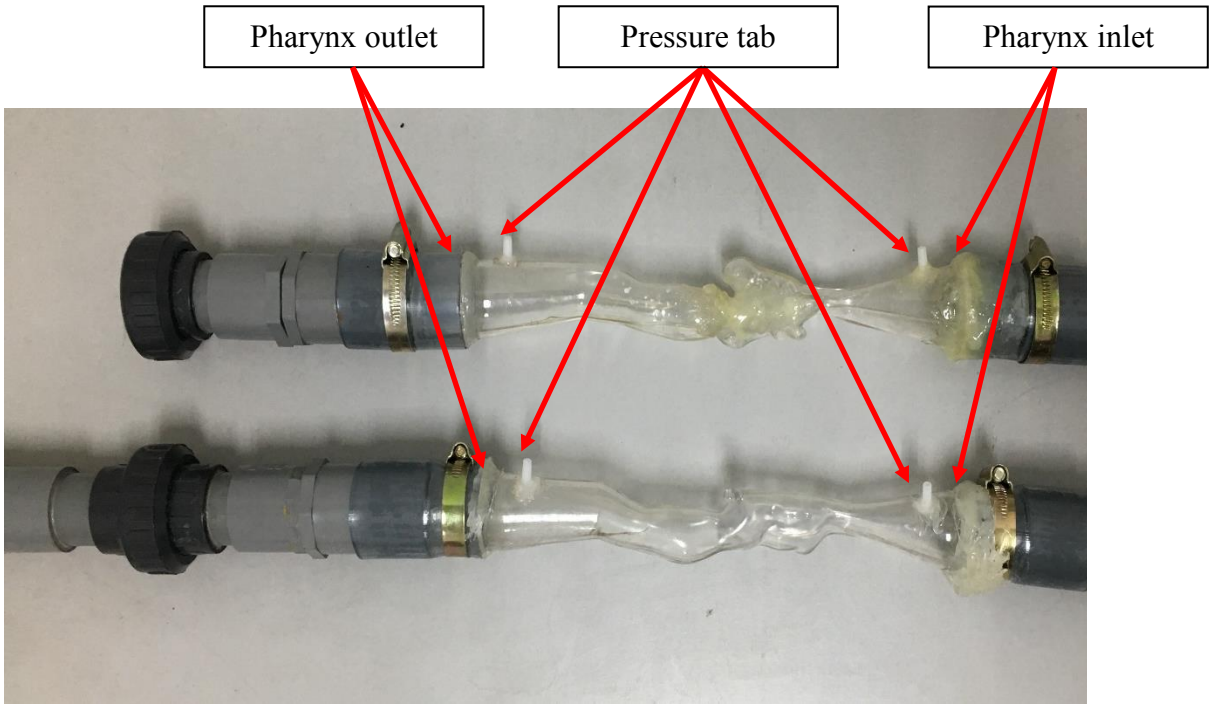

Figure 8.8: The location of the pressure taps on the pharynx experimental models.

The pressure taps located at the inlet and outlet were connected to a digital manometer which reads pressure in Pascal, Pa. The pressure tap and the pressure manometer were connected by using plastic tubes. The compressor drives the airflow from the pharynx outlet to the pharynx inlet which represents expiratory airflow. Pressure drop were obtained for various exhalation rates and plotted against the pressure inlet. The pressure drop values obtained from the experimental work were

compared with the pressure drop obtained from the numerical simulation of expiratory airflow through the same model to validate the numerical results obtained from this research study.

8.5 Experimental Error Analysis

The experimental error analysis was performed to improve the accuracy of the measured data. As reported by Taylor, 1997, error analysis can be defined as the study of uncertainties in physical measurements (i.e. experimental error). Hence, experimental error is the difference between two or more measured values. Mean and standard deviation as proposed by Taylor, 1997 will be used in this study to calculate the experimental error. Several number of measurements will be obtained to calculate the mean and standard deviation value. Mean value describes the central value of the measures, while the standard deviation describes the spread or deviation of the measured values about the mean. The mean of x is represented by and it is calculated by the following formula from a set of N measured values for some quantity x:

$$x_{best} = \bar{x} \tag{8.10}$$

Where

$$\bar{x} = \frac{x_1 + x_2 + x_3 + \cdots . + x_N}{N} = \frac{\sum x_i}{N} \tag{8.11}$$

The standard deviation, σ_x and can be written as:

$$\sigma_x = \sqrt{\frac{\sum_{x_i}(|x_i - \bar{x}|)^2}{N-1}} \tag{8.12}$$

where, $x_i$is the value obtained in the i-th measurement. According to the theory of probability, if N measurements of a quantity x is made, there is a probability that68% of the measurements will fall within the range$\bar{x} \pm \sigma_{x\ldots}$

8.6 Experimental Results

Figure 8.9 shows the pressure drop obtained for a range of pressure inlet of 10 to 150 Pa for the pre-operative pharynx model. As can be seen in Figure 8.9, as the pressure inlet increased, the pressure drop also was observed increased. The pressure drop obtained for the pressure inlet of 10 Pa was approximately 12 Pa. At a higher pressure inlet of 100 Pa the pressure drop obtained was around 110 Pa. Figure 8.10 shows the pressure drop obtained through the post-operative pharynx model. Similar to the pre-operative case, the pressure drop through the post-operative pharynx model was observed increased ad the pressure inlet increased. However, for the same pressure inlet of 10 Pa, the pressure drop obtained through the post-operative pharynx model was found does not changed as compared to the pre-operative case. However, as the pressure inlet increased, the pressure drop obtained for the post-operative case was observed increased about 3 %. For pressure inlet of 100 Pa, the pressure drop obtained for the post-operative case is 113 Pa, and pre-operative case 110 Pa.

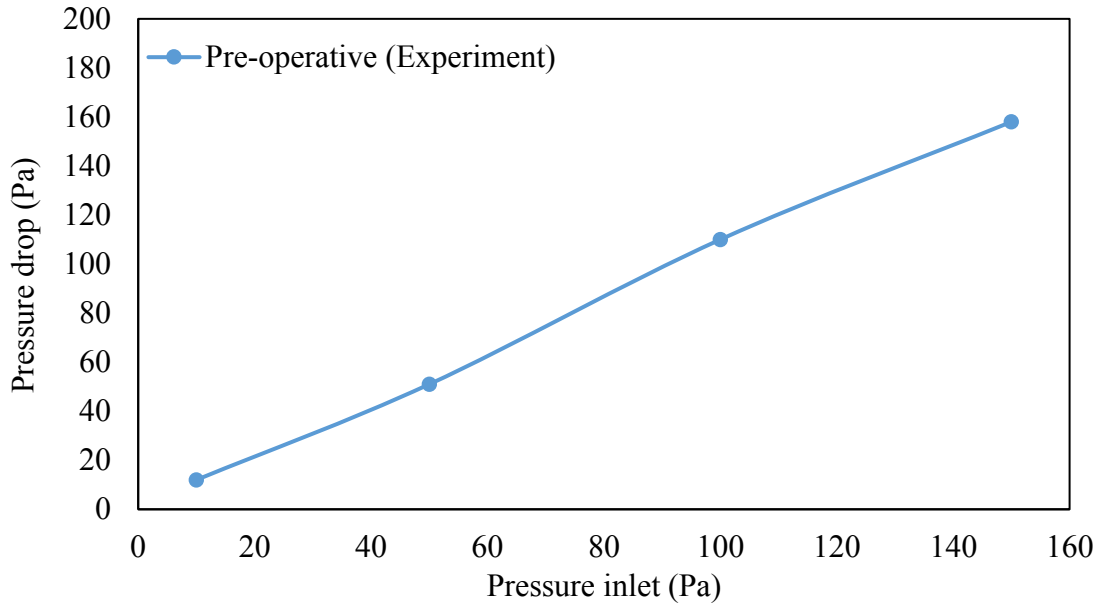

Figure 8.9: Pressure drop for pre-operative pharynx model.

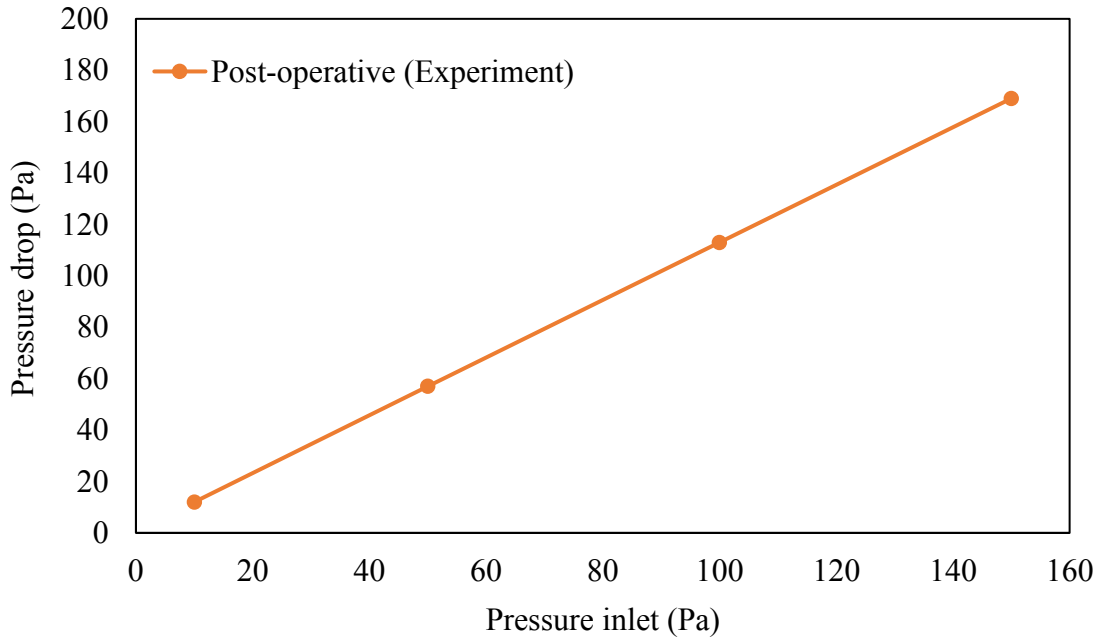

Figure 8.10: Pressure drop graph for post-operative pharynx model.

Table 8.3 shows the experimental error measurement calculated for the different pressure drop values obtained for both pre- and post-operative pharynx experimental model. As can be seen in Table 8.3, the maximum calculated standard deviation is approximately 6.5 which is significantly small. Hence the results obtained can be deem reliable.

Table 8.3: Experimental error measurement for different pressure drop values.

	Pressure drop (Pa)	Standard Deviation
Pre-operative case	12	0.6
	51	0.4
	110	4.8
	158	6.5
Post-operative case	12	0.6
	57	1.3
	113	3.9
	168	4.6

8.7 Comparison of Experimental and Numerical Investigations

Numerical simulation of expiratory flow were carried out using the pharynx experimental model developed for both pre- and post-operative cases. Air was defined as the fluid properties used in the simulation. Pressure drop values obtained from the numerical study were compared with that of the experimental results. Figure 8.11 shows the comparative study of pressure drop plot for numerical and experimental investigation for the pre-operative model, whereas, Figure 8.12 shows for the post-operative model. As shown in Figure 8.11 and 8.12, the pressure drop obtained from the numerical study follow the same pattern and match closely with the pressure drop obtained from the experimental study. As can be seen in Figure 8.11, for the pre-operative model, the pressure drop obtained for pressure inlet of 10 Pa was 12 Pa from experiment and 10.1 Pa from simulation. For a higher pressure inlet of 150 Pa, the pressure drop obtained from the experimental study was approximately 158 Pa and 153 Pa from the numerical simulation study. The variation between the pressure drop obtained from the numerical study and experimental study is significantly small at approximately 3.3 %. For the post-operative case, as can be observed in Figure 8.12, the pressure drop calculated for pressure inlet of 10 Pa was 12 Pa for experiment and 10.5 Pa for simulation. For a higher pressure inlet of 150 Pa, the pressure drop obtained from the experimental analysis was 169 Pa whereas 166.9 Pa from numerical analysis. The variation between results obtained from the experiment investigation and numerical study of post-operative pharynx model is significantly small at approximately 1.2 %.

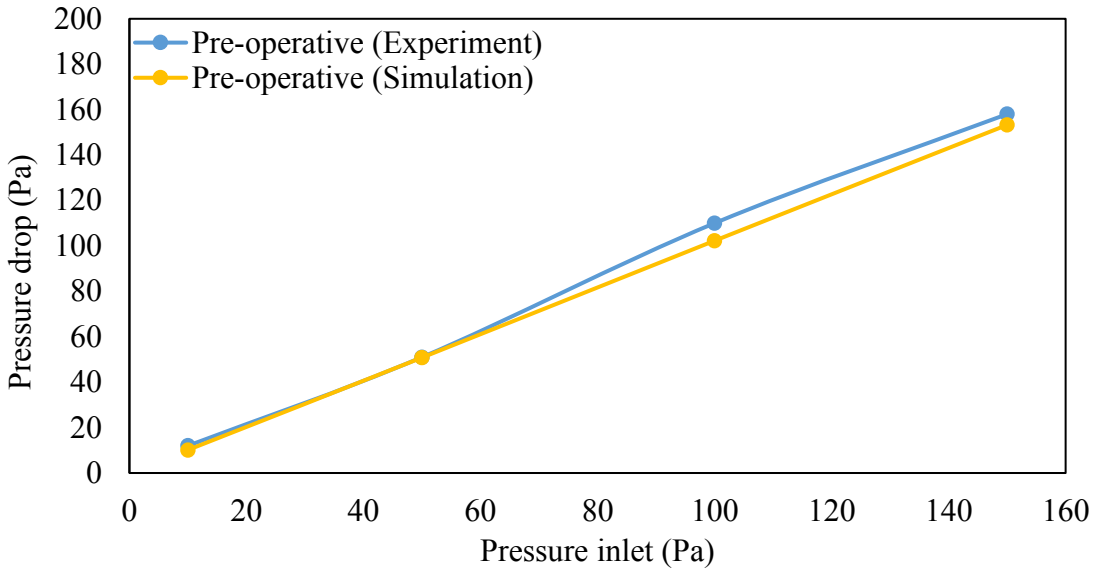

Figure 8.11: Comparative study of pressure drop plot for numerical and experimental investigation for pre-operative model.

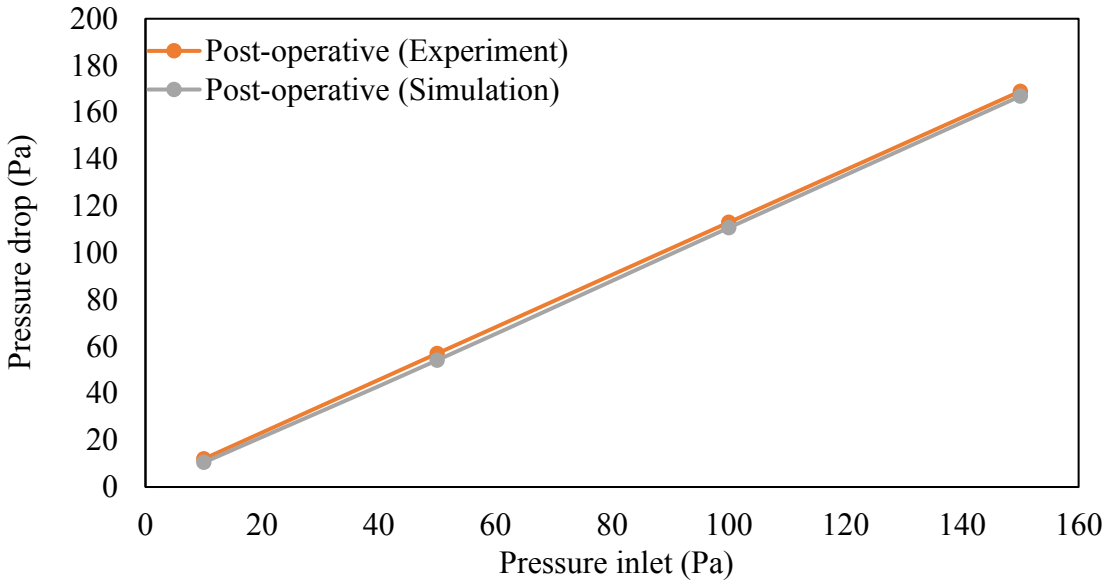

Figure 8.12: Comparative study of pressure drop plot for numerical and experimental investigation for post-operative model.

8.9 Conclusions

The variation between the pressure drop obtained from the numerical study and experimental study is significantly small at approximately 3.3 % and 1.2 % for the pre-operative case and post-operative case respectively. Thus, from the comparative study between the results of the pressure drop values obtained from the experimental investigation and numerical analysis, it can be safely concluded that the results obtained from the numerical simulation is acceptable. Hence, from this comparative study, it can be concluded that the numerical method used was successfully verified and can be further used to conduct parametric study for various morphological geometry.

CHAPTER 9

CONCLUSION REMARKS AND FUTURE RECOMMENDATION

9.1 Introduction

Realistic three-dimensional diseased human upper airway of male and female patients was developed by using the CT scans images source from the hospital. Numerical simulation of airflow was performed for inhalation rates of 4, 7.5, 10, 20 and 40 L/min though the developed, diseased nasal airway, constricted pharyngeal representing OSA and diseased upper airway model with chronic nasal obstruction and OSA for the pre- and post-operative cases. By assuming one-way coupling, the Lagrangian particle tracking approach was used to investigate the transport and deposition of microparticle through the diseased upper airway. The injected particle diameter are 1, 5, 10, 20 and 40 μm. Experimental test rig was developed, and realistic pharynx model was fabricated, and experimental study of expiratory flow was conducted. Numerical simulation of expiratory airflow through the pharynx model was conducted for the same flow rate used during experiment. Results obtained from the numerical study was compared and validated with the experimental results. In this chapter, major results and recommendation for future study are discussed.

9.2 Conclusion Remarks

Three-dimensional realistic diseased human upper airway computational models were successfully developed by using the CT scans images obtained before and after surgery. CFD analysis on both the pre- and post-operative diseased nasal airway were also successfully performed. From the first case study, numerical simulation of airflow and particle transport deposition of inhaled pollutant through chronic diseased nasal airway were investigated. In this case study, it was found that nasal surgeries which include septoplasty, inferior turbinate reduction, and partial concha bullosa resection substantially increased nasal volume and influenced flow partitioning and decreases the pressure drop and flow resistance of the nasal passage. Hence, the computed airway resistance has significantly improved after surgery and less effort is needed for breathing the same flow rate into the lung. However, the post-operative model experienced approximately about a 50 % decrease in total particle filtering efficiency. Hence after surgery, more particles can pass through the nasal passage and flow into the lower respiratory tract which could cause adverse health effect to the patient with breathing allergy history.

From the second case study, numerical simulation of laminar and turbulent inspiratory airflow and particle transport and deposition in a constricted upper airway region representing OSA were conducted. In this case study, it was found that the morphology of the upper airway significantly affects the airflow pattern and the deposition fraction of microparticles. The pressure drop from the choanae to the OSA region was larger than the pressure drops through the nasal passages highlighting the effect of OSA on adverse flow behavior in that region. The local deposition fractions

proved that the upper airway plays a significant role in filtering large micro-particles. It was found that, as the diameter of the particle increase, the location of the highest particle deposited region will shift to the anterior part of the upper airway. The presented regional deposition fraction may be used in specifying the site of highest possibility for respiratory lesions.

In the third part of this study, numerical simulation of airflow and particle deposition in the human upper airway with chronic nasal obstruction and OSA were performed. In this case study, it was found that the surgical procedure performed in the nasal airway was found improve the airflow distribution through the upper airway during inhalation process. The combination of the decrease of the airflow resistance and decrease of the magnitude of the negative pressure found in the pharynx region contribute to the improvement of the breathing quality for the OSA patient and reduce the risk of pharyngeal collapse during inspiration. The total deposition efficiency increased as the inhalation rate and particle size increased. The total particle deposition efficiency and particle deposition fraction in regions were found affected by the morphology of the upper airway. For the post-operative case, as the morphology of the upper airway changed after surgery, the local particle deposition hot spot was found located in different region as compared to the pre-operative case.

The comparative study between the results obtained from the experimental investigation and numerical analysis, show that the variation between the pressure drops obtained from the numerical study and experimental study is significantly small at approximately 3.3 %. Hence, the numerical simulation is considered accurate and

the numerical method used was successfully verified and can be further used to conduct parametric study for various morphological geometry.

9.3 Future Recommendations

Based on the presented research findings, several recommendations can be drawn to facilitate and provide future direction of research works.

i. In the present study, particle transport and deposition in the human upper airway with a constricted pharyngeal section is limited to micrometer-sized particles. However, it is known that nanoparticles have a different deposition mechanism. Hence, further work can focus on the transport and deposition of inhaled nanometer-sized particles.

ii. When studying inhaled aerosol particles, most of the researchers used the common simplifications that the aerosol particles are spherical, non-interacting, and monodisperse. These underlying assumptions allow for decoupling of the fluid phase from the particle phase. However, in reality, inhaled particles are possibly not in spherical shape, colliding and aggregating.

iii. Further study may also be carried out to investigate the effect of mucous layer on the particle deposition efficiency in the upper airway.

REFERENCES

Abouali, O., Keshavarzian, E., Farhadi Ghalati, P., Faramarzi, A., Ahmadi, G., & Bagheri, M. H. (2012). Micro and nanoparticle deposition in human nasal passage pre and post virtual maxillary sinus endoscopic surgery. *Respiratory Physiology and Neurobiology*, *181*(3), 335–345. http://doi.org/10.1016/j.resp.2012.03.002

ANSYS FLUENT Theory Guide. (2009). Theory Guide Release 12.0. *ANSYS Inc.*

Austin, C. E., & Foreman, J. C. (1994, January). Acoustic rhinometry compared with posterior rhinomanometry in the measurement of histamine- and bradykinin-induced changes in nasal airway patency. *British Journal of Clinical Pharmacology*.

Bahmanzadeh, H., Abouali, O., Faramarzi, M., & Ahmadi, G. (2015). Numerical simulation of airflow and micro-particle deposition in human nasal airway pre- and post-virtual sphenoidotomy surgery. *Computers in Biology and Medicine*, *61*, 8–18. http://doi.org/10.1016/j.compbiomed.2015.03.015

Bailie, N., Hanna, B., Watterson, J., & Gallagher, G. (2006). An overview of numerical modelling of nasal airflow. *Rhinology*, *44*(1), 53–57.

Banabilh, S. M., Suzina, a. H., Mohamad, H., Dinsuhaimi, S., Samsudin, a. R., & Singh, G. D. (2010). Assessment of 3-D nasal airway morphology in Southeast Asian adults with obstructive sleep apnea using acoustic rhinometry. *Clinical Oral Investigations*, *14*(5), 491–498. http://doi.org/10.1007/s00784-009-0342-9

Basri, E. I., Basri, A. A., Riazuddin, V. N., Farhana, S., Zuber, M., & Ahmad, K. A. (2016). Computational Fluid Dynamics Study in Biomedical Applications : A Review. *International Journal of Fluid and Heat Transfer*, *1*(2), 2–14.

Cheng, Y. S. (2003). Aerosol Deposition in the Extrathoracic Region. *Aerosol Science and Technology*, *37*(8), 659–671. http://doi.org/10.1080/02786820300906

Cho, K., & Cho, Y. (1994). Acute lung disease after exposure to fly ash. *Chest* ..., 309–311. Retrieved from http://journal.publications.chestnet.org/article.aspx?articleid=1067670

Chouly, F., Van Hirtum, a., Lagrée, P. Y., Pelorson, X., & Payan, Y. (2008). Numerical and experimental study of expiratory flow in the case of major upper airway obstructions with fluid-structure interaction. *Journal of Fluids and Structures*, *24*(2), 250–269. http://doi.org/10.1016/j.jfluidstructs.2007.08.004

Chung, S.-K., Son, Y. R., Shin, S. J., & Kim, S.-K. (2006). Nasal airflow during respiratory cycle. *American Journal of Rhinology*, *20*(4), 379–384. http://doi.org/10.2500/ajr.2006.20.2890

Corey, J. P. (2006). Acoustic rhinometry: should we be using it? *Current Opinion in Otolaryngology & Head and Neck Surgery*, *14*(1). Retrieved from http://journals.lww.com/co-otolaryngology/Fulltext/2006/02000/Acoustic_rhinometry__should_we_be_using_it_.7.aspx

Croce, C., Fodil, R., Durand, M., Sbirlea-Apiou, G., Caillibotte, G., Papon, J. F., …

Louis, B. (2006). In Vitro Experiments and Numerical Simulations of Airflow in Realistic Nasal Airway Geometry. *Annals of Biomedical Engineering*, *34*(6), 997–1007. http://doi.org/10.1007/s10439-006-9094-8

Dastan, A., Abouali, O., & Ahmadi, G. (2014). CFD simulation of total and regional fiber deposition in human nasal cavities. *Journal of Aerosol Science*, *69*, 132–149. http://doi.org/10.1016/j.jaerosci.2013.12.008

De Backer, J. W., Vanderveken, O. M., Vos, W. G., Devolder, a., Verhulst, S. L., Verbraecken, J. a., … De Backer, W. a. (2007). Functional imaging using computational fluid dynamics to predict treatment success of mandibular advancement devices in sleep-disordered breathing. *Journal of Biomechanics*, *40*(16), 3708–3714. http://doi.org/10.1016/j.jbiomech.2007.06.022

Doorly, D., Taylor, D. J., Franke, P., & Schroter, R. C. (2008). Experimental investigation of nasal airflow. *Proceedings of the Institution of Mechanical Engineers. Part H, Journal of Engineering in Medicine*, *222*(4), 439–453. http://doi.org/10.1007/s10439-005-4388-9

Eccles, R. (1998). The relationship between subjective and objective measures of nasal function. *Japan Rhinologic Society*, *37*(2), 61–69.

Elad, D., Liebenthal, R., Wenig, B. ., & Einav, S. (1993). Analysis of airflow patterns in the human nose. *Medical and Biomedical Engineering and Computing*, (November), 585–592.

Elad, D., Wolf, M., & Keck, T. (2008). Air-conditioning in the human nasal cavity. *Respiratory Physiology & Neurobiology*, *163*(1–3), 121–127. http://doi.org/10.1016/j.resp.2008.05.002

Ephros, H. D., Madani, M., & Yalamanchili, S. C. (2010). Surgical treatment of snoring & obstructive sleep apnoea. *The Indian Journal of Medical Research*, *131*(February), 267–276.

Farhadi Ghalati, P., Keshavarzian, E., Abouali, O., Faramarzi, A., Tu, J., & Shakibafard, A. (2012). Numerical analysis of micro- and nano-particle deposition in a realistic human upper airway. *Computers in Biology and Medicine*, *42*(1), 39–49. http://doi.org/10.1016/j.compbiomed.2011.10.005

Fogel, R. B., Malhotra, A., & White, D. P. (2004). Sleep · 2: Pathophysiology of obstructive sleep apnoea/hypopnoea syndrome, (February 2008), 159–164. http://doi.org/10.1136/thx.2003.015859

Garcia, G. J. M., Bailie, N., Martins, D. a, & Kimbell, J. S. (2007). Atrophic rhinitis: a CFD study of air conditioning in the nasal cavity. *Journal of Applied Physiology (Bethesda, Md. : 1985)*, *103*(3), 1082–1092. http://doi.org/10.1152/japplphysiol.01118.2006

Ghahramani, E., Abouali, O., Emdad, H., & Ahmadi, G. (2014). Numerical analysis of stochastic dispersion of micro-particles in turbulent flows in a realistic model of human nasal/upper airway. *Journal of Aerosol Science*, *67*, 188–206. http://doi.org/10.1016/j.jaerosci.2013.09.004

Grotberg, J. B. (2001). and T Ransport P Rocesses. *Transport*.

Guha, A. (2008). Transport and Deposition of Particles in Turbulent and Laminar Flow. *Annual Review of Fluid Mechanics*, *40*(1), 311–341. http://doi.org/10.1146/annurev.fluid.40.111406.102220

Guilleminault, C., Tilkian, a, & Dement, W. C. (1976). The sleep apnea syndromes. *Annual Review of Medicine*, *27*, 465–484. http://doi.org/10.1146/annurev.me.27.020176.002341

Hahn, I., Scherer, P. W., & Mozell, M. M. (1993). Velocity profiles measured for airflow through a large-scale model of the human nasal cavity. *J Appl Physiol*, *75*(5), 2273–2287. Retrieved from http://jap.physiology.org/content/75/5/2273

Harkema, J. R., Carey, S. a, & Wagner, J. G. (2006). The nose revisited: a brief review of the comparative structure, function, and toxicologic pathology of the nasal epithelium. *Toxicologic Pathology*, *34*(3), 252–269. http://doi.org/10.1080/01926230600713475

Heyder, J. (2004). Deposition of inhaled particles in the human respiratory tract and consequences for regional targeting in respiratory drug delivery. *Proceedings of the American Thoracic Society*, *1*(4), 315–320. http://doi.org/10.1513/pats.200409-046TA

Heyder, J., Gebhart, J., Rudolf, G., Schiller, C. F., & Stahlhofen, W. (1986). Deposition of particles in the human respiratory tract in the size range 0.005–15 μm.pdf. *Journal of Aerosol Science*, *17*(5), 811–825.

Hilberg, O., Jackson, A. C., Swift, D. L., & Pedersen, O. F. (1989). Acoustic rhinometry: evaluation of nasal cavity geometry by acoustic reflection. *Journal of Applied Physiology (Bethesda, Md. : 1985)*, *66*(1), 295–303.

Hopkins, L. M., Kelly, J. T., Wexler, a. S., & Prasad, a. K. (2000). Particle image velocimetry measurements in complex geometries. *Experiments in Fluids*, *29*(1), 91–95. http://doi.org/10.1007/s003480050430

Inthavong, K., Wen, J., Tian, Z., & Tu, J. (2008). Numerical study of fibre deposition in a human nasal cavity. *Journal of Aerosol Science*, *39*(3), 253–265. http://doi.org/10.1016/j.jaerosci.2007.11.007

Inthavong, K., Zhang, K., & Tu, J. (2009). Modelling Submicron and Micron Particle Deposition in a Human Nasal Cavity. *Seventh International Conference on CFD Inthe Minerals and Process Industries CSIRO, Melbourne, Australia*, (December), 1–7.

Ishikawa, S., Nakayama, T., Watanabe, M., & Matsuzawa, T. (2009). Flow Mechanisms in the Human Olfactory Groove. *Archives of Otolaryngology--Head & Neck Surgery*, *135*(2), 156–162. http://doi.org/10.1001/archoto.2008.530

Ito, Y., Cheng, G. C., Shih, A. M., Koomullil, R. P., Soni, B. K., Sittitavornwong, S., & Waite, P. D. (2011). Patient-specific geometry modeling and mesh generation for simulating Obstructive Sleep Apnea Syndrome cases by Maxillomandibular Advancement. *Mathematics and Computers in Simulation*, *81*(9), 1876–1891. http://doi.org/10.1016/j.matcom.2011.02.006

Jayaraju, S. T. (2009). *Study of the air flow and aerosol transport in the human upper airway using LES and DES Methodologies*. Vrije Universiteit Brussel.

Jeong, S. J., Kim, W. S., & Sung, S. J. (2007). Numerical investigation on the flow characteristics and aerodynamic force of the upper airway of patient with obstructive sleep apnea using computational fluid dynamics. *Medical Engineering & Physics*, *29*(6), 637–651. http://doi.org/10.1016/j.medengphy.2006.08.017

Jones, A. S., & Lancer, J. M. (1987). Rhinomanometry. *Clinical Otolaryngology & Allied Sciences*, *12*(3), 233–236. http://doi.org/10.1111/j.1365-2273.1987.tb00193.x

Karakosta, P., Alexopoulos, A. H., & Kiparissides, C. (2013). Computational model of particle deposition in the nasal cavity under steady and dynamic flow. *Computer Methods in Biomechanics and Biomedical Engineering*, *18*(5), 514–526. http://doi.org/10.1080/10255842.2013.819856

Keyhani, K., Scherer, P. W., & Mozell, M. M. (1995). Numerical simulation of airflow in the human nasal cavity. *Journal of Biomechanical Engineering*, *117*(4), 429–441. http://doi.org/10.1115/1.2794204

Keyhani, K., Scherer, P. W., & Mozell, M. M. (1997). A numerical model of nasal odorant transport for the analysis of human olfaction. *Journal of Theoretical Biology*, *186*(3), 279–301. http://doi.org/10.1006/jtbi.1996.0347

Kim, S. K., & Chung, S. K. (2004). An investigation on airflow in disordered nasal cavity and its corrected models by tomographic PIV. *Measurement Science and Technology*, *15*(6), 1090–1096. http://doi.org/10.1088/0957-0233/15/6/007

Kim, S. K., Na, Y., Kim, J. I., & Chung, S. K. (2013). Patient specific CFD models of nasal airflow: Overview of methods and challenges. *Journal of Biomechanics*, *46*(2), 299–306. http://doi.org/10.1016/j.jbiomech.2012.11.022

Kimbell, J. S., Frank, D. O., Laud, P., Garcia, G. J. M., & Rhee, J. S. (2013). Changes in nasal airflow and heat transfer correlate with symptom improvement after surgery for nasal obstruction. *Journal of Biomechanics*, *46*(15), 2634–2643. http://doi.org/10.1016/j.jbiomech.2013.08.007

Kjaergaard, T., Cvancarova, M., & Steinsvag, S. K. (2009). Relation of nasal air flow to nasal cavity dimensions. *Archives of Otolaryngology--Head & Neck Surgery*, *135*(6), 565–570. http://doi.org/10.1001/archoto.2009.50

Lal, D., & Corey, J. P. (2004). Acoustic rhinometry and its uses in rhinology and diagnosis of nasal obstruction. *Facial Plastic Surgery Clinics of North America*, *12*(4), 397–405, v. http://doi.org/10.1016/j.fsc.2004.04.002

Lindemann, J., Brambs, H. J., Keck, T., Wiesmiller, K. M., Rettinger, G., & Pless, D. (2005). Numerical simulation of intranasal airflow after radical sinus surgery. *American Journal of Otolaryngology - Head and Neck Medicine and Surgery*, *26*(3), 175–180. http://doi.org/10.1016/j.amjoto.2005.02.010

Lipton, A. J., & Gozal, D. (2003). Treatment of obstructive sleep apnea in children: do we really know how? *Sleep Medicine Reviews*, *7*(1), 61–80. http://doi.org/10.1053/smrv.2001.0256

Liu, Y., Matida, E. a., Gu, J., & Johnson, M. R. (2007). Numerical simulation of aerosol deposition in a 3-D human nasal cavity using RANS, RANS/EIM, and

LES. *Journal of Aerosol Science*, *38*(7), 683–700. http://doi.org/10.1016/j.jaerosci.2007.05.003

Lu, M. Z., Liu, Y., Ye, J. Y., & Luo, H. Y. (2014). Large Eddy Simulation of Flow in Realistic Human Upper Airways with Obstructive Sleep. *Procedia Computer Science*, *29*, 557–564. http://doi.org/10.1016/j.procs.2014.05.050

Mamikoglu, B., Houser, S., Akbar, I., Ng, B., & Corey, J. P. (2000). Acoustic rhinometry and computed tomography scans for the diagnosis of nasal septal deviation, with clinical correlation. *Otolaryngology--Head and Neck Surgery : Official Journal of American Academy of Otolaryngology-Head and Neck Surgery*, *123*(1 Pt 1), 61–68. http://doi.org/10.1067/mhn.2000.105255

Menter, F. R. (1994). Two-equation eddy-viscosity turbulence models for engineering applications. *AIAA Journal*, *32*(8), 1598–1605. http://doi.org/10.2514/3.12149

Mihaescu, M., Murugappan, S., Kalra, M., Khosla, S., & Gutmark, E. (2008). Large Eddy simulation and Reynolds-Averaged Navier-Stokes modeling of flow in a realistic pharyngeal airway model: An investigation of obstructive sleep apnea. *Journal of Biomechanics*, *41*(10), 2279–2288. http://doi.org/10.1016/j.jbiomech.2008.04.013

Mihaescu, M., Mylavarapu, G., Gutmark, E. J., & Powell, N. B. (2011). Large Eddy Simulation of the pharyngeal airflow associated with Obstructive Sleep Apnea Syndrome at pre and post-surgical treatment. *Journal of Biomechanics*, *44*(12), 2221–2228. http://doi.org/10.1016/j.jbiomech.2011.06.006

Min, Y. G., & Jang, Y. J. (1995). Measurements of cross-sectional area of the nasal cavity by acoustic rhinometry and CT scanning. *The Laryngoscope*, *105*(7 Pt 1), 757–759. http://doi.org/10.1288/00005537-199507000-00014

Moghadas, H., Abouali, O., Faramarzi, a., & Ahmadi, G. (2011). Numerical investigation of septal deviation effect on deposition of nano/microparticles in human nasal passage. *Respiratory Physiology and Neurobiology*, *177*(1), 9–18. http://doi.org/10.1016/j.resp.2011.02.011

Morsi, S. A., & Alexander, A. J. (2006). An investigation of particle trajectories in two-phase flow systems. *Journal of Fluid Mechanics*, *55*(2), 193. http://doi.org/10.1017/S0022112072001806

Mylavarapu, G., Mihaescu, M., Fuchs, L., Papatziamos, G., & Gutmark, E. (2013). Planning human upper airway surgery using computational fluid dynamics. *Journal of Biomechanics*, *46*(12), 1979–86. http://doi.org/10.1016/j.jbiomech.2013.06.016

Mylavarapu, G., Murugappan, S., Mihaescu, M., Kalra, M., Khosla, S., & Gutmark, E. (2009a). Validation of computational fluid dynamics methodology used for human upper airway flow simulations. *Journal of Biomechanics*, *42*(10), 1553–1559. http://doi.org/10.1016/j.jbiomech.2009.03.035

Mylavarapu, G., Murugappan, S., Mihaescu, M., Kalra, M., Khosla, S., & Gutmark, E. (2009b). Validation of computational fluid dynamics methodology used for human upper airway flow simulations. *Journal of Biomechanics*, *42*(10), 1553–1559. http://doi.org/10.1016/j.jbiomech.2009.03.035

Reber, M., Rahm, F., & Monnier, P. (1998). The role of acoustic rhinometry in the pre- and postoperative evaluation of surgery for nasal obstruction. *Rhinology*, *36*(4), 184—187. Retrieved from http://europepmc.org/abstract/MED/9923062

Riazuddin, V. N., Zubair, M., Abdullah, M. Z., Ismail, R., Shuaib, I. L., Hamid, S. A., & Ahmad, K. A. (2011). Numerical study of inspiratory and expiratory flow in a human nasal cavity. *Journal of Medical and Biological Engineering*, *31*(3), 201–206. http://doi.org/10.5405/jmbe.781

Riazuddin, V. N., Zubair, M., Ahmadi, M., Tamagawa, M., Rashid, N. H. A., Mazlan, N., & Ahmad, K. A. (2016). Computational Fluid Dynamics Study of Airflow and Microparticle Deposition in a Constricted Pharyngeal Section Representing Obstructive Sleep Apnea Disease. *Journal of Medical Imaging and Health Informatics*, *6*(6), 1507–1512. http://doi.org/10.1166/jmihi.2016.1839

Riechelmann, H., O'Connell, J. M., Rheinheimer, M. C., Wolfensberger, M., & Mann, W. J. (1999). The role of acoustic rhinometry in the diagnosis of adenoidal hypertrophy in pre-school children. *European Journal of Pediatrics*, *158*(1), 38–41.

Sarkar, A., Rano, R., Mishra, K. K., & Sinha, I. N. (2005). Particle size distribution profile of some Indian fly ash—a comparative study to assess their possible uses. *Fuel Processing Technology*, *86*(11), 1221–1238. http://doi.org/10.1016/j.fuproc.2004.12.002

Schwab, R. J., Gefter, W. B., Hoffman, E. A., Gupta, K. B., & Pack, A. I. (1993). Dynamic Upper Airway Imaging during Awake Respiration in Normal Subjects and Patients with Sleep Disordered Breathing. *American Review of Respiratory Disease*, *148*(5), 1385–1400. http://doi.org/10.1164/ajrccm/148.5.1385

Segal, R. A., Kepler, G. M., & Kimbell, J. S. (2008). Effects of differences in nasal anatomy on airflow distribution: A comparison of four individuals at rest. *Annals of Biomedical Engineering*, *36*(11), 1870–1882. http://doi.org/10.1007/s10439-008-9556-2

Shaheen, S. M., Hooda, P. S., & Tsadilas, C. D. (2014). Opportunities and challenges in the use of coal fly ash for soil improvements – A review. *Journal of Environmental Management*, *145*, 249–267. http://doi.org/http://dx.doi.org/10.1016/j.jenvman.2014.07.005

Shelton, D. M., & Eiser, N. M. (1992). Evaluation of active anterior and posterior rhinomanometry in normal subjects. *Clinical Otolaryngology & Allied Sciences*, *17*(2), 178–182. http://doi.org/10.1111/j.1365-2273.1992.tb01068.x

Shi, H., Kleinstreuer, C., & Zhang, Z. (2007). Modeling of inertial particle transport and deposition in human nasal cavities with wall roughness. *Journal of Aerosol Science*, *38*(4), 398–419. http://doi.org/10.1016/j.jaerosci.2007.02.002

Sipila, J., & Suonpaa, J. (1997). A prospective study using rhinomanometry and patient clinical satisfaction to determine if objective measurements of nasal airway resistance can improve the quality of septoplasty. *European Archives of Oto-Rhino-Laryngology : Official Journal of the European Federation of Oto-Rhino-Laryngological Societies (EUFOS) : Affiliated with the German Society for Oto-Rhino-Laryngology - Head and Neck Surgery*, *254*(8), 387–390.

Sittitavornwong, S., Waite, P. D., Shih, A. M., Koomullil, R., Ito, Y., Cheng, G. C., & Wang, D. (2009). Evaluation of Obstructive Sleep Apnea Syndrome by Computational Fluid Dynamics. *Seminars in Orthodontics*, *15*(2), 105–131. http://doi.org/10.1053/j.sodo.2009.01.005

Subramaniam, R. P., Richardson, R. B., Morgan, K. T., Kimbell, J. S., & Guilmette, R. A. (1998). Computational Fluid Dynamics simulations of inspiratory airflow in the human nose and nasopharynx. *Inhalation Toxicology*, *10*(2), 91–120. http://doi.org/10.1080/089583798197772

Sung, S. J., Jeong, S. J., Yu, Y. S., Hwang, C. J., & Pae, E. K. (2006). Customized three-dimensional computational fluid dynamics simulation of the upper airway of obstructive sleep apnea. *Angle Orthodontist*, *76*(5), 791–799. http://doi.org/10.2319/071305-231

Suratt, P. M., Dee, P., Atkinson, R. L., Armstrong, P., & Wilhoit, S. C. (1983). Fluoroscopic and computed tomographic features of the pharyngeal airway in obstructive sleep apnea. *The American Review of Respiratory Disease*, *127*(4), 487–492. http://doi.org/10.1097/00004728-198312000-00059

Suzina, A. H., Hamzah, M., & Samsudin, A. R. (2003). Active anterior rhinomanometry analysis in normal adult Malays. *The Journal of Laryngology and Otology*, *117*(8), 605–608. http://doi.org/10.1258/002221503768199924

Tomkinson, A., & Eccles, R. (1995). Errors arising in cross-sectional area estimation by acoustic rhinometry produced by breathing during measurement. *Rhinology*, *33*(3), 138–140.

Tomkinson, A., & Eccles, R. (1998). Acoustic rhinometry: an explanation of some common artefacts associated with nasal decongestion. *Clinical Otolaryngology and Allied Sciences*, *23*(1), 20–26.

Tsuda, A., Henry, F. S., & Butler, J. P. (2013). Particle transport and deposition: basic physics of particle kinetics. *Comprehensive Physiology*, *3*(4), 1437–71. http://doi.org/10.1002/cphy.c100085

Versteeg, H. K., & Malalasekera, W. (1995). An Introduction to Computational Fluid Dynamics - The Finite Volume Method. *Fluid Flow Handbook. McGraw-Hill ...*. http://doi.org/10.2514/1.22547

Vos, W., De Backer, J., Devolder, a., Vanderveken, O., Verhulst, S., Salgado, R., … De Backer, W. (2007). Correlation between severity of sleep apnea and upper airway morphology based on advanced anatomical and functional imaging. *Journal of Biomechanics*, *40*(10), 2207–2213. http://doi.org/10.1016/j.jbiomech.2006.10.024

Wang, S. M., Inthavong, K., Wen, J., Tu, J. Y., & Xue, C. L. (2009). Comparison of micron- and nanoparticle deposition patterns in a realistic human nasal cavity. *Respiratory Physiology and Neurobiology*, *166*(3), 142–151. http://doi.org/10.1016/j.resp.2009.02.014

Wang, Y., Wang, J., Liu, Y., Yu, S., Sun, X., Li, S., … Zhao, W. (2012). Fluid–structure interaction modeling of upper airways before and after nasal surgery for obstructive sleep apnea. *International Journal for Numerical Methods in Biomedical Engineering*, *28*, 528–546. http://doi.org/10.1002/cnm

Wang, Z., Hopke, P. K., Ahmadi, G., Cheng, Y. S., & Baron, P. a. (2008). Fibrous particle deposition in human nasal passage: The influence of particle length, flow rate, and geometry of nasal airway. *Journal of Aerosol Science*, *39*(12), 1040–1054. http://doi.org/10.1016/j.jaerosci.2008.07.008

Weinhold, I., & Mlynski, G. (2004). Numerical simulation of airflow in the human nose. *European Archives of Oto-Rhino-Laryngology*, *261*(8), 452–455. http://doi.org/10.1007/s00405-003-0675-y

Wen, J., Inthavong, K., Tian, Z., Tu, J., Xue, C., & Li, C. (2007). Airflow patterns in both sides of a realistic human nasal cavity for laminar and turbulent conditions. *16th Australasian Fluid Mechanics Conference (AFMC)*, (December), 68–74. Retrieved from http://espace.library.uq.edu.au/view/UQ:132285

Wen, J., Inthavong, K., Tu, J., & Wang, S. (2008). Numerical simulations for detailed airflow dynamics in a human nasal cavity. *Respiratory Physiology & Neurobiology*, *161*(2), 125–135. http://doi.org/10.1016/j.resp.2008.01.012

Wexler, D., Segal, R., & Kimbell, J. (2005). Aerodynamic effects of inferior turbinate reduction: computational fluid dynamics simulation. *Archives of Otolaryngology--Head & Neck Surgery*, *131*(12), 1102–1107. http://doi.org/10.1001/archotol.131.12.1102

Xi, J., & Longest, P. W. (2007). Transport and deposition of micro-aerosols in realistic and simplified models of the oral airway. *Annals of Biomedical Engineering*, *35*(4), 560–581. http://doi.org/10.1007/s10439-006-9245-y

Xi, J., Si, X., Kim, J. W., & Berlinski, A. (2011). Simulation of airflow and aerosol deposition in the nasal cavity of a 5-year-old child. *Journal of Aerosol Science*, *42*(3), 156–173. http://doi.org/10.1016/j.jaerosci.2010.12.004

Xiong, G.-X., Zhan, J.-M., Zuo, K.-J., Rong, L.-W., Li, J.-F., & Xu, G. (2011). Use of computational fluid dynamics to study the influence of the uncinate process on nasal airflow. *The Journal of Laryngology & Otology*, *125*(1), 30–37. http://doi.org/10.1017/S002221511000191X

Xiong, G., Zhan, J.-M., Jiang, H.-Y., Li, J.-F., Rong, L.-W., & Xu, G. (2008). Computational fluid dynamics simulation of airflow in the normal nasal cavity and paranasal sinuses. *American Journal of Rhinology*, *22*(5), 477–482. http://doi.org/10.2500/ajr.2008.22.3211

Xu, C., Sin, S., McDonough, J. M., Udupa, J. K., Guez, A., Arens, R., & Wootton, D. M. (2006). Computational fluid dynamics modeling of the upper airway of children with obstructive sleep apnea syndrome in steady flow. *Journal of Biomechanics*, *39*(11), 2043–2054. http://doi.org/10.1016/j.jbiomech.2005.06.021

Zamankhan, P., Ahmadi, G., Wang, Z., Hopke, P. K., Cheng, Y.-S., Su, W. C., & Leonard, D. (2006). Airflow and Deposition of Nano-Particles in a Human Nasal Cavity. *Aerosol Science and Technology*, *40*(6), 463–476. http://doi.org/10.1080/02786820600660903

Zhang, Z., & Kleinstreuer, C. (2011). Computational analysis of airflow and nanoparticle deposition in a combined nasal-oral-tracheobronchial airway model. *Journal of Aerosol Science*, *42*(3), 174–194.

http://doi.org/10.1016/j.jaerosci.2011.01.001

Zhang, Z., Kleinstreuer, C., Donohue, J. F., & Kim, C. S. (2005). Comparison of micro- and nano-size particle depositions in a human upper airway model. *Journal of Aerosol Science*, *36*(2), 211–233. http://doi.org/10.1016/j.jaerosci.2004.08.006

Zhao, K., Scherer, P. W., Hajiloo, S. a., & Dalton, P. (2004). Effect of anatomy on human nasal air flow and odorant transport patterns: Implications for olfaction. *Chemical Senses*, *29*(5), 365–379. http://doi.org/10.1093/chemse/bjh033

Zhao, M., Barber, T., Cistulli, P. a., Sutherland, K., & Rosengarten, G. (2013a). Simulation of upper airway occlusion without and with mandibular advancement in obstructive sleep apnea using fluid-structure interaction. *Journal of Biomechanics*, *46*(15), 2586–2592. http://doi.org/10.1016/j.jbiomech.2013.08.010

Zhao, M., Barber, T., Cistulli, P., Sutherland, K., & Rosengarten, G. (2013b). Computational fluid dynamics for the assessment of upper airway response to oral appliance treatment in obstructive sleep apnea. *Journal of Biomechanics*, *46*(1), 142–150. http://doi.org/10.1016/j.jbiomech.2012.10.033

Zhu, J. H., Lim, K. M., Thong, K. T. M., Wang, D. Y., & Lee, H. P. (2014). Assessment of airflow ventilation in human nasal cavity and maxillary sinus before and after targeted sinonasal surgery: A numerical case study. *Respiratory Physiology and Neurobiology*, *194*(1), 29–36. http://doi.org/10.1016/j.resp.2014.01.004

Zubair, M., Ahmad, K. A., Abdullah, M. Z., & Sufian, S. F. (2015). Characteristic airflow patterns during inspiration and expiration: experimental and numerical investigation. *Journal of Medical and Biological Engineering*, *35*, 387–394.

Zubair, M., Riazuddin, V. N., Abdullah, M. Z., Ismail, R., Shuaib, I. L., & Ahmad, K. A. (2013). Computational fluid dynamics study of the effect of posture on airflow characteristics inside the nasal cavity. *Asian Biomedicine*, *7*(6), 835–840. http://doi.org/10.5372/1905-7415.0706.247

Zubair, M., Riazuddin, V. N., Zulkifly, M., & Ismail, R. (2010). Airflow inside the nasal cavity : visualization using computational fluid dynamics. *Asian Biomedicine*, *4*(4), 657–661.

APPENDIX I

ETHICAL APPROVAL LETTER FROM THE CLINICAL RESEARCH CENTRE COMMITTEE

PUSAT PENYELIDIKAN KLINIKAL
(CLINICAL RESEARCH CENTRE)
ARAS 2 HOSPITAL SERDANG
JALAN PUCHONG
43000 KAJANG
SELANGOR DARUL EHSAN

CRC
Research that matters to patients
Telefon : 03-89475467
Fax : 03-89475467

Ruj kami : HSDG/P/CRC/710/11/9(182)
Tarikh : 13hb. JULAI, 2015

Tuan,

KELULUSAN MENJALANKAN PENYELIDIKAN DI HOSPITAL SERDANG

Dengan segala hormatnya merujuk kepada perkara di atas,

2. Sukacita dimaklumkan bahawa Jawatankuasa Pusat Penyelidikan Klinikal (CRC) Hospital Serdang telah meluluskan permohonan penyelidikan tuan seperti yang berikut :

Penyelidik:	**Dr. Nur Hashima binti Abdul Rashid**
NMRR ID:	**NMRR-15-758-27582**
Tajuk:	**Numerical Investigation of the Airflow and Particle Deposition on the Pre- and Post-Operative Diseased Nasal Airway.**
Tarikh Penyelidikan:	**13hb. Julai, 2015**
Penyelia:	**Dr. Sharifah @ Masturs binti Syed Abu Bakar (Jabatan Radiologi)**

3. Penyelidikan tuan adalah tertakluk kepada kelulusan *Medical Research Ethics Committee* (MREC) dan *National Medical Research Register* (NMRR), Kementerian Kesihatan Malaysia (MOH).

4. Sila kemukakan **Laporan Akhir** kepada Pusat Penyelidikan Klinikal (PPK) Hospital Serdang sebaik sahaja penyelidikan tamat .

Sekian, terima kasih.

"BERKHIDMAT UNTUK NEGARA"

"PENYAYANG, BEKERJA BERPASUKAN DAN PROFESIONALISMA ADALAH BUDAYA KERJA KITA"

Saya yang menurut perintah,

DR. GOH BAK LEONG
Ketua
Pusat Penyelidikan Klinikal
Hospital Serdang

APPENDIX II

ETHICAL APPROVAL LETTER FROM THE MEDICAL RESEARCH AND ETHICS COMMITTEE

JAWATANKUASA ETIKA & PENYELIDIKAN PERUBATAN
(Medical Research & Ethics Committee)
KEMENTERIAN KESIHATAN MALAYSIA
d/aInstitut Pengurusan Kesihatan **Tel. : 03 2282 9082/03 2282 9085**
Jalan Rumah Sakit, Bangsar **03 2287 4032/03 2282 0491**
59000 Kuala Lumpur **Faks: 03 22828072/03 2282 0016**

Ruj. Kami : (5) KKM/NIHSEC/P15-881
Tarikh: 23 Julai 2015

Dr Nur Hashima binti Abdul Rashid
Unit Otorinolaringologi,
Jabatan Pembedahan,
Fakulti Perubatan dan Sains Kesihatan
Universiti Putra Malaysia (UPM)

Tuan/Puan

NMRR-15-758-25782 (IIR)
Numerical Investigation of the Airflow and Particle Deposition on the Pre- and Post-operative Diseased Nasal Airway

Lokasi Kajian: Hospital Serdang

Dengan hormatnya perkara di atas adalah dirujuk

2. Jawatankuasa Etika & Penyelidikan Perubatan (JEPP), Kementerian Kesihatan Malaysia (KKM) tiada halangan, dari segi etika, ke atas pelaksanaan kajian tersebut. JEPP mengambil maklum bahawa kajian tersebut tidak mempunyai intervensi klinikal ke atas subjek dan hanya melibatkan imej imbasan CT sahaja

3. Segala rekod dan data adalah SULIT dan hanya digunakan untuk tujuan kajian ini dan semua isu serta prosedur mengenai ***data confidentiality*** mesti dipatuhi. Kebenaran daripada Pegawai Kesihatan Daerah/Pengarah Hospital dan Ketua-Ketua Jabatan atau pegawai yang bertanggung jawab disetiap lokasi kajian di mana kajian akan dijalankan mesti diperolehi sebelum kajian dijalankan. Tuan/Puan perlu akur dan mematuhi keputusan tersebut.

4. Adalah dimaklumkan bahawa kelulusan ini adalah sah sehingga **23 Julai 2016**. Tuan/Puan perlu menghantar dokumen-dokumen seperi berikut selepas mendapat kelulusan etika . Borang-borang berkaitan boleh dimuat turun daripada laman web MREC (*http://www.nih.gov.my/mrec*).

I. *'Continuing Review Form'* selewat-lewatnya 2 bulan sebelum tamat tempoh kelulusan ini bagi memperbaharui kelulusan etika.
II. Laporan tamat kajian pada penghujung kajian.
III. Laporan mengenai *"All adverse events, both serious and unexpected"/Protocol Deviation* atau *Violation* kepada Jawatankuasa Etika & Penyelidikan Perubatan, KKM jika berkenaan.
IV. Memaklumkan jika terdapat pindaan keatas sebarang dokumen kajian